NIRS－M－64

特別研究「重粒子線等の医学利用に関する調査研究」論文集

第　2　集

（昭和60年４月－61年３月）

放射線医学総合研究所

Collected Papers of Project Research "Medical Use of Accelerated Heavy Ions"

No. 2

(April 1985 – March 1986)

National Institute of Radiological Sciences
9-1, Anagawa 4-chome, Chiba-shi, 260 Japan

序

昭和６０年度には重粒線がん治療装置の概念設計研究が行なわれることになった。昭和５９年度に行なわれた重粒子加速器の概念調査では医療装置としての仕様が討議されてその目標が定められた。今年度はその仕様に基ずいて医療用加速器を基本設計するために必要な工学的な研究が国内の主要加速器メーカーの参加を求めて行なわれ、その成果は昭和６１年３月６日、７日の両日にわたり放医研で開催された「放医研重粒子線がん治療装置国際ワークショップ」のもとで討議され評価された。このワークショップには米国、西独、フランスから加速器物理の専門家が招かれ、概念設計研究の内容は国際的な視野のもとに肉付されると共に、日本の計画が世界に、それも公式に紹介されたことは、これからの計画を進める上で大きく寄与するものと考えられる。

一方、ポジトロン核医学の分野では念願であったサイクロトロン棟の増築計画が２年計画のもとで実現できることが決まり、これまで短寿命ＲＩの生産から薬剤の投与に至る一貫したシステムの流れが不十分であったがために存在した問題点を一挙に解決できる見通しがついた。

昭和６０年度は特別研究を進めるために極めて重要な設備の計画と建設が具体化された年度として記録されよう。

論文集第２集をまとめるに当り、研究の推進に御協力していただいた方々に感謝するとともに今後の力添えを期待するものである。

特研班長　　恒　元　　博

目　　次

日本医放会誌：45（12），1532—1539，1985（昭60）

放医研サイクロトロンによる速中性子線の胸部不均質組織における線量計算法の検討

放射線医学総合研究所臨床研究部
中村　譲　古川　重夫　飯沼　武
物理研究部
川島　勝弘　星野　一雄　平岡　武
病院部
恒　元　博

（昭和60年4月22日受付）
（昭和60年7月31日最終原稿受付）

Studies on Dose Calculation of Thorax Inhomogeneity for Fast Neutron Beam from NIRS Cyclotron

Yuzuru Kutsutani-Nakamura, Shigeo Furukawa and Takeshi A. Iinuma
Division of Clinical Research, National Institute of Radiological Sciences
Katsuhiro Kawashima, Kazuo Hoshino and Takeshi Hiraoka
Division of Physics, National Institute of Radiological Sciences
Hiroshi Tsunemoto
Division of Hospital, National Institute of Radiological Sciences

Research Code No. : 203.2

Key Words : Thorax dose calculation, Tissue inhomogeneity correction, Fast neutron, Power law TAR method, Cyclotron

The power law tissue-air ratio (TAR) method developed by Batho appears to be most accurate for inhomogeneity corrections to the dose calculated in a layered media for photon beam therapy. The power law TAR equation for tissue inhomogeneity correction of fast neutron beam therapy was examined to make the implicit approximation clear. The neutron beam is produced by bombarding a thick beryllium target with 30 MeV deuterons. Lung phantom was made of granulated tissue equivalent (TE) plastic which resulted in the densities of 0.30 and 0.60 g/cm^3. Depth dose distributions in thorax tissues for neutron beam were measured by an air-filled cylindrical ionization chamber with TE plastic wall. The power law TAR equation considering the physical density correction was compared with the measured data. A good result has been obtained that the calculated dose is within ±4% against the measured.

I. 緒　言

放射線医学総合研究所（以下放医研という）における医用サイクロトロンによる速中性子線治療の clinical trial は昭和50年11月から開始された．この clinical trial のために基礎的な線量分布を測定し，その結果について報告を行った[1)2)]．今回は不均質組織として胸部不均質組織の線量分布をとりあげた．

速中性子線の線量分布はphotonと似ているので，速中性子線の胸部不均質組織での線量分布はphotonで用いられている補正法が適用できると考えられる．Photonでの胸部不均質組織の線量分布は水中の標準線量分布を補正し求める方法が一般的である．そこで肺組織を含めた胸部組織中の線量分布を測定し，photonで用いられている補正法として比較的精度の高いBatho[3]及びSontagら[4]のべき乗組織/空中線量比（TAR）法（以下べき乗TAR法という）をとりあげ，速中性子線に対しても適用できるかどうか検討した．比較的良い結果がえられたのでその結果について報告する．

II. 方　法

中性子線源は放医研サイクロトロンから発生する30MeV重陽子（電流30μA）を厚いベリリウムターゲットにあて生ずる速中性子線（d(30)＋Be速中性子線と書く）を用いた．速中性子線は垂直下方に射出される．コリメータは圧縮木材（Benelex 402）と鋼材とから構成され，照射野は鋼材によって作られる[5]．

組織等価（以下TEという）ファントムはTEプラスチック（密度（ρ）＝1.10g/cm^3）を用いた[6]．肺ファントムの材料は密度を0.30g/cm^3，0.60g/cm^{3}になるようにMcGinleyとMcLarenによる方法[7]を用い，TEプラスチックを粉砕機（池田理化製ウィレー粉砕機W-100）で1mmϕ（ρ＝0.30g/cm^3）と2mmϕ（ρ＝0.60g/cm^3）の粒状にしたもの（以下これを肺用TEプラスチックという）を用いた．肺ファントムは枠組みされたプラスチック板（板の厚さ1mm，枠の大きさ20×20cm^2）をサランラップで包み，それに密度0.30g/cm^{3}及び0.60g/cm^{3}の肺用プラスチックを入れて作成した（枠の厚さ1cm，2cm，3cmの3種類．）．胸部ファントムはTEファントム，肺ファントム，TEファントムの順に重ねた．線量計は空気を電離気体とした内径6mm，長さ16mm，壁厚0.5mmのTEプラスチック製円筒形電離箱に4.5mmのTEプラスチックビルドアップキャップを被せたものを用いた．

ファントム中の線量分布はビーム軸上の線量を測定した．

不均質組織中の線量分布の補正法

不均質組織中の線量分布の補正法としてべき乗TARを用い，本報で用いた方法を以下に示す．

Fig. 1 (a)に示されるように密度ρ_1の組織中における深さd_1（点P）での線量D_1は空中線量をD_{air}とすると（1）式で表わされる．

$$D_1 = D_{air}\ T(d_1, A)^{\rho_1} \quad \cdots\cdots(1)$$

但し，A：深さd_1での照射野

T（d_1, A）：密度1.0g/cm^{3}の組織中，深さd_1，照射野AでのTAR

密度ρ_1の組織中のTARは（1）式から（2）式で表わされる．

$$D_1/D_{air} = T(d_1, A)^{\rho_1} \quad \cdots\cdots(2)$$

密度ρ_0の組織中，深さd_1（点P）でのTAR及び線量をそれぞれ$T_0(d_1, A)$及びD_0とするとT_0

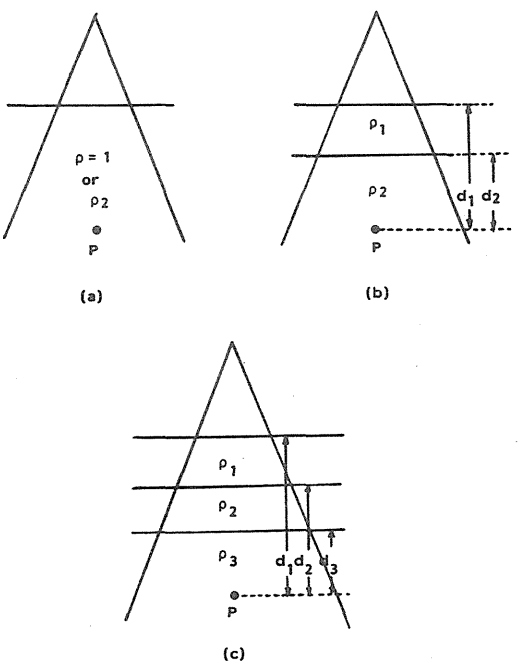

Fig. 1 Schematic diagram showing an inhomogeneous tissue.
(a) In tissue of density ρ at depth d.
(b) In tissue of density ρ_2 at depth d_2 beyond tissue of density ρ_1.
(c) In tissue of density ρ_3 at depth d_3 beyond heterogeneous tissue of (b).

(d_1, A) は (3) 式で表わされる.

$$T_0(d_1, A)=D_0/D_{air}=T(d_1, A)^{\rho_0} \cdots\cdots(3)$$

(2) 式と (1) 式を (3) 式, 即ち $T_0(d_1, A)$ を用いて表わすとそれぞれ (4) 式と (5) 式で表わされる.

$$D_1/D_{air}=T_0(d_1, A)^{\rho_1/\rho_0} \cdots\cdots(4)$$

$$D_1=D_0T_0(d_1, A)^{(\rho_1-\rho_0)/\rho_0} \cdots\cdots(5)$$

もし密度 ρ_0 の組織中の TAR 及び線量が分ると密度の異なる組織 (密度 ρ_1) での TAR 及び線量は (4) 式及び (5) 式を用い求めることができる.

(5) 式で, $\rho_0=\rho_1$ の時, (5) 式は (6) 式と表わされる.

$$D_1=D_0 \cdots\cdots(6)$$

速中性子線の測定に用いられる TE ファントムの密度は通常1.0g/cm³でない場合が多いので, $T_0(d_1, A)$ 及び D_0 を用い表わした方が一般的である.

次に Fig. 1(b) に示されるように密度 ρ_1 の組織中に密度 ρ_2 の組織がある時, 点 P での線量を D_2 とすると D_2 と D_1 との比は (7) 式又は (8) 式で表わされる.

$$D_2/D_1=T(d_2, A)^{\rho_2}/T(d_2, A)^{\rho_1}$$
$$=T(d_2, A)^{\rho_2-\rho_1} \cdots\cdots(7)$$

$$D_2/D_1=T_0(d_2, A)^{(\rho_2-\rho_1)/\rho_0} \cdots\cdots(8)$$

但し, d_2 は密度 ρ_2 の組織中の入り口から点 P までの距離である.

(7) 式は (9) 式に, (8) 式は (5) 式とから (10) 式のように表わされる.

$$D_2=D_1T(d_2, A)^{\rho_2-\rho_1} \cdots\cdots(9)$$

$$D_2=D_1T_0(d_2, A)^{(\rho_2-\rho_1)/\rho_0}$$
$$=D_0T_0(d_1, A)^{(\rho_1-\rho_0)/\rho_0}$$
$$\cdot T_0(d_2, A)^{(\rho_2-\rho_1)/\rho_0} \cdots\cdots(10)$$

(10) 式でもし $\rho_0=\rho_1$ の時, (10) 式は (11) 式で表わされる.

$$D_2=D_0T_0(d_2, A)^{(\rho_2-\rho_1)/\rho_0} \cdots\cdots(11)$$

Fig. 1 (c) に示す2つの密度の異なる組織に密度 ρ_3 の組織が加わった場合, 密度 ρ_3 の組織の入り口から点 P までの距離を d_3, 点 P での線量を D_3 とすると D_3 は (12) 式又は (13) 式で表わされる.

$$D_3=D_1T(d_2, A)^{\rho_2-\rho_1}T(d_3, A)^{\rho_3-\rho_2}$$
$$=D_1\prod_{i=2}^{3}T(d_i, A)^{\rho_i-\rho_{i-1}} \cdots\cdots(12)$$

$$D_3=D_0T_0(d_1, A)^{(\rho_1-\rho_0)/\rho_0}T_0(d_2, A)^{(\rho_2-\rho_1)/\rho_0}$$
$$\cdot T_0(d_3, A)^{(\rho_3-\rho_2)/\rho_0}$$
$$=D_0\prod_{i=1}^{3}T_0(d_i, A)^{(\rho_i-\rho_{i-1})/\rho_0} \cdots\cdots(13)$$

(13) 式でもし $\rho_0=\rho_1$ の時, (13) 式は (14) 式

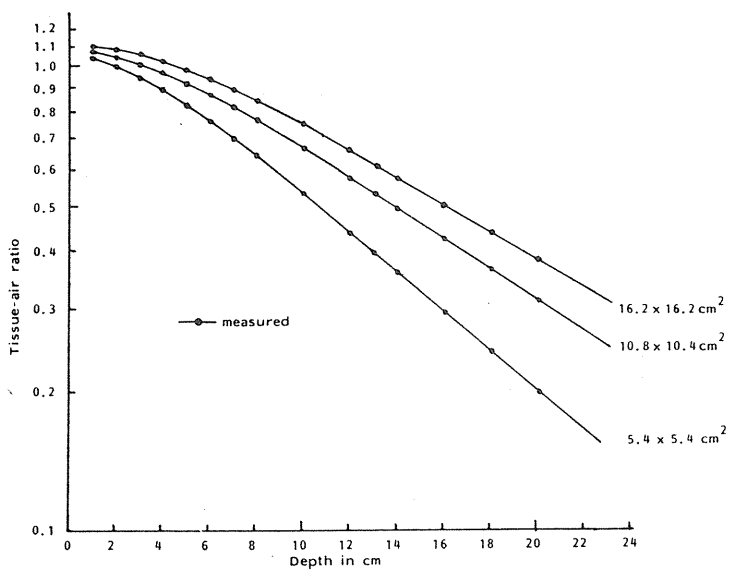

Fig. 2 Tissue-air ratio measured in tissue equivalent phantom for NIRS d(30)+Be neutrons.

と表わされる．

$$D_3=D_0\prod_{i=2}^{3}T_0(d_i,A)^{(\rho_i-\rho_{i-1})/\rho_0}\cdots\cdots\cdots\cdots(14)$$

もし密度が既知の組織中の TAR 及び線量が分ればそれと異なった密度の組織中の線量は(5)式，(6) 式及び (9)～(14) 式を用い求めることができる．

III. 結　果

1. 肺ファントム中の組織/空中線量比 (TAR)

線源一線量計間距離 (SCD) 190cm での TE ファントム中 ($\rho=1.10g/cm^3$) の TAR を照射野 (A) 5.4×5.4，10.8×10.8及び16.2×16.2cm²についての測定結果を Fig. 2の黒丸として示す．実線は黒丸を結んだものである．Fig. 3に密度0.60 g/cm³の肺用プラスチックで作成した肺ファントム中の TAR を Fig. 2と同様の条件で測定した結果を黒丸として示す．Fig. 3の実線は (4) 式を用い，Fig. 2の TAR を $\rho_1/\rho_0=0.60/1.10=0.55$乗して求めたものを示してある．両者は良く一致している．

2. 胸部ファントム中の線量分布

TE ファントム3cm の次に密度0.60g/cm³の肺ファントム10cm をおき，その後に TE ファントム10cm をおいた胸部ファントム中の深部量百分率を測定した．線源—ファントム表面間距離 (SSD)を190cm，ファントム表面での照射野(A_0) 5.4×5.4，10.8×10.8及び16.2×16.2cm²の胸部ファントム中の深部量百分率の測定結果をそれぞれ Figs. 4 (a)，(b) 及び (c) に黒丸として示す．実線は黒丸を結んだものである．鎖線は TE ファントム中の深部量百分率，点線は TE ファントム3cm の後に肺ファントムをおいた場合の深部量百分率の測定結果をそれぞれ示している．

胸部ファントム中の線量分布と均一 TE ファントム中の線量分布との比較では深さとともにその差は大きく変るが，TE ファントム後におかれた肺ファントム中の線量分布とは深さ20cm までそれ程大きく相違していない．

Fig. 4の白丸は Fig. 2の TE ファントム中の TAR 及び Fig. 4の鎖線で示す深部量百分率の測定値と $\rho_2=0.60g/cm^3$，$\rho_0=\rho_1=\rho_3=1.10g/cm^3$を (11) 式及び (14) 式に代入し胸部ファントム中の深部量百分率として求めた計算値である．胸部ファントム中の線量分布の測定値と計算値との比較では TE ファントムから肺ファントムに入る領域では計算値は実測値より深部量百分率で1～3％多くなり，逆に肺ファントムから後方の TE ファントムに入る領域では計算値は実測値より深部量百分率で1～3％少なくなっているが良く一致している．

胸部ファントムのビーム入射側の TE ファントムの厚さを厚くし5cm にした場合，深部量百分率の測定結果を Fig. 5の黒丸として示す．照射野，照射条件は Fig. 4と同様である．実線は Fig. 4の白丸の時と同様な方法で求めた深部量百分率の計

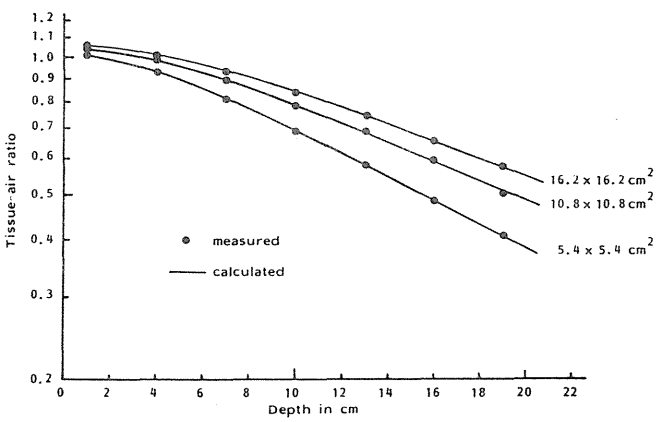

Fig. 3　Comparison of measured and calculated values of tissue-air ratio in lung phantom of 0.60g/cm³.

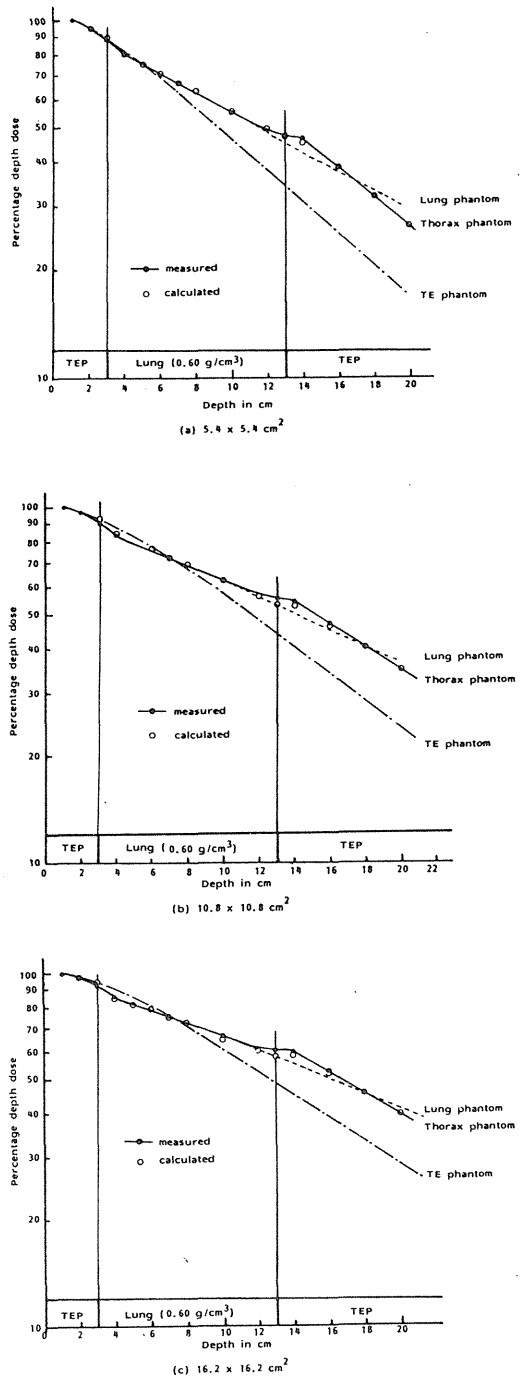

Fig. 4 Comparison of percentage depth dose measured and calculated by the power law TAR method in thorax phantom (TE 3cm+lung 10 cm+TE 10cm) with lung density of 0.60g/cm³.

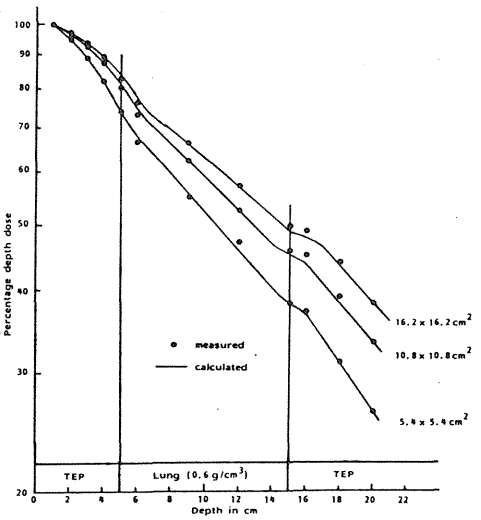

Fig. 5 Comparison of percentage depth dose measured and calculated by the power law TAR method in thorax phantom (TE 5cm+lung 10cm+TE 10cm) with lung density of 0.60g/cm³.

算値を示したものである．ビーム入射側のTEファントムの厚さが厚くなってもFig. 4と同様の結果がえられ，不均質組織の境界近傍で値の相違がみられるが深部量百分率で多くて±3%の差で良く一致している．

次に肺ファントムの密度を小さくし，人体肺組織の平均値近くである0.30g/cm³の肺用TEプラスチックで作成した肺ファントムを用いた場合の胸部ファントム中の深部量百分率をSSD=175 cm，A_0=5.0×5.0，10×10，15×15cm²の条件で測定した．ビーム入射側のTEファントムの厚さを3cmにした場合をFig. 6(a)に，厚さを5cmにした場合の測定結果をFig. 6(b)にそれぞれ黒丸として示す．実線はTEプラスチックのTAR，深部量百分率の測定値を用い計算により求めた胸部ファントム中の深部量百分率の計算値を示す．

線量分布の実測値と計算値との比較では傾向はFig. 4及びFig. 5と同様であるが，肺ファントムの密度が0.30g/cm³と小さくなったためか密度0.60g/cm³と比べ，値の差が生じ，とくに大照射野の不均質組織の境界近傍と小照射野の肺ファントムに入った領域で大きく，しかし深部量百分率

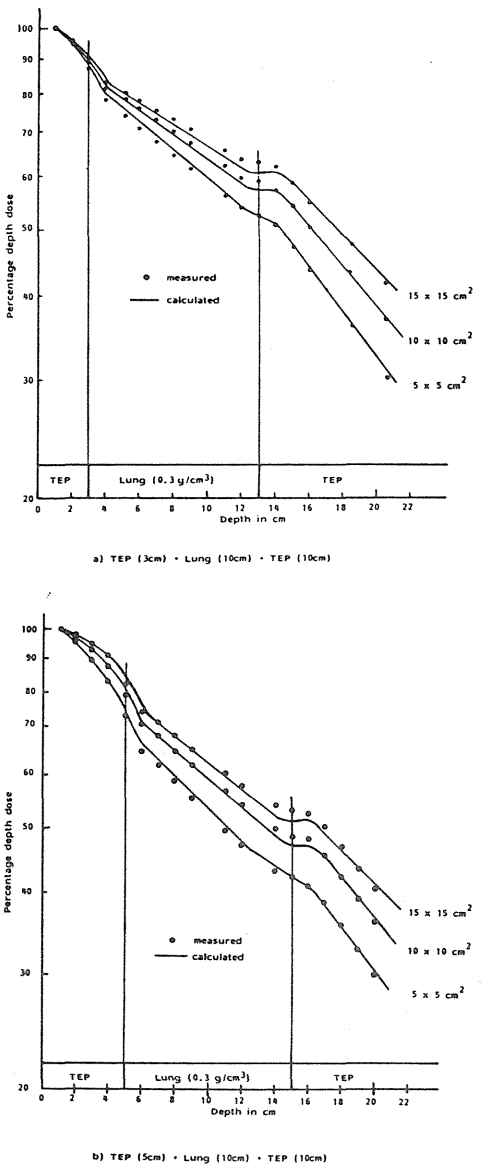

Fig. 6　Comparison of percentage depth dose measured and calculated by the power law TAR method in thorax phantom with lung density of 0.30g/cm³.

で±4％程度である．

IV. 考　察

本報では不均質組織として胸部不均質組織の線量分布をとりあげた．

胸部不均質組織の肺ファントム材料としてphotonではコルクが良く用いられているが，原子組成が人体軟組織に近いTEプラスチックを用い，密度を小さくするためにMcGinleyとMcLarenの粒状にする方法を採用した[7]．

胸部ファントム中の線量分布を測定し，photonで用いられている線量分布補正法としてのべき乗TAR法による計算値との比較を行った．Figs. 4～6から肺ファントムの密度0.3～0.6g/cm³に対し及び肺ファントム前面のTEファントムの厚さが変っても計算値は実測値と不均質組織の境界領域で深部量百分率で最大±4％程度の相違を生ずるが良く一致し，胸部不均質組織の線量分布を求める補正法としてべき乗TAR法はphotonと同様に速中性子線の場合でも良い精度で計算できることが分った．

次に速中性子線の胸部不均質組織における線量計算法についてphotonで用いられている方法が適用できるか，今まで報告された文献は数少ないが考察する．

べき乗TAR法についてはWoottonらの報告のみでそれも肺ファントム背後の組織中の線量についてである[8]．即ちd(21.5)＋Be速中性子線に対し，肺ファントム材料に有機繊維板(ρ＝0.29g/cm³)を用い，肺ファントムの厚さ1.3cm，3.8cm及び5.5cmの背後2cm深さ以降の組織中の線量はべき乗TAR法を用いた場合4％以下の相違で一致したと報告している．

WilliamとMijnheer[9]はphotonと同じ補正法が適用できるものとして等価深さ（equivalent depth)法にふれ，それをd(50)＋Be速中性子線の場合に適用し，後述するSmithらの方法[10]と比較すると高い値を示し，等価深さ法は速中性子線の胸部不均質組織の補正法に適さないので，ICRU 24に述べられている位置の補正係数（position correction factor)[11]の必要性を述べている．

このように速中性子線の胸部不均質組織の線量分布の補正法にphotonで用いられている方法が必らずしも適用できず，その理由として，①本報で用いた速中性子線の深部量百分率は^{60}Coガンマ線とほぼ等しいが[1]，用いているSSDが長いので速中性子線のTARは^{60}Coガンマ線より^{137}Cs

ガンマ線に近く異なっていること，② Fig. 4から明らかのように大きい照射野において肺ファントムに入る境界領域と肺ファントムから出る境界領域の線量分布で，前者はTEファントム中の線量分布より低くなり，後者は肺ファントム中の線量分布より高くなり，後方からの散乱線の寄与が高エネルギーphotonに比し大きいことなどがあげられる．

そこで速中性子線に適した独自の補正法を用いることも必要である．

McGinleyとMcLarenは本報で採用した方法で肺ファントム材料を作成し，肺の形状をした肺ファントムをTE液体で作った楕円形をした胸部ファントムに入れ，d(35)＋Be速中性子線を用いて胸部不均質組織中の線量補正係数を指数関数で近似する方法を提案し良く一致したと報告している[7]．Smithらはd(50)＋Be速中性子線を用いてサルによるin vivo実験で肺組織中の深さと肺組織前面の組織の厚さとの比に対する線量補正係数を簡単な1次式で近似する方法を提案し，患者のin vivo測定でも4％以下で適した報告している[10]．

以上photonで用いられているべき乗TAR法以外による方法は必らずしも速中性子線に適用できるとはいえず，速中性子線に適した独自の補正法か，本報で採用したべき乗TAR法を用いる必要がある．

最後にWoottonらのべき乗TAR法を用いた場合の実測値との比較で本報に比べ幾分悪いがそれは①重陽子の加速エネルギーが21.5MeVなので速中性子線のエネルギーが本報に比べ低いこと，②TEファントムの密度は本報では1.10g/cm³を用い1.0g/cm³と異なり，そのために（14）式を用いたが，Woottonらの方法ではその考慮がなされていないことなどがあげられる．

V. 結　論

速中性子線の胸部不均質組織の肺ファントム物質としてTEプラスチックを用い，密度を0.30，0.60g/cm³にするために1mmϕ，2mmϕの粒状にした．胸部ファントムは肺ファントムをTEファントムでサンドイッチにし，それをビーム中心軸に垂直におき，ビーム中心軸上の線量をTE壁電離箱を用い測定した．TEファントムで測定したTAR，深部量百分率を用い，不均質組織での線量補正法としてphotonで用いられるべき乗TAR法によってえられる計算値と測定値とを比較した．不均質組織の境界領域で両者の値に幾分相違がみられるが比較的良く一致し，べき乗TAR法が速中性子線の場合にも適用できることが分った．

本稿を終わるに当り，安定したビームの供給に留意された技術部サイクロトロン管理課の諸氏に謝意を表する．

本論文の要旨は第45回及び第46回日本医学放射線学会物理部会大会において報告した．

（本研究は厚生省がん研究助成金　尾内斑56—32から一部援助を受けた．）

文　献

1) 星野一雄，川島勝弘，平岡　武，久津谷譲：放医研サイクロトロンからの速中性子線の線量分布．日本医放会誌，37：248—255，1977
2) 中村　譲，古川重夫，飯沼　武，恒元　博，川島勝弘，星野一雄，平岡　武，丸山隆司：放医研サイクロトロンによる速中性子線用ウェッジフィルタ．日本医放会誌，43：691—699，1983
3) Batho, H.F.: Lung corrections in cobalt 60 beam therapy. J. Can. Assoc. Radiol., 15: 79—83, 1964
4) Sontag, M.R. and Cunningham, J.R.: Correction of absorbed dose calculations for tissue inhomogeneities. Med. Phys., 4: 431—436, 1977
5) 丸山隆司，稲田哲雄，平岡　武，河内清光，橋詰雅，恒元　博，久津谷譲，梅垣洋一郎：速中性子線治療用コリメータの設計およびその特性．日本医放会誌，38：633—642，1978
6) 平岡　武，川島勝弘，星野一雄，松沢秀夫：中性子線用組織等価物質の試作．日本医放会誌，36：420—424，1976
7) McGinley, P.H. and McLaren, J.R.: Perturbation of neutron dose distributions by lung tissue. Med. Phys., 1: 219—222, 1974
8) Wootton, P., Weaver, K. and Eenmaa, J.: Treatment planning for neutron radiation therapy. Int. Rad. Oncol. Biol. Phys., 3: 177—183, 1977
9) Williams, J.R. and Mijnheer, B.J.: Survey of determinations of dose distributions, influence of oblique incidence, tissue composition and wedge filters. (In) Burger G., Breit A., Broerse

J.J. ed: Treatment for external beam therapy with neutrons. Strahlentherapie Suppl., 77: 93—99, 1981, Urban & Schwarzenberg, Munchen
10) Smith, A.R., Jardine, J.H., Rauson, G.L., Almond, P.R. and Boyd, D.D.: In vivo measurements of fast neutron therapy. Med. Phys., 3: 391—396, 1976
11) ICRU: Determination of absorbed dose in a patient irradiated by beams of X or gamma rays in radiotherapy procedures. ICRU Report 24, 21—24, 1976

日本医放会誌：45（7），1039—1046，1985（昭60）

放医研におけるCo-60ガンマ線ドシメトリの国際相互比較

放射線医学総合研究所物理研究部
星野　一雄　　川島　勝弘　　平岡　　武　　松沢　秀夫
千葉県がんセンター放射線治療部
佐　方　　周　防

（昭和60年1月7日受付）
（昭和60年2月5日最終原稿受付）

The International Co-60 Gamma Ray Dosimetry Intercomparisons at NIRS

Kazuo Hoshino, Katsuhiro Kawashima, Takeshi Hiraoka and Hideo Matsuzawa
Division of Physics, National Institute of Radiological Sciences
Suoh Sakata
Department of Radiology, Chiba Cancer Center Hospital

Research Code No. : 203.9

Key Words : Dosimetry, Intercomparison, ^{60}Co-gamma ray, JARP dosimeter

The National Institute of Radiological Sciences (NIRS) is a medical standard dosimetry center in Japan accredited by the Japan Radiological Society for the purpose of the standardization of dose estimation in radiotherapy. It is equipped with a secondary standard dosimeter (Called JARP sab-standard dosimeter) that has been calibrated at a national standard against ^{60}Co-gamma rays. In order to confirm reliability of a JARP sub-standard dosimeter, the international ^{60}Co-gamma ray dosimetry intercomparisons at NIRS have been made between NIRS and the institutes of the other countries. During the years 1976-1983, four intercomparisons were made. The excellent agreement was obtained for each intercomparison. This paper describes the results of those intercomparisons and discusses the implication of the findings.

I. 緒　　言

高エネルギーX・γ線および電子線治療における線量評価基準の全国的統一を目的として，1971年に日本医学放射線学会のもとに，医療用線量標準センターが，全国各地区に開設され活動している．放射線医学総合研究所物理研究部第2研究室内にも，関東地区センターが設置されている．本センターは地区センターの一つとして，地域の医療施設の線量計の校正や，治療装置の出力測定を行うのみならず，我が国の医療線量標準として，全センターの中心的存在になっている．従って，我れわれは，医療標準を精度良く推持・管理して行く責任がある．基準器は，JARP準標準線量計と呼ばれている電離箱線量計である（これは1982年8月末日迄，JAPM準標準線量計と呼ばれていた．今後，この年月日以前を単にJAPMと，以後をJARPと呼ぶことにする）．本線量計は毎年1回，我が国の国家標準である．電子技術総合研究所（電総研）の，^{60}Co-γ線標準場による校正を受けているが，機会ある毎に，外国の諸施設との相互比較を行って，国際的信頼性を確めている．

本論文は1976年以来，放射線医学総合研究所（放医研）において実施された．種々のドシメトリ相互比較の際行われた，^{60}Co-γ線ドシメトリ相互比

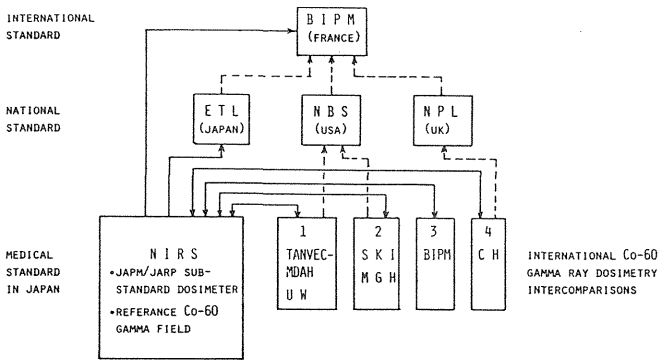

Fig. 1 Schema for the ^{60}Co-gamma ray dosimetry intercomparisons participants and their traceablities to the national and international standard dose laboratories.

Table 1 The title of intercomparisons, the kind of dosimeters used by the participants and the measuring conditions

No.	Title	Date	Participant	Kind of dosimeter	Source to dosimeter distance	Field size	Quantity	In air or in water
1	Neutron dosimetry intercomparison between Japan and USA	April 16, 1976	NIRS	Ionization chamber	75 cm	10×10 cm²	Exposure	In air
			TAMVEC-MDAH	Ionization chamber	75 cm	10×10 cm²	Exposure	In air
			UW	Ionization chamber	75 cm	10×10 cm²	Exposure	In air
2	Neutron and proton dosimetry inter-comparison between Japan and USA	April 21, 1980	NIRS	Ionization chamber	80 cm	10×10 cm²	Exposure	In air
			SKI	Ionization chamber	80 cm	10×10 cm²	Exposure	In air
			MGH	Ionization chamber	80 cm	10×10 cm²	Exposure	In air
3	International Fricke dosimeter intercomparison	February 1981	NIRS	Ionization chamber Fricke	61 cm	14× 7 cm²	Absorbed dose	In water
			BIPM	Ionization chamber Calorimeter	Unknown	Unknown	Absorbed dose	In water
4	Photon dosimetry intercomparison between Japan and UK	April 12—13, 1983	NIRS	Ionization chamber	80 cm	10×10 cm²	Exposure	In air
			CH	Ionization chamber	80 cm	10×10 cm²	Exposure	In air

較の総括である．なお，本総括には，国内の他の参加施設は含めない．

II. 相互比較とトレーサビリティ

本論文で報告する^{60}Co-γ線ドシメトリ国際相互比較を，標準に対するトレーサビリティの立場から，レベル別に位置付けると，Fig. 1の如くなる．放医研（NIRS）と相互比較を行った外国施設は，1．テキサスA＆M大学—MDアンダーソン病院連合チーム（TAMVEC-MDAH, 米国）とワシントン大学（UW, 米国）．2．メモリアルスローンケタリング癌研究所（SKI, 米国）とマサチューセッツ総合病院（MGH, 米国）．3．国際度量衡局（BIPM, 仏国）．4．クリスティー病院（CH, 英国）である．これらの相互比較は，Table 1の Title 欄に示した種々の相互比較の一環として実施された[1)2)]．放医研と各参加施設とは，これらの相互比較により，お互に直接トレーサブルなので，Fig. 1にこの関係を実線と矢印で示した．また，各参加施設は，それぞれの国の国家標準に対しトレーサブルである．米国では国立標準局（NBS）に，英

Table 2　The ionization chambers used by the participants and the results of intercomparison No. 1

Participant	Ionization chamber				Exposure	Ratio
	Type	Shape	Volume	Gas		
NIRS	JAPM, No. 2	Cylindrical	0.6 ml	Air	36.84 R	1.000
TAMVEC-MDAH	72TG (IC-18)	Cylindrical	0.1 ml	Air	37.01 R	
	57TG	Sperical	1 ml	Air	36.84 R	
	63MG	Sperical	2 ml	Air	37.28 R	
	57TE (IC-17)	Sherical	1 ml	TE	36.77 R	
					Mean	
					36.89±0.34 R	1.001
UW	IC-17	Sherical	1 ml	Air	37.18 R	1.009

Table 3.　The ionization chambers used by the participants and the results of intercomparison No. 2

Participant	Ionization chamber				Exposure	Ratio
	Type	Shape	Volume	Gas		
NIRS	JAPM, No. 2	Cylindrical	0.6 ml	Air	86.69 R	
	JAPM, No. 4	Cylindrical	0.6 ml	Air	86.85 R	
					Mean	
					86.77±0.11 R	1.000
SKI	IC-17	Sherical	1 ml	TE	87.15 R	
	IC-18	Cylindrical	0.1 ml	TE	86.15 R	
	T-2	Cylindrical	0.55 ml	TE	86.69 R	
					Mean	
					86.76±0.53 R	1.000
MGH	IC-18	Cylindrical	0.1 ml	Air	86.65 R	
	IC-18	Cylindrical	0.1 ml	TE	86.65 R	
					Mean	
					86.65±0.00 R	0.999

国では国立物理学研究所（NPL）に国家標準が設定されている．各国の国家標準は，BIPM のもとに実施されている国家標準機関を対象とした相互比較により，国際標準にトレーサブルである．従って，放医研の JAMP/JARP は，間接的に NBS, NPL および BIPM にトレーサブルである．この関係を Fig. 1に破線と矢印で示した．なお，BIPM には相互比較3. により直接トレーサブルなので，電総研（ETL）の場合同様に実線で結んだ．

III. 方法および結果

本論文に示す^{60}Co-γ線ドシメトリ国際相互比較は，何れも放医研の^{60}Co 遠隔治療装置の γ 線場において行ったものである．実施年月日，線量計の種類，測定条件等を年次順に No. を付けて Table 1に示す．No. 3以外は，何れも電離箱による空中の照射線量 X での比較である．これらの場合は，外国施設から研究者が，線量計を携え来所された．それぞれの電離箱のタイプ名称，形状，電離容積，電離気体について，Table 2～4に示す．

X の評価法は各施設とも基本的には同じで，(1)式の如くである．

$$X = M \cdot k_1 \cdot Nc \qquad (R) \qquad (1)$$

ここで，M は線量計の読み値，k_1は大気補正係数である．Nc は校正定数で，日本，米国では^{60}Co-γ線，英国では2MV-X 線により与えられている．読み値は安定後5回の測定の平均値である．

相互比較 No. 1, 2および4の結果を，Table 2, 3および4の Exposure 欄に示す．各測定共，標準偏差は零か僅小なので示してない．同施設で複数個の電離箱を使用した場合には，平均値をもって，その施設値とし，標準偏差と共に示してある．Ratio 欄には放医研値を基準とした比を与えた．

以上の3回の電離箱同士の相互比較に比べ，以下に述べる相互比較 No. 3は方法を異にする．

Table 4 The ionization chambers used by the participants and the results of intercomparison No. 4

	Participant	Ionization chamber				Exposure	Retio
		Type	Shape	Volume	Gas		
(April 12)	NIRS	JARP, No. 2	Cylindrical	0.6ml	Air	58.88 R	
		JARP, No. 4	Cylindrical	0.6ml	Air	58.78 R	
						Mean	
						58.83±0.07 R	1.000
	CH	Farmer	Cylindrical	0.6ml	Air	58.98 R	1.003
(April 13)	NIRS	JARP, No. 2	Cylindrical	0.6ml	Air	58.88 R	
		JARP, No. 4	Cylindrical	0.6ml	Air	58.70 R	
						Mean	
						58.79±0.13 R	1.000
	CH	Farmer	Cylindrical	0.6ml	Air	58.88 R	1.002

1980年から81年かけて，国際度量衡委員会の電離放射線諮問委員会の要請により，Fricke 線量計（以下，単に Fricke と呼ぶ）の国際相互比較が NPL の協力を得て BIPM により実施された．この計画は，Fricke が水の吸収線量測定の相互比較の手段として使用し得るか否かを見極るために行われた[3]．放医研も電総研の要請により，この計画に参加した．本相互比較は以下の要領で実施された．

(1) 分光々度計のチェック

(2) Fricke による水の吸収線量の測定比較

(1)は Fricke 使用上の基本に係わる重要事項ではあるが，本論文に直接関係ないので，ここでの記述は省略する．(2)は以下の方法で実施された．「各参加施設で Fricke 溶液を調製し，独自の照射容器に封入して BIPM へ郵送する．BIPM では，これに^{60}Co-γ 線の水中照射を行って参加施設へ返送，この際，線量は知らされない．参加施設では，この照射済 Fricke から，水の吸収線量を評価し，BIPM に報告，BIPM で照射した線量（BIPM 線量）と評価線量との比較を行う」．

われわれは標準的手法[4]に従って Fricke 溶液を調製し，内径13.8mmϕ，外径17.7mmϕ，長さ（内法）52mm，容積約7.8ml のパイレックスガラス容器に封入した試料を作製した．試料への BIPM の標準照射は1981年2月に行われた．水の吸収線量 Dw は，吸光々度分析法による，吸光度 A の測定より(2)式の如くして評価した．

Table 5 The result of Fricke dosimeter intercomparison

BIPM (Irrad. dose)	NIRS (Est. dose)	Ratio (NIRS/BIPM)
30.0 Gy	29.9 Gy	0.997
29.9 Gy	30.2 Gy	1.007
49.9 Gy	49.8 Gy	0.998
49.9 Gy	50.2 Gy	1.006
70.0 Gy	70.1 Gy	1.001
69.9 Gy	69.8 Gy	0.999
		Mean
		1.001±0.004

$$D_W = \Delta A_{25} \cdot C \frac{(\mu_{en}/\rho)_W}{(\mu_{en}/\rho)_F} \cdot K_V \quad \text{(Gy)} \quad (2)$$

ここで，ΔA_{25} は照射済と未照射 Fricke 溶液の，304nm 紫外線に対する吸光度の差で，光路長1 cm，溶液温度25℃における値である．C は吸光度から Fricke 溶液の吸収線量 D_F への変換係数であり，Fricke の G 値を15.5 $(100eV)^{-1}$，Fricke 溶液温度25℃における Fe^{3+} イオンの分子吸光係数を2205$lmol^{-1}$ cm^{-1}[4]，アボガドロ数を$6.0225\times10^{23}mol^{-1}$，Fricke 溶液密度を1.024g cm^{-3}，光路長1cm としたとき2.757×10^{2}Gy A_{25}^{-1}である．また，$(\mu_{en}/\rho)_W/(\mu_{en}/\rho)_F$ は水と Fricke 溶液の質量エネルギー吸収係数の比で，D_F から D_W への換算係数であり，1.003である[5]．

後日発表された BIPM からの報告[6]（参加施設評価線量/BIPM 線量をプロットしたグラフ）による BIPM 線量と，評価した線量を，それぞれTable 5の BIPM（Irrad. dose），NIRS（Est. dose）

Table 6 The results of comparison of the Fricke dosimeter and JAPM sub-standard dosimeter (chamber No. 4)

Date	Fricke	JAPM, No. 4	Ratio (Fricke/JAPM)
Feb 13	27.1±0.14 Gy	27.18 Gy	0.997
Feb 14	28.8±0.22 Gy	28.79 Gy	1.000
Feb 16	28.8±0.06 Gy	28.78 Gy	1.001
			Mean 0.999±0.006

欄に示す．Ratio (NIRS/BIPM) は上記報告から直接読み取った値である．これらより，比の平均値と標準偏差が計算され，1.001±0.004が得られた．

以上はFricke国際相互比較の概略であるが，われわれは，この機会を利用して次の比較を行った．即ち，放医研の ^{60}Co 遠隔治療装置による．本FrickeとJAPMの比較である．これによりJAPMとBIPMの比較が，Frickeを介して可能になった．本比較は，水中5cmにおける水の吸収線量を，両者で測定する方法によった．この場合，照射野を14×7cmとしたのは，Fricke試料の中心軸を通る断面を，入射γ線に対し直角に置いたとき，この断面内の線量の平坦度を最良にする配慮による．平坦度はMix-DPファントムとX線フィルム（Kodak X-Omat TL）にてチェックした．

まず，JAPMによる水の吸収線量を，標準測定法[7]に従って測定した．このとき，ラド変換係数 C_λ は0.95[7]とした．これより水の吸収線量率を求めた．次に，Fricke試料の照射を行った．照射は1個ずつ1日に3個，合計9個行った．これらの試料より，前記の方法で水の吸収線量を求めた．結果をTable 6のFricke欄に与える．値は1日分の平均値と標準偏差を示す．一方，JAPM(電離箱No. 4のみ使用）の結果は，JAPM, No. 4欄に与える．これは前記の水の吸収線量率に，Frickeの照射時間を乗じ，^{60}Coの減衰を補正して求めたものである．なお，照射時間は日毎に若干異なる．Ratio (Fricke/JAPM) 欄には日毎の比の平均値を与えてあるが，全平均値と標準偏差は個々の試料の比から計算した値である．

Fricke国際相互比較とFrickeとJAPMの比較の結果から，BIPM/JAPMが求められ，0.999/1.001＝0.998が得られた．

IV. 考　察

1976年から1983年迄の間に，4回の^{60}Co-γ線ドシメトリ国際相互比較が行われ，外国の6施設との比較ができた．最初の比較の時点では，JAPMは電離箱No. 2を基準にしていたが，1977年よりNo. 4が加わり，基準を此れに変更し今日に至っている．この間，両電離箱共 N_C の変更はなかった．相互比較全体を見比べるべく，Table 2, 3および4のRatio欄と，BIPM/JAPMをFig. 2にプロットした．これらの比の全平均値と標準偏差は1.002±0.004となり，大変良好な一致がみられた．MDアンダーソン病院，メモリアルスローンケタリング癌研究所は米国における医療用線量の校正機関である．また，クリスティー病院も英国において同様の立場にある．これらは，放医研同様に国家標準（1次標準）に対して2次標準機関である．国際度量衡局も含めて，標準と云われる機関だけ取り出すと，結果の一致は更に良好な1.000±0.0018となる．この結果は，放医研のJAPM/JARPが，国際的にも十分なる信頼性を有することを立証すると共に，この間，品質管理が十分行き届き，高い精度を維持し得たことを示すものであろう．

Fricke国際相互比較における，BIPM線量は，米国（NBS），仏国（LMRI），西独（PTB）およびオランダ(RIV)の国家標準研究所による，グラファイトカロリメータを用いた測定と，BIPM自身による，電離箱を用いた測定の結果から決定された．従って，この値は国際的合意に基ずくものであろう．BIPM線量と放医研評価線量の1.001±0.4%と云う優れた一致は，われわれのFrickeが高精度であることの証拠となろう．

FrickeとJAPMの比較では，G値を15.5 (100 eV)$^{-1}$ [8]，C_λ を0.95としたとき，0.999±0.6%と良い一致をみた．ここで変動係数が，Fricke国際相互比較時に比べて，やや大きいのは，照射した線量が約28Gyと，Frickeとしては不足しているためである．十分な線量を与え得なかったのは時間

的制約による．

最近，C_λ の見直しが各国で行なわれていて，新らしいプロトコールが出されている[10)~12)]，我が国でも，日本医学放射線学会物理部会の測定委員会により，見直し作業が進められている．これらは，C_λ（またはこれは換る諸係数）は電離箱の種類別に決定すべきである，と云う立場に立っている．最近の白貝[13)]による英国および米国のプロトコールに従った計算では，^{60}Co-γ 線に対する JARP の C_λ は旧値より0.4~0.5%大きくなっている．また，川島[14)]の計算では0.3%小さくなっている．しかしながら，前者は W/e として33.8$_5$JC^{-1}を後者は33.7JC^{-1}を用いているので，同一のW値を用いれば，両者の差は小さい．W値として何れを用うべきかは，本論より外れるので，ここでは論じない．最近，阻止能も新らしい値が発表された[15)]．とは云え，Fricke 相互比較の時点で用いた，G値は C_λ は相対関係としては正しい値であろう．それは，G値の決定が従属的であり，旧データに従って決定されているからである．今後，G値に関しても，新らしい諸データにてらして見直す必要はあろう．

最後に，これら相互比較に関する諸測定の不確定度を検討する．まず，Table 7に^{60}Co-γ 線または2MV-X 線により校正されている電離箱線量計で，^{60}Co-γ 線の照射線量を測定したときの不確定度を示す．また，Table 8および9には JAPM および Fricke で水の吸収線量を測定したときの不確定度を示す．系統的不確定度は考え得る最大値を与えた．これらのうち，N_C, k_1, A, G 値，ε_m および D_F から D_W への換算係数については，ICRU レポート14[8)]に准じた．K_V は実験的に決定したので，測定値の変動係数をあてた．ランダム

Table 7 Uncertainties in determination of exposure from a calibrated ionization chamber

Source	Uncertainty
1. Calibration factor, N_c and themperature-pressure correction factor, k_1	2.0%
2. Random uncertainty	0.2%
Over-all	2.0%

Table 8 Uncertainties in determination of absorbed dose in water from a JAPM sub-standard dosimeter

Source	Uncertainty
1. Calibration factor, N_c and temperature-pressure correction factor, k_1	2.0%
2. Rad conversion factor, C_λ	1.1%
3. Random uncertainty	0.2%
Over-all	2.3%

Table 9 Uncertainties in determination of absorbed dose in water from a Fricke dosimeter

Source	Uncertainty
1. Measurement of absorbance, A	0.5%
2. G-value	1.3%
3. Molar extinction coefficient, ε_m	0.5%
4. Determination of D_W from D_F	0.2%
5. Irradiation vessel correction factor, k_V	0.2%
6. Random uncertainty	0.6%
Over-all	1.6%

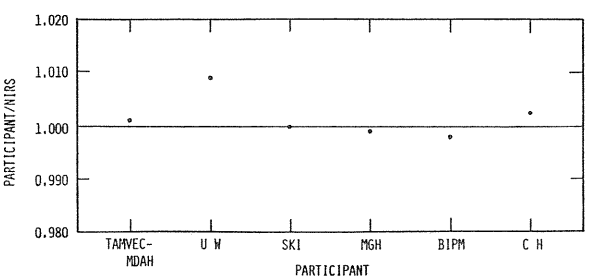

Fig. 2 Summary of the results of the ^{60}Co-gamma ray dosimetry intercomparisons. The deta are normalized to NIRS values.

不確定度は各測定の変動係数の中から最大のものをあてた．全不確定度は各不確定度の自乗和の平方根とした．

これら個々の測定における不確定度から，相互比較における不確定度を推定した．これに先立ち，本相互比較が何れも置換法で行われたので，タイマ，線源位置，線量計位置の再現性に基因する不確定度を推定しておかねばならない．前2者は，IAEA技術レポート185[9]を参考にして，各々0.1%とした．線量計位置は，最大1mmの設定誤差を想定して0.3%とした．Frickeが介在する相互比較No. 3では，BIPM線量の不確定度が不明なので，主として用いられたグラファイトカロリメータでの不確定度をあてることにし，ICRUレポート14[8]を参考にして0.5%と推定した．これらを総合した結果，電離箱同士の相互比較で2.9%，Frickeを介してBIPMとJAPMの比較で3.3%となった．これらは真値からの片寄りの範囲を示すものであり，相互比較における施設間の相違を示すものでないことは云うまでもない．

V. 結　論

(1) ^{60}Co-γ線ドシメトリ国際相互比較を，1976年から1983年にわたって，4回延6カ所の外国施設と行った．その結果，外国施設値/放医研値の全平均値と標準偏差は1.002±0.004であり，良好な一致をみた．これらのうちから，標準機関だけ取り出せば，1.000±0.0018と更に優れた一致を得た．これにより，我が国の医療線量標準の信頼性の高さが，国際的レベルで確められた．

(2) Fricke線量計国際相互比較の結果，放医研評価値/BIPM値は1.001±0.004で大変優れた一致をみた．これにより，放医研のFricke線量計の高精度なることが確められた．

本論文の要旨は松本に於ける第43回日本医学放射線学会総会において発表した．

稿を終えるに臨み，これらの相互比較に直接参加された，MDアンダーソン病院のDr P.R. Almond，テキサスA & M大学教授のDr J.B. Smathers，ワシントン大学教授のDr H. Bichsel，メモリアルローンケタリング癌研究所のDr J.C. McDonald，Mr I-chang Ma，マサチューセッツ総合病院のDr L.J. Verheyおよびクリスティー病院のDr D. Greeneに深甚なる謝意を表します．また，Fricke線量計相互比較の橋渡しをして下さった電子技術総合研究所大阪支所長の森内和之博士，Fricke試料の照射に携わられた国際度量衡局のDr M.T. Nialetに深謝致します．（各氏の所属は相互比較当時のものです）

文　献

1) Kawashima, K., Hoshino, K., Hiraoka, T., Matsuzawa, H., Hashizume, T., Itoh, A., Almond, P.R., Smathers, J.B. and Bichsel, H.: The second neutrom dosimetry intercomparison between Japan and USA. Jpn. Radiol. Phys., 1: 31—40, 1981
2) Greene, D., Hiraoka, T., Hoshino, K., Irifune, T., Kato, K., Kawashima, K., Sakata, S. and Tomaru, T.: Dosimetry intercomparison between UK and Japanese institutes. Brit. J. Radiol., 57: 194, 1984
3) Henry, H.W.: Report from the consultative committee on standards for the mesurement of ionizing radiations (CCEMRI), Section I, X-rays, gamma rays and electrons. Phys. Med. Biol., 29: 1443—1446, 1984
4) 日本医学放射線学会物理部会編：放射線治療における高エネルギー電子線の標準測定法．pp. 25—28, 1974, 通商産業研究社，東京
5) Evans, R.D.: X-ray and γ-ray interactions. (In) Attex, F.H., Roesch, W.C. ed.: Radiation dosimetry. Second Edition, Vol. I. pp. 94—153, 1968, Academic Press, New York and London
6) Report from the Consultative Committee on Standards for the Measurement of Ionizing Radiation (CCEMRI), Section I, X-rays, gamma rays and electrons, 6th Meeting p. 14, 1981, BIPM, Sèvres
7) 日本医学放射線学会物理部会編：放射線治療における^{60}Coガンマ線および高エネルギーX線の標準測定法，pp. 13—15, 1977, 通商産業研究社，東京
8) ICRU Report 14: Radiation dosimetry: X-ray and gamma rays with maximum photon energy between 0.6 and 50 MeV. pp. 1—18, 1969, ICRU, Washington, D.C.
9) IAEA Technical Report Series No. 185: Calibaration of dose meters used in radiotherapy. p. 39, 1979, IAEA, Vienna
10) The Nordic Association of Clinical Physics (NACP): Procedures in external radiation therapy dosimetry with electron and photon beams with maximum energies between 1 and 50 MeV. Acta Radiologica Oncology, 19: 55—79, 1980
11) Radiation Therapy Committee, American As-

sociation of Physicists in Medicine: A protocal the determination of absorbed dose from high-energy photon and electron beams. Medical Physics, 10: 741—771, 1983

12) Hospital Physicists' Association (HPA): Revised code of practice for the dosimetry of 2 to 35 MeV X-ray, and of caesium-137 and coblt-60 gamma-ray beams. Phys. Med. Biol., 28: 1097—1104, 1983

13) 白貝彰宏：Absrobed dose coversion factor C_λ and C_E. 日医放物理会誌, Supplement No. 20, 1—22, 1984

14) 川島勝弘：私信. 第9回医療用標準線量研究会資料

15) ICRU Report 37: Stopping power for electrons and positrons. pp. 1—269, 1984, ICRU, Washington, D.C.

Int. J. Radiation Oncology Biol. Phys., Vol. 11, pp. 1495–1502
Printed in the U.S.A.

0360-3016/85 $03.00 + .00

● *Original Contribution*

THE RELATIONSHIP BETWEEN LUNG COLONY AND *IN SITU* ASSAYS

KOICHI ANDO, D.D.S., PH.D. AND SACHIKO KOIKE, M.S.

Division of Clinical Research, National Institute of Radiological Sciences, 9-1, 4-Chome, Anagawa, Chiba 260, Japan

The relationship between three different assays: tumor control, tumor growth delay and lung colony formation, was examined after fast neutron and γ ray irradiations. Fibrosarcomas (NFSa) in syngeneic C3Hf mice were irradiated locally with ^{60}Co γ rays, fast neutrons or mixed beams (γ rays and fast neutrons). A comparison between the lung colony assay and the TRT_{50} (50% tumor growth delay time) assay when cells were exposed to single doses of fast neutrons or γ rays, resulted in identical growth delay times. The fraction of cells surviving a single dose of fast neutrons, was 10 times higher than the surviving fraction of cells after a single dose of γ rays. Both doses resulted in the same tumor control probability (TCD_{50} assay). Neither repair of potentially lethal damage nor tumor bed effect was sufficient to explain the difference between cell survival and tumor control probability. The surviving fraction of cells following fractionated irradiations of γ rays and fast neutrons were identical at 50% tumor control probabilities.

Lung colony, TCD_{50}, TRT_{50}, Fast neutron, Repair of potentially lethal damage, Tumor bed effect.

INTRODUCTION

Tumor control probability, tumor growth delay, and colony formation have been widely used to determine the biological effectiveness of new radiation modalities. We recently reported that RBE (relative biological effectiveness) values of fast neutrons, whether determined by the TCD_{50} (50% tumor control dose) assay or the lung colony assay, were identical when daily fractionated doses were examined.[2] Following single dose irradiations, however, larger RBE values were obtained by the TCD_{50} assay than by the lung colony assay. RBE values decrease with increasing doses of fast neutrons.[3] Therefore, it is unlikely that a TCD_{50} assay following a single dose to cells would give a larger RBE value than a lung colony assay, because the former employs a larger radiation dose. This raises the question of whether lung colonies assay tumor cells that determine tumor control *in situ*. Many factors involved in these two assays could affect RBE values; they include repair of potentially lethal damage (PLDR), enzymatic damage to tumor cell membrane, repopulation of tumor cells and immune and other host reactions.[11] A significant difference between the TCD_{50} and the lung colony assay is that the tumors are excised immediately after irradiation in the lung colony assay, yet are left *in situ* in the TCD_{50} assay. In this study we focused on PLDR and the tumor bed effect to examine the relationship between the excision assay (lung colony formation) and the *in situ* assays (tumor growth delay and TCD_{50}).

METHODS AND MATERIALS

Mice and tumors

The original tumor was a fibrosarcoma that arose spontaneously in a C3Hf/Kam female mouse at the Department of Experimental Radiotherapy, M. D. Anderson Hospital and Tumor Institute, Houston, TX. Isotransplants at the 18th generation were used throughout. Animals were 8 to 12 week old C3H/HeMsNrsfICR male mice. Mice received an i.m. injection of 10^6 tumor cells to their right hind legs 7 to 8 days before irradiation. Preparation of single cell suspensions by trypsinization is described elsewhere.[2] As determined by phase-contrast microscopy, over 95% of the cells for single dose experiments, and 70% of the cells for the fractionation experiments were intact. Less than 1% of the cells were in aggregates.

Irradiation

Fast neutrons were produced by bombarding a thick beryllium target with 30 MeV cyclotron produced deuterons. The mean energy of the fast neutrons was 13

This report was supported in part by a Grant-In-Aid from the Ministry of Education, Science and Culture, Japan (590-10088).

Reprint requests to: Koichi Ando.

Acknowledgments—We thank Dr. Luka Milas for providing the NFSa tumors, and Dr. Nobuo Fukuda for statistical analysis of data. We would also like to thank Dr. Muneyasu Urano and Dr. Hiroshi Ohara for their constructive criticisms and editing of this manuscript.

Accepted for publication 12 March 1985.

MeV and the γ ray contamination was 3–5% of the total dose.[6] Leg tumors with an average diameter of 7 ± 0.5 mm were placed in a rectangular field of 20 × 3 cm. Mice were anesthetized with 50 μg/g sodium pentobarbital* prior to irradiation, and were restrained by being taped to an acrylic plate. Doses were measured in each experiment with a tissue equivalent chamber. During this series of experiments the dose rate was about 0.73 Gy/min.

Gamma rays were obtained using a ^{60}Co therapy machine with a dose rate of 1.00 Gy/min at an FSD of 47 cm. The irradiation field size was identical to that for neutron irradiation. The beam build-up was obtained by placing a 5 or 8 mm thick acrylic plate over the surface of the tumors for ^{60}Co or fast neutron irradiation, respectively. The scattered dose to the whole body was 1–3% of tumor dose[10] for both neutrons and γ rays. Irradiations were made to air breathing animals. Irradiation schedules were: single γ ray (1γ) or fast neutron (1N) dose, 5 daily γ ray (5γ) or fast neutron (5N) doses, and a mixed-beam scheme of 2N doses plus 3γ doses in the sequence N-γ-γ-γ-N. The interval between treatments was 24 hours. A detailed method and rationale for the mixed gamma neutron beam scheme have been described elsewhere.[2] Briefly, 5 daily doses (5γ, 5N) result in surviving fractions of SF(5γ) and SF(5N), which can be experimentally obtained. If SF(1γ) and SF(1N) are theoretical surviving fractions after each fractionated dose, and SF(5γ) and SF(5N) result from repeated doses of 1γ and 1N for five fractions, then theoretical surviving fractions at each fractionated dose would be given by

$$SF(1\gamma) = SF(5\gamma)^{1/5} \quad \text{and} \quad SF(1N) = SF(5N)^{1/5}$$

When using the mixed beam scheme N-γ-γ-γ-N, assuming no interaction between the two types of beam, the expected surviving fractions would be given by

$$SF(3\gamma + 2N) = SF(5\gamma)^{3/5} \times SF(5N)^{2/5}.$$

As in cell survival studies, the tumor control probability was calculated for "3γ + 2N doses." It is assumed that the probability of tumor recurrence after 5γ or 5N is

$$1 - P(5\gamma) \quad \text{and} \quad 1 - P(5N)$$

respectively, where P(5γ) and P(5N) are tumor control probabilities following 5γ and 5N. In this scheme, the probabilities of failure in tumor control for each γ and N dose are

$$\{1 - P(5\gamma)\}^{1/5} \quad \text{and} \quad \{1 - P(5N)\}^{1/5}$$

respectively. Accordingly, the tumor control probabilities following the mixed-beam scheme N-γ-γ-γ-N can be given by

$$1 - \{1 - P(5\gamma)\}^{3/5} \times \{1 - P(5N)\}^{2/5}$$

when there is no predicted damage caused by beam interaction. The γ-ray dose per fraction was fixed as 22 Gy. Each neutron dose varied from 6 to 10 Gy in order to determine the TCD_{50} value.

Assay methods

1. *in situ* assays
   (a) TCD_{50} assay: after irradiation of the leg tumors, irradiated areas were palpated once a week for 120 days, and the tumor control rates were scored. Each dose group consisted of from 5 to 20 mice. A total of 295 mice were used. All experiments were performed at least twice.
   (b) TRT_{50} assay: Each tumor was measured in three dimensions, a, b, c, with calipers 3 times a week. Tumor volume was calculated by πabc/6. The number of days for a tumor to regrow to 5 times its initial volume was determined on the regrowth curve, and TRT_{50} (days required for half of the tumors to reach 5 times the initial volume) was calculated by probit analysis.[19]
2. Excision Assay: The lung colony assay was used to determine clonogenic cell survival. Tumors were excised either immediately, or 24 hours after the last irradiation, and single cell suspensions were prepared. Two to four tumors were used for each dose group. Each suspension, containing an appropriate number of tumor cells and 10^6 heavily irradiated (HIR) cells, was injected i.v. into recipient mice that had received treatment with 150 μg/g Cyclophosphamide 24 hours prior to injection. The addition of HIR cells and pretreatment with Cyclophosphamide increased lung colony forming efficiency by a factor of 50. There were five mice per group; a total of 250 mice were used. Lungs were removed 10 to 13 days after the i.v. injection, and the number of tumor nodules on the surface of each lobe was counted macroscopically. As a control, the lung colony forming efficiency of nonirradiated tumor cells was shown to be between 3 and 8%.
3. TD_{50} Assay: Single cell suspensions containing an appropriate number of cells were injected into right hind legs, which had been locally irradiated 3 months in advance. Each group consisted of 8 mice and a total of 200 mice were used. Legs were palpated for tumors once a week for 13 weeks.
4. Estimation of tumor cell number: The number of tumor cells in a tumor was estimated by counting the number of tumor cell nuclei.[19] Immediately after

* Nembutal; Abbott Laboratories, Chicago, IL.

the mice were killed, the tumor tissue was excised and minced in 2 to 3 ml of an 1% ice-cold citric acid solution, placed in a blender, and mixed at 3000 rpm for 5 min. This mixture was then suspended in 20 ml of an 1% citric acid solution. One drop of octyl alcohol was added to reduce foaming and the homogenate was centrifuged at 5000 rpm for 10 min. The sediment was suspended in from 5 to 20 ml of an 0.2% citric acid solution, and large, round nuclei were counted. To determine the loss of cell nuclei during this procedure, a known number of single cells were processed in an identical manner. It was found that 36.9% of nuclei were lost. Efficiency of tumor cell yield by this method is comparable to other methods including DNA measurements and morphometry.[18]

Analysis

Probit analysis was carried out to obtain TCD_{50} and TD_{50} values. For survival curves, the multi-target model was fitted to the data. D_0 values (radiation dose to reduce surviving fractions by a factor of 1/e in the exponential portion of the survival curve) and extrapolation numbers, n, with 95% confidence limits were determined for each curve.

RESULTS

Cell survival was examined immediately after irradiation (Fig. 1, Table 1). D_0 values after 1N and 5N were identical (1.81 vs. 1.85 Gy), while the D_0 value after 5γ was greater than after 1γ (4.38 vs. 5.55 Gy). When 24 hour intervals occurred between irradiation and tumor excision, the D_0 values increased approximately 8% and 2% after 1γ and 1N irradiation, respectively (Fig. 1 and Table 1). The resulting RBE value was 2.56.

The TRT_{50} was examined after 1N and 1γ (Fig. 2). Dose response curves showed a single component after 1N as well as 1γ. RBE values of fast neutrons relative to γ rays, compared at various levels of TRT_{50}, ranged between 2.67 and 2.70. It should be noted that the dose

Table 1. Cell survival parameters of the NFSa after single, 5-fractionated and mixed-beam doses

Radiation schemes	D_0 (Gy)	n
1N	1.81 (1.73–1.89)*,†	1.19 (0.98–1.40)†
	1.84 (1.52–2.17)‡	1.07 (0.48–1.66)‡
5N	1.85 (1.76–1.94)	2.75 (1.83–3.65)
1γ	4.38 (4.22–4.52)†	1.18 (1.00–1.34)†
	4.71 (4.49–4.93)‡	1.08 (0.87–1.29)‡
5γ	5.55 (4.96–6.14)	2.51 (1.40–3.62)
Mixed Beam	4.24 (3.90–4.57)	2.55 (1.30–3.79)

* Mean and 95% confidence limit.

Assays were performed either immediately (†) or 24 hours (‡) after irradiation.

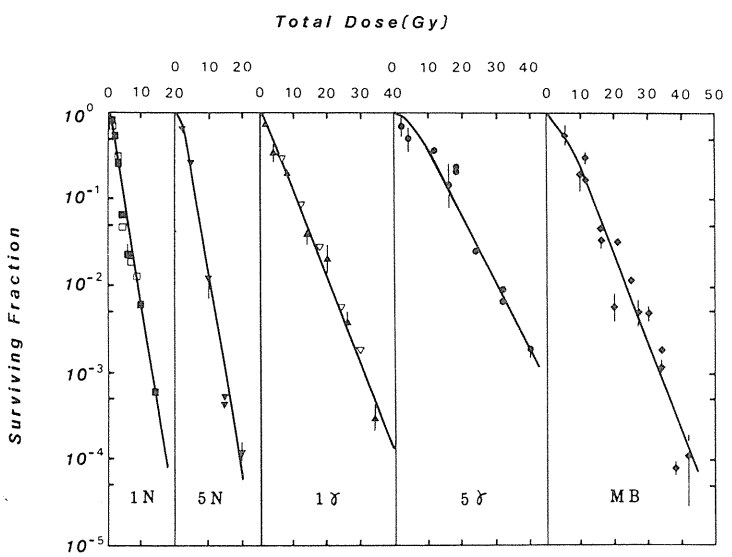

Fig. 1: Clonogenic cell survivals. NFSa tumors were irradiated with single or 5 daily fractionated doses. Tumors were excised immediately (closed symbols) or 24 hours (open symbols) after final irradiation. Abbreviations at the bottom of the figure are; 1N: Single fast neutron dose, 5N: 5 daily neutron doses, 1γ: single γ ray dose, 5 γ: 5 daily γ ray doses, MB: a mixed-beam scheme of N-γ-γ-γ-N given with a treatment interval of 24 hours. Symbols and bars indicate mean and S.E., respectively.

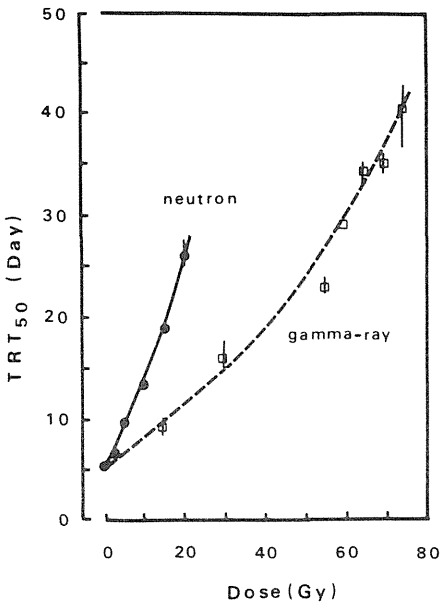

Fig. 2. Tumor growth delay times after single doses of fast neutrons and γ rays. Time for half the tumors to regrow to 5 times initial volume (TRT_{50}) was obtained by measuring tumor volume. Closed circles and open squares are tumors irradiated with fast neutrons and γ rays, respectively. Symbols and bars indicate mean and 95% confidence limit, respectively.

required to produce a TRT_{50} of 26 days with 1N treatment resulted in complete tumor regression in 1 of 7 animals. 1γ treatment controlled no tumors until the dose required to produce a TRT_{50} of 41 days was reached. The volume doubling time of tumors was 5.5 ± 1.5 days (mean ± SD) for 1N and 5.2 ± 0.63 days for 1γ.

Tumor control probabilities were investigated after 1N, 1γ, 5N, 5γ, and the mixed-beam scheme (Table 2). Dose dependency of tumor control probabilities were observed in each radiation modality. TCD_{50} values were calculated from these data and listed in Table 3.

The relationships between surviving fractions (when irradiation and excision were separated by 24 hours) and TRT_{50} values were obtained from data shown in Figs. 1 and 2. Values below 10^{-4} for cell survival were obtained by the extrapolation of survival curves. The relationships after 1N and 1γ were slightly upward-concave (Fig. 3), but were identical, indicating that the relationship between cell killing and growth delay time was independent of the LET (linear energy transfer). The relationship between surviving fractions and tumor control probabilities indicated that, at given survival levels, 1N resulted in a higher tumor control probability than 1γ (Fig. 4). In other words, fast neutrons required less cell killing than γ rays to achieve the same tumor

Table 2. Tumor control probabilities of the NFSa after single, 5-fractionated and mixed-beam doses

Radiation schemes	Total dose (Gy)	Number of cured tumors/ Number of irradiated tumors	(%)
1N	20.5	1/6	16.7
	23.0	1/8	12.5
	25.5	2/8	25.0
	28.0	4/7	57.0
	30.5	7/8	87.5
	33.0	6/7	85.7
	35.5	8/8	100.0
5N	32.0	2/8	25.0
	35.0	3/6	50.0
	38.0	4/7	57.0
	41.0	6/7	85.7
	44.0	5/5	100.0
1γ	70.0	0/8	0.0
	75.0	0/8	0.0
	80.0	2/8	25.0
	85.0	6/8	75.0
	90.0	5/6	83.3
	95.0	6/7	85.7
5γ	80.0	0/9	0.0
	90.0	7/18	38.9
	100.0	5/16	31.3
	110.0	10/16	62.5
	120.0	13/18	72.2
	130.0	15/20	75.0
	140.0	15/18	83.3
Mixed beam	78.0	5/10	50.0
	80.0	4/10	40.0
	82.0	5/10	50.0
	84.0	8/10	80.0
	86.0	8/10	80.0

Table 3. Surviving fractions and number of cells surviving 50% tumor control doses

Radiation schemes	TCD_{50} (Gy)	Surviving fraction*	Number of cells
1N	27.1 (24.8–29.6)†	$(3.7 \pm 1.2) \times 10^{-7}$†§	55.8
		$(4.3 \pm 1.3) \times 10^{-7}$‡§	64.1
5N	35.8 (28.9–40.4)	$(1.1 \pm 2.06) \times 10^{-8}$	1.6
1γ	83.2 (68.2–87.6)	$(6.7 \pm 16) \times 10^{-9}$	1.0
		$(2.3 \pm 2.97) \times 10^{-8}$‡	3.5
5γ	104.4 (87.9–113.9)	$(1.7 \pm 2.6) \times 10^{-8}$	2.5
Mixed Beam	81.3 (66.9–83.4)	$(1.2 \pm 2.1) \times 10^{-8}$	1.8

* Surviving fractions were obtained by extrapolating survival curves down to TCD_{50} doses. 95% confidence limit was obtained by $1.96 \times \sqrt{S/N}$ where S and N represented surviving fractions at TCD_{50} and number of clonogenic tumor cells, respectively.

† Mean and 95% confidence limit.

‡ Survival parameters of delayed assay were used.

§ These values were significantly ($p < 0.05$) different from the other groups.

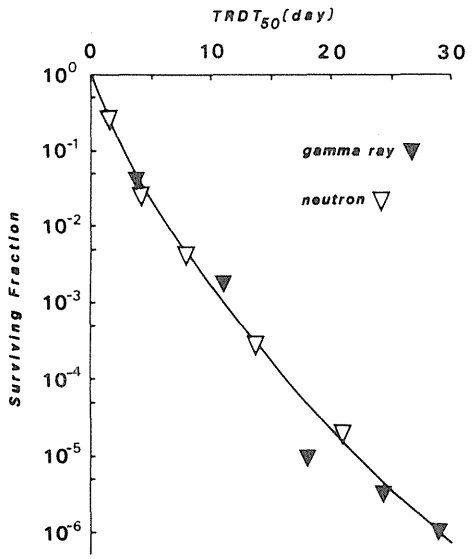

Fig. 3. Relationships between surviving fractions and tumor growth delay times after single doses of fast neutrons and γ rays. The surviving fraction after a dose which results in a given TRT_{50} was calculated from Figs. 1 and 2, partly determined by extrapolation. Survival parameters used for the calculations were those obtained with delayed assay. $TRDT_{50}$, on the abscissa, indicates the difference in TRT_{50} between irradiated and control groups.

control probability. For example, surviving fractions at 50% tumor control probability following 1N and 1γ were 4.3×10^{-7} and 2.3×10^{-8}, respectively. Fractionated irradiations including 5N, 5γ, and the mixed-beam scheme, resulted in a similar surviving fraction, i.e., between 1.1×10^{-8} and 1.7×10^{-8}.

The fact that surviving fractions at 50% tumor control probability were as low as 10^{-8} raised the question of how many tumor cells were contained in a tumor. We examined the number of tumor cells in a 7 mm NFSa tumor (Fig. 5); it contained 1.6×10^8 cells. Although the tumor cell to host cell ratio in the NFSa is not known, it is reasonable to assume that about half of the cells would be tumor cells. Therefore, the 7 mm tumor would contain approximately 1×10^8 tumor cells. The number of tumor cells that survived TCD_{50} dose was then calculated by multiplying the surviving fraction by 10^8 (Table 3). We calculated that 65 cells had survived after a TCD_{50} dose of 1N, whereas less than 4 cells had survived after that of 1γ.

In the course of treatment the tumor bed was irradiated. Previous work has shown that preirradiation of the tumor bed retards tumor growth,[5,22] although the precise effect of fast neutrons has not been established. We investigated the tumor bed effect of fast neutrons as well as of γ rays using tumor transplantability. A single dose of 15 Gy fast neutrons and of 50 Gy γ rays were delivered to the right hind legs of normal mice. These doses were chosen because the RBE in the TCD_{50} assay was about 3 (see Table 2). Three months thereafter, mice received tumor cell challenges into the irradiated legs. TD_{50} values in preirradiated legs were substantially reduced (Fig. 6), being 412 (207–616) in unirradiated mice, 126 (39–213) in 1N irradiated mice and 94 (32–157) in 1γ irradiated mice. However, no difference was detected between 1N and 1γ.

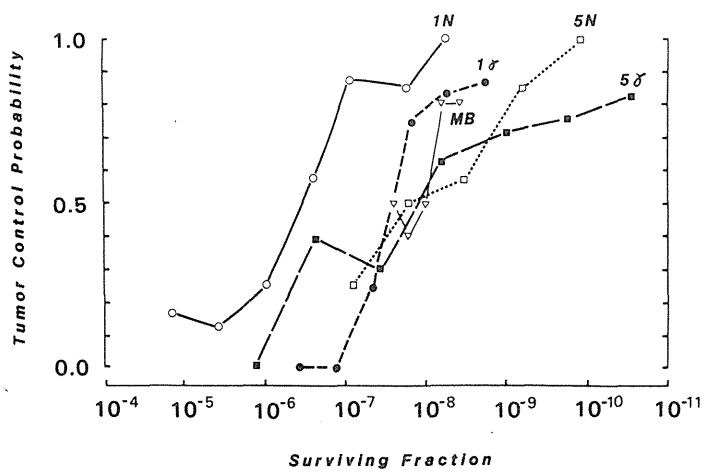

Fig. 4. Relationships between surviving fraction and tumor control probability. Surviving fraction was calculated by extrapolating survival curves at a dose which resulted in a given tumor control probability in Table 2. Survival parameters used for the calculations were those obtained with delayed assay. Abbreviations in the figure are identical to those in Fig. 1.

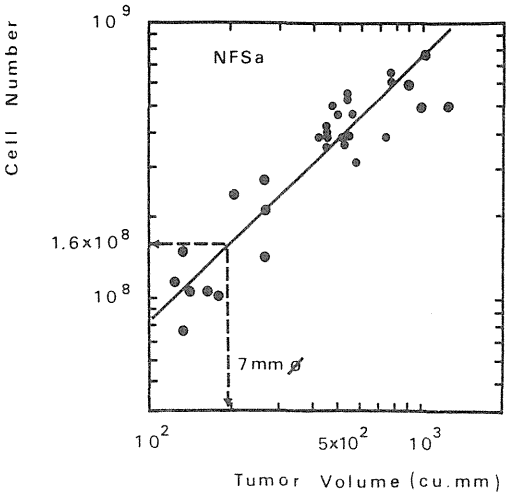

Fig. 5. Number of tumor cells in the NFSa tumor. Each symbol represents one tumor. The regression line was Log Y = 0.87 × Log X + 6.22. The coefficient of correlation was 0.903. The broken line indicates that a 7 mm tumor contained 1.6×10^8 cells.

DISCUSSION

The NFSa tumor showed a uniform radiosensitivity in cell survival curves after single doses of γ rays. This may be a result of acute hypoxia induced by sodium pentobarbital.[2] The extrapolation number of the NFSa tumor was comparable to that of EMT-6 tumors,[14,16] but smaller than mammary adenocarcinomas,[19] NR-S1 squamous cell carcinomas,[21] RIF-1 fibrosarcomas,[15] FSa fibrosarcomas[4] and Lewis lung carcinomas.[17]

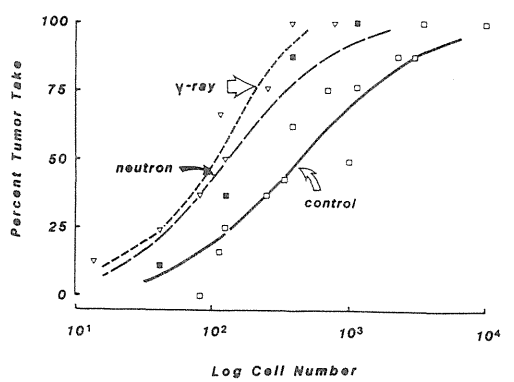

Fig. 6. Tumor bed effect of fast neutrons and γ rays. A single dose of 15 Gy fast neutrons (■), or that of 50 Gy γ rays (▽) was delivered to right hind legs 3 months before tumor cell challenge. (□) indicates unirradiated control. TD_{50} values were; unirradiated control: 412 (207–616), 1N: 126 (39–213), and 1γ: 94 (32–157).

Our present study demonstrated that the relationships between cell survival and growth delay time following 1N and 1γ were comparable. This may indicate that, regardless of the LET value, the same level of cell killing results in the same growth delay time. The 1N-RBE determined by the lung colony assay and that by the growth delay assay were also similar, that is, 2.56 and 2.70, respectively. The survival curves after 1N and 1γ were both single component. This might be attributed to the increase in the hypoxic cell fraction, which may be a result of anesthesia.[2] The single component survival curves resulted in constant RBE values throughout the dose range tested.

A notable discrepancy between 1N and 1γ was observed in the relationship between cell survival and tumor control probability. Namely, less cell killing was required after 1N than after 1γ to obtain the same tumor control probability. A possible explanation of this discrepancy could be the magnitude of PLDR: cells sampled immediately after irradiation by the lung colony assay would yield a lower surviving fraction than if allowed to complete PLDR (estimated to take 8 hours).[9] However, present results from experiments where a 24 hour delay occurred between the irradiation treatment and tumor excision (delayed assay) do not support this possibility. The increase in the D_0 values with a 24 hour delay was only 2% for 1N and 8% for 1γ, and was too small to account for the discrepancy. PLDR capacity might be smaller in the NFSa tumor compared to other tumors.[9,12,17,20] The use of sodium pentobarbital in our experiments may, in part, be responsible for the small increase in the D_0 values: hypoxic cells which were artificially induced by sodium pentobarbital in the NFSa tumors, might have failed in repairing PLD.[12]

The tumor bed effect might also account for the difference between the neutron and γ ray results. The tumor bed effect is induced by radiation damage to the stroma, which in turn, modifies tumor growth.[5] Radiation damage to the endothelium of blood vessels seems to be important. Low LET preirradiation of the tumor bed has a substantial effect on tumor growth but not on tumorigenicity.[5,22] Although preirradiation of the tumor bed reduced the TD_{50} value to approximately one third of that in the non-irradiated mice, the TD_{50} values in the neutron-irradiated and γ ray-irradiated legs were comparable. It follows that the tumor bed effect cannot completely account for the discrepancy.

The fact that the TD_{50} value (~100 cells) was 25 times larger than the number of tumor cells (<4 cells) surviving at TCD_{50} may raise a question about the validity of extrapolating the survival curves down to 10^{-8}. This is difficult to answer because no precise method is available to obtain survival fractions that low. However, as fractionated regimens including 5N, 5γ,

and the mixed-beam scheme resulted in good correlations between the surviving fraction estimated from the lung colony assay and the tumor control probability obtained by TCD_{50} assays, it is reasonable to assume that the extrapolation may be valid under certain conditions. The difference between the TD_{50} values and the calculated number of tumor cells at TCD_{50} doses may be due to the microenvironment surrounding the tumor cells; first, tumor cells in the TD_{50} assay lodge in the tissue and grow while evoking a blood supply. However, tumor cells in the TCD_{50} assay have already been provided with a blood supply. Second, TCD_{50} experiments produce a preponderance of heavily irradiated tumor cells, which are known to increase tumorigenicity by a factor of as much as 100[13] whereas in our TD_{50} experiments heavily irradiated tumor cells were not used.

Why did the survival values following 1N differ from those after other modalities? A possible explanation may be that a small but significant fraction of a radioresistant subpopulation could be heterogenously contained in the tumor, and single neutron doses would kill these cells more effectively than γ rays (Fig. 7A). True survival at TCD_{50} would be, say, 10^{-7} that is identical to the cell survival after 1N; 10^{-8} of cell survival after 1γ would be incorrect. The resistant cells may then move into the sensitive fraction during fractionated doses, eliminating the discrepancy between the cell survival following 1N and that following 1γ (Fig. 7). Therefore, recruitment of resting cells into a cycling state[8] might have been responsible for the disparate survival values with different modalities.

However, based on two facts, this hypothesis can be refuted. First, if there had been a radioresistant population, then the TRT_{50} curve after 1γ should have revealed the resistant population at large doses. The curve reflected rather a uniform radiosensitivity of the tumor, and did not suggest any radioresistant population (Fig. 2). Second, this hypothesis cannot explain the difference in cell survival results between 1N and 5N.

An alternative explanation is that, after large doses of 1N, the rate of cell survival declines more rapidly at large doses (Fig. 7B). True survival at TCD_{50} would be 10^{-8}, which is identical to the cell survival after 1γ; 10^{-7} of cell survival after 1N would be incorrect. According to this hypothesis, the TRT_{50} curve after 1γ should show uniform radiosensitivity of the tumor, and the experimental results agree (Fig. 2). As dose size per fraction of 5N might have been smaller than the neutron dose corresponding to the change in slope of the 1N curve, fractionated doses of fast neutron should result in cell survival differing from single neutron doses. This was also seen in the experimental results (Fig. 4). This hypothesis suggests that fast neutrons may possess large β values in α-β models, though the lung colony assay can not detect the β term due to technical limitations. The β term of fast neutrons may originate from recoil protons.[7]

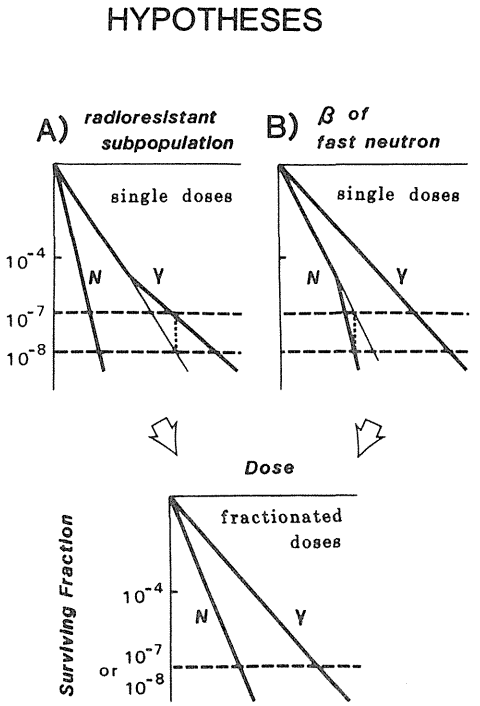

Fig. 7. Hypotheses explaining the difference between 1N and the other radiation modalities. Lines are survival curves for fast neutrons and γ rays. Bold lines are true survival curves while thin lines falsely extrapolate the survival curves which were obtained by the lung colony assay. Horizontally dotted lines are cell survivals at 50% tumor cure. Vertically dotted lines correlate true cell survivals and false cell survivals.

Discrepancies between colony formation and TCD_{50} assays have been reported both in the sensitizer enhancement ratio (SER) of misonidazole[12] and in RBE values of fast neutrons.[14] TCD_{50} assays resulted in larger SER but smaller RBE values than colony formation assays. In the case of the EMT-6 tumors, cell survival at TCD_{50} was 100 times higher after single doses of X rays than after those of fast neutrons.[14] These results are contradictory to our results. This contradiction could be due to cell survival levels at doses that result in tumor cure. As the EMT-6 tumor is strongly immunogenic in its syngeneic host,[14] cell survival at TCD_{50} is quite high: 10^{-2} after X rays and 10^{-4} after fast neutrons. Immunogenicity of the NFSa tumor is weak,[1] and cell survival at TCD_{50} was 10^{-7} after fast neutrons and 10^{-8} after γ rays (Fig. 4). If the population size of cells which determine tumor cure is smaller than 10^{-4} (Fig. 7), then the radiosensitivity of these cells is critical for the cure of weakly immunogenic tumors but unimportant for the cure of immunogenic tumors.

REFERENCES

1. Ando, K., Hunter, N., Peters, L.J.: Immunologically non-specific enhancement of artificial lung metastases in tumor-bearing mice. *Cancer Immunol. Immunother.* **6:** 151–156, 1979.
2. Ando, K., Koike, S., Fukuda, N., Kanehira C.: Idenpendent effect of a mixed-beam regimen of fast neutrons and gamma rays on a murine fibrosarcoma. *Radiat. Res.* **98:** 96–106, 1984.
3. Fowler, J.F., Denekamp, J., Page, A.L., Begg, A.C.: Fractionation with X-rays and neutrons in mice: Response of skin and C3H mammary tumours. *Br. J. Radiol.* **45:** 237–249, 1972.
4. Grdina, D.J., Basic, I., Guzziro, S., Mason, K.A.: Radiation response of cell populations irradiated *in situ* and separated from a fibrosarcoma. *Radiat. Res.* **66:** 634–643, 1976.
5. Hewitt, H.B., Blake, E.R.: The growth of transplanted murine tumours in pre-irradiated sites. *Br. J. Cancer* **22:** 808–824, 1968.
6. Hiraoka, T., Kawashima, K., Hoshino, K., Matsuzawa, H.: Dosimetry of fast neutron beam at the NIRS cyclotron. *Nippon Acta Radiol.* **37:** 369–379, 1977.
7. Hornsey, S., Field, S.: On the differences in RBE observed with different tissues and the factors governing cell sensitivity which these differences imply. *Proceedings Fifth Symposium on Microdosimetry.* Booz, J., Ebert, H.G., Smith, B.G.R. (Eds.). Verbania Pallanza, Italy, EUR 5452 d-e-f. 1975, pp. 275–287.
8. Kallman, R.F., Combs, C.A., Franko, A.J., Furlongo, B.M., Kelley, H.L., Miller, R.G., Repacchietta, D., Schoenfeld, D., Takahashi, M.: Evidence for the recruitment of noncycling clonogenic tumor cells. In *Radiation Biology in Cancer Research,* R.E. Meyn and H.R. Withers (Eds.). New York, Raven Press. 1980, pp. 397–414.
9. Little, J.B., Hahn, G.M., Frindel, E., Tubiana, M.: Repair of potentially lethal radiation damage *in-vitro* and *in-vivo.* *Radiology* **106:** 689–694, 1973.
10. Maruyama, T., Inada, T., Hiraoka, T., Kawachi, K., Hashizume, T.: Design and evaluation of a semicontinuously variable collimator for a cyclotron neutron radiotherapy. *Nippon Acta Radiol.* **38:** 633–642, 1978.
11. McNally, N.J., DeRonde, J.: Radiobiological studies of tumours *in situ* compared with cell survival. *Br. J. Cancer* **41**(Suppl. IV)**:** 259–265, 1980.
12. McNally, N.J., Sheldon, P.W.: The effect of radiation on tumour growth delay, cell survival and cure of the animal using a single tumour system. *Br. J. Radiol.* **50:** 321–328, 1977.
13. Peters, L.J., Hewitt, H.B.: The influence of fibrin formation on the transplantability of murine tumour cells: Implications for the mechanism of the Révész effect. *Br. J. Cancer* **29:** 279–291, 1974.
14. Rasey, J.S., Carpenter, R.E., Nelson, N.J.: Response of EMT-6 tumors to single fractions of X rays and cyclotron neutrons. *Radiat. Res.* **71:** 430–446, 1977.
15. Rasey, J.S., Nelson, N.J.: Discrepancies between patterns of potentially lethal damage repair in the RIF-1 tumor system *in vitro* and *in vivo. Radiat. Res.* **93:** 157–174, 1983.
16. Rockwell, S., Kallman, R.: Cellular radiosensitivity and tumor radiation response in the EMT 6 tumor cell system. *Radiat. Res.* **53:** 281–294, 1973.
17. Shipley, W.U., Stanley, J.A., Courteny, V.D., Field, S.B.: Repair of radiation damage in Lewis lung carcinoma cells following *in situ* treatment with fast neutrons and γ-rays. *Cancer Res.* **35:** 932–938, 1975.
18. Stephan, T.C., Peacock, J.H.: Cell yield and cell survival following chemotherapy of the B16 melanoma. *Br. J. Cancer* **38:** 591–598, 1978.
19. Urano, M., Fukuda, N., Ando, K., Koike, S., Tanaka, N.: Tumor control and regrowth probability after a single radiation of experimental animal tumors. *J. Natl. Cancer Inst.* **53:** 517–525, 1974.
20. Urano, M., Koike S.: Comparison of effects of neutron and/or photon irradiation on spontaneous squamous-cell carcinoma in mice. *Radiology* **134:** 219–225, 1980.
21. Úrano, M., Nesumi, N., Ando, K., Koike, S., Ohnuma, N.: Repair of potentially lethal radiation damage in acute and chronically hypoxic tumor cells *in vivo. Radiology* **118:** 447–451, 1976.
22. Urano, M., Suit, H.D.: Experimental evaluation of tumor bed effect for C3H mouse mammary carcinoma and for C3H mouse fibrosarcoma. *Radiat. Res.* **45:** 41–49, 1971.

J. RADIAT. RES., 26, 334–338 (1985)

Enhanced Killing of HeLa Cells Pre-Labeled with 5-Bromodeoxyuridine by Monochromatic Synchrotron Radiation at 0.9 Å: An Evidence for Auger Enhancement in Mammalian Cells

KUNIO SHINOHARA, HIROSHI OHARA*, KATSUMI KOBAYASHI**, HIROSHI MAEZAWA***, KOTARO HIEDA+, SHIGEFUMI OKADA++ and TAKASHI ITO+++

Department of Radiation Research, Tokyo Metropolitan Institute of Medical Science, Bunkyo-ku, Tokyo 113, Japan
*Division of Physiology and Pathology, National Institute of Radiological Sciences, Chiba-shi, Chiba 260, Japan
**Institute of Biological Sciences, University of Tsukuba, Niihari-gun, Ibaraki 305, Japan
***Department of Radiology, School of Medicine, Tokai University, Isehara-shi, Kanagawa 259-11, Japan
+Biophysics Laboratory, Department of Physics, Rikkyo (St. Paul's) University, Toshima-ku, Tokyo 171, Japan
++Department of Radiation Biophysics, Faculty of Medicine, University of Tokyo, Bunkyo-ku, Tokyo 113, Japan
+++Institute of Physics, College of Arts and Sciences, University of Tokyo, Meguro-ku, Tokyo 153, Japan

(Received December 7, 1984)
(Revised accepted Japanuary 23, 1985)

Auger effect/Monochromatic synchrotron radiation/Bromodeoxyuridine/HeLa cells/Survival

The HeLa cells labeled with 5-bromodeoxyuridine were irradiated with monochromatic synchrotron radiation at 0.90 Å or 1.00 Å, below or above the wavelength of the K absorption edge (0.92 Å) of bromine. Although non-specific sensitization of labeled cells to the radiation was observed irrespective of the wavelengths, the labeled cells were killed at a higher rate by the irradiation at 0.90 Å than at 1.00 Å. The non-labeled cells showed no difference in the sensitivity to the radiation at the two wavelengths. The enhanced lethality of labeled cells at 0.90 Å may be inferred to be due to the induction of Auger effect in bromine atom of the DNA selectively absorbed the photon at 0.90 Å. Implications of this finding for the photon activation therapy was discussed.

篠原邦夫，大原　弘*，小林克己**，前沢　博***，檜枝光太郎+，岡田重文++，伊藤　隆+++：東京都臨床医学総合研究所放射線医学研究部　東京都文京区本駒込 3-18-22　〒113
* 放射線医学総合研究所生理病理研究部　千葉県千葉市穴川 4-9-1　〒260
** 筑波大学生物科学系　茨城県新治郡桜村　〒305
*** 東海大学医学部放射線科　神奈川県伊勢原市望星台　〒259-11
\+ 立教大学理学部物理学教室　東京都豊島区西池袋 3-34-1　〒171
\++ 東京大学医学部放射線基礎医学教室　東京都文京区本郷 7-3-1　〒113
\+++ 東京大学教養学部物理学教室　東京都目黒区駒場 3-8-1　〒153

INTRODUCTION

Auger effect has been demonstrated to be highly effective to the killing of the cells when emitters of Auger electrons are located to the DNA (e.g., ^{125}I-iodouracil in place of thymine)[1-5]. The mode of this action was characterized by the similarity to the high LET radiation: Low oxygen enhancement ratio[6] and localized dose distribution[7, 8]. The average energy deposited in small target spheres by decaying ^{125}I has been estimated to be more than that by a passing 5 MeV alpha-particle with an LET of 100 keV/μm[9]. In considering these advantages of the possible Auger effect, a new mode of radiation therapy, photon activation therapy, has been proposed in recent years[10-12]. Photon activation therapy is based on the expectation that the selected monochromatic X-rays induce the vacancy of K shell in the key atoms in cellular molecules followed by Auger cascade at high frequency. Fairchild et al.[10] have proposed the combination of iodine in the form of 5-iododeoxyuridine and the X-rays with a wavelength slightly shorter than the K absorption edge of iodine for the photon activation therapy.

The enhanced radiation effects by the induction of Auger effect have been observed in the decomposition of amino acid[13], the radical formation of 5-bromodeoxyuridine[14], the inactivation of the Zn-containing enzymes[15], and the killing of bacteria under dehydrated conditions[16].

In the present communication, we wish to report an enhanced lethality of 5-bromodeoxyuridine-labeled HeLa cells with monochromatic synchrotron radiation at 0.90 Å as compared with the effect at 1.00 Å (the K absorption edge of bromine is 0.92 Å), probably attributable to the Auger effect in the incorporated bromine.

MATERIALS AND METHODS

HeLa cells were grown in Eagle's minimum essential medium supplemented with 10% foetal bovine serum under 5% CO_2 and 100% humidity. The cells at the exponentially growing phase were attached on a membrane filter disc as described elsewhere[17]. They were grown in the presence or absence of 5-bromodeoxyuridine (BUdR, 5×10^{-5} M) and deoxycytidine (CdR, 10^{-5} M) for one generation time (18 hr), and incubated for additional one hour in the fresh medium without BUdR and CdR after rinsing the cells with medium. The growing rate of the cells was not changed in the presence of BUdR and CdR during the incubation period, although it was decreased at longer incubation intervals. The plating efficiency of the cells grown in the presence of BUdR and CdR was 81.8 ± 8.1% of the control.

The cells on the membrane filter were kept wet (not dried) during the irradiation under atmosphere by the way that the membrane filter was placed on the filter paper soaked with Dulbecco's phosphate buffered saline. Since the beam size was smaller than the area to be irradiated, irradiation with monochromatic synchrotron radiation (0.90 Å or 1.00 Å) was performed on the sample-scanning stage[18]. The monochromatic radiation was obtained with 111-channel cut Si crystal (monochromater) from synchrotron radiation produced by the electron storage ring at the Photon Factory, National Laboratory for High Energy Physics. Intensity of monochromatic radiation was monitored by a free-air ionization chamber. Details

of the source of monochromatic radiation and the measurement of exposure have been described elsewhere[19]. The irradiated cells were collected from the membrane filter disc by trypsinization with 0.1% trypsin solution. Cell survival was determined by colony forming ability.

RESULTS AND DISCUSSION

As shown in Fig. 1, HeLa cells cultured in the presence of BUdR were more sensitive to the radiation at 0.90 Å than to that at 1.00 Å allowing a general sensitization of bromine irrespective of the wavelength of synchrotron radiation. This was confirmed by three different

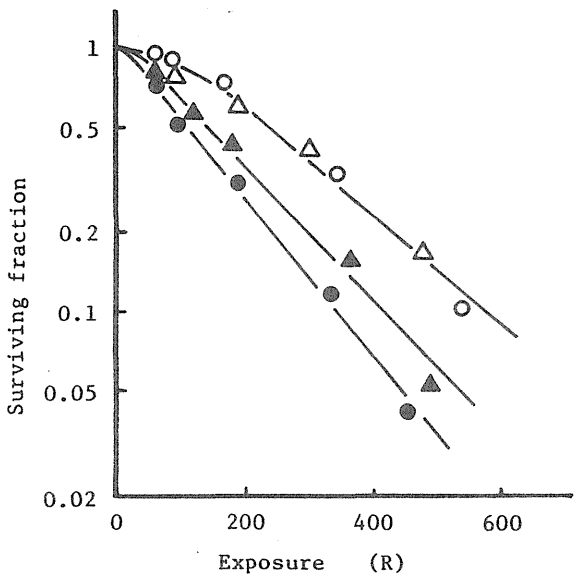

Fig. 1. Survival curve of HeLa cells irradiated with synchrotron radiation. HeLa cells were cultured in the presence (solid symbols) or absence (open symbols) of 5-bromodeoxyuridine and irradiated with synchrotron radiation at 0.90 Å (circle) or 1.00 Å (triangle).

Table 1. The ratio of D_0 with respect to the presence and absence of bromine at 0.90 Å and 1.00 Å.

	$D_0(-Br)/D_0(+Br)$	
	Wavelength (Å)	
Experiment	0.90	1.00
1	1.43	1.22
2	1.43	1.21
3	1.38	1.22

sets of experiments (Table 1) which were performed at three different beam times allotted in the period from June, 1983 till June, 1984 at the Photon Factory. Since the K absorption edge of bromine is 0.92 Å (13.47 keV), irradiation of bromine-containing DNA in the cells at 0.90 Å will produce the vacancy at K shell followed by Auger cascade in the bromine. Therefore, the additional killing effect of the radiation at 0.90 Å may be due to the toxicity of Auger electrons emitted from the bromine. Preliminary results showed the increased frequency of the induction of chromosome type of aberrations in the BUdR-labeled CHO cells when irradiated with synchrotron radiation at 0.90 Å, which may also be attributable to the Auger effect[20]. The increase in the lethality caused by the Auger effect was significant but not so large. One of the reason(s) of this small increase may be the relatively small attenuation coefficient of bromine in the DNA as compared with that of water corresponding to DNA[10]. Therefore, much higher increase in the lethality could be expected by taking 5-iododeoxyuridine instead of BUdR and the corresponding monochromatic synchrotron radiation, since iodine is superior to bromine in this respect[10].

The present results were in good agreement with the findings of Halpern and Mütze[16] in which they have shown the increased killing of BUdR-labeled dried bacteria with monoenergetic 14.4 keV X-rays compared with that of 12.1 keV. Myers et al.[21] have reported that no difference was observed in the killing enhancement of the radiations between 16 keV X-rays and ^{60}Co gamma-rays on T4 phages completely substituted with 5-bromouracil for thymine in its DNA irradiated under wet condition. In view of the wrong selection of radiation, the comparisons may not be warranted for the purpose of demonstrating the Auger effect.

The lethal effect of Auger electrons has been documented with ^{125}I labeled 5-iododeoxyuridine[1-5] and also with ^{77}Br labeled BUdR[22]. The toxicity of ^{125}I is much higher than that of ^{3}H or ^{131}I either on the basis of the lethality per disintegration or on the basis of the absorbed dose in the nucleus. The higher toxicity of ^{125}I has been inferred to be due to the Auger effect induced by the disintegration of ^{125}I[5].

The present results, i.e. the induction of Auger effect in mammalian cells by the external radiation, suggest the possibility of the photon activation therapy with the use of 5-iododeoxyuridine and the corresponding monochromatic synchrtron radiation which penetrates more than that in the present experiments.

ACKNOWLEDGEMENTS

The authors are grateful to kind cooperation of Dr. T. Yamada of the National Institute of Radiological Sciences, Dr. A. Ito of the University of Tokyo, Dr. H. Majima of the University of Tokyo, Mr. Y. Furusawa of Tokai University, Mr. I. Maeda of Rikkyo University, rest of the members of radiation biology working group, and the staffs at the Photon Factory, National Laboratory for High Energy Physics. One of the authors (K.S.) are very thankful to Dr. H. Orii of the Tokyo Metropolitan Institute of Medical Science for warmful encouragement. This work was supported in part by Grants-in-Aid from the Ministry of Education, Science, and Culture, Japan.

REFERENCES

1. Hoffer, K. G. and Hughes, W. L. (1971) Radiotoxicity of intranuclear tritium, ^{125}iodine and ^{131}iodine. Radiat. Res. 47: 94-109.
2. Burki, H. J., Roots, R., Feinendegen, L. E. and Bond, V. P. (1973) Inactivation of mammalian cells after disintegrations of ^{3}H or ^{125}I in cell DNA at −196°C. Int. J. Radiat. Biol. 24: 363-375.
3. Feinendegen, L. E. (1975) Biological damage from the Auger effect, possible benefits. Radiat. Environm. Biophys. 12: 85-99.
4. Bloomer, W. D. and Adelstein, S. J. (1978) 5-(^{125}I)-Iododeoxyuridine and the Auger effect: biological consequences and implications for therapy. Pathobiol. Annu. 8: 407-421.
5. Commerford, S. L., Bond, V. P., Cronkite, E. P. and Reincke, U. (1980) Radiotoxicity of intranuclear ^{125}I atoms not bound to DNA. Int. J. Radiat. Biol. 37: 547-554.
6. Koch, C. J. and Burki, H. J. (1975) The oxygen-enchancement ratio for reproductive death induced by ^{3}H or ^{125}I damage in mammalian cells. Int. J. Radiat. Biol. 28: 417-425.
7. Warters, R. L., Hoffer, K. G., Harris, C. R. and Smith, J. J. (1977) Radionuclide toxicity in cultured mammalian cells: elucidation of the primary site of radiation damage. Curr. Topics Radiat. Res. Q. 12: 389-407.
8. Martin, R. F. and Haseltine, W. A. (1981) Range of radiochemical damage to DNA with decay of iodine-125. Science 213: 896-898.
9. Hoffer, K. G., Keough, G. and Smith, J. M. (1977) Biological toxicity of Auger emitters: molecular fragmentation versus electron irradiation. Curr. Topics Radiat. Res. Q. 12: 335-354.
10. Fairchild, R. G., Brill, A. B. and Ettinger, K. V. (1982) Radiation enhancement with iodinated deoxyuridine. Invest. Radiol. 17: 407-416.
11. Halpern, A. (1982) Damage to biomolecules and cells by low-energy X-rays and vacuum ultraviolet light. In "Uses of Synchrotron Radiation in Biology", Ed. H. B. Stuhrmann, pp. 255-283, Academic Press, London.
12. Shinohara, K. (1984) Photon activation therapy. Igaku no ayumi 129: 822-823 (in Japanese).
13. Diefallah, E.-H. M., Stelter, L. and Diehn, B. (1970) Chemical consequences of the Auger effect: iodine yield from iodoamino acids as a function of X-ray dose and energy. Radiat. Res. 44: 273-281.
14. Halpern, A. and Stöcklin, G. (1974) A radiation chemical resonance effect in solid 5-bromodeoxyuridine; chemical consequences of the Auger effect. Radiat. Res. 58: 329-337.
15. Diehn, B., Halpern, A. and Stöcklin, G. (1976) Specific inactivation of solid carbonic anhydrase upon X-ray resonance absorption in the constituent zinc atom. J. Am. Chem. Soc. 98: 1077-1079.
16. Halpern, A. and Mütze, B. (1978) Irradiation of micro-organisms with mono-energetic X-rays; biological consequences of the Auger effect. Int. J. Radiat. Biol. 34: 67-72.
17. Shinohara, K., Inoue, Y. and Yamamoto, K. (1983) Increase in the apparent sensitivity of HeLa cells on a membrane filter to ultraviolet radiation. J. Radiat. Res. 24: 339-344.
18. Photon Factory Activity Report 1982/83 (1984) Instruments for X-ray irradiation experiments. p. V-37, National Laboratory for High Energy Physics.
19. Hieda, K., Kobayashi, K., Maezawa, H., Ito, T., Ito, A. and Ando, M. (1984) Irradiation system of monochromatic X-rays (0.85–2 Å) for radiation biology studies. Photon Factory Activity Report 1983/84, p. VI-17, National Laboratory for High Energy Physics.
20. Ohara, H., Shinohara, K., Yamada, T., Hieda, K., Kobayashi, K., Maezawa, H. and Ito, T. (1985) Chromosome aberrations in CHO cells irradiated by synchrotron radiations (abstract). J. Radiat. Res. 26: 23.
21. Myers, D. K., Childs, J. D. and Jones, A. R. (1977) Sensitization of bacteriophage T4 to ^{60}Co-γ radiation and to low-energy X radiation by bromouracil. Radiat. Res. 69: 152-165.
22. Kasis, A. I., Adelstein, S. J., Haydock, C., Sastry, K. S. R., McElvany, K. D. and Welch, M ^{Y}. (1982) Lethality of Auger electrons from the decay of bromine-77 in the DNA of mammalian cells. Radiat. Res. 90: 362-373.

RADIATION RESEARCH 104, S-235–S-243 (1985)

Proton Therapy in Japan

HIROSHI TSUNEMOTO, SHINROKU MORITA, TATSUO ISHIKAWA,*
SHIGEO FURUKAWA,* KIYOMITSU KAWACHI,† TATSUAKI KANAI,†
AND HIROSHI OHARA‡

*Division of Hospital, *Division of Clinical Research, †Division of Physics, ‡Division of Physiology and Pathology, National Institute of Radiological Sciences, 9-1, 4-chome, Anagawa, Chiba-shi, 260 Japan*

AND

TOSHIO KITAGAWA AND TETSUO INADA§

Particle Radiation Medical Science Center, §Department of Basic Medical Sciences, Tsukuba University Medical School, 1-1-1, Tennodai, Sakura-mura, Niihari-gun, Ibaragi-ken, 300-31 Japan

TSUNEMOTO, H., MORITA, S., ISHIKAWA, T., FURUKAWA, S., KAWACHI, K., KANAI, T., OHARA, H., KITAGAWA, T., AND INADA, T. Proton Therapy in Japan. *Radiat. Res.*, Suppl. 8, **104**, S-235–S-243 (1985).

There are two facilities for clinical trials with protons in Japan: the National Institute of Radiological Sciences (NIRS), Chiba, and the Particle Radiation Medical Science Center (PARMS), University of Tsukuba. At the National Institute of Radiological Sciences, patient treatment with the 70 MeV proton beam began in November 1979, and 29 patients were treated through December 1984. Of 11 patients who received protons only, 9 have had local control of the tumor. Two of the 9 patients, suffering from recurrent tumor after radical photon beam irradiation, developed complications after proton treatment. In the patients treated with photons or neutrons followed by proton boost, tumors were controlled in 12 of 18 patients (66.6%), and no complications were observed in this series. Malignant melanoma could not be controlled with the proton beam. A spot-beam-scanning system for protons has been effectively used in the clinical trials to minimize the dose to the normal tissues and to concentrate the dose in the target volume. At the Particle Radiation Medical Science Center, University of Tsukuba, treatment with a vertical 250 MeV proton beam was begun in April 1983, and 22 patients were treated through February 1984. Local control of the tumor was observed in 14 of 22 patients (63.6%), whereas there was no local control in the treatment of glioblastoma multiforme. There have been no severe complications in patients treated at PARMS. The results suggest that local control of tumors will be better with proton beams than with photon beams, whereas additional modalities are required to manage radioresistant tumors.

INTRODUCTION

There are two facilities for clinical trials with protons in Japan: the National Institute of Radiological Sciences (NIRS), Chiba, and the Particle Radiation Medical Sciences Center (PARMS), Tsukuba University, Ibaragi Prefecture. In this paper, the present status of proton radiotherapy in Japan is described, and the preliminary results of treatment are discussed. Clinical trials at NIRS with 70 MeV protons began in November 1979, while 250 MeV protons have been used for clinical trials at PARMS

0033-7587/85 $3.00

since April 1983. The aim of the studies in both facilities is to develop techniques to make charged particles suitable for therapy and to confirm the rationale for proton radiotherapy. The trials have been performed with close collaboration between the two facilities.

MATERIALS AND METHODS

Clinical trials with protons were performed with a horizontal beam at NIRS and with a vertical beam at PARMS. Intercomparison of the biological effects of the protons was performed between NIRS and Massachusetts General Hospital, Boston, and between NIRS and PARMS to evaluate the clinical results on a common basis.

1. Treatment System at NIRS

The cyclotron installed at NIRS can accelerate protons to 70 MeV, which can penetrate up to 36 mm in the tissue-equivalent phantom. To develop the techniques for proton radiotherapy and to establish clinical trials, a new beam line and a treatment chamber have been constructed in the physical experimental room of the cyclotron building. The beam line consists of three monitoring chambers, two sets of beam shaping slits, a beam shutter, and two orthogonal bending magnets.

The power supplies of these bending magnets are digitally controlled by minicomputer, and the 10-mm^2 spot beam of protons can be directed by those magnets to any point within a 20-cm^2 radiation field. This two-dimensional (2-D) spot-beam-scanning system has made it possible to achieve an irradiation field of any irregular shape and intensity distribution and to correct fluctuation in the beam intensity (*1*). In principle, it is not necessary to have any collimator in the spot-beam-scanning method. However, a multileaf collimator is used as a shield for back-up collimation. The collimator is made of forty 1 cm^2 brass rods and is able to conform to any desired irradiation field.

Based on the practical use of the 2-D spot-beam-scanning technique, a three-dimensional spot-beam-scanning method (3-D) was developed for proton radiotherapy at NIRS. The schematic diagram of the system is shown in Fig. 1.

In the treatment planning, the target volume is sliced into 1-mm Lucite equivalent thickness for the plane perpendicular to the beam direction. Each slice is further divided into square spots. The beam scanning method is in principle the same as the 2-D spot-beam-scanning system, but the scanning pattern and dose delivered are different at every slice and every spot to make a desirable spatial dose distribution in tissue.

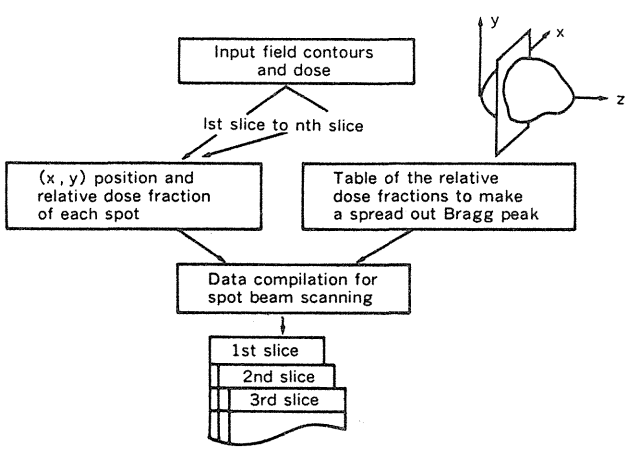

FIG. 1. Schematic diagram of the procedures for data compilation with the 3-D spot-beam-scanning method.

The dose-scanning pattern is dependent on the shape and size of the target volume and on its location in the body.

Before starting the 3-D spot-beam-scanning, the degrader thickness is adjusted to coincide with the depth of the Bragg peak of protons and the depth of the first scanning slice. The spot-beam-scanning of the proton irradiation starts from the deepest region of the target volume and goes to gradually more shallow regions. After completion of the scanning irradiation of each slice, the beam is directed to the shielded resting point, and a minicomputer sends a signal to the degrader to change the Lucite thickness. Then the scanning irradiation of the next slice starts under the control of the minicomputer. These procedures are repeated throughout the entire 3-D spot-beam-scanning irradiation.

The experimental results showed fairly good agreement between the planned and the measured isodose distributions. A typical example of those results is shown in Fig. 2. These results also indicate that the 3-D spot-beam-scanning method for proton conformation radiotherapy was very effective for reducing the dose to normal tissue compared with the 2-D spot-beam-scanning or the broad beam irradiation. This irradiation method will probably be useful for heavy-charged-particle radiotherapy in the future.

2. Treatment System at PARMS

PARMS started proton radiotherapy in 1983, utilizing a 2 μA beam of 500 MeV protons from the booster synchrotron of the High Energy Physics Laboratory. For proton therapy, the beam energy has been degraded down to 250 MeV by passing the primary beam through a graphite absorber. The beam pulses were delivered at a rate of 45 pulses per each cycle period of 2.5 s. A 50-ns-width pulse includes 5×10^9 protons of 250 MeV, which delivers a dose rate of greater than 1 Gy per minute at the irradiation site.

PARMS has three therapy rooms, one for neutrons and two for protons. One of the proton rooms features an irradiation system for a vertical beam (Fig. 3). The 250-MeV proton beam is bent vertically with a 90° bending magnet down to the second basement. To obtain a large uniform field (up to 20×20 cm^2), the proper geometry of the scatterer and ring-stopper combination was semiempirically determined (*2*). The fine degrader or shutter-oil-bath adjusts the range of the incident proton beam to match the tumor depth and spreads the Bragg peak width by using a microcomputer. The ridge filter and the range modulator have been alternatively used to spread the beam.

The resultant dose distribution indicated that there must be a considerable beam divergence and scattered component in this radiation field, which are inevitable when the degraded proton beam is used. These data have been formulated for each irradiation modality and applied to the treatment planning program.

The treatment planning system (TPS) at PARMS has been developed using a minicomputer (VAX 11/750) with a graphic display (Graphica I-7048) and other additional peripherals. The CT imaging is obtained with a GE-CT/T at the University Hospital, and data are transferred to TPS by magnetic tapes.

FIG. 2. Typical experimental results of a 3-D spot-beam-scanning irradiation with 0.5 Gy. Photograph at the transverse cross section of the target volume by 3-D spot-beam-scanning irradiation.

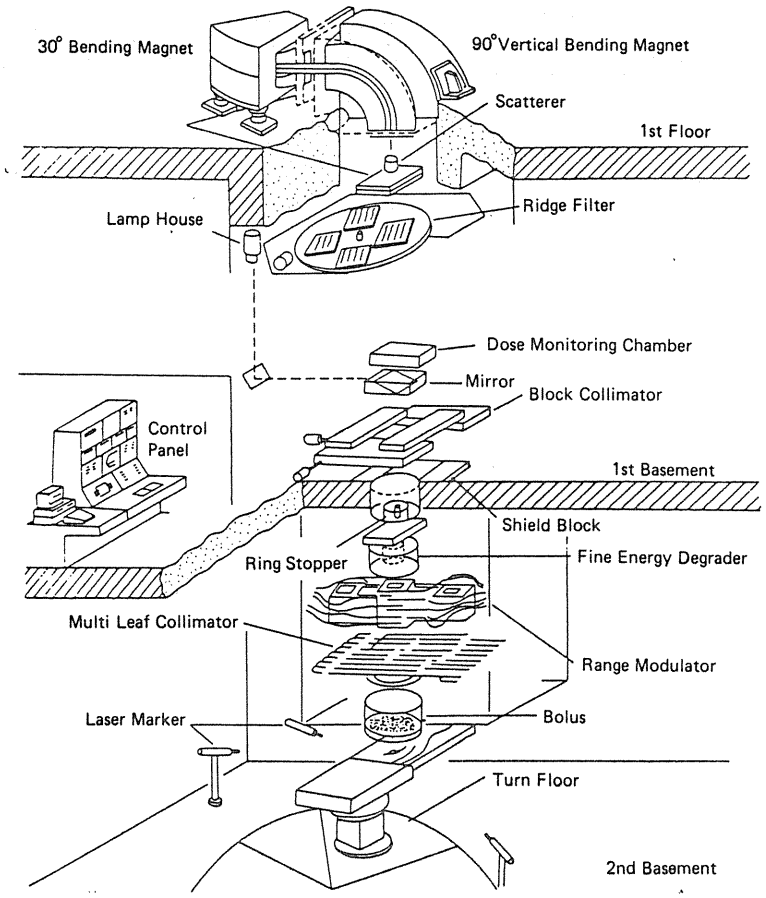

FIG. 3. Vertical proton beam irradiation assembly at PARMS.

A treatment-planning program with various functions for proton therapy was developed at Massachusetts General Hospital by Goitein *et al.* (*3, 4*), who kindly allowed us to use it, and the program was successfully interpreted for the different type of graphic display at PARMS and loaded on the TPS.

In addition, a simpler program has been developed at PARMS which enables us to process the treatment planning for each CT slice within 4 min. The body contour and the target outline are written on the CT image display. The beam directions within the CT plane (ventral, dorsal, right, and left) are selected corresponding to the vertical and horizontal proton beams at PARMS. The dorsal direction in the prone position can be applied in specific cases such as brain or head and neck tumors. By these means, we calculate the bolus shape and the optimized dose distribution. A typical example of the bolus shapes and the isodose distributions for a case of cervical cancer is displayed in Fig. 4.

3. Biological Effects of the Proton Beams

A comparison of the biological effects of proton beams was performed between NIRS and PARMS (*5*). One group of C3H mice with NFSa mouse fibrosarcoma growing in the lung was irradiated to the thorax with protons at the NIRS and a second group was irradiated at PARMS. The cell survival curves obtained at each institution were compared, and RBE values relative to ^{60}Co γ rays were evaluated. There was no significant difference between the two curves, which showed RBE values very close to 1.06.

A second comparison of proton beams was performed between NIRS and Massachusetts General Hospital

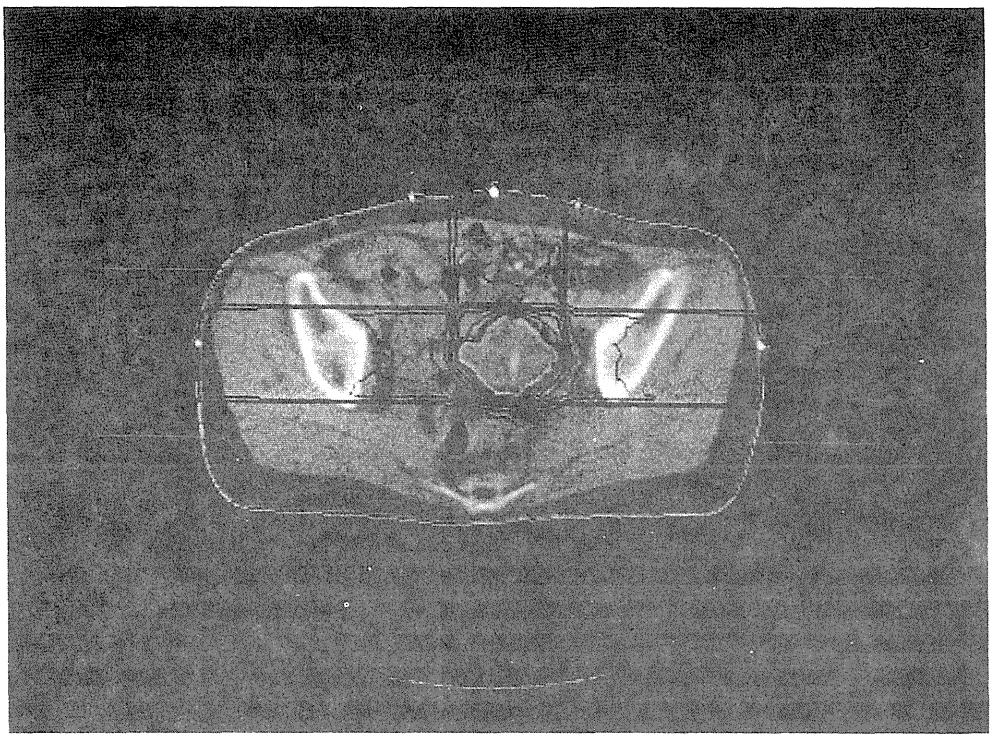

FIG. 4. Graphic display of an isodose distribution and the shape of compensating boluses illustrated on a CT slice of a cervical carcinoma case for a three-portal proton irradiation. Isodose contours indicate 10 to 100% levels with 10% step.

(MGH). The dose cell-survival curves of Chinese hamster ovary (CHO) cells irradiated with proton beams were studied. The results show that the average RBE value for protons relative to ^{60}Co γ rays at different survival levels was 1.1 for 70 MeV protons at NIRS and 1.24 for 160 MeV protons at MGH. Consequently, the therapy schedule and protocol were identical to the photon beam treatment.

The standard schedule at NIRS was 40 Gy of protons delivered in four fractions over 4 weeks; this was because the beam was prescribed for clinical trials every Friday morning. Dose per fraction was 10 Gy, which was used because of the exerience in the MGH (*6*). When the volume to be irradiated was large, doses of 8 or 9 Gy were used in the fractions.

RESULTS

At NIRS, superficial cancers were selected for clinical trials because the beams were able to penetrate only 36 mm into tissue.

Tumor responses and normal tissue reactions were evaluated by a five-step scoring system. Reactions and responses that developed within 6 months after completion of the treatment were scored as early reactions, and those that developed thereafter were recorded as late reactions. The late reaction scores for tumors and skin can be seen in Table I.

Of the 29 patients treated with 70 MeV protons at NIRS between November 1979 and December 1984, 11 received proton therapy only and 18 received a boost irradiation of protons following either photon beam or fast neutron therapy.

TABLE I

Late Reaction Scores for Radiation Effects and Skin Reactions

Radiation effect score
1. Complete disappearance without scar formation
2. Complete disappearance with scar formation
3. Residual and nongrowing tumor
4. Residual and slow-growing tumor
5. Rapidly growing residual tumor

Skin reaction score
1. None
2. Pigmentation, small telangiectasias, and skin atrophy
3. Extensive telangiectasias and skin atrophy
4. Severe skin atrophy
5. Necrotic ulcer

Table II shows the list of the patients treated with protons only. Local failure was seen in two patients; one of them was suffering from an advanced synovial sarcoma of the thigh which had recurred after surgery and was still regressing in size 12 months after completion of proton irradiation; the second was a 7-year-old boy who received salvage surgery for residual leiomyosarcoma of the back and thereafter had no evidence of disease during 31 months. Complications were observed in two patients, both of whom were suffering from tumors that continued to grow after radical photon beam irradiation. In one patient (53972) who had recurrent fibrosarcoma in his chest wall,

TABLE II

Results of Treatment with Protons Only (70 MeV); NIRS (1979–1984)

Case number	*Age*	*Sex*	*Target*	*Dose (Gy/f/days)*	*Effect*		*Length of follow-up (months)*
					Tumor	*Skin*	
54395	62	Male	Skin cancer	40/4/22	CR	3	4(+)[a]
54486	59	Female	Skin cancer	30/3/15	CR	2	54
56297	79	Female	Skin cancer	32/4/29	CR	2	19
53697	80	Male	Fibrosarcoma (Node)	40/4/22	CR	3	6(+)[a]
53972	26	Male	Fibrosarcoma (Rec.)	30/3/21	CR	4	40
55011	7	Male	Leiomyosarcoma	20/2/8	PR	2	31
55243	71	Male	Synovial sarcoma	30/2/8	PR	2	12
53775	70	Female	Breast cancer (Rec.)	26/2/8	CR	3	43
54180	54	Female	Breast cancer (Rec.)	26/2/8	CR	3	50
54598	65	Female	Breast cancer (Rec.)	40/5/36	CR	3	13
54340	53	Female	Thyroid cancer (Rec.)	24/3f/15	CR	4	48

Note. CR: Complete regression; PR: Partial regression.
[a] Cause of death: metastasis.

an ulcer developed in the radiation field and was cured by conservative treatment in 31 months of follow-up. Another female patient (54340) with recurrent thyroid cancer of the neck suffered dysfunction of the brachial nerve 1 year after proton therapy and had local control of the tumor in 48 months of follow-up.

For proton boost irradiation, protons were delivered to the target volume where photon beams or fast neutrons had already been given. The total doses were equivalent to TDF 75-160 and were chosen according to the response of the tumors. The results show that, in 12 of 18 cases, the tumors were controlled without severe complications (Table III). Failures were seen in six patients, five of them received salvage surgery thereafter and had no evidence of disease without complications (6–68 months).

At PARMS, clinical trials with 250 MeV protons were begun in April 1983, and 22 patients had been treated through February 1984. In this clinical trial, a daily fractionation scheme was used. Doses of 65 to 75 Gy of protons were delivered to the target area in 20–26 fractions over 6–7 weeks.

Of the 22 patients, 4 had skin cancers, 2 had tongue cancers, 1 had cancer of the buccal mucosa, 1 had cancer of the middle ear, 1 had cancer of the parotid gland, 1 had cancer of the uterine cervix, and 2 had hepatic cancers. These 12 patients have had local control of their tumors without complications and 11 have survived for 11–17 months after completion of the therapy.

The remaining 10 patients in this group suffered from malignant brain tumors, i.e., two malignant meningiomas, three astrocytomas (grade III), and five glioblastoma multiformes. Four of the five patients with malignant meningioma and astrocytoma achieved local control of the tumor. None of the patients suffering from glioblastoma multiforme, however, had local control of the tumor, and two of them died. No severe complications have been observed during 7 to 13 months of follow-up.

The preliminary results of clinical trials performed at NIRS and PARMS suggest that proton therapy will improve local control rates of tumors with reduced complication rates of the normal tissues. However, additional modalities are required to manage radioresistant tumors.

DISCUSSION

Radiation therapy has made steady progress in local control of tumors following the introduction of high-energy X-ray and high-energy electron accelerators. Nevertheless, the fact that the doses delivered to the target volume are strongly dependent on the radiation tolerance of the surrounding normal tissues remains a critical problem.

Conformation radiation therapy with high-energy X rays has been developed to deliver a larger dose to the target volume than conventional treatment and to reduce the dose given to the surrounding normal tissues. Adjusting the shapes of the leaf collimator to the treatment fields during rotational irradiation enables us to irradiate only the target volume (7).

On the other hand, when charged particles such as protons are used, sophisticated computer programs make it possible to control the particle beams with bending magnets.

The proton spot-beam-scanning method will be used effectively for further improving the dose localization within the target volume and will also be applied to other charged particle treatments.

TABLE III

Results of Treatment with Proton Boost (70 MeV); NIRS (1979–1984)

Case number	*Age*	*Sex*	*Target*	*Dose (TDF)*	*Effect*		*Length of follow-up (months)*
					Tumor	*Skin*	
53214	64	Male	Skin cancer (Rec.)	80	PR	3	10(+)[b]
53376	78	Male	Cancer parotid gland	78	PR (OP).	3	68
53784	60	Female	Cancer parotid gland	100	CR	3	62
53898	57	Male	Cancer parotid gland	100	CR	2	57
50054	63	Male	Fibrosarcoma	87	CR	2	6(+)[b]
54765	73	Male	Malignant fibrous histiocytoma	130	CR	1	36
53896	57	Male	Malignant melanoma	133	PR (OP.)	3	58
54871[a]	72	Male	Malignant melanoma	128	PR (OP.)	3	9(+)[b]
55524	71	Male	Malignant melanoma	140	PR (OP.)	3	26
54302	42	Female	Breast cancer (Rec.)	120	CR	3	18(+)[b]
54704	36	Female	Breast cancer (Rec.)	75	CR	2	12
51155	46	Female	Breast cancer (Rec.)	81	CR	2	25
55721	59	Female	Breast cancer (Rec.)	140	CR	2	19
53877	77	Male	Metastatic lymph node (squamous cell cancer)	120	CR	3	2(+)[c]
54871[a]	72	Male	Metastatic lymph node (Melanoma)	128	PR (OP.)	2	9(+)[b]
55032	83	Female	Metastatic lymph node (squamous cell cancer)	160	CR	1	30
55189	75	Female	Metastatic lymph node (squamous cell cancer)	128	CR	2	9
55524	75	Female	Metastatic lymph node (squamous cell cancer)	160	CR	3	27

Note. CR: complete regression; PR: partial regression.
[a] Tumor response was evaluated separately.
[b] Cause of death: metastasis.
[c] Cause of death: other disease.

The proton clinical trials performed in the United States and Europe show that a 10% higher dose could be delivered to target volume without increasing radiation damage to normal tissues compared to photon beam irradiation (*8, 9*).

The Japanese experience suggests that the complication rate could be reduced by proton treatments due to their superior dose localization. Proton clinical trials will be continued to evaluate the clinical benefit of dose localization.

REFERENCES

1. T. KANAI, K. KAWACHI, Y. KUMAMOTO, H. OGAWA, T. YAMADA, H. MATSUZAWA, and T. INADA, Spot scanning system for proton radiotherapy. *Med. Phys.* **7**, 365–369 (1980).
2. A. M. KOEHLER, R. J. SCHNEIDER, and J. M. SISTERSON, Flattening of proton dose distributions for large-field radiotherapy. *Med. Phys.* **4**, 297–301 (1977).
3. M. GOITEIN and M. ADAMUS, Multi-dimensional treatment planning: I. Delineation of anatomy. *Int. J. Radiat. Oncol. Biol. Phys.* **9**, 777–787 (1983).
4. M. GOITEIN, M. ADAMUS, D. ROWELL, H. POLLARI, and J. WILES, Multi-dimentional treatment planning: II. Beam's eye-view, back projection and projection through CT sections. *Int. J. Radiat. Oncol. Biol. Phys.* **9**, 789–797 (1983).
5. K. ANDO, S. KOIKE, K. KAWACHI, T. HIRAOKA, H. OHARA, M. YOKOTA, T. INADA, Y. HIROKAWA, S. SATO, K. EGUCHI, and M. URANO, Relative biological effectiveness of the therapeutic proton beams at NIRS and Tsukuba University. *Nippon Act. Radiol.* **45**, 531–535 (1985).
6. H. D. SUIT, M. GOITEIN, J. E. TEPPER, L. VERHEY, A. K. KOEHLER, and R. SCHNEIDER, Clinical experience and expectation with protons and heavy ions. *Int. J. Radiat. Oncol. Biol. Phys.* **3**, 115–125 (1977).
7. T. MATSUDA and K. INAMURA, Computer controlled multi-leaf conformation radiotherapy. *Nipp. Act. Radiol.* **41**, 965–974 (1981).
8. J. R. DUTTENHAVER, W. U. SHIPLEY, T. PERRONE, L. G. VERHEY, M. GOITEIN, J. E. MUNZENRIDER, G. R. PROUT, E. C. PARKHURST, and H. D. SUIT, Protons or megavoltage x-rays as boost therapy for patients irradiated for localized prostatic carcinoma. *Cancer* **51**, 1599–1604 (1983).
9. S. GRAFFMAN and B. JUNG, Clinical trials in radiotherapy and the merits of high energy protons. *Acta Radiol. Ther. Phys. Biol.* **9**, 1–23 (1970).

眼球内melanocytomaに対する陽子線治療経験

中野隆史[1] 森田新六[1] 恒元博[1] 五味弘道[1] 荒居龍雄[1] 松本健[2] 古川重夫[2] 中村譲[2]
石川達雄[2] 平岡武[3] 河内清光[3] 金井達明[3] 川島勝弘[3] 赤沼篤夫[4] 金子明博[5] 佐野雄太[6]
放医研 病院部[1] 臨床研究部[2] 物理研究部[3] 東大医放[4] 国立ガンセンター眼科[5]
慈恵医大眼科[6]

Clinical experience of proton radiotherapy for ocular melanocytoma

Takashi Nakano,[1] Shinroku Morita,[1] Hiroshi Tsunemoto,[1] Hiromichi Gomi,[1]
Tatsuo Arai,[1] Ken Matsumoto,[2] Shigeo Hurukawa,[2] Yuzuru Nakamura,[2]
Tatsuo Ishikawa,[2] Takeshi Hiraoka,[3] Kiyomitsu Kawachi,[3] Tatsuaki Kanai,[3]
Katsuhiro Kawashima,[3] Atsuo Akanuma,[4] Akihiro Kaneko[5] and Yuta Sano.[6]
1) Division of Hospital, 2) Division of Clinical Reseach,
3) Division of Physics, Naional Institute of Radiological Sciences (NIRS).
4) Dept. of Radiology, Tokyo Univ.
5) Dept. of Ophthalmology, Naional Cancer Center Hospital.
6) Dept. of Ophthalmology, Jikei Univ.

Seventy MeV proton beam irradiation has been used for the treatment of superficial tumors since 1979 at NIRS. The physical characteristics of protons, namely Bragg peak of the ionization offers the posibility of highly localized dose distribution which has clinical advantages in the field of ocular radiotherapy. To arrest the progressive symptomes of melanocytoma in the optic disk on a female patient, 30Gy of proton radiation delivered in 3 fractions over 28 days (TDF 80). In spite of a short follow-up period, the lesion showed depigmentation and the field of vision improved slightly. No side effect were ovserved. The radiation planning method and the treatment techniques of proton radiotherapy were also discussed.
Key words: proton radiotherapy, radiation planning and technique, Ocular melanocytoma

緒言

放医研では昭和54年から医用サイクロトロンからの70MeVの陽子線で臨床試験を開始している。この陽子線のビーム到達距離は38mmと浅いので浅在性の腫瘍が対象となり60年12月現在で34症例の照射が行なわれ、良好な局所制御と軽度な正常組織反応を観察している。

今回、視野欠損などの臨床症状が進行性で治療を要する視神経乳頭部のmelanocytomaに対し症状の改善を図る目的で陽子線治療が施行された症例を経験したので報告する。

陽子線は現在、放射線治療に用いられる放射線の中では最も優れた線量分布が得られる。即ちbragg peakを有し、一定の深部到達距離より先にはビームが進まないこと、側方散乱が少ないことなどの優れた特性を持っている。これにより水晶体を避けて網膜や硝子体内の腫瘍のみに大線量の照射が可能で、しかも他側の眼球や脳実質の被曝を避けることができる。

症例 44歳 女性 左眼球視神経乳頭部のmelanocytoma

*主訴 視力低下、霧視
*既往歴、家族歴 なし
*現病歴 昭和58年6月 左霧視
右視力 1.2 左視力 0.8
左マリオット盲点の拡大
左鼻側下方 1／4盲
昭和60年10月 左視野欠損の進行 瞳孔反応の異常出現

左眼球視神経乳頭部に半円状に軽度隆起した黒色色素沈着を示すmelanocytomaが存在した(Fig. 1)。昭和58年より慈恵医大眼科にて経過観察を行なってきた。melanocytomaは組織学的には良性の腫瘍であるが、この症例は視野欠損が進行性であることから陽子線治療の適応

と判断し十分の治療計画と経過観察を行なうことを条件にひかえめの線量で照射が実行された。

I　陽子線の特性

1線量分布：

放医研の医用サイクロトロンで加速された陽子線は70MeVのエネルギーを持ち均一軟部組織では38㎜の飛程を有する。即ちこの陽子線は表面より38㎜の深さでエネルギーを急激に失いビームはそれより先に進まない(bragg peak)特性を有する。bragg peakの幅は1～2㎜なので治療の際にはtargetの腫瘍の厚さにあわせてレンジモジュレーターによりpeak幅を広げて用いている。また電子線と比較して側方散乱が極めて少なく、隣接臓器の被曝を避ける点で有利である。

2)RBE値

陽子線の生物効果比はほぼ1であり(培養細胞で1.0～1.1、皮膚や腫瘍で0.8～0.9、)、X線やガンマ線とほぼ等しい。また速中性子線にみられる低OERなどの利点も認められない。

II　治療計画法

線量分布が優れた特性を持つ陽子線の特徴を生かすには腫瘍の局在の正確な診断、照射中の患者の確実な固定が要求される。腫瘍の局在診断にはX線CTやMRIや超音波診断法が活用され、さらにこの診断法は腫瘍や組織の照射効果の経過観察にも用いられた。

X線CT診断では治療体位での撮影が必要で、これにより腫瘍の大きさ、広がり厚さ、深さが計測される。腫瘍の大きさ、広がりは照射野の大きさやブロックの位置の指標となり、その厚さはレンジモジュレーターの選択の、深さはボーラスで深部線量分布を調節する時の指標となる。ボーラスの材質にはX線CT値が水に近く、皮膚への密着度がよく、照準用のレーザービームが透過するものであることが必要で、水や寒天やアクリルが用いられる。

患部の固定にはソフラン発泡剤で鋳型をとる方法を用いている。放医研の陽子線は水平固定一門ビームなのでこのビーム方向に合う体位を設定し、固定することが必要であり、正確な照射を行なうには治療計画時と照射時の患者の体位の再現性が最も重要である。

1)治療計画

腫瘍の位置は眼底写真を参考にした。腫瘍が微小のためにX線CT画像やMRIでは描出不能であったが、視神経は十分に確認できるので、照射計画はそれを指標にして行なわれた。水晶体を避けるために、患者を右側臥位とし、顔を斜め下方を向かせ、かつ右前方を注視させた状態で、左外側眼球結膜より照射ビームを入射した。1回の照射時間は10秒程度なので、目を開いた状態で照射が可能である。頭部の固定は古川により頭軸方向に回転でき微量調節可能な円筒形固定具が考案された。眼球の大きさは直径25㎜で視神経の直径は6㎜であった。眼球表面より眼底までの距離は24.8㎜、眼角より水晶体までの距離は20㎜であった。従って陽子線のピーク幅を15㎜に広げ、5㎜のアクリル板をボーラスに用いて直径10㎜のビームを用いれば視神経の周囲3㎜、網膜の前後7㎜の治療域が得られる(Fig. 2)。しかし平岡らが直径10㎜の照射野でコリメーターから14㎝離れた位置での線量分布を実測したところ中心線束に垂直面の側方線量分布で半影が比較的大きく(Fig. 3)、また深部線量分布でも大照射野に比較して治療域での平坦度が＋5％程度と均一性が劣化していた(Fig. 4)。

2)照射線量

陽子線のマシンタイムは週1回なので週1回大量照射法が行なわれた。腫瘍線量は30Gy／3回／4週間TDF80が計画され実行された。しかし、線量分布の悪さから、ターゲットに対するビームのわずかなずれを考慮すると実際の線量はこの80％程度と考えたい。

3)治療経過

2回目の照射後、左偏頭痛が増強し4回のおう吐が出現した。鎮痛剤にて頭痛は改善しおう吐も消失した。治療開始後20日目の検査で視野の改善が軽度見られ、視力が0.8から1.0と回復し、眼底鏡でも腫瘍の高さと直径の縮小化ならびに色素脱出が認められた。また後極部全体に軽度の浮腫が認められた。30Gy照射12日後腫瘍の色素脱出が進み全体に褐色調となり、軽度の高さの変化が認められたが20Gy時の変化に比べると軽度であり、蛍光眼底検査にて腫瘍の染色性が高くなった。1か月後には視野も照射前に比し外部イソプターで約30度の拡大が認められた(Fig. 5)。患者も新聞を読んでもそれほど疲れなくなってきた、と症状の改善を喜んでいる。

考　案

眼球内に発生する腫瘍のうち放射線治療の対象となる疾患の主なものに乳幼児の網膜芽細胞腫ならびに大人のmalignant melanomaがある。共に放置すれば失明そして死亡の転帰をとり、適切な治療が必要である。生命を保持する点では眼球摘出手術が最上であるが患者の失明は必至でありその後の生活に大きな支障となる。放射線療法は視力を保持できる可能性のある治療法であり、できるならば第一選択の治療法として採択されるべきである。

視神経乳頭のmelanocytomaはmalignant melanomaと

の鑑別が難しい希な良性腫瘍である。視神経乳頭に原発する腫瘍は一般に良性であり、臨床症状の悪化、腫瘍の急速な拡大を見ぬ限り悪性と考える必要はなく、眼球摘出の適応とはならないと考えられている。[2,3] この症例は中心視力の低下などの症状の悪化がみられ、治療が必要と判断し、眼球摘出を避けるため、陽子線治療が施行された。

眼球内腫瘍への陽子線治療の試みは小児の網膜芽細胞腫症例が最初に計画されたが、患者の固定や麻酔の問題を含め、体位の再現性などの解決が不十分であったので治療を実行できなかった。このために本症例が眼球内腫瘍に対する陽子線治療の日本で最初の症例となった。

欧米ではmalignant melanomaに陽子線治療が試みられている。[1] malignant melanoma はDqが大きいために1回の分割線量は６００cGy以上が局所制御に必要とされており、１回線量を１０００cGy～２０００cGy 投与している施設も多い。しかし、眼球は比較的放射線感受性の高い組織も多く、被曝が避けられないので放射線障害の点から極めて治療の難しい部位である。melanocytomaの放射線生物学的特性が知られていないため、もしmalignant melanomaに準じるDqであっても生物学的効果が得られるように１回分割線量を１０００cGyとし、腫瘍の増殖の抑制を狙い、また視神経の耐容線量はＴＤＦ１００前後とされており、放射線障害を避けるためにＴＤＦ８０と控え目な照射線量が選ばれた。眼球腫瘍を照射する場合、眼球が極めて小さい臓器であり、水晶体を避けて照射する必要があるので、その照射範囲は極めて限局したものとなる。従来の高エネルギーX線の側方照射では比較的放射線感受性の高い網膜芽細胞腫には根治線量の投与が可能となるが、放射線抵抗性のmalignant melanomaでは根治線量の投与は不可能に近い。ここに陽子線の線量分布の特性が十分生かされ、局所に大線量の照射が可能となれば放射線抵抗性のmalignant melanomaといえども眼球内の小さな腫瘍ならば十分に根治可能と考えられる。

放医研の治療装置ではレンジモジュレーターとコリメーターが接近しているため、レンジモジュレーターにより生じた散乱線が大きな半影を生じる。このために細いビームでは陽子線本来の持ち味である線量分布の良さを十分活用できない。この場合は眼球の近傍で二次遮蔽を行なうことにより、改善できる。それでも電子線に比べれば表面線量が少なく、治療域より深部で飛程が急峻に切れる点でこの治療には陽子線がより有効である。眼球内腫瘍の治療に陽子線の特徴を生かすためには小照射野における線量分布の改善が必要である。

また治療部位に正確に照射されているかどうかの確認をどのように行なうかも今後の課題となった。眼球を固定したまま線量を病巣に集中する治療技術は対象が乳幼児となると更に困難なものとなる。照射部位を設定する適当な装置が無いことと病巣線量を実測する良い方法がない点が問題である。

治療後の組織反応については眼底鏡や蛍光眼底写真や視野測定に加えて、組織の微妙な質的変化を捕らえうるＭＲＩにても治療経過を追っているが明らかな変化は認められない。ただ治療中一過性の頭痛が認められた。これは眼底鏡にて変化がつかめなかったが、局所の照射による浮腫のための可能性が強い。治療後まだ経過が浅いが、すでに視野の回復が認められ、腫瘍の変化も認められている。正常組織の反応としてはまだ軽度の浮腫のみであるが白内障や緑内障など慢性の放射線障害については厳重な観察が必要と考えている。

結　語

眼球内melanocytomaに対して臨床症状の改善を図る目的で陽子線治療を行なった。治療後まだ経過が浅いが、すでに視野の回復が認められ、腫瘍の変化も認められた。線量分布が優れた特性を持つ陽子線の特徴を生かすには腫瘍の局在の正確な診断、照射中の患者の確実な固定が要求された。小照射野の陽子線の線量分布はまだ良好と言えず、改善の可能性が残されている。

参考文献

1　Gragoudas E. S. et al :Current results of proton beam irradiation of uveal melanomas. Ophthalmology 92:284～291,1985.
2　高橋俊博　他:視神経乳頭のmelanocytomaの１症例. 日眼紀28:1027～1035,1977.
3　Joffe L. et al :Clinical and follow-up studies of melanocytomas of the optic disc. Ophthalmology 86:1067～1078,1979.

Fig. 1
左眼　眼底のMelanocytoma

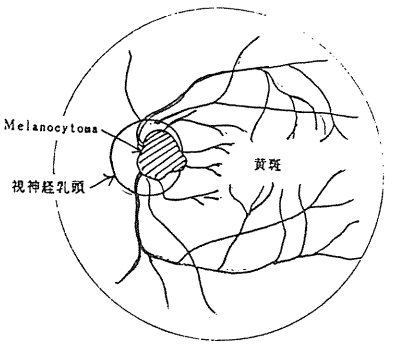

Fig.2 Planning of proton beam radiotherapy

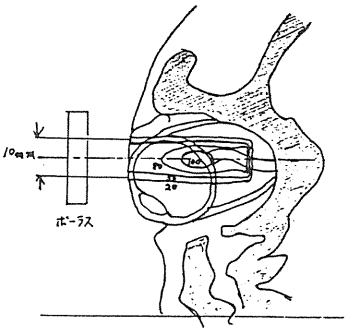

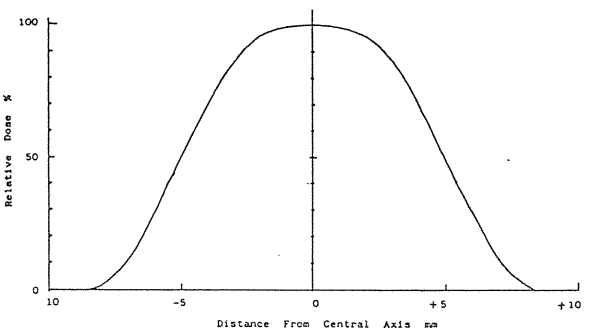

Fig.3　Relative Dose distribution in 10X 10 mm Field

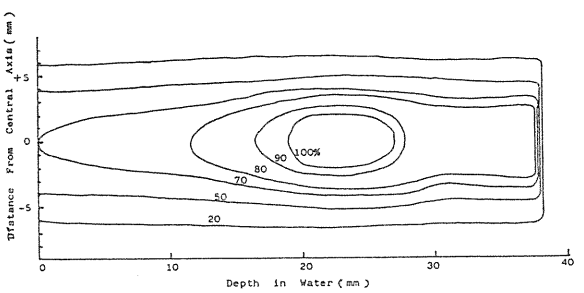

Fig.4　Dose Distribution of Proton Beam in 10X 10 mm Field

Fig. 5　左視野の治療後の変化

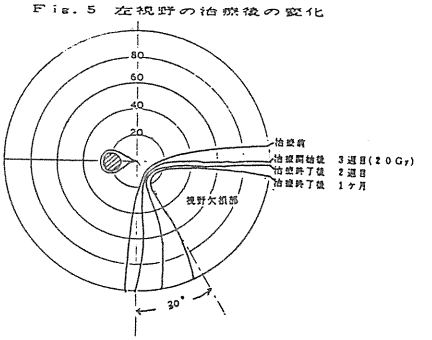

〔原　著〕

陽子線治療のボーラス作成

古川重夫*，赤沼篤夫*2，青木幸昌*3，中村　譲*1，森田新六*4
石川達雄*1

*1：放医研　臨床研究部　　*3：都立豊島病院　放射線科
*2：東京大学　放射線科　　*4：放医研　病院部

(昭和60年10月22日受付)

Bolus Construction in Proton Beam Radiotherapy

Shigeo FURUKAWA,*1 Atsuo AKANUMA,*2 Yukimasa AOKI,*3
Yuzuru KUZUTANI-NAKAMURA,*1 Shinroku MORITA*4 and
Tatsuo ISHIKAWA*1

*1 Div. of Clin. Researches, Natl. Inst. of Rad. Sciences
*2 Dept. of Radiology, Faculty of Medicine, Univ. of Tokyo
*3 Dept. of Radiology, Metropolitan Toshima Hospital
*4 Hospital Division, Natl. Inst. of Radiological Sciences

National Institute of Radiological Sciences initiated its proton beam radiotherapy in October, 1979. The beam energy is 70 MeV and its penetration is 38mm. Proton beam radiotherapy has the possibilities to avoid dose to a critical organ perfectly and to concentrate dose to the target. Bolus technique is one the methods to realise the above possibilities. In recent radiotherapy CT-views are applied to institute the target and to perform treatment planning. Hence in this study facile construction methods of various boluses for proton radiotherapy and their materials are investigated employing CT-views and CT-scan nre too. As the material for it we consider water is the best, since it's perfectly clear. It helps a therapist very much in setting up a patient for irradiation. Moreover majority of physics data are obtained with water phantoms. Hence the method to apply water for bolus was studied.

Key words : Proton beam, radiotherapy, bolus, CT, water.

〒260 千葉市穴川4－9－1

はじめに

放射線医学総合研究所では，1979年10月に70MeVの陽子線を用いて臨床治療を開始した。1984年7月までに27症例，28部位の治療を行った。28部位の内訳は皮膚癌3，耳下腺癌3，乳癌2，軟部組織肉腫5，乳癌及び皮膚転移5，悪性黒色腫3，頸部リンパ節転移7，であった。陽子線の特長としていずれの症例も治療容積（Treatment Volume）は小さい。50㎜×50㎜前後のものが多く，最大は140㎜×120㎜のものもあった。しかし，70MeVの陽子線の最大飛程は38㎜で容積としては小さい。治療容積が小さくなるので正常組織の耐容線量は大きくなる。放医研の基本線量配分は40Gy/4回/22日でTDFでは120。飛程が短いので照射治療の適応も限定され，表在性の腫瘍の照射に限られてくる。しかし，耐容線量は高くなり，TDF 160照射した症例も障害がでていない，よって，X線やガンマー線で治療した後に再発した症例にも用いられてきた。より一層陽子線治療での可能性を実現するため色々の研究が行われている。その可能性とは，

1. 重要臓器への線量をなくすこと。
2. 標的容積へ線量を集中する。

これらの可能性を実現するためには，まず腫瘍(Target)の位置と大きさの評価が問題であろう。X線CTをかなり自由に使えるようになった現在では，[1),2)]この評価もかなり正確にできるようになったと言えるが，まだ軟部組織間の腫瘍はわからないし腫瘍の輪郭はわからない。NMR－CT等今後の発展を待たなければならない。次に患部の固定が問題である。[3)]これには，患部が体に対して相対位置を変動さす場合と，体自体が照射装置の物理系に対して動く場合がある。前者についてはその対策が今まで殆んど進んでいないといえるが，後者については発泡ウレタン[4),5)]を用いる等の対策を試みてきている。次にビームのコントロールの問題である。まず入射方向を自由に制御したいわけではあるがこれは加速器技術的に非常にむつかしい。現在側方向からの固定となっている。次にビームの大きさ，すなわち照射野の問題であるがこれには散乱法と走査法が考えられるのである。放医研では世界唯一ケ所である走査法という高度な技術を利用している。現在まで用いた照射野の最大のものは140㎜×120㎜であるが走査法では大変大きな線量の均一な照射野を作ることができる。次に線量投与位置の制禦である。陽子線はブラツクピークをもち，ここでほとんどの線量は放出される。このブラツクピークをターゲット内の思った所にもってゆかなければならない。すなわちビーム到達距離の制禦である。現在の加速器の性格上，ビームのエネルギーを自由に変えることはできない。一定エネルギーのビームが放出されるからこれをエネルギー吸収体を通してエネルギーを変化させ到達距離を制禦するのである。これには二つの方法がある。その一つは走査法である。これは一定の厚さのエネルギー吸収体を通過したビームで一定の深さを走査し，又吸収体の厚さを変えて次の深さの所を走査する方法で現在放医研で三次元走査法として研究中である。[6)]もう一つの方法はボーラス法である。ボーラスはX線治療に於いてよりよい線量分布を得るために用いられた。例えば喉頭癌や上顎癌の治療時四角い均等な線量分布を得るためウエッジ技法を用いるがこの時直角なターゲットにするために用いられる，ここで

はボーラスの厚さを成形して，陽子線がターゲットの下側の縁で止まるように工夫するのである。ボーラスの典型的な材料はパラフインである。しかし陽子線治療ではパラフインは問題があるので色々な材料を試みた結果，水ボーラスが最も好ましいと考えられる。故に水ボーラス利用について議論する。

方法

まず腫瘍の範囲や位置を，診断用画像（主にCT画像）から判断し，患者の照射しやすい体位等を決定しなければならない。次に患部を皮膚上にマークして（図1）患者を照射の状態に寝かす。患部に石膏ギプス（図2，図3）又はアルギン酸（図4，図5）で鋳型をとる。アルギン酸は皮膚面が汚れない等の扱い易さはあるが，軟らかくて取外したとき原形が保たれない恐れがある。この鋳型に石膏を流し込み，患部の石膏模型を作る（図6）皮膚マークは鋳型にうつり，更に石膏模型に写るので患部の位置を石膏模型のうえでも正確に知ることができる。石膏模型が充分に乾いた後，0.5㎜もしくは1.0㎜の塩ビ板又はアクリル板を電気ヒーターで充分に暖めて軟化させてこの石膏模型の患部の部分に押し付けて表面の形を作ることができる。軍手をはめ指で押さえつけるだけで形成することができる。アクリル板より塩化ビニール板の方が成形しやすい。次に成形した樹脂板を切るのであるが塩ビ板は金工用ハサミできることができるがアクリルはハサミではひびわれをしてきれないこともありグラインダー等をもちいて削るようにしたほうが良い。患部を充分に覆うことができる広い範囲でその縁にゴムねんどまた

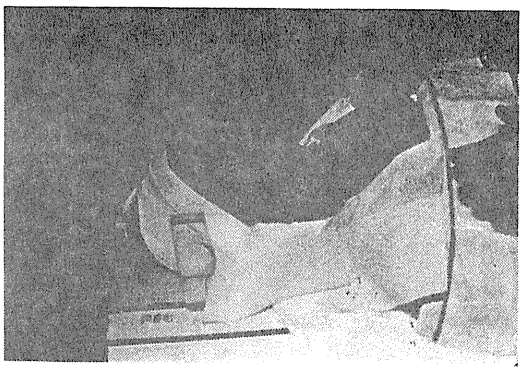

Fig. 1. A physician makes skin marks and the patient is laid in treatment position.

Fig. 2. A plaster cast is made in the treatment position. This cast is a mold to make boluses and can be also used for the fixation device.

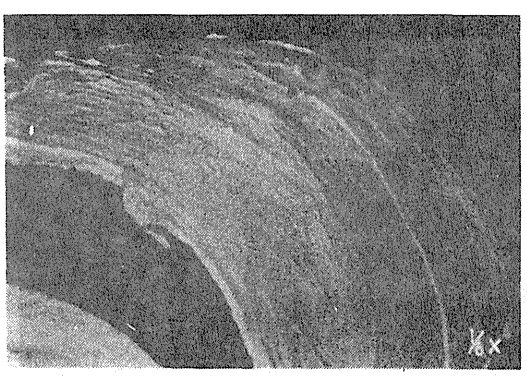

Fig. 3. The mold is made with plaster tapes in a case of chest wall recurrences from breast carcinoma.

Fig. 4. A face mold is made with alginate. The patient is a case of angiosarcoma which is shown in Fig. 13.

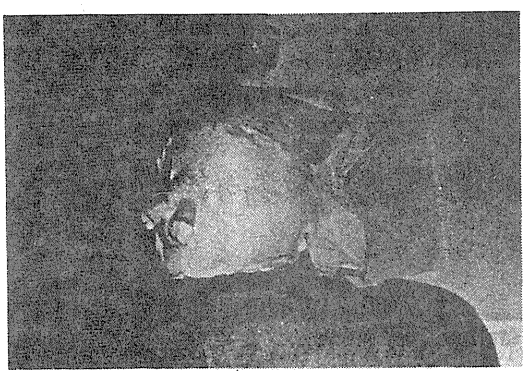

Fig. 5. Face is covered with alginate. Plaster is better used over the alginate, otherwise alginate mold is too soft.

Fig. 6. Plaster model made from the mold in Fig. 15.

はチューイングガムベースを置いてゆく。必要な形成をした樹脂板を上から押し付けてこの板をはりあわせる。注射針をとうして中の空気をとりだしながら水を入れていく（図７）。密着性のよい（図９）ボーラス内の均一性の良いものができあがる。保存は低温保存がよい。高さの調整はＣＴスキャンを行い，腫瘍の遠端から距離をスキャナーで測り樹脂板を照射時このボーラスの前に置き調整する。厚さを正確にしなければならないとき，あるいは，持運びを自由にしたい時は側壁をチューイングガムベースではなく樹脂板を用いて作らなければならない(図10)。先に模型から皮膚面の型に形成した樹脂板に照射野を充分におおう大きさの四角又は円の線を引き，この線上に薄い樹脂板をフイットさせながら張りつけてゆく。この時成形した基板にフイットさせるにはハサミで切りながら合わせなければならないが塩化ビニール板の方が都合がよい。水漏れをしないように充分に接着する必要がある。小さな水漏れはチューイングガムベースまたはゴム粘土等で防ぐことができる。塩化ビニール板の接着にはヒシボンドがよくアクリル板には塩化メチレンで良い。このボーラスの装着固定にはプレスネットがよい（図８）。

結果

図８は乳癌の胸壁転移の症例で皮膚面を照射するための水ボーラスである。固定はプレスネットで行われている。図９にそのＣＴ像を示す。この患者では皮膚表面から胸壁の脂肪層までをターゲットとして照射することを目的としている。よってボーラス表面から脂肪層までをＣＴスキャナーで測り飛程の補正をする。図10は前胸壁皮膚の悪

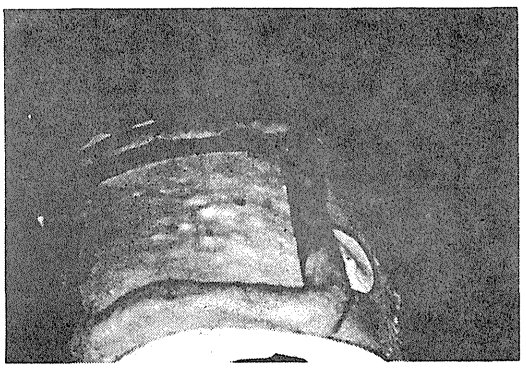

Fig. 7. One milimeter thick vynil chloride plate is heated and softened. And it is pressed on the plaster model of the chest wall shown in Fig. 3. A square frame of vynil plate with appropriate height is placed on it. Sticky chewing gum base is placed surrounding the frame and a thin vynil plate is placed on it and pressed down to the height of the frame.

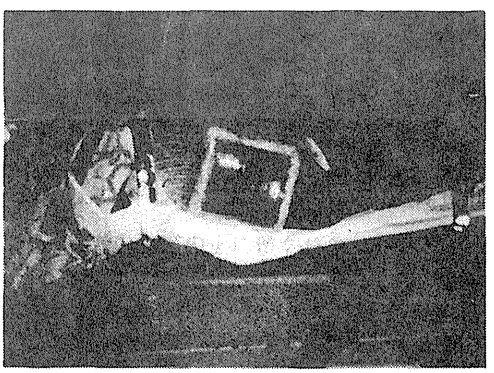

Fig. 8. The water bolus mode which is in Fig. 7 are worn with present.

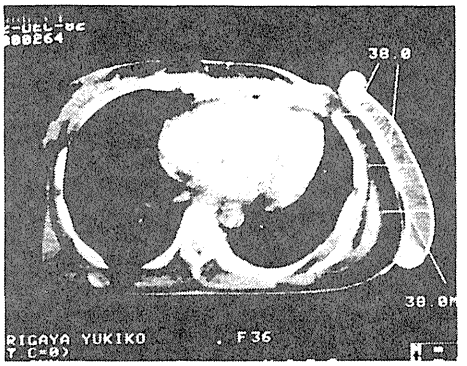

Fig. 9. The patient is scanned with the bolus on to assure the treatment depth.

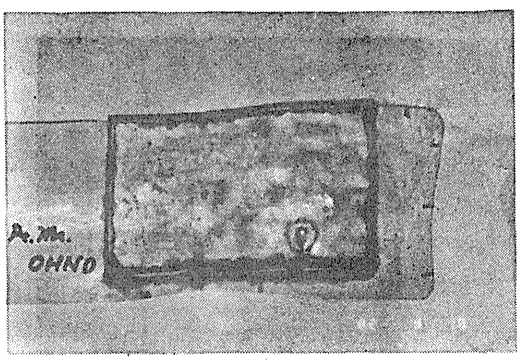

Fig. 10. Water bolus made from accryl plates.

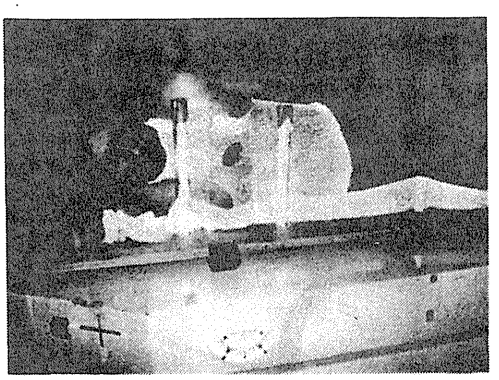

Fig. 11. The patient is being scanned in treatment position which ought to be formed on the proton treatment table.

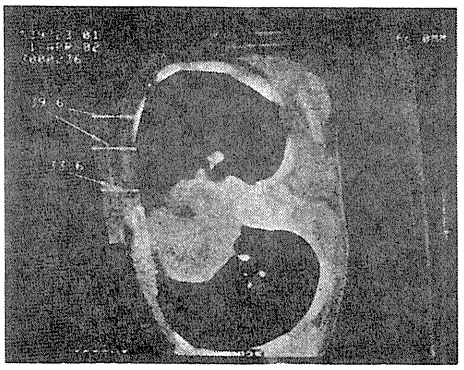

Fig. 12. CT view in Fig. 11 to assure treatment depth.

Fig. 15. Neck node metastasis of malignant melanoma.

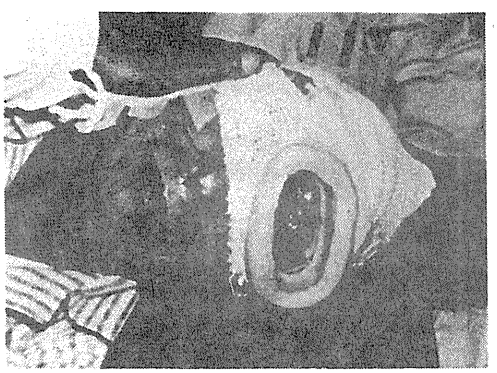

Fig. 13. Proton irradiation to angiosarcoma on left upper eyelid.

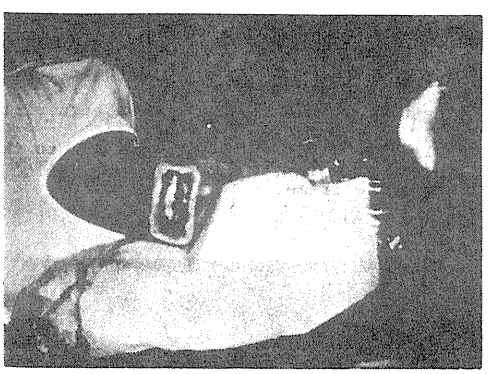

Fig. 16. Metastasis of malignant melanoma to upper lip.

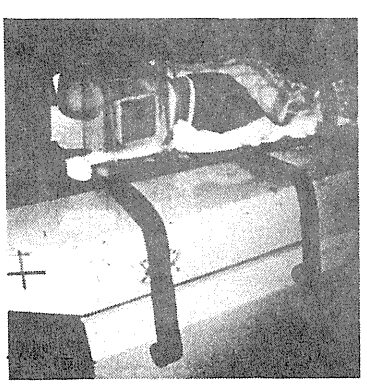

Fig. 14. A case of leiomyosarcoma on back in right side.

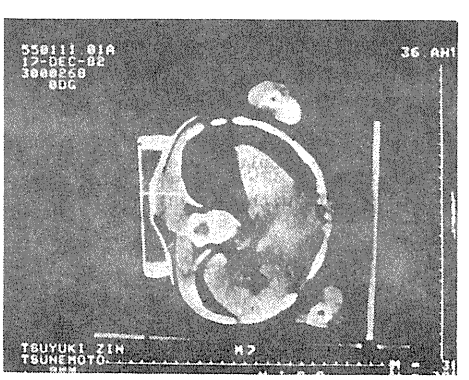

Fig. 17. CT view of the case of leiomyosarcoma in Fig. 14.

性 histiocytomaの手術後再発で胸壁全厚を照射する目的で作られたボーラスである。装着にはプレスネットをつかえば軽いバンソウコウ固定ですむ(図11)。ボーラス作成後は装着して必ず確かめのCTスキャンを行うべきである(図12)。このボーラスの側壁はアクリルでできている。図13は目の左上眼瞼の悪性血管腫の為眼瞼のみを照射する目的で作成されたボーラスである。図14は右背部の平滑筋腫の再発への照射である。図11に似たケースであるが，この場合は側壁はチューイングガムベースでつくられている。図15，図16は悪性黒色腫症例である。図15は頸部転移のための水ボーラスであり，図16は上口唇への転移の治療の為のものである。これらの使用経験からつぎの結果を得た。

1）通常のパラフインやシリコンで作るボーラスに比べて，製作は特に煩雑とは言えない。

2）陽子線における飛程等物理基本データの測定は水フアントームを基本としているから飛程等の補正の必要がない。

3）このボーラスの場合光の透過性が大変良いので，患者の皮膚の上に書かれたマークが良く見え患者のセットアップがしやすい。

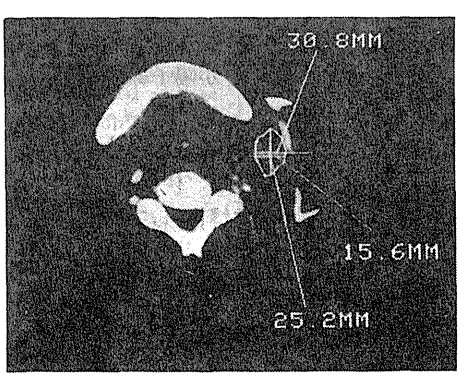

Fig. 18. CT view of malignant melanoma metastatic to neck.

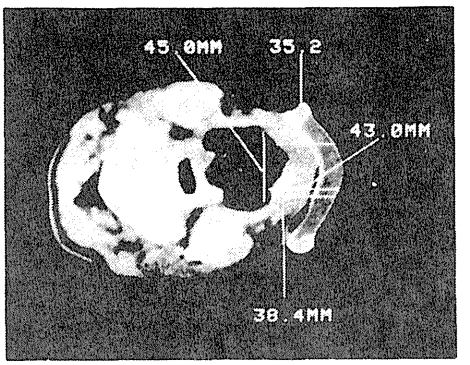

Fig. 19. CT view of malignant melanoma metastatic to upperlip.

4）図17，図18，図19は，図14，図15，図16に対応するCTスキャン像であるがこれらの図に見られるようにボーラス内の均一性は大変良く又，皮膚面への密着も大変良い。

考察

放射線治療を行う場合，治療医は腫瘍の範囲と其の周辺で治療されるべき部分を指定する。これをターゲットと呼ぶ。医師の指定するターゲット内を，幾つかの小さな区分に分け，その一つ一つを陽子線のピークでスキャンしていき，全体を均等な線量分布にできることが望ましい。放医研ではスキャンニングで照射する技術は進んでいるがまた二次元的照射野を作る方法が実現しているが，三次元的に治療容積をスキャンで作る方法は研究中である。[6]原理的には三次元のスポットスキャンが実用化されればボーラスは必要無くなるわけである。しかし，機械によるビームの制御は大まかであるので細かい所の調整はボーラスを使うという必要性は残ると考えられる。

陽子線を利用した放射線治療に於いては陽子線の線量分布特性を生かさなければならない。スポ

ットスキャンを行うのもその一つであるが，このためには陽子線の体内での飛程を制御しなければならない。即ち陽子線のエネルギーを調整しなければならない。加速器から必要に応じたエネルギーを瞬時に取り出すことができたら好ましいのだが現在の加速器技術では不可能である。因って細かいエネルギーの調整にはエネルギー吸収体を用いる。三次元のスポットスキャンでもエネルギーの調整には吹収体を使う。現在の陽子線治療ではこのエネルギー吸収体を用いるには次の二つの目的がある。

A．種々な厚さのエネルギー吸収体を重ね合わせてピークの巾を広げるために使用するもの。

B．ピークの位置を手前に移動させたり，遠端の縁を変形させたりするために使用するもの。

前者はビームデグレーダー，又はピークモデファイアと呼ばれる。加速器からでてくる陽子線は一定のエネルギーをもち，飛程は一定である。因ってその飛程の深さでエネルギーを放出する。しかし，range straggleがあるので，エネルギーが放出される位置はある巾をもつ。これがピークであり，1㎝前後の巾である。よって色々の厚さの吸収体を通うしてピークを重ね合わせ放射線治療に必要な厚さのピークにする。すなわち，放射線治療医に与えられる放射線は陽子線の場合ある可変の厚さと巾と長さをもつ長方体のようなものである。これが通常のX線と大きく違う。

しかし，これでは不必要な所が照射されたり時には照射されてはならない要注意臓器がこの長方体に入る。よってこの長方体を変形させる必要がある。これが先に述べた後者B.であり，ボーラスと呼ばれる。[7), 8)]ボーラスは本来線量分布を整えるために用いたが，陽子線では線量分布を変形させるために用いる。その目的は不必要なところに照射されないようにすることと要注意臓器への線量をなくすことにある。すなわち，よりよい線量分布を作るためである。三次元のスキャンニング照射が始まるまではビームデグレーダとボーラスの二段階のフィルターを使用する必要がある。ビームデグレーダーは患者別に作成されるわけでなく照射設備として何種類か準備されている。ボーラスは照射部分の体の輪郭や腫瘍の形が多種多様であるため患者一人一人に個別につくらなければならない。

現在の放射線治療では一般にターゲットの設定や治療計画にＣＴ画像が利用される。よってＣＴ画像を利用してより簡単により正確にボーラスを作成する方法を研究すべきである。その場合ＣＴ値と飛程の関係が関数関係にあるのが好ましい。その材料が問題であるが，まず高価であるが加工しやすいシリコン合成材を用いたが，これはＣＴを利用するにはあまり適当でない。比重も高く飛程の袖正も原子番号等が関与して複雑である。次に縦来よく用いられたパラフィンを利用した。これは加工が楽でない。シリコンは比重がかなり水に比べて重いのに対しパラフィンはかなり軽い。よってＣＴで測定した厚さが陽子線の飛程とならない。その補正がむつかしいので，ボーラス材料は水の比重と原子組成に近い材料が使いやすいといえる。次に比重の低い材料としてアルギン酸を選んだ。これも表１に示す如く飛程補正係数は，1.06で充分とは言えない。ガムベースもカルシウムを少なくすることにより比重を小さくすることができるが今のところ飛程の補正係数が1.14であ

る。又保する場合低温にしないと形が変わる。比重が低いものはＣＭＣ（カーボメチルセルローズ）や寒天である。これらは，このままではボーラスとして使用できない。薄いプラスチックケースに入れて使用することになる。表１に示すごとく寒天に比べてＣＭＣの方が少し比重が高いが飛程補正係数は小さい。寒天の方が透明度が良く皮膚に書いたマーキング等がよくみえる。特にサイドポインターが赤色レーザービームなら良く見える。透明度の一番よいのは水で，どうせ体表面の形をしたプラスチックケースを作らなければならないならば水を入れるボーラスにした方がよい。但し水が漏れないように作るには技術を要する。寒天は固めたあと低温に保てば流れでるようなことはない。ボーラスを用いる皮膚表面は不正形であり，また，腫瘍の形にビームの遠端の形を作ろうとすると更に複雑となりコンピュータが必要となってくる。コンピュータ化すれば飛程補正係数が１でなければならないこともないし，比重も気にしなくてもよい。ＣＴの各スライスの輪郭データとターゲットデータから飛程等を補正してコンピュータがデザインすれば良いのである。ＣＴが設計用コンピュータに与えることのできる材質情報はＣＴ値であるので将来コンピュータにてボーラスをデザインさせるに飛程の補正はＣＴ値で行うのが好ましいと考え，表１に示す如く各種の材質のＣＴ値及び飛程を測定した。図20及び図21は其の結果である。図20に示す如く飛程補正係数と比重はよく相関しているが補正係数とＣＴ値の相関（図21）はあまりよくない。しかし，ＣＴ値200－300を示しているシリコン複合体を除けば利用可能程度の相関はある。因ってボーラス材料としてカルシウムやシリコン等原子番号の高いものを除けばＣＴ値から飛程補正はできる。作成したボーラスがそれでよいのかを確かめる必要がある。これには一つはファントームを使ってフィルムを陽子線

Materials	Number of CT(S.D.)	Number of CT of Reference (S.D) (Water)	Physical Density (g/cm^3)	Conversion Factor
Paraffin wax (red)	-106.6 (4.2)	-5.3 (4.4)	0.91	0.96
Parrafin wax	-104.4 (4.8)	-6.9 (4.5)	0.94	0.93
Silicone 1	273.2 (5.7)	1.4 (4.7)	1.14	-
Silicone 2	452.3 (9.7)	0.8 (5.0)	1.38	-
S 5005 (Silicon A)	238.7 (6.8)	-2.8 (6.4)	1.12	1.06
SX (Silicon B)	288.9 (7.2)	-3.5 (7.1)	1.06	1.05
Dental compound	520.7 (20.9)	-6.1 (4.7)	1.45	-
Gum base (A)	135.1 (8.3)	-0.4 (3.7)	1.17	1.13
Gum base (B)	123.4 (37.6)	-13.5 (3.9)	1.17	1.14
Alginate 0	27.4 (5.7)	-6.0 (4.8)	1.03	1.06
Alginate 12	27.7 (5.3)	-6.1 (4.8)	1.03	1.06
Latex	- 53.4 (5.0)	-6.2 (4.1)	0.99	1.00
Wheat flour with oil	151.4 (16.0)	-2.0 (7.8)	1.22	1.20
CMCNa 3.5%	3.9 (4.3)	1.6 (5.6)	-	-
CMCNa 5.0%	1.1 (4.8)	-2.2 (5.4)	1.01	0.95
CMCNa 7.0%	7.2 (4.8)	-2.5 (4.9)	1.04	0.98
Agar A	27.8 (5.3)	-6.8 (5.5)	1.00	1.01
Agar B	2.0 (6.1)	-8.3 (5.3)	1.00	1.02

Table 1. CT number, physical density and conversion facter of various bolus materials.

爆射し黒化の深さから調べられる。もう一つはボーラスを患者に装着して，治療体位でＣＴスキャンをして深さを測定する。図22はアルギン酸ボーラスを付けてＣＴをとったところである。陽子線は38㎜の深さまで達してこの範囲で治療できる。アルギン酸の飛程補正係数は1.06であるが，この図ではその補正はしていない。現在のＣＴスキャナーのこのようなソフトでは，距離を測る機能は付いているが，それを補正できるものがないからである。因って現在のところ水に類似の材質を用い，飛程補正をしなくてもよいものを使用しなければならない。

皮膚への密着性のよいボーラスを作らなければならない。密着が悪いと，ボーラスとターゲットの相対位置関係がずれやすいだけでなくＣＴで深さを確かめるとき空間をさしひかなくてはならないので作業が複雑になり精度が悪くなる。故に皮膚に密着性のよいものである必要がある。しかし，これは材質よりも型取法等に関係する。

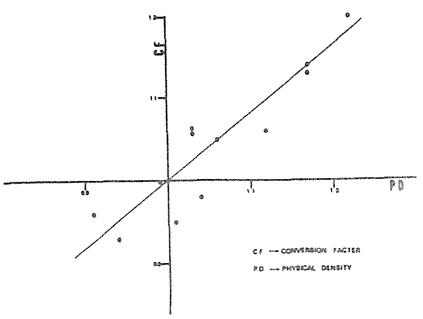

Fig. 20. Correlation between physical density and conversion facter.

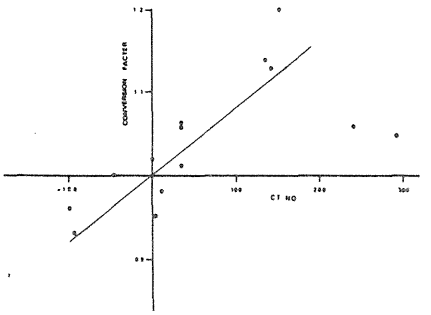

Fig. 21. Correlation between CT number and conversion facter.

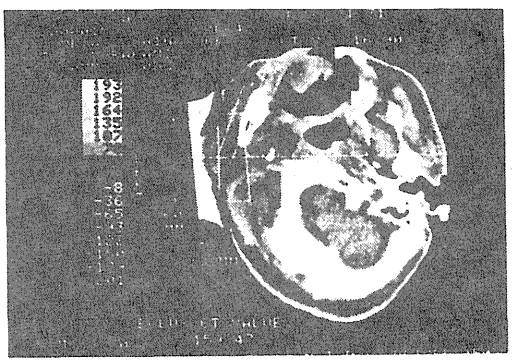

Fig. 22. CT view of neck metastasis with alginate bolus.

文献

1) Goitein, M：The utility of compu ed tomography in Radiation therapy：An estimate of outcome. Int. J. Radiat. Oncol. Biol. Phys. 5：1799－1807, 1979

2) Townley, J.F.：Aid for use with EMI CT 5005 general purpose scanner in tumor localization for radiotheral purpose scanner in tumor localization for radiotherapy treatment planning. Brit. J. Radiol. 52：830－832, 1979

3) Kligerman, M. M., Hogstrom, K. R., Lane, R. G., et al : Prior immobolization and positioning for more efficient radiotherapy. Int. J. Radiation Oncol. Biol. Phys. 2 : 1141−1144, 1977

4) 赤沼篤天：放射線治療とCT。癌の臨床 1212−1218, 1979

5) Lanberg, T., Suvahn, G., Bengstrom, C. : Whole body−casts for patient immobilization in Mantle treatment, treatment in the invered−Y and moving strip. Int. J. Radiat. Oncol. Biol. Phys. 2 : 809−813, 1977

6) Kawachi, K., Kanai, T., Matsuzawa, H., et al : Preliminary experiments of three dimensional proton spot beam scanning. Presented at US−Japan Coop. Cancer Seminar. Nov. 10−12, 1980

7) Goitein M. : Compensation for inhomogeneities in charged particle radiotherapy using computed tomography. Int. J. Radiat. Oncol. Biol. Phys. 4 : 499−508, 1978

8) Hogstrom, K. R., Smith, A. R., Sommers, J. W., et al : Measurement of the effect of inhomogeneities and compensating bolus in clinical pion beams. Medical Phys. 6 : 26−31, 1979

9) Gillin, M., Foley, W. D., Kline, R. W., et al : The computed tomograph : A method of correlating axial tomographic images with simulation and port films. Int. J. Radiat. Oncol. Biol. Phys. 7 : 1603−1606, 1981

Int. J. Radiation Oncology Biol. Phys., Vol. 11, pp. 1439–1445
Printed in the U.S.A.

0360-3016/85 $03.00 + .00

● *Original Contribution*

CLINICAL EXPERIENCE OF FAST NEUTRON THERAPY FOR CARCINOMA OF THE UTERINE CERVIX

SHINROKU MORITA, M.D.,[1] TATSUO ARAI, M.D.,[1] TAKASHI NAKANO, M.D.,[1]
TATSUO ISHIKAWA, M.D.,[1] HIROSHI TSUNEMOTO, M.D.,[1]
KENJIRO FUKUHISA, B.SC.[1] AND TATSUHIRO KASAMATSU, M.D.[2]

[1]Division of Hospital, National Institute of Radiological Sciences (NIRS), 4-9-1, Anagawa, Chiba-shi, 260, Japan; [2]Department of Gynecology, National Cancer Center Hospital (NCCH), 5-1-1, Tsukiji, Chuo-ku, Tokyo, 104, Japan

Fast neutron therapy for locally advanced or radioresistant malignant tumors was started in November 1975 at the National Institute of Radiological Sciences (NIRS), Chiba, Japan. To evaluate the effectiveness of fast neutron therapy, mixed neutron-photon fractionated irradiation, on squamous cell carcinoma of the uterine cervix, 98 patients with Stage IIIb disease were examined to study the correlation between local control rate and histological types. The local control rate after neutron-mixed beam therapy was 73%, which decreased to 66% with photon irradiation. The five year survival rate was 49% for patients receiving neutron therapy and 49% for those receiving photon therapy. There was no statistical significance between neutron and photon therapy; we then attempted to analyze histological types to check for any gain using neutron therapy. This study was a non-randomized trial. The preliminary results however, gave us useful information for the next step of neutron therapy.

Fast neutron irradiation, Carcinoma of the uterine cervix, Histological study.

INTRODUCTION

Fast neutron radiotherapy, using 30 MeV (d-Be) neutrons produced by a medical cyclotron, was initiated in November 1975 at the NIRS, Chiba, Japan. A total of 1125 patients with malignant tumors that were locally advanced or radioresistant, such as osteosarcoma, soft tissue sarcoma or malignant melanoma, were treated by the end of 1983.

Fairly satisfactory results have been obtained by radiotherapy as well as surgery in the treatment of early stage carcinoma of the uterine cervix. Radiotherapy plays a major role in the treatment of late stage disease, which is advanced and inoperable, but the results have not been satisfactory so far.[6,12,18] Greater LET radiation, such as fast neutron therapy, is now being introduced in an attempt to improve results.

The present paper describes the preliminary results of clinical trial of fast neutron therapy for advanced Stage IIIb carcinoma of the uterine cervix, and attempts to discover a correlation between local control rate and histological types.

METHODS AND MATERIALS

Characteristics of the neutrons

Fast neutron beams used in this clinical trial were produced by bombarding a thick beryllium target with 30 MeV deuterons delivered from the NIRS medical cyclotron. Mean energy was about 13 MeV.[16] The output dose rate was 42 cGy per minute (n. γ) for an 11.4 cm × 11.4 cm field at source-target-distance (STD) of 200 cm. Contamination with gamma rays was estimated to be less than 4%. The depth dose and the dose distribution obtained at source-skin-distance (SSD) of 175 cm were about the same as those of Co-60 gamma rays at SSD 65 cm. The maximum build-up of the dose was located at 5 mm below the surface. (Fig. 1)[8]

Patient selection

Patients selected for the present study had previously untreated Stage IIIb squamous cell carcinoma of the uterine cervix (FIGO), with medium and large tumor volume, and whose work-up studies included the histological examination and classification.

Reprint requests to: Shinroku Morita, M.D.

Accepted for publication 12 March 1985.

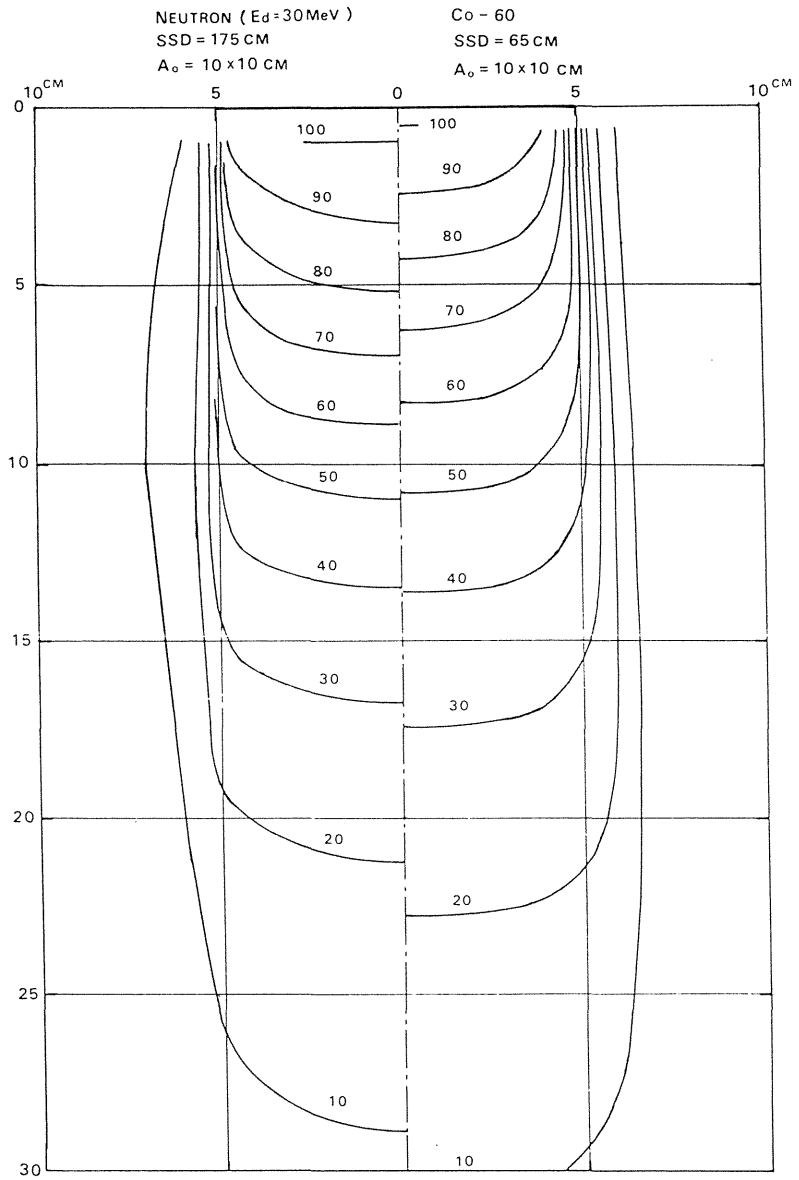

Fig. 1. Comparison of isodose charts in a tissue-equivalent liquid phantom for neutrons (Ed = 30 MeV) and ^{60}Co gamma rays measured at Ao = 10 × 10 cm. Courtesy: Hoshino *et al.*[8]

Radiation therapy program

Patients were divided into two groups, with treatment by photon or fast neutron, according to the availability of the cyclotron machine time when the patients were accrued. The machine time available for neutron therapy throughout the year consisted of three periods as follows: 1st period, middle of January to middle of April, 2nd period, middle of May to end of July, and 3rd period, middle of September to middle of December. The intervals between those periods were spent for the maintenance and improvement of the machine. Photon group: The patients who were referred during the off-

periods of cyclotron were treated with photon irradiation. Fast neutron group: The patients who were referred during the periods when the machine was in operation and who were judged able to undergo the planned course of treatment were treated with fast neutrons.

The whole pelvis was irradiated by two opposing external portals with a mixed schedule, three times weekly by photon therapy and twice weekly by neutron therapy. The dose range was 5000–5500 cGy per 5–5.5 weeks, with an RBE value of 3.0 for neutron therapy, namely 720 cGy per 10 fractions for neutron therapy and 2550 cGy per 15 fractions for photon therapy. The photon radiation group were treated to the whole pelvis with two opposing portals by photon beam in the dose range of 5000–5500 cGY per 5–5.5 weeks, 5 times weekly. All patients in both groups then underwent intracavitary irradiation by means of RALS (remote afterloading high dose rate intracavitary irradiation.)[2] The high intense small sources of ^{60}Co (4.0 Ci for tandem and 2.0 Ci for ovoids) were used. Irradiation time was 5 to 10 minutes. The treatment was done in two fractions with one week intervals during the last two weeks of external irradiation, to give the dose of 1100–1300 cGy at point A.

Histological classification

Squamous cell carcinomas of the uterine cervix were classified into 3 types of histological classification as proposed by Wentz and Reagan.[20] These classifications are: K: keratinizing carcinoma, L: nonkeratinizing large cell carcinoma, S: nonkeratinizing small cell carcinoma.

Distribution of patients

In total, 98 patients (45 in the fast neutron group and 53 in the photon group) with Stage IIIb squamous cell carcinoma of the uterine cervix were divided into histological classification: K, 20, L, 72, S, 6, respectively. All patients were treated within protocol guidelines or with only minor modification of the protocol. They were followed at an out patient clinic every one to three months. Once a year patients were admitted to the hospital for 3 days for chest and urinary tract X ray diagnosis, or cystoscopic and proctoscopic examinations, for the next 5 years (Table 1).

RESULTS

Local control rate and frequency of distant metastasis

Patients in both therapy groups were classified into two types according to volume of tumor, that is, large (parametrium infiltrated massively on both sides), and medium (parametrium infiltrated massively on one side).

The local control rate after neutron therapy was 73% (33/45) in total and 66% (35/53) after photon irradiation. For medium tumors, local control rate increased, though not statistically significant (χ^2 test = 1.067), to 83% (19/23) for the neutron group and 65% (17/26) for the photon group. This table also indicated the frequency of distant metastasis in both treatment groups; however, there was no statistical significance because of the small number of patients (Table 2).

Table 1. Number of patients with Stage IIIb squamous cell carcinoma of the uterine cervix (November 1975–November 1979)

Types of histology	Fast neutrons IIIb	Photons IIIb	Total IIIb
K	11	9	20
L	33	39	72
S	1	5	6
Total	45	53	98

Cumulative survival curves

Figure 2 shows the cumulative survival curves of neutron series (closed circle) and photon series (open circle). Five year survival rate indicated 49% in neutron therapy and 49% in photon therapy. Complete coincidence was observed (χ^2 test = 0.00001112).

Frequency of radiation complication

The grading system of radiation complication in NIRS[11] was modified from the grading system of Kottmeier and Gray,[9] indicated in Table 3.

The frequency and severity of radiation complication are shown in Table 4. When the complication was observed in several organs, the highest grade was adopted. About 60% of patients in both groups had no trouble with radiation complication (Grade 1 and 2). There was no significant difference in complications between the neutron therapy and photon therapy group. Only one patient died of radiation complication (Grade 4). The causes of death in this patient were old age (69 yr), severe rectal bleeding and repeated blood transfusions.

Table 2. Local control rate and distant metastatic rate in patients with Stage IIIb squamous cell carcinoma of the uterine cervix (November 1975–November 1979)

Volume of tumor	Fast neutrons		Photons	
	Large	Medium	Large	Medium
Local control rate (%)	64 (14/22)	83 (19/23)	67 (18/27)	65 (17/26)
Total	73 (33/45)		66 (35/53)	
Distant metastatic rate (%)	45 (10/22)	22 (5/23)	26 (7/27)	15 (4/26)
Total	33 (15/45)		21 (11/53)	

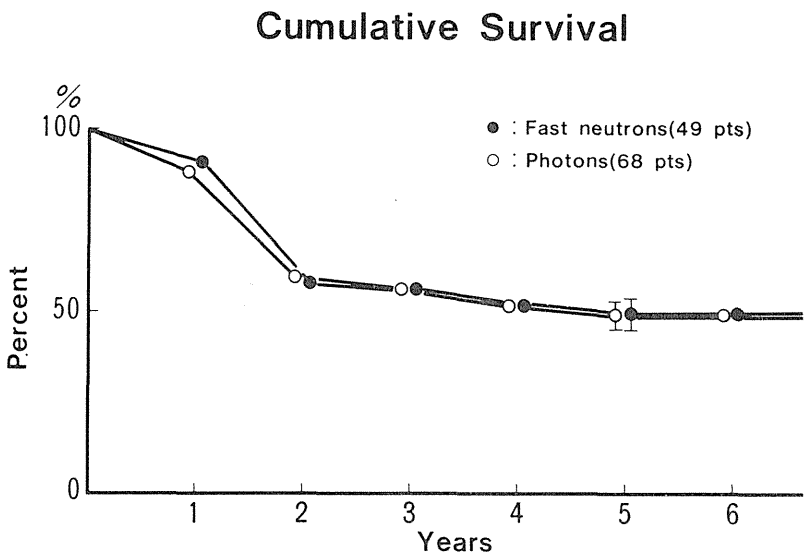

Fig. 2. Cumulative survival curves of irradiated patients with Stage IIIb carcinoma of the uterine cervix (1975–1980, NIRS). Neutrons (n = 49, mean age = 53.12 y., standard error = 8.028%), Photons (n = 68, mean age = 53.60 y., standard error = 7.188%). χ^2 test = 0.00001112.

An analysis of prognostic pattern

Figure 3 indicates the prognostic pattern of the patients treated with fast neutron and photon therapy. There seemed to be no significant difference.

Histological classification, K, L and S type

Table 5 showed the local control rate and the frequency of distant metastasis on K, L and S type histological classification. The differences between neutron and photon therapy in L type revealed a statistical significance at 90% level of risk (χ^2 test = 3.084). The frequency of distant metastasis is also shown in Table 5.

DISCUSSION

In view of our considerable experience in the treatment of carcinoma of the uterine cervix (approximately 40% of the patients treated at the NIRS have carcinoma of the uterine cervix) we chose patients with carcinoma of advanced Stage IIIb as the subjects for clinical trial of fast neutron therapy. Since the prognosis of cancer patients treated with radiation clearly depends on the size of tumor, it was considered in patient selection for fast neutron therapy. For Stage IIIb carcinoma of the uterine cervix, the five year survival rate and local failure rate observed according to the tumor volume are indicated in Table 6. This was our basic data for the selection of the patients when the neutron trial started in NIRS hospital at 1975.[19] Since the scope of our study was to examine the effectiveness of neutron therapy on

Table 3. Grading system for radiation complication at NIRS

Grade	Category
1	Not recognizable
2	Mild, no treatment required
3	Moderate, temporary treatment required
4	Severe, continuous treatment or surgical reconstruction required
5	Life threatening or radiation induced cancer

Table 4. Frequency and severity of radiation complication in Stage IIIb squamous cell carcinoma of the uterine cervix, treated with fast neutron mixed schedule and photon (1975–1980, NIRS)

	Fast neutrons*		Photons*	
Grade	No.	%	No.	%
1 and 2	21	62	23	58
3	11	32	13	33
4	2	6	3	8
5	0	0	1†	3

* 11 patients out of 45 (fast neutrons) and 13 patients out of 53 (photons) were dropped because of a short follow-up time.

† 69 years-old, suffered from severe radiation proctitis, required repeated blood transfusions.

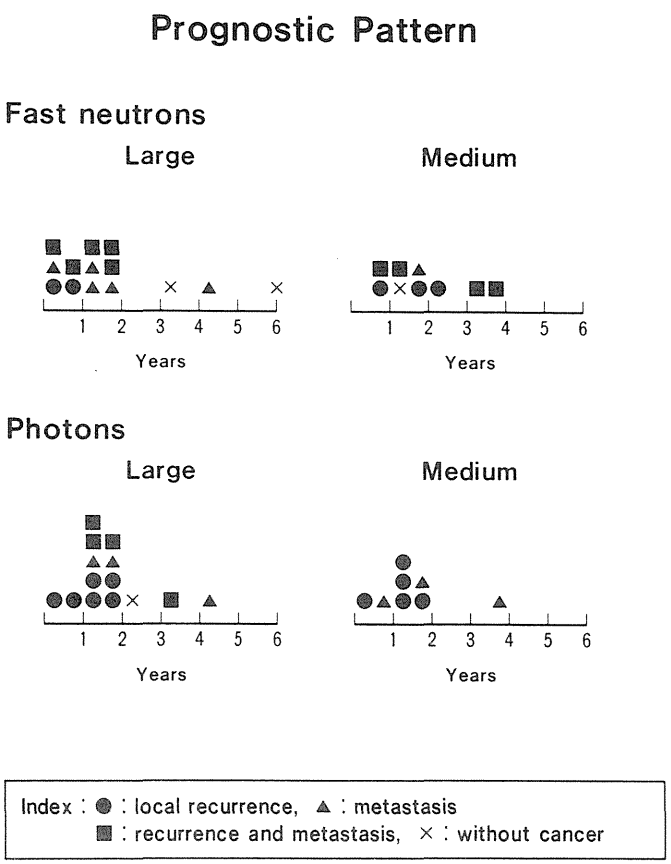

Fig. 3. Analysis of prognostic pattern of irradiated carcinoma of the uterine cervix (1975–1980, NIRS). Fast neutron group: tumor volume Large: alive 8 patients, dead 12 patients with cancer and 2 patients with other diseases. Medium: alive 14 patients, dead 8 patients with cancer and 1 patient with other disease. Photon group: Large: alive 13 patients, dead 13 patients with cancer and 1 patient with radiation complication. Medium: alive 18 patients, dead 8 patients with cancer.

Table 5. Correlation between K, L, S type—Histological classification and local control rate or distant metastatic rate in Stage IIIb squamous cell carcinoma of the uterine cervix (NIRS)

Histological type	Fast neutrons (%)	Photons (%)
(1) Local control rate		
K	55 (6/11)	89 (8/9)
L	79 (26/33)*	56 (22/39)*
S	100 (1/1)	100 (5/5)
(2) Distant metastatic rate		
K	36 (4/11)	0 (0/9)
L	30 (10/33)	26 (10/39)
S	100 (1/1)	20 (1/5)

* χ^2 test = 3.084.

locally advanced or incurable cases, only those patients with medium and large tumors were included in the trial with fast neutron therapy.

From the present clinical results, no significant differences were shown in the local control rate, survival rate, frequency of radiation complication or prognostic pattern between the neutron therapy group and the photon therapy group. These results were similar to those of M.D. Anderson hospital.[10,13]

In the present study, we expected that analyzing the histological types may have given us some useful information to demonstrate the advantages of neutron therapy. Many authors have reported on the correlation between histological types and radiosensitivity for carcinoma of the uterine cervix.[5,7,15,17,20] In this regard, we

Table 6. Difference of clinical results according to the volume in Stage IIIb carcinoma of the uterine cervix (1962–1971, NIRS)

Tumor volume	Number of patients	Five year survival rate (%)	Local failure rate (%)	Distant metastatic rate (%)
Small	79	69	14	9
Medium	122	50	34	15
Large	64	44	36	17
Total	264	54	28	14

Small = Scattered, small dense nodules in the parametrium on both sides; Medium = Parametrium involved massively on one side; Large = Parametrium involved massively on both sides.

have referred to one system of histological study in this paper, i.e., K, L and S types.[20] According to Wentz and Reagan,[20] the histology of carcinoma of the uterine cervix was classified into three sub-types (K, L, S) with the grading of squamous cell carcinoma. Their results indicated that the keratinizing cancer (K) was found to have a worse survival rate than the large cell non-keratinizing carcinoma (L). We expected that neutron therapy might be more effective in treating radioresistant tumors, such as the K type; however, the results were contrary to our expectations. The local control rates of K type were 55% with neutron therapy and 89% with photon therapy.

The reasons considered were as follows: (a) *Dose distribution.* In the treatment of carcinoma of the uterine cervix, external and intracavitary irradiation should be used in adequate and individualized combination for each patient. Dose distribution was relatively well controlled by conventional radiotherapy, because the dose concentration for tumor target was achieved by means of intracavitary irradiation. When our trial had started, the treatment schedule was designed to follow the U.S. trial,[4] with the aim of intercomparison of studies between both countries. At that time, only external irradiation with fast neutron beam was emphasized, and the problem of dose concentration was given little consideration in the treatment schedule. The whole pelvis was irradiated with two opposing portals, without using the four-field box technique, which was used at M.D. Anderson Hospital. The number of intracavitary irradiation was also reduced. Thus, only a modest neutron dose was given, to avoid severe radiation complications, and might be the causes of some inadequency in the treatment method of fast neutron therapy. (b) *Mixed beam schedule.* It is known that whole pelvis irradiation by photon beam five times weekly was well tolerated for the patients with carcinoma of the uterine cervix; however, patient tolerance was not known for neutron beam alone given three times weekly. Therefore, this schedule was adopted when the pelvic cavity, a relatively large field, was to be irradiated, in order to obtain a better gain factor of tumor control against radiation complication. The effects of neutron therapy and photon therapy delivered in a mixed beam, i.e., mixed neutron-photon fractionated irradiation, were merely additive with no evidence of synergism on the biological experiments.[1,14] So far we are using the γ ray intracavitary irradiation, and a percentage of neutron dose was used in the dose distribution of mixed beam treatment. There was little advantage of using neutron therapy under such a treatment schedule. If we want to gain from neutron therapy, we must change the treatment schedule, i.e., daily neutron irradiation with a smaller given dose or use of small neutron source (Cf-252) insertion instead of gamma source intracavitary irradiation, etc. (c) *Neutron therapy.* Neutron therapy is considered to be more effective for slow growing tumor,[3] however, squamous cell carcinoma of the uterine cervix was characterized as a relatively rapid growing tumor, thus it has a minor indication for fast neutron therapy.

It was true that the biological advantage of neutron therapy showed a better effect on a radioresistant tumor, which is not true in conventional radiation; however, the problem of inferior dose concentration was the weakness of neutron therapy at present. This was the limiting factor in improving the local control rate. We are now expecting better results from the next step, which is fast neutron therapy using an iso-centric, full rotating machine which has excellent dose concentration.

REFERENCES

1. Ando, K., Ohara, H., Fukuda, N., Majima, H., Koike, S.: Effects of fast neutrons on experimental tumors in fractionated schemes. US-Japan Seminar, High LET Particle Irradiation and Other Approaches to Increase Effectiveness of Radiation Therapy for Cancer. Chiba & Kyoto, 1982.
2. Arai, T., Morita, S., Kutsutani, Y., Iinuma, T., Masubuchi, K., Tsuya, A., Onai, Y., Ito, Y., Tazaki, E.: Relationship between total iso-effect dose and number of fractions for the treatment of uterine cervical carcinoma by high dose-rate intracavitary irradiation. *Brit. J. Radiol.* (Special Report No. 17): 89–92, 1981.
3. Battermann, J.J., Breur, K., Hart, G.A., Van Peperzeal, H.A.: Observations on pulmonary metastasis in patients after single doses and multiple fractions of fast neutrons and cobalt-60 gamma rays. *Europ. J. Cancer* **17**: 539–548, 1981.
4. Caderao, J.B., Hussey, D.H., Fletcher, G.H., Sampiere, V.A., Johnson, D.E., Wharton, J.T.: Fast neutron radiotherapy for locally advanced pelvic cancer. *Cancer* **37**: 2620–2629, 1976.
5. Fink, F.M., Denk, M.: Cervical carcinoma: Relationship between histology and survival following radiation therapy. *Obstet. Gynecol.* **35**: 339–343, 1970.
6. Fletcher, G.H., Rutledge, F.N.: Carcinomas of the uterine

cervix. *Modern Radiotherapy, Gynaecological Cancer.* London, Butterworths. 1971, pp. 11–52.
7. Gunderson, L.L., Weems, W.S., Hebertson, R.M., Plenk, H.P.: Correlation of histopathology with clinical results following radiation therapy for carcinoma of the cervix. *Am. J. Roentgenol.* **120:** 74–87, 1974.
8. Hoshino, K., Kawashima, K., Hiraoka, T., Kutsutani, Y.: Dose distribution of fast neutron beams from a NIRS cyclotron. *Nippon Acta Radiol.* **37:** 248–255, 1977.
9. Kottmeier, H.L., Gray, M.J.: Rectal and bladder injuries in relation to radiation dosage in carcinoma of the cervix. *Am. J. Obst. Gynecol.* **82:** 74–82, 1961.
10. Morales, P., Hussey, D.H., Maor, M.H., Hamberger, A.D., Fletcher, G.H., Wharton, J.T.: Preliminary report of the M.D. Anderson Hospital randomized trial of neutron and photon irradiation for locally advanced carcinoma of the uterine cervix. *Int. J. Radiat. Oncol. Biol. Phys.* **7:** 1533–1540, 1981.
11. Morita, S., Tsunemoto, H., Arai, T., Iino, Y., Takada, N., Akanuma, A.: Complication of fast neutron therapy of NIRS and IMS, scoring and incidence. US-Japan Seminar, High LET Particle Irradiation and Other Approaches to Increase Effectiveness of Radiation Therapy for Cancer. Chiba & Kyoto, 1982.
12. Perez, C.A., Breaux, S., Modoc-Jones, H., Bedwink, J.M., Camel, H.M., Purdy, J.A., Walz, B.J.: Radiation therapy alone in the treatment of carcinoma of uterine cervix. *Cancer* **51:** 1393–1402, 1983.
13. Peters, L.J., Hussey, D.H., Fletcher, G.H., Wharton, J.T.: Second preliminary report of the M.D. Anderson study of neutron therapy for locally advanced gynecological tumors. In *High-LET Radiations in Clinical Radiotherapy,* Barendsen, G.W., Broerse, J.J. and Breur, K. (Eds.) Oxford, Pergamon Press. 1979, pp. 3–10.
14. Rasey, J.S., Nelson, N.J.: Effect of roentgen, cyclotron neutron, or mixed neutron-photon fractionated irradiation of mice. *Acta Radiol. Ther. Phys. Biol.* **16:** 525–528, 1977.
15. Reagan, J.W., Fu, Y.S.: Histologic types and prognosis of cancer of the uterine cervix. *Int. J. Radiat. Oncol. Biol. Phys.* **5:** 1015–1020, 1979.
16. Smith, A.R., Almond, P.R., Smathers, J.B., Otte, V.A., Attix, F.H., Theus, R.B., Wootton, P., Bichsel, H., Eenmaa, J., Williams, D., Bewley, D.K., Parnell, C.J.: Dosimetry intercomparisons between fast-neutron radiotherapy facilities. *Med. Phys.* **2:** 195–200, 1975.
17. Swan, D.S., Roddick, J.W.: A clinical-pathological correlation of cell type classification for cervical cancer. *Am. J. Obstet. Gynecol.* **5:** 666–670, 1973.
18. Tsunemoto, H.: Radiotherapy in Japan. *Radiat. Med.* **1:** 174–185, 1983.
19. Umegaki, Y., Tsunemoto, H., Iino, Y., Tsuya, A.: Fast neutron therapy protocols in Japan. The third, High LET Radiotherapy Workshop, the US-Japan Cooperative Cancer Research Program, Tokyo, 1977.
20. Wentz, W.B., Reagan, J.W.: Survival in cervical cancer with respect to cell type. *Cancer* **12:** 384–388, 1959.

III. 臨床における基準化と最適化の問題点と将来

その1　因子別における問題点と将来

速中性子線治療の適応と問題点

森田新六[*1]　中野隆史[*1]　五味弘道[*1]
青木芳朗[*1]　柴山晃一[*1]　熊谷和正[*1]
荒居竜雄[*1]　恒元博[*1]　安藤興一[*2]
石川達雄[*2]

はじめに

放医研医用サイクロトロンによる速中性子線治療は1975年11月より開始され，10年弱の年月を経過し，約1,200例の治療経験を重ねることができた．今回はこれらの治療成績をもとにして，速中性子線照射の適応症例，問題点，将来への展望につき検討した．

1. 物理学的，生物学的基礎

重陽子 30 MeV，ターゲットでのビームカレント 30 μA による，4 mm 厚の Be ターゲットからの速中性子線が用いられている．線源，皮膚間距離（SSD）200 cm，照射野 11.4×11.4 cm における線量分布は Co-60 γ 線の場合とほぼ同様で，スキン・スペアリングは組織 4～6 mm，γ 線混在比は 10 cm の深さで約5％，線量率は毎分 42 cGy である[1]．

垂直ビームで，8対の鉄の羽根のコリメーターやタングステン・ブロックを利用し，コリメーターの固定性を補うためにピッチング・ローリングの機能をもたせた治療台を使っているが，これは患者の体位固定技術の不完全さのため利用の機会は少ない．しかし実際には線量分布を良くするために，速中性子線の対向2門照射に加えて，併用のX線，γ 線の斜・横照射を行っている．

照射野の確認は同一治療台で，シュミレーターによるX線撮影と中性子線の治療照射の二重曝射法によっている．30 MeV 重陽子における Be (d.n) B 反応による中性子線の LET 値は平均で，ミクロンあたり 10.7 KeV で，10から 1000 KeV までの幅広いスペクトルをもつ高 LET 放射線である．

細胞の不活性化と LET 値は密接な関連を有するが，LET 値がミクロンあたり 100～200 KeV の範囲が最も効果が強いとされる．すなわち，LET 値が 10 KeV なら RBE はほぼ 1.0 であるが，140～160 KeV で最大の約 3.0 となる[3]．高 LET 放射線の生物学的特徴は，1）酸素効果が大きい，すなわち腫瘍内の低酸素細胞の不活性化能力が高い．放医研中性子線の酸素効果比（oxygen enhancement ratio, OER）は 1.7 である．2）細胞周期依存性の感受性の変動が少ない．すなわち S 期後半の抵抗性が弱まる．3）照射された細胞の亜致死障害，潜在的致死障害からの回復を弱める．

放医研の実験での種々の RBE 値を表1にまとめた[5]．腫瘍と正常組織に分けて Do, TCD_{50} LD_{50} で調べて，1回照射と分割照射，混合照射の値を示した．RBE 値は分割するほど高くなる．混合照射では RBE は 1.3 なので，速中性子線と γ 線の相互作用は，分割間隔が1日の場合は，認められないということである．正常組織の RBE は 1.2～2.0であった．

混合照射（mixed beam 法）は比較的広い照射野のとき，放射線障害に対する gain を得る目的で用いられるが，この場合の中性子線と γ 線の相

*1 放射線医学総合研究所病院部
*2 放射線医学総合研究所臨床研究部

表1　放医研サイクロトロンによる速中性子線の RBE 値（安藤，1984[5]）

		腫瘍				正常組織		
		線維肉腫 7mm 腫瘍		微少腫瘍	扁平上皮癌	口腔粘膜	皮膚	骨髄幹細胞
生物効果の基準		D_0	TCD_{50}	D_0	D_0	LD_{50}	skin score	D_0
照射法	1回	2.4	3.1	1.7～2.2	1.9*	1.6	2.0*	1.2～1.3*
	分割	3.0	2.9	2.8	3.1*	1.9		
	混合	1.3	1.3	1.4～1.6				

* 200 kvp X線で得られた値を補正係数0.85でもって γ 線等価に補正したもの

互作用は，単なる相加効果であり，相乗効果ではない[6]．しかし照射間隔を短くすることで，中性子線とX線の相乗効果が生ずる可能性があり，また2分割照射で，中性子線を先行させた方が効果が強くなるとの報告がある[7]．今後の臨床的な検討課題といえる．

2. 症例と治療方法

1975年11月より1984年3月までに，放医研で速中性子線治療をうけた患者数は1,171例に達した．年間約120例のペースで，初回治療例921例，再発例250例であった（表2）．

頭頸部，食道，婦人科領域の癌はそれぞれ100例を越えたが，その他の部位では，未だ少数例であり，臨床的治療成績を評価するにたる十分な症例数とはいえない．しかし骨肉腫や，悪性黒色腫といった比較的頻度の少ない放射線抵抗性癌が多く集まっているのは全国レベルでの各施設の協力のおかげといってよい．

治療スケジュールは年間を通してサイクロトロンの調整改善期間が長く，本年度の運転期間との比率は5カ月対7カ月である．したがって中性子線とX線のランドマイズド・クリニカルトライアルを行う場合も，サイクロトロンの運転期間は中性子線照射を調整期間はX線照射を行うという放医研方式のランドマイゼイションを行った方が実用的であった．マシンタイムは週3回の午後なので，従来のX線の週5回照射法との比較のために，線量と効果関係を推定する手段としての生物学的等価 TDF による治療計画法[8]を採用した．速中性子線単独照射，混合照射（mixed beam 法），速中性子線ブースト照射を用いている．単独照射の基本線量配分は 1560 cGy/12回/4週間（TDF 99）または 1620 cGy/18回/6週間（TDF 97）である．Mixed beam 法は中性子線を週2回，X線を週3回照射する方法，ブースト法はX線を30～40 Gy 照射後中性子線を TDF 110～120 の線量まで追加照射する方法である．速中性子線と手術との併用で，術前照射の場合は TDF 60に相当する線量を，術後照射の場合は TDF 80に相当する線量が照射された．

表2　速中性子線治療症例数
1975. 11～1984. 3　放医研

疾患部位	例数	初回治療例	再発治療例
頭頸部	272	196	76
肺	99	93	6
食道	125	115	10
肝・胆・膵	35	33	2
婦人生殖器	226	164	62
泌尿器	64	56	8
骨	78	67	11
軟部組織	89	64	25
悪性黒色腫	60	45	15
脳	55	46	9
その他	68	42	26
合計	1171	921	250

3. 結果

1）頭頸部癌

T_3, T_4 の進行期症例が適応された．全体の局所制御率は速中性子線の照射のみで39%（58/148），Salvage Surgery の31例を加えると60%（89/148）

表 3　進行頭頸部癌の速中性子線治療成績

(1975～1984.3 放医研)
分析評価　1984.11

部　位	例　数	局所制御	救助手術で局所制御	高度の障害
口腔底　T3～T4	8	1	—	1
口蓋　T3	2	2	—	1
歯ぎん　T3～T4	10	1	4	1
舌　T2～T4	17	2	1	2
頬粘膜　T3～T4	2	—	1	—
中咽頭　T3～T4	3	1	—	2
鼻咽頭　T2～T4	5	2	—	—
喉頭　T1～T4	49	30	11	—
下咽頭　T2～T3	9	3	5	1
上顎洞	17	—	6	2
耳下腺　新鮮例	4	1	3	—
術後例	11	(11)	—	—
その他	11	4	—	—
合　計	148	58 (39%)	31 (21%)	10 (6.7%)
		89 (60%)		

表 4　喉頭癌の局所制御度，速中性子線ブースト治療例　(1975～1983. 放医研)

部　位	T1	T2	T3	T4
声　門	3/5 (48/57)	5/8 (8/19)	0/2 (3/27)	0/1 (0/1)
声門上部	2/2 (4/8)	3/3 (12/34)	4/6 (7/31)	2/2 (2/27)
声門下部		1/1 (0/5)	0/1 (0/5)	

( ) 内：X線対照例 (1964～1971　癌研病院)

となる．高度の皮膚粘膜障害は10例（6.7%）にみられた（表3）．治療中に発生した強い粘膜炎は治療の一時中断，線量の10～20%減などで回復可能だが，上顎癌，咽頭癌の治療に伴って発生した開口障害は訓練を繰り返しても難治の場合が多い．

(1) 喉頭癌

速中性子線のブースト照射を基本スケジュールとして，臨床トライアルを進めている．癌研頭頸科との共同研究治療の結果を表4に示した．31例の成績を癌研のX線治療対照例と対比させると声門上部癌に速中性子線治療が効果的に思えた．その傾向は T_1～T_4 の各期について共通している．しかし声帯癌では局所制御率の差は認められていない．速中性子線治療の特徴を明らかにさせるためには，同じ臓器癌に焦点を合わせた場合でも，適切な配慮が必要であるということである．

(2) 下咽頭癌

新鮮症例9例のうち，速中性子線治療のみで局所制御された症例は3例のみで他の症例は全てSalvage surgery の対象となった．

(3) 唾液腺癌

新鮮症例4例のうち1例は速中性子線治療によって局所制御され，残る3例は Salvage surgery をうけた．そのうち1例には腫瘍細胞の残存が認められなかった．

(4) 上顎癌

15例中6例が Salvage surgery によって局所制御されたが，そのうち3例は上顎骨より発生した骨肉腫であった．

(5) 舌　癌

進行期症例が対象になったので，結果は良くなく，放射線治療のみならず，癌治療の限界を越えた症例が対象であったといえる．

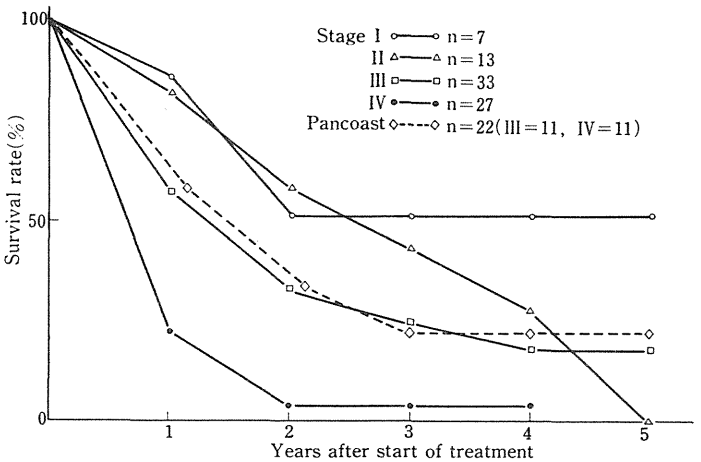

図 1　Cumulative survival curves of lung cancer, treated with fast neutrons. (NIRS, 1975～1984)

(6) 下顎癌

10例中1例が照射のみで局所制御されたが，他は salvage surgery の適応であった．

2) 肺　癌

81例の新鮮症例の組織分類は扁平上皮癌27例，腺癌40例，大細胞癌7例，未分化・小細胞癌7例であった．照射範囲は原発巣と同側肺門および縦隔を含めて，線量は肺門，縦隔には TDF 80 を原発には TDF 110 を目標に，対向2門照射，順次照射野を縮小する方法で照射している．速中性子線単独照射は6%，mixed beam 法が38%，ブースト法が56%であった．化学療法は原則として維持療法として使用している．

累積生存率は1期7例（全例腺癌）が3年，5年で52%，2期13例の3年43%，5年0%，3期34例の3年24%，5年19%，4期27例の3年，4年が4%，またパンコスト型肺癌（3期11例，4期11例）の3年，5年が23%であった（図1）．1期腺癌とパンコスト型肺癌の優れた成績は，速中性子線の優れた局所制御効果が示されたものと考える．

局所制御率は全体で53% (41/77)，TNM 分類の T_1, T_2 群で67% (20/30)，T_3 群で45% (21/47) であった．照射線量との関連は，T_1, T_2 群では TDF 110 以上で76%に対し以下では54%，T_3 群では TDF 117 以上で67%，以下で34%であった．障害発生頻度は中等度以上のなんらかの治療を必要とする一時的，あるいは持続的な障害が45% (21/47) で，そのうち外科的治療を要する高度の障害は13% (6/47)，致命的障害は0%であった．線量との関係は，TDF 120 以上で60%に対し以下では41%であった．

表 5　手術不適食道癌例の局所制御率．TDF 90 以上照射例　(1975～1984．放医研)

照 射 法	症例数	局所制御率
速中性子線	34	44% (15/34)
Mixed beam 法	20	35%
ブースト法	14	57%
X 線*	81	30% (24/81)

* 対照例は historical control (1961-1984)

以上の結果より肺癌治療における至適線量の範囲を推定すると，T_1, T_2 群では TDF 110 から 120 まで，T_3 群では TDF 117 から 120 までが相当すると考えた．

3) 食道癌

消化器系悪性腫瘍の症例数は167例で，食道癌125例，胃癌15例，肝，胆，膵癌18例，大腸癌9例であった．食道癌のうち44例は，中性子線単独の術前照射例として，TDF 60 が照射され，切除標本の病理組織学的検討が行われた[10]．その他の症例は手術不能と判断された進行期例である．放射線根治照射として TDF 90 以上が照射された例の局所制御率を表5に示す．X線の局所制御率

表6　再発子宮頸癌の速中性子線治療　5年生存例　(1975～1984. 放医研)

No.	氏　名	年　齢	前回の治療	再発部位	照射野	線量 cGy		TDF	障　害
						中性子線	X線		
1	O.K.	61	放射線	骨盤壁	大	500	4000	100	尿路変更
2	M.M.	48	放射線	骨盤壁	中	700	2800	93	なし
③	N.M.	28	手　術	骨盤リンパ節	大	320	4400	90	なし
④	M.K.	43	手　術	骨盤壁	大	600	4200	107	なし
⑤	M.I.	62	放射線	腟断端	小	1400	—	88	尿路変更
6	H.A.	53	放射線	骨盤壁	大	1300	1290	102	なし
⑦	S.K.	53	放射線	骨盤壁	小	1400	—	86	膀こう潰瘍
⑧	A.M.	50	放射線	骨盤壁	小	1400	—	86	膀こう潰瘍

○印は，中性子線でなければ治療不可能と考えられた症例

が30%（24/81）に対し，速中性子線は44%（15/34）で，ことに mixed beam 法の35%に対し，ブースト法が57%を示したのが注目される．この理由の1つは両治療群の進行度の差が関与していると考えられ今後の検討が必要である．この他の検討を総合すると，速中性子線は，らせん型，ロート型，壁深達度が深い例，高分化型扁平上皮癌に有効であるとの知見を得ている[11]．

その他の消化器癌では，膵癌と大腸癌に1例ずつの局所制御例が得られており，速中性子線の有用性を示唆するものとして期待される．

4）子宮頸癌

子宮頸部扁平上皮癌は比較的治しやすい癌であるが，癌の容積が大きくなると治しにくくなる．そこで子宮頸癌の3期のうち腫瘍容積の大きいものと，4a 期を対象にして，2群に分けて前述のランドマイズトクリニカルトライアルを行った．外部照射は速中性子線群は mixed beam 法で，X線群は 10 MV X線で全骨盤腔を照射し，腔内照射は RLAS 法を用いて外部照射を補足した．

速中性子線群とX線群の5年生存率は43%（18/42）と52%（27/52）であり，局所障害発生頻度は高度の障害で外科的治療を必要としたものが速中性子線群0例，X線群2例（いずれも直腸障害で人工肛門造設），放射線障害死が速中性子線群2例，X線群1例でいずれも小腸障害によるものであった．両群に統計学的有意差は認められない．病理組織学的検討を両群に対して行ったが差は認められなかった[12]．臨床における治療効果の評価として，再発，転移，あるいは再発・転移のパターンが両群で違うことを期待したが，特徴的な相違は認められず，同傾向であった[13]．再発子宮頸癌の治療では5年生存率が27%（8/30）で，その8例の生存症例を表6に示す．症例3と4は手術後の再発であるが大きな腫瘤であった．症例5，7，8は放射線治療を十分実施したあと，骨盤壁と腟断端部に再発した症例で，小さな照射野（5×5 cm）による速中性子線単独照射が効果あったものである．これらの結果から子宮頸癌に対する速中性子線治療の効果は，現行の mixed beam 法の対向2門照射では期待が薄いが，小さな照射野での単独照射やブースト照射ならある程度の期待がもてるのではないかと考える．

5）悪性黒色腫

悪性黒色腫は，放射線感受性が著しく低い腫瘍で小さくても早期に転移が生ずることが多い．速中性子線単独照射で TDF 110～120 に相当する線量を照射し，残存腫瘍は Salvage surgery を限局した部位に行うことにした．皮膚原発の新鮮21例の病期分類では1a 期4例1b 期15例，2期，3期1例ずつで，臨床分類では末端黒子型黒色腫が16例，結節型が4例，悪性黒子型が1例であった．これら症例は速中性子線単独治療によって，2/21，手術との併用で17/21の局所治癒が得られた．累積5年生存率は47%で，1b 期の増加にしたがって生存率の向上のきざしが認められている．しかし術後残存症例や局所再発例では5年生存者はいない（図2）．

発生母地に腫瘍細胞を残さないことが患者の治癒率の向上に連なる前提であるので，岐阜大医皮

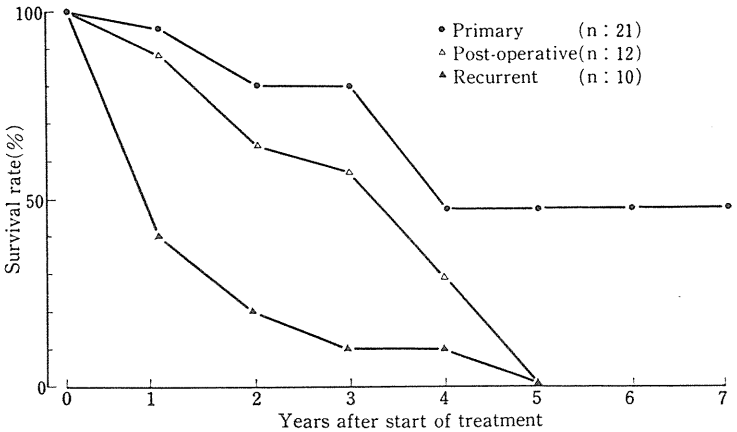

図 2　Cumulative Survival Rates of the Patients suffering from Malignant Melanoma of the Skin treated with Fast Neutrons (NIRS) (November 1983)

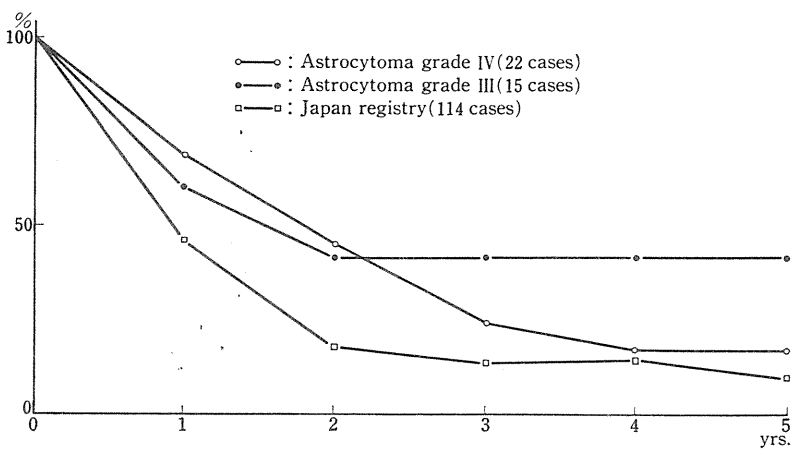

図 3　Cumulative Survival Rate of Astrocytoma Grade III and IV Treated with Fast Neutron

膚科教室との協力研究により，術前照射を悪性黒色腫の治療方針として積極的に導入した[14]．その成績は8例の治療で半数は切断手術をうけていない．心疾患のため死亡した1例を除き，全ての症例が生存している．その他の部位の悪性黒色腫では頭頸部原発の進行期例で，12例中2例の長期生存例が得られた．

6）悪性神経膠腫（Glioblastoma multiforme）

欧米の臨床トライアルでは速中性子線の脳実質に対する高 RBE のため，障害が強調されて成績が良いとはいえなかったが[15,16]，放医研では局所に照射野を絞った速中性子線のブースト照射で TDF 90 を目標に照射し，累積生存率で Grade 3が41%，Grade 4が17%という結果を得た．全国統計の Grade 3と4を含めた結果に比べて良好な成績といえる（図3）．この原因は照射に耐えられる症例が選択されたということにもあるが，全脳照射を実施しなかったことがよかったと考えられる．欧米では死亡原因が brain necrosis であると報告[17]しているが，われわれの症例では調べ得た範囲では局所再発であった．

7）その他の臓器

骨肉腫[18]，軟部組織肉腫[19]，前立腺癌[20]，膀胱癌[21]などで関連施設との協力研究治療が行われて良好な結果を得ている．

4. 考　察

高 LET 放射線としての速中性子線の治療効果に対する現状での世界的な評価は，局所制御では少なくてもX線よりよい，しかし副作用は少し高い．扁平上皮癌の頭頸部癌では多少よいが，Mixed beam 治療では差がない．消化器の腺癌，耳下腺癌，膵癌，骨肉腫，軟部組織肉腫，悪性黒色腫には有効である．脳腫瘍は治療可能比が小さくむずかしい[22]．頭頸部癌の成績もハマースミス病院の成績[23]と頸部リンパ節に対する効果[24]を除けばX線と差がなく，かえって膀胱癌の術前照射と前立腺癌によい結果を見出した[25]という報告がある．今回の放医研の成績をみても，ランドマイズド・クリニカルトライアルを行った子宮頸癌では速中性子線の有利を示すことができなかったが，ランドマイズドでなく症例数も少ないけど，声帯上部癌，耳下腺癌，パンコスト型肺癌，再発子宮頸癌，術前照射の悪性黒色腫，化学療法と併用の骨肉腫に優位を認めている．

これらの結果をみると，速中性子線単独で線量を十分に照射し得て，局所制御が可能であった疾患に特長が出ていることがわかる．確かに速中性子線の局所制御能力は強いので，障害を恐れずに照射できる部位，あるいは患部の切除，機能保存を目的とする部分切除を前提にした疾患には速中性子線照射の適応があるように思える．

ハマースミス病院の頭頸部癌の成績が良好なのはエネルギーが，16 MeV で LET 値が多少高いこともあるが，彼らの線量分布をよくするための努力が好成績につながったと考えたい．今回の成績について反省すればわれわれの線量分布改善に対する，きめの細かい配慮が装置上のハンディキャップを含めて多少不足していたように思える．速中性子線治療の対象患者は難治性癌で放射線治療で治せるか治せないかのぎりぎりの症例を選んでいるので，いかに優れた生物効果があるといえ，線量分布の悪さのための障害面が，局所制御の最後の詰での線量増加の妨げになると局所制御に失敗することになる．放射線治療の基本は線量分布であることを再確認したところである．幸いにして最近 iso centric の，回転照射が可能な速中性子線照射装置が開発され，欧米の数施設に設置された．これによる線量分布の改善が今後の治療成績の向上に役立ってくると期待されている．

現在日本で行われている粒子線治療には，速中性子線治療の他に陽子線治療がある．放医研（エネルギー 70 MeV)[26]に筑波大，粒子線医科学センター（250 MeV)[27]で開発研究が進められている．この治療法はブラッグピークという優れた線量分布を生かして障害をおそれずに，局所に十二分の線量を照射することが可能なのが特徴である．予備的な治療経験から得られたその局所制御率の高さと，障害発生率の低さは特記すべきものである．線量分布が優れていればいるほど腫瘍局在の正確な診断と，そこにビームを照準する精確な治療技術の現在より一層の発展が必要であることはいうまでもないが，将来が大いに期待される照射方法であることにまちがいない．

さらにその先の目標は，速中性子線の生物効果と陽子線の線量分布の良さを合わせ持った重粒子線治療にある．現在，アメリカ，バークレイ研究所で，He, C, Ne, Si, Ar といった重イオンを加速してその研究治療が進められている．放医研でも重イオン加速器の建設準備が着々と進行中であり，その実現の1日も早いことを希望したい．

粒子線治療はまだ始まったばかりであり，その有用性の結論を出すのはまだ早すぎる．今後共治療成績の向上に努力を重ねなければならないので，関連諸施設のご協力，ご鞭撻をお願い致します．

文　献

1) 星野一雄，川島勝弘，平岡　武，久津谷譲：放医研サイクロトロンからの速中性子線の線量分布．日本医放会誌，**37**: 248-255, 1977.
2) 野田　豊，丸山隆司：Rossi 型比例計数管によるファントム内外でのγ分布の測定と防護への応用．特別研究「粒子加速器の医学利用に関する調査研究」最終報告書，放医研: 104-111, 1984, 12.
3) Blakely, E.A., et al.: Physical and cellular radiobiological properties of heavy ions in relation to cancer therapy applications. *LBL*, **11220**: 73-86, 1980.

4) Urano, M. & Koike, S.: Comparison of the effects of neutron and/or photon irradiation on spontaneous squamous cell carcinoma in mice. *Radiology*, **134**: 219-225, 1980.
5) 安藤興一，小池幸子，福田信男：放医研サイクロトロンによる腫瘍の治療効果および正常組織障害に関する実験的研究，特別研究「粒子加速器の医学利用に関する調査研究」最終報告書，放医研：120-126，1984，12.
6) Ando, K. Ohara, H., et all: Effects of fast neutrons on experimental tumors in fractionated schemes. US-Japan Seminar "High LET particle irradiation and other approaches to incrase effectiveness of radiation therapy for cancer" Chiba & Kyoto, 1982.
7) 馬嶋秀行，大原　弘，安藤興一，恒元　博：中性子線とX線の混合二分割照射によるマウス扁平上皮癌由来の培養細胞における回復に関する研究，特別研究「粒子加速器の医学利用に関する調査研究」最終報告書，放医研：136-141，1984，12.
8) 中村　譲：速中性子線における生物学等価TDFによる治療計画法．日本医放会誌，**38**：950-960，1978.
9) 沢田勤也，福間誠吾，関　保雄，田中文隆・他：pancoast 型肺癌に対する速中性子線治療について．癌の臨床，**29**：111-114，1983.
10) 石川達雄：食道癌に対する速中性子線術前合併療法の効果—組織学的効果について—．日消外会誌，**16**：1738-1746，1983.
11) 石川達雄，佐藤　博，磯野可一，小野田昌一，恒元　博・他：食道癌における速中性子線治療—術前照射と組織学的効果について—．癌の臨床，**27**：11-19，1981.
12) 森田新六，荒居竜雄，恒元　博，笠松達弘，近江和夫，福久健二郎：速中性子線照射をした子宮頸癌症例の組織型分類と局所制御の関連性．癌の臨床，**30**：1280-1284，1984.
13) Morita, S., Arai, T., Nakano, T., Ishikawa, T., Tsunemoto, H., Fukuhisa, K. and Kasamatu, T.: Clinical experience of fast neutron therapy for carcinoma of the uterine cervix. *In. J. Radiation Onology Biol. Phys.*, **11**: 1439-1445, 1985.
14) 恒元　博，森田新六，石川達雄，森　俊二：速中性子線治療臨床トライアルにおける放射線生物学—悪性黒色腫の治療を中心に—．癌の臨床，**29**：1554-1560，1983.
15) Parker, R.G., Berry, H.C., Gerdes, A.J., Soronen, M.D. & Shaw, C.M.: Fast neutron beam radiotherapy of glioblastoma multiforme. *Am. J. Roentgenol.*, **127**: 331-335, 1976.
16) Griffin, T.W, Davis, R., Laramore, G.E., et al.: Fast neutron radiation therapy for glioblastoma multiofrme: Results of an RTOG study. *Am. J. Clin. Oncol.*, **6**: 661-667, 1983.
17) Catterall, M., Bloom, H.J., Ash, D.V., et al.: Fast neutrons compared with megavoltage X-rays in the treatment of patients with supratentorial glioblastoma: A controlled pilot study. *Int. J. Radiation Oncology Biol. Phys.*, **6**: 261-266, 1980.
18) Tatezaki, S.: Systematic multimodal treatment of osteosarcoma, with special reference to the role of fast neutron radiotherapy. *J. Jap. Orthop. Ass.*, **53**: 831-846, 1979.
19) 花岡英弥：私信（1984）.
20) 丸岡正幸，安藤　研，野積邦義，伊藤晴夫・他：前立腺癌の速中性子線療法．日泌尿会誌，**74**：409-417，1983.
21) 井坂茂夫，五十嵐辰男，伊藤晴夫・他：進行性膀胱腫瘍に対する術前照射の近接効果．日泌尿会誌，**74**：1778-1783，1983.
22) Cohen, L., Hendrickson, F.R., Kurup, P.D., Mansell, J.A. et al.: Clinical evaluation of neutron beam therapy. current results and prospects, 1983. *Cancer*, **55**: 10-17, 1985.
23) Catterall, M. & Bewley, D.K.: Fast neutrons in the treatment of cancer. London, Academic Press, 1979.
24) Griffin, T.W., Davis, L., Laramore, G.E., Hussey, D.H., et al.: Fast neutron irradiation of metastatic cervical adenopathy: The results of a randomized RTOG study. *Int. J. Radiat. Oncol. Biol. Phys.*, **9**: 1267-1270, 1983.
25) Parker, R.G.: Particle radiation therapy. *Cancer*, **55**: 2240-2245, 1985.
26) 森田新六，恒元　博，石川達雄，安藤興一，他：陽子線治療の基礎的臨床的研究．文部省がん特（I），高 LET 放射線によるがん治療及び診断の基礎的研究，58年度報告書，95-107，1984.
27) 北川俊夫，広川　裕，稲田哲雄，小林克之，丸橋　晃：陽子線診療の基礎的臨床的研究，文部省がん特（I），高 LET 放射線によるがん治療及び診断の基礎的研究．58年度報告書，121-127，1984.

放医研における中性子線被曝管理について

Radiation Safety programme in NIRS Neutron Facilities

丸山隆司、隈元芳一、野田　豊*
放射線医学総合研究所
〒260　千葉市穴川4丁目9番1号

Takashi Maruyama、Yoshikazu Kumamoto* and Yutaka Noda
Division of physics and Division of Technical Services*
National Institute of Radiological Sciences,
9－1, Anagawa-4-chome, Chibashi 260 Japan

放医研には中性子被ばく管理を必要とする施設として、サイクロトロン、Van de graaff 装置、RI中性子源、医用直線加速器などがある。これらの施設の個人管理はNTA・フィルム・バッジで行われ、環境管理はBF_3比例計数管やレム・カウンタで行われている。個人モニタは事故被曝用と考え、平常は中性子被曝が起らない施設・設備の放射線防護に留意している。放医研では医療に高エネルギー放射線を利用しており、これにより患者が無駄な中性子被曝を受けないように心がけている。医用直線加速器からの光核反応中性子発生量の測定および中性子遮蔽に対する対策、速中性子線治療時の患者の正常組織の被曝評価など患者の被曝管理についても研究を行っている。本報告は、患者の被曝管理のためのエッチピット法による光核反応中性子の線量当量測定およびLET比例計数管による平均の線質係数決定を含めて、放医研の中性子被曝管理について述べる。

In NIRS, the facilities at which neutron monitoring is required are a medical cycltron, a Van de Graaff apparatus, medical linear accelerator and RI neutron sources. A nuclear track film is used for the personnel monitor and a rem counter is used for the environmental monitor at these facilities. In NIRS, the cyclotron and the lienar accelerator are used for radiotherapies of cancer patients. In order to ensure patients from harmful neutron exposure on the basis of the concept of ALARA, the neutron dosimetry and neutron shielding have been actively investigated. This paper will describe the radiation safety programme aginst neutrons in NIRS, including a measurement of neutrons from photonuclear reactions with an etch pit method of polycarbonate and a determination of effective quality factors with a LET proportional counter.

key words: Neutron monitoring, Etching pit method, LET proportional counter, reduction of patient exposure,

1. 緒　言

現在、放医研にある中性子線源としては、①医用サイクロトロン、②Van de graaff 装置、③Am—BeなどRI中性子源、さらに、④光核反応中性子源と考えられている医用直線加速器の4種類である。これらの使用施設で放射線作業に従事する約60名の職員が中性子線の個人被ばく管理を受けている。これらの職員のほとんどは医用サイクロトロンで作業している。ここでは、速中性子線治療（週3回午後のみ）、陽子線治療（週1回午前のみ）、短寿命RI製造（週1.5日）および物理・生物研究（週1.5日）が行われている。

Van de graaff 装置は現在、大部分が2.8 MeV 以下の陽子線によるPIXEを用いた分析実験に使用されている。医用直線加速器は患者の治療に用いられている。RI中性子線源は測定器のチェックなどに月あたり平均10日程度使用されている。

速中性子線治療を行っている関係上、放医研では対電離箱法を中心とした中性子線量測定は確立しており、日米相互比較なども活発である。また、細胞や小動物を用いた生物実験も盛んで、サイクロトロンやVan de graaff 装置で発生した中性子の生物効果についてかなりのデータを有している。従って、中性子を取扱う職員の大部分が自分達の利用している中性子の物理学的、生物学的特性を十分に理解しているのも放医研の特徴かも知れない。放医研の放射線安全管理業務は行政職職員によって法規制遵守の方針でかなり厳しく遂行されている。

2. 中性子被ばく管理

中性子被ばくの可能性のある職員はコダックNTAフィルムを内蔵した広範囲用のバッジを装着している。しかし、現在のところ1カ月の装着期間で有意な速中性子線被ばくをした例は皆無である。NTAフィルムが原理的に500 keV程度未満のエネルギーの中性子を検出できないことから当然予想されるところである。アルベド法などを用いた速中性子線用個人モニタの装着を考えたことはあるが、同じ職員がサイクロトロン、Van de graaff 装置、さらにはRI中性子線源を、同一装着期間中に不定期に使用するため、平均的な中性子スペクトルの推定も困難であるので、スペクトル情報を要するアルベド法の適用は困難とみられた。しかし、現状では数100 keV程度から数eVの中性子を検出できる個人線量計を得ることは困難である。このような事情から中性子使用施設の遮蔽設計を十分に行い、作業環境のモニタリングに心がけ中性子に被ばくする可能性をなくすことこそ最善の個人被ばく管理と考えてきた。

中性子線用サーベイメータとして目下のところ安全管理業務には、レム・カウンタを使っているが、これが最適だからというより他に適当な測定器がないから使用しているわけである。使用しているのはStudsvik製2202Dレム・カウンタで、電総研の単一エネルギー中性子と ^{252}Cf や $^{241}AmBe$ のRI中性子源に対して校正されている。1974年ごろサイクロトロンの使用前の測定が行われたが、そのときにこのレムカウンタは電離箱サーベイメータと共に主役であった。サイクロトロンの生物照射室へのビームポートは、本体からのビーム取出しポートに対して4°の角度である。Fig.1に示す BS_0（ビーム・ストッパー）を閉じて重陽子ビームを完全に遮断したとき、生物照射室にある C_4 ポートでは中性子発生はないはずであった。しかし、C_4 の位置で30 MeV、30 μA重陽子ビームについてレムカウンタで測定したところ、100 mrem／hr（中性子の平均エネルギー14 MeVとし、線量当量率を算定した）であり、左右に位置をずらすと中性子線量当量率はこの1／10以下に減少した。これは BS_0 で発生した中性子がビームポートを伝わって、C_4 に漏洩してくることを示唆している。そのため、厚さ30 cmの鉄製中性子シャッタ[1)]（BS_N）を設置し、生物照射室およびその直下にある速中性子線治療照射室（地階にある）にビームを通さない場合はこれによって C_4 への中性子漏洩を遮蔽している。現実には、図の C_4 近辺はBeターゲットなどの残留放射能が高く、β、γ線による被曝の方が大きいことは言うまでもない。しかし、中性子の生物効果を考慮すれば、このシャッターは無駄ではなかったと考えている。サイクロトロン施設の建物は普通コンクリートを遮蔽材としているが、その厚さは本体室で3.5 mである。周辺環境への中性子線管理は、BF_3 比例計数管、ポリカーボネイトを用いたエッチピット法などによって行われている。現在までのところ、サイクロトロン以外の施設を含めて環境への中性子線漏洩はみられない。

3. 医療における中性子線管理

放医研では、職業上の被曝だけでなくICRPの勧告するALARAの精神から、患者に対する目的外の放射線によ

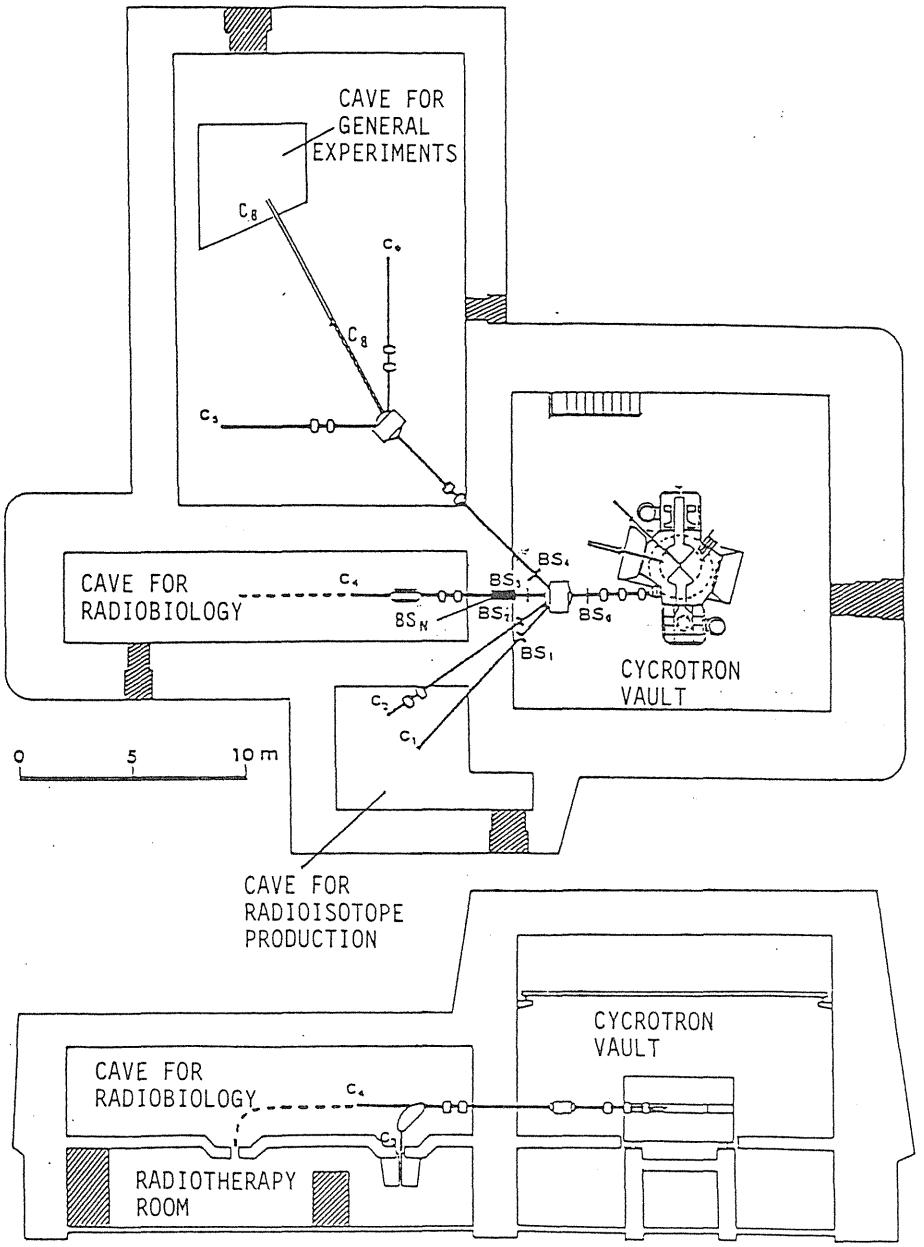

Fig.1 Beam transport systems in NIRS cyclotron facility
BS_0 - BS_4 : beam stoppers, BS_N : neutron shutter. C_8 and C_4 ports have thick beryllium target to produce fast neutron beams

る被曝の低減が行われている。こゝでは、医療用直線加速器からの高エネルギーX線による光核反応中性子およびサイクロトロン速中性子線治療時における患者の正常組織（利用線錐外ビーム）の中性子被曝について述べる。

3.1. 光核反応中性子の測定

医療用あるいは工業用直線加速器やベータトロン、さらにはマイクロトロンからの6MeVを超える電子線およびX線による光核反応からの中性子線を測定した。これらの加速器施設の照射室内では、パースト状の中性子のため、レムカウンタの使用はほとんど不可能である。ここでは、レムカウンタのBF_3計数管の代わりに^{10}B－α線ラジエータとポリカーボネイトを用いたFig.2のようなレムメータを用いた。中性子エネルギーに対するレムレスポンスは市販のレムカウンタと同様である。レムメータの校正は^{241}Am－Be中性子線源で行われている。^{241}Am－Be線源に対するエッチピット・レスポンスは47.2（ピット・cm^{-2}／mrem・hr^{-1}）であり、^{252}Cf線源に対して53.9であった。

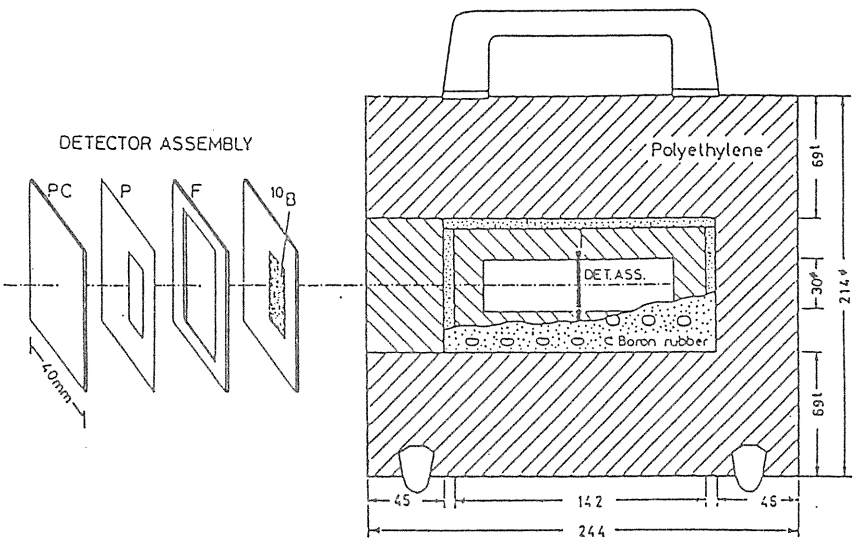

Fig.2 Cross sectional view of a rem meter using ectch pit method of polycarbonates as the thermal neutron detector.
PC: polycarbonate plate, P: collimator made from paper, F: flame made from paper, ^{10}B: Alpha-ray radiator.

Fig.3は国立ガンセンタのマイクロトロンや放医研の直線加速器でX線を照射したとき、ターゲットから1mの位置でのX線の線量（rad）あたりの中性子線量当量を示している。一般によく用いられている10 MVX線では、Wターゲットでradあたり0.5 mrem、Cuターゲットでは Wターゲットの場合の約1／4であった。

エッチピットを用いたレムメータはパースト状の中性子の測定には適しているが、ポリエチレンなどの減速材を併用するため個人線量計には不向きである。医療用直線加速器などが中性子発生源であることが明らかとなったため、今後、これらの装置使用施設では中性子に対する被曝管理が必要となった。CR－39、アルベド型など低エネルギー中性子に対する個人モニタが要求される。

3.2. 線質係数決定法

市販されているFig.4のようなRossi型LET比例計数管を用い、中性子・γ線混合場における平均線質係数決定法について検討した。ICRU－33[2]によれば、水中の衝突阻止能の関数で与えられている線質係数Q（L_∞）、L_∞を関数とする線量D（L_∞）を用いたとき、平均の線質係数$\bar{Q}$は次式で与えられる。

$$\bar{Q} = \frac{\int_0^\infty Q(L_\infty)\, D(L_\infty)\, dL_\infty}{\int_0^\infty D(L_\infty)\, dL_\infty} \qquad (1)$$

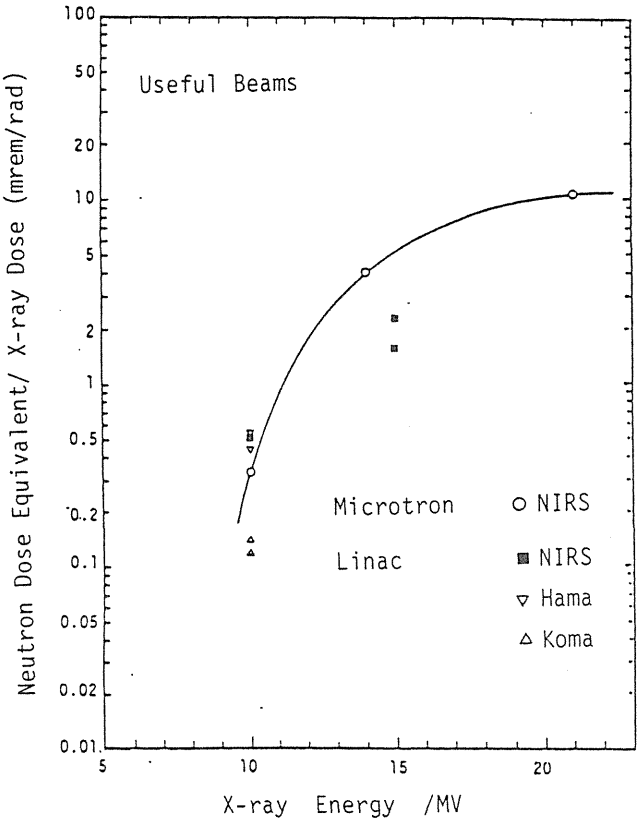

Fig. 3 Neutron yields from photonuclear reactions due to high energy X-rays produced by medical linear accelerators and a microtron. The dose equivalents were measured with the rem meter shown in Fig. 2

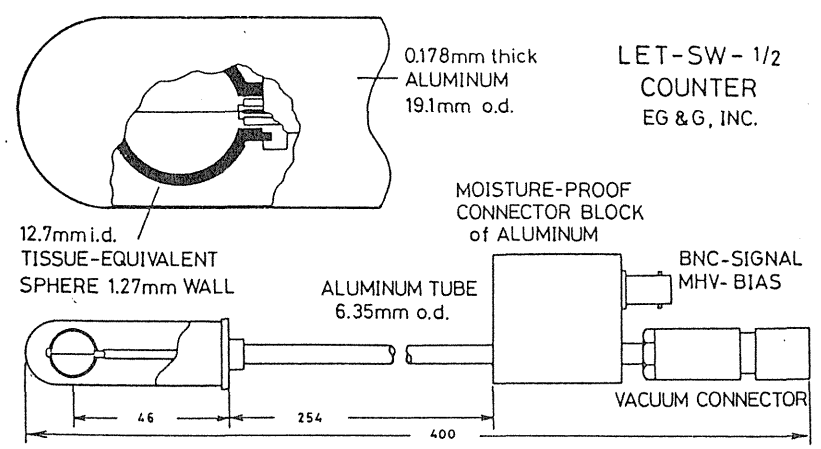

Fig. 4 Cross sectional view of LET proportional counter

ある放射線場に対する確率y（線エネルギー）の分布は、マイクロドシメトリの出発点となったRossiの比例計数管によって測定できると考えられる[3]。この計数管でD（L_∞）の分布を測定し、ICRPの勧告[4]しているQ（L_∞）を乗じて上式から$\bar{Q}$を求める。

放医研での速中性子治療は30MeV重陽子線によるBe（d、n）B反応からの中性子線が用いられている。治療にはベネレックス（圧縮木材：密度1.4 g/cm^3）を主遮蔽材とし、ビーム方向の長さ55cmの鉄板（約1.99cmの厚さ）8枚を左右に動かして不整形照射野をつくるコリメータ[5]が用いられている。Beターゲットから200cmの位置で治療を行っており、重陽子30 MeV、30 μAのとき線量率は約50 rad／min（照射野11.4×11.4cm）である。このとき利用線錐の中心から50cmの位置で、350 mrad／minの線量が推定される。

直径1／2インチの比例計数管を用い、ターゲットから200cmの位置で11.4×11.4cmの照射野としたとき、組織等価ファントムの深さ2.5cmのy分布をビームの中心からいろいろな距離で測定した。Fig.5にD(y)分布を示す。y

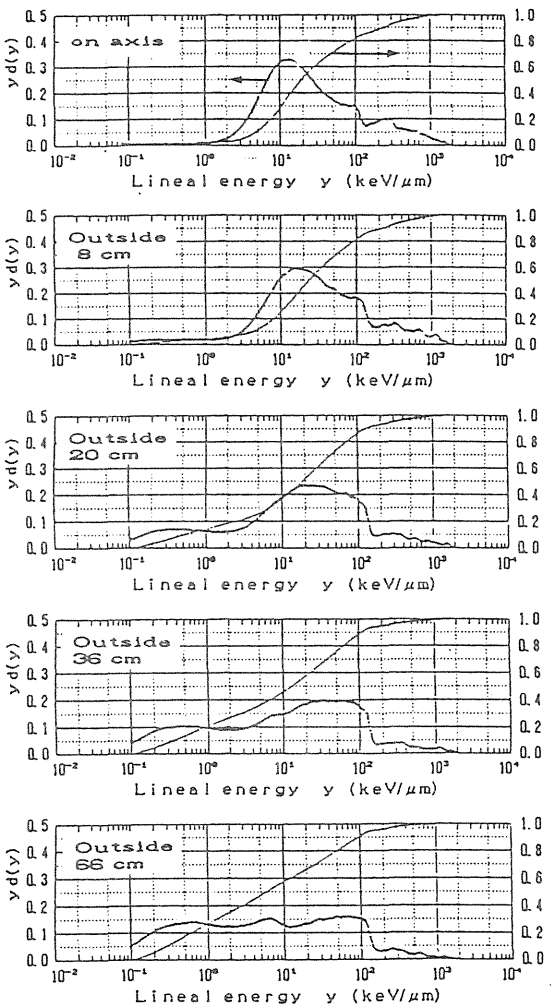

Fig.5 Distribution of lineal energy(y) in a tissue equivalent phantom irradiated using neutron beams produced by Be(d,n)B reaction with 30MeV deuterons accelerated by a cyclotron. Field size: 11.4×11.4 cm, phantom: 30×80×20 cm (thick), Depth: 5 cm

を近似的にL∞に等しいとして(1)式によって求めたQ(L∞)・D(L∞)分布をFig.6に示し、これらのデータから計算した$\bar{Q}$の値をTable.1に示す。Fig.6でQ(L∞)は実線で、Q(L∞)・D(L∞)をヒストグラムで表わしている。

利用線錐中心から50cmでの平均の線質係数は約6.6となり、6.6×350mrad/min≒2.3 rem/minとなる。速中性子線治療で100 radを患部に照射したとき、その中心から50cm離れた正常組織は約5 remの被曝があったと考えられる。治療中に患者以外は照射室に滞留しないので被曝しない。

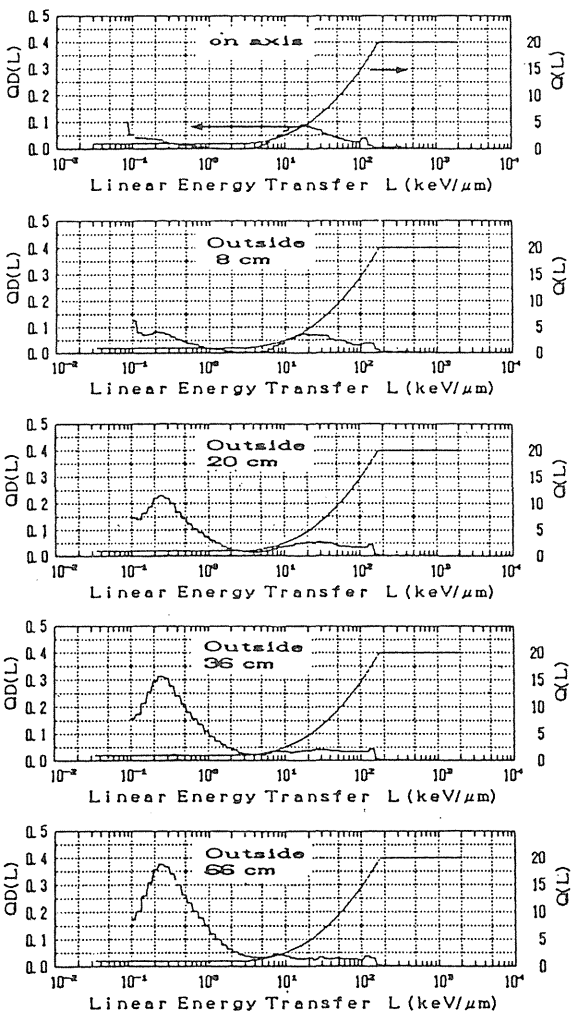

Fig.6 Schema for the determination of effective quality factor using the experimental data on LET distribution in dose given in Fig.5, assuming the lineal energy is approximately equivalent to LET

Table.1 Averaged lineal energies: $\bar{y}_f$ in frequency and $\bar{y}_d$ in dose and effective quality factor

Distance from beam center (cm)	averaged values $\bar{y}_f$	$\bar{y}_d$ (keV/um)	Effective quality factor, $\bar{Q}$
0 (center) cm	6.45	85.0	9.0
6	5.35	84.2	9.2
8	4.21	89.8	9.5
12	2.36	82.1	9.2
20	1.70	67.6	8.2
36	1.22	56.3	7.3
51	1.04	49.7	6.6
66	0.97	40.9	6.0

4. 結　言

(1) 放医研の中性子被曝個人管理は、速中性子線用フィルム・バッジによって行われているが、これは事故時の線量推定に役立てるもので、平常はレムカウンタによってモニタし、中性子被曝がないよう施設内外の個人・作業環境管理を行っている。

(2) 医療における中性子線管理は、医師や看護婦等の職業被曝だけでなく、ICRPの勧告しているALARAの精神から患者の医療被曝にも適用されている。このために必要な測定・評価法は、研究的立場から常時検討されている。

(3) 同一個人が、ある短期間に線量率は勿論、エネルギーも異なる中性子・γ線の混合場で放射線作業を行うためには、中性子に対する被曝を皆無にすることが必要不可欠であると考える。

(4) 医療用加速器使用施設における中性子線被曝管理の早期確立が要求されている。

参考文献

1) T. Yamada and M. Tazawa: A neutron Shutter for a cyclotron facility, Nucl. Instr. Meth., 146, 457－458, (1977)

2) ICRU－33: Radiation Quantites and Units, International Commission on Radiation Units and Measurements, (1980)

3) H. H. Rossi: Microscopic energy distribution in irradiated matter, in Radiation Dosimetry (Eds. F. H. Attix and W. C. Roesch), Vol.1, 43－92, (1968)

4) ICRP－26: 国際放射線防護委員会勧告、(日本アイソトープ協会 翻訳) (1977)

5) 丸山隆司 他: 速中性子線治療用コリメータの設計およびその特性、日医放学会誌 38, 633～642, (1978)

Int. J. Appl. Radiat. Isot. Vol. 36, No. 5, pp. 345–347, 1985
Printed in Great Britain

0020-708X/85 $3.00 + 0.00
Pergamon Press Ltd

Labeling of ^{13}N Labeled Adenosine and Nicotinamide by Ammonolysis

TOSHIAKI IRIE, OSAMU INOUE, KAZUTOSHI SUZUKI and TOSHIYOSHI TOMINAGA

National Institute of Radiological Science 9-1, Anagawa-4-chome, Chiba-shi (CHIBA) 260, Japan

(*Received* 17 *October* 1984; *in revised form* 3 *December* 1984)

The labeling of adenosine and nicotinamide with nitrogen-13, a short-lived positron emitter, was tried by ammonolysis of 6-halogenated ribofuranosylpurine and nicotinic acid chloride in aqueous ^{13}N ammonia solution. From examination of the labeling condition, it was found that adenosine and nicotinamide could be labelled with ^{13}N in an amino or amidegroup by a short-time reaction. The radiochemical yields were about 20% for adenosine and 28% for nicotinamide. The labeling was possible in a non-carrier-added state.

Introduction

For studies of biological functions and biodistributions of physiologically active amines and amides it is very interesting to utilize ^{13}N labeled compounds as *in vivo* tracers. However, there are few reports concerning ^{13}N chemical labeling[1,2] (except for ^{13}N labeled amino acids by means of enzymatic reactions) perhaps because of its very short half-life (10 min) and the limitations of its labeled precursors.

We attempted to develop a rapid chemical ^{13}N labeling by means of ammonolysis using aqueous ^{13}N labeled ammonia as a precursor, since ammonolysis is a simple one-step reaction and since aqueous ^{13}N labeled ammonia is easily obtained on a large radioactive scale. Adenosine and nicotinamide are biologically important natural compounds, whose positron-radiotracers may be potential for nuclear-medical studies. We first tried to label these compounds with ^{13}N by ammonolysis.

Experimental

Materials

6-chloro-9-β-D-ribofuranosylpurine was purchased from Aldrich Chem. Comp. Inc. 6-fluoro-9-β-D-ribofuranosyl purine was prepared by Kiburis and Lister's method by fluorination of 6-trimethylammonium derivative.[3] Nicotinic acid chloride was prepared as its hydrochloride by the reaction of nicotinic acid with thionyl chloride.[4]

Aqueous [^{13}N]ammonia was obtained by the following method. An aqueous solution of ^{13}N-labeled oxides of nitrogen, produced via the $^{16}O(p,\alpha)^{13}N$ reaction with 18 MeV proton on water, was reduced with Devarda's alloy and sodium hydroxide in a glass flask; then [^{13}N]ammonia was distilled in a stream of nitrogen and collected in a vial. Typically the solution was obtained in a volume of about 5 mL, and its radioactivity was about 200 mCi after distillation. Trace radiocontaminants, such as ^{18}F, ^{11}C and ^{48}V, were not present in the distilled aqueous solution as confirmed by γ ray spectroscopy utilizing a Ge(Li) detector.

Labeling of adenosine

The labeling of adenosine was examined for the ammonolysis of two substrates, 6-chloro-9-β-D-ribofuranosylpurine and 6-fluoro-9-β-D-ribofuranosylpurine with aqueous [^{13}N]ammonia, shown in Fig. 1. First the efficiency of the pH in the reaction medium was studied in a carrier-added state. Typically, 20 μL of aq. NaOH (10^{-3}–10^{-1}N) and 5 μmols of carrier ammonia were added to 200 μl of aqueous [^{13}N]-ammonia solution in a glass vial, and 10 μmol of substrate was added to the mixture. The sealed glass vial was stirred for 10 min in an oil heated to 100°C. Identification of labeled adenosine and determination of the radiochemical yield were performed by TLC analysis with a radiograph or column chromatography. In TLC analysis, a silica-gel plate spotted with the reaction mixture was developed with distilled water. Unreacted [^{13}N]ammonia remained at the origin, and adenosine ran at the point of R_f 0.75. Column chromatography was performed as follows. After cooling and slightly acidifying the reaction mixture with acetic acid, the mixture was loaded on the column of Parapak Q (polystyrene resin, 8 × 55 mm), well pre-eluted with distilled water after loading with acetone, and eluted with distilled water followed

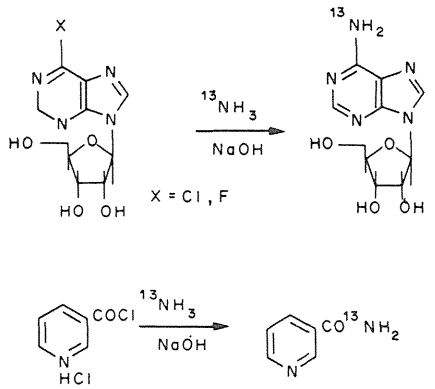

Fig. 1. Labeling of [^{13}N]adenosine and [^{13}N]nicotinamide.

by methanol. A typical column chromotogram is shown in Fig. 2.

The results of the labeling in a carrier-added state are summarized in Table 1, in which the pH means the initial value of the reaction mixture calculated with molars of added alkali and carrier ammonia.

In a similar manner the labeling in a non-carrier-added state was examined. The results are shown in Table 2. Furthermore, the labeling time and temperature effects were studied in order to determine optimal labeling conditions. The reaction at 80°–100°C was favorable, and the radiochemical yield reached a maximum after 10 or 15 min at 100°C.

Labeling of nicotinamide (Fig. 1)

Nicotinic acid chloride hydrochloride, freshly prepared, was examined as a substrate by ammonolysis with aqueous [^{13}N]ammonia. Typically, about 140 μmol of a substrate was added to a solution

Table 1. Effect of pH on the yield of [^{13}N]adenosine—carrier added

aq. NaOH	pH	Radiochemical yield (%)	
		F-deriv	Cl-deriv.
—	10.8	18.2	—
10^{-5}N	10.8	20.4	2.3
10^{-3}N	10.9	22.5	—
10^{-2}N	11.2	21.2	3.5
10^{-1}N	12.0	24.5	5.2

Reaction conditions: aq. [^{13}N]ammonia: 200 μL, carrier 1 N NH_4OH: 5 μL, aq. NaOH: 20 μL, substrate: 10 μmol, temp. and time: 100°C, 10 min.

Table 2. Effect of pH on the yield of [^{13}N]adenosine—non-carrier added

Alkali (aq. NaOH 20 μL)	pH (calculated)	Radiochemical yield (%)
—	—	2
10^{-4}N	9	2
10^{-3}N	10	2.5
10^{-2}N	11	5.0
10^{-1}N	12	11.0

Reaction conditions: aq. N-13 ammonia: 200 μL, substrate (F-deriv.): 10 μmol, 10 min heating at 100°C.

containing 250 μL of aqueous [^{13}N] ammonia, alkali, and 10 μmol of 1 N ammonia in the case of carrier-added labeling. The mixture was sealed and left to stand at the test temperature for 1–10 min. The labeling yield was determined by TLC analysis with a silica gel plate developed with acetone. The identification of ^{13}N-labeled nicotinamide was performed by HPLC using Bondapak C-18 column eluted with the solution of methanol:0.02MkH_2PO_4 (1:9) at a flow rate of 1.5 mL/min. The radiochromatograph is shown in Fig. 3.

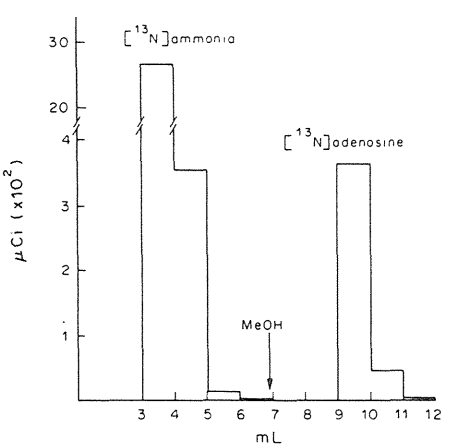

Fig. 2. Isolation of [^{13}N]adenosine by Parapak-Q column chromatography. Conditions; column size: 8 mm × 55 mm, 100–120 mesh, eluent: distilled water–methanol.

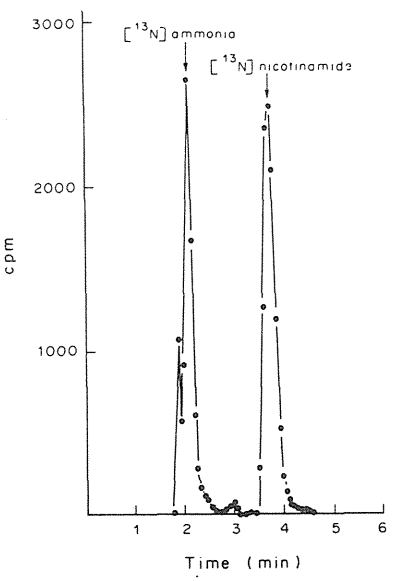

Fig. 3. Radiochromatogram of [^{13}N]nicotinamide by HPLC. Conditions; column: μ-Bondapak C-18, eluent: methanol/0.02 M KH_2PO_4 (1:9) (1.5 mL/min).

Table 3. Labeling efficiency of [^{13}N]nicotinamide

Alkali (μmol)	Radiochemical yield (%)	
	Carrier-added	Non-carrier-added
10–50	2	2
100	14.6	6.4
200	19.5	18.9
500	28.5	25.3
1000	18.9	19.3

Reaction conditions: aq. [^{13}N]ammonia 250 μL, substrate: 140 μmol, carrier ammonia (in carrier-added): 10 μmol, 1 min reaction at 20°C.

The labeling reaction was instantaneous and the radiochemical yield was almost constant for 10 min after the addition of a substrate at temperatures of 20°–50°C. The yield decreased with the elevation of reaction temperature over 60°C. The results under the condition of a 1-min reaction at room temperature are summarized in Table 3.

Discussion and Conclusion

Ammonolysis is generally carried out in an excess liquid ammonia or alcoholic medium. In the labeling procedure, [^{13}N]ammonia as a reagent should be used in a non-carrier-added state or with a very small amount of carrier in order to obtain a high radiochemical yield and a high specific activity. Under such conditions preliminary labeling was successful via ammonolysis of reactive substrates such as 6-fluoro-9-β-D-ribofuronosylpurine or acid chloride with aqueous [^{13}N]ammonia.

In order to increase the efficiency for such a labeling in an aqueous solution, the [^{13}N]ammonia should be kept in the neutral form by maintaining the pH of the reaction medium higher than the pK_a of ammonia (= 9.3). The pH effect was clearly demonstrated in the labeling of adenosine. In carrier-added labeling using 5 μmol of carrier ammonia, the initial pH of such a reaction medium was calculated to be about 10.8 without addition of alkali, where [^{13}N]ammonia almost exists in a neutral form, so that a good radiochemical yield, about 18%, was obtained with 6-fluoro-derivative. However, in non-carrier added labeling, the optimal yield, about 10% was obtained only by pH adjustment with alkali addition. Much excess alkali lowered the yield.

As a substrate, 6-fluoro-derivative gave a much higher yield than 6-chloro-derivative. This probably results from the more intensive induction effect of the fluorine atom.

In the labeling of nicotinamide, much more alkali was required to obtain a high yield because of the need to compensate for hydrogen chloride from the substrate. The reaction was quite rapid: about 28 and 25% of the radiochemical yields were obtained in carrier-added and non-carrier added labeling respectively, in a 1 min-reaction at room temperature. This labeling method should be applicable to other amides, and amides are expected to be precursors of amines by Hofman rearrangement.

The very short reaction time and moderate radiochemical yields for both adenosine and nicotinamide would be of practical use regarding the half life of ^{13}N (10 min). However, in clinical use, it would be necessary to perform rapid purification and preparation of the solutions of these compounds for injection.

The column chromatography used in the separation of labeled adenosine is not suitable for this purpose because of the considerably long period required (20 min) and the presence of some non-radioactive by-products (mainly inosine). In the case of nicotinamide, preparative separation has not yet been established.

In the research reported in this paper, labeling by ammonolysis was examined with aqueous [^{13}N]-ammonia. However, if non-aqueous [^{13}N]ammonia is available, it seems to be more favorable for the labeling by ammonolysis of various compounds such as amides or amines.

Acknowledgements—The authors are grateful to the cyclotron team of the NIRS for carrying out the irradiation, to Mr K. Tamate for the production of [^{13}N]ammonia, and to Mr T. Kobayashi for technical assistance with preparation of substrates.

References

1. Finn R. D., Christman D. R. and Wolf A. P. *J. Labelled Compd. Radiopharm.* **18,** 909 (1981).
2. Petlit W. A., Tilbury R. S., Digenis G. A. and Mortara R. H. *Ibid.* **13,** 119 (1979).
3. Kiburis J. and Lister J. H. *J. Chem. Soc. C*, 3942 (1971).
4. Mayer H. and Graf R. *Chem. Ber.* **61,** 2202 (1928).

Int. J. Nucl. Med. Biol. Vol. 12, No. 5, pp. 369–374, 1985
Printed in Great Britain.

0047-0740/85 $3.00 + 0.00

Alterations in Biodistribution of [^{3}H]Ro 15-1788* in Mice by Acute Stress: Possible Changes in *In Vivo* Binding Availability of Brain Benzodiazepine Receptor

OSAMU INOUE, YOSHIO AKIMOTO,[1] KENJI HASHIMOTO and TOSHIRO YAMASAKI

National Institute of Radiological Sciences, Division of Clinical Research, Chiba-shi, Anagawa 4-9-1, Japan and [1]Tohō University, School of Pharmaceutical Science, Funabashi-shi, Miyama 2-2-1, Japan

(*Received* 10 *July* 1985)

The biodistribution of [^{3}H]Ro 15-1788 in control and stress-loaded mice (forced swimming) was compared. In control mice, carrier-free [^{3}H]Ro 15-1788 was selectively and highly distributed in Bz receptor rich brain regions, while radioactivity in the brain was very low following administration of carrier-added tracer, which suggested that *in vivo* non-specific binding of this tracer was very low. Significant changes in biodistribution of carrier-free [^{3}H]Ro 15-1788 were observed in stress-loaded mice, which strongly indicated that *in vivo* binding availability of Bz receptor in the brain was rapidly and reversibly reduced by acute stress. The degree of these changes was very dependent upon the stressful conditions, such as swimming duration and water temperature, and a significant alteration in biodistribution of [^{3}H]Ro 15-1788 was particularly observed in the cerebral cortex. Simplified Scatchard analysis of *in vivo* binding of this tracer was performed, and results suggested that these alterations were mainly caused by changes in the K_d value rather than the B_{max} value.

Introduction

Stress has an important role in some kinds of disease state as a trigger or an effector. In animal experiments, significant changes in the neurotransmission system in the brain have been reported.[1,2] However, there had been no direct method for the measurement of such alterations in brain function caused by stress. Recently, several reports indicated that the Bz receptor in the brain was capable of alteration in response to physiological stimuli.[3–5] Further, a new method using a positron emitter labelled ligand for the *in vivo* visualization or quantitative analysis of brain neuroreceptors has been developed.[6–8] Concerning Bz receptor mapping, a specific radioligand ^{11}C-Ro 15-1788 was synthesized and evaluated.[9,10,11] In this study, we evaluated the biodistribution of [^{3}H]Ro 15-1788 in control and stress-loaded mice, and discuss here the possibility of *in vivo* detection of changes in Bz receptor function by acute stress.

Materials and Methods

Materials

Ro 15-1788 was kindly provided by Japan Roche Ltd, Kamakura, Japan. [^{3}H]Ro 15-1788 (87 Ci/mmol) and [^{14}C]iodoantipyrine (53 mCi/mmol) were obtained from New England Nuclear, Boston, MA, U.S.A. Other chemicals used were of the highest grade available commercially.

Biodistribution of [^{3}H]Ro 15-1788 in control or stress-loaded mice

Male C3H (8–9 weeks old) weighing about 30 g were used. All animal experiments were performed at 14:00–16:00 h in order to avoid the effect of circadian rhythm. [^{3}H]Ro 15-1788 was dissolved into 10% vegetable oil emulsion with or without carrier Ro 15-1788 (1.5 mg/mL). Two-tenth mL (1 μCi, 0.01 nmol) was intravenously injected into control or stress-loaded mice. One, 5, 15 and 30 min after the injection of the tracer, mice were lightly anaethetized with chloroform and killed by decapitation, and blood, cerebral cortex, cerebellum and pons-medulla were quickly removed and weighed. Each sample was incinerated by a Packard 306 sample oxidizer, and the percent dose per gram (% dose/g) in each sample was determined by Beckmann 6800 scintillation counter. In order to confirm the reproducibility of biodistribution of the tracer in stress-loaded mice, independent experiments were performed in duplicate.

The stress was induced by forcing the mice to swim in a water basin (30 cm dia. × 30 cm height, 20 cm water depth) at 16°C ± 1°C for 5 min. Within 3 min

* Ro 15-1788, Ethyl 8-fluro-5,6-dihydro-5 methyl-6-oxo-^{4}H-imidazo [1, 5a] [1, 4] benzodiazepine-3-carboxylate.

after the mice were removed from the water, the tracer was injected.

Effect of swimming conditions (swimming duration and temperature)

Mice were forced to swim for 5 min at 15°, 25° and 37°C respectively, and then about 1 μCi of [^{3}H]Ro 15-1788 was injected within 3 min after swimming. Mice were also forced to swim for a period of 1, 2, 3, 5 and 10 min at 16°C, then about 1 μCi of the tracer was injected within 3 min after swimming. Biodistribution at 5 min after injection of the tracer was determined as described above.

Effect of injected dosage of carrier Ro 15-1788

Various dosage (carrier-free, 34 ng/kg, 0.1 μg/kg, 3 μg/kg, 30 μg/kg and 300 μg/kg of carrier-added) of [^{3}H]Ro 15-1788 were intravenously injected into control or forced-to-swim (16°C for 5 min) mice, and biodistribution at 5 min after injection of the tracer was determined.

Relative regional blood flow

About 1 μCi of [^{14}C]iodoantipyrine was intravenously injected into control and stress-loaded mice, and radioactivities at 1 min after injection were determined.

Stability of [^{3}H]Ro 15-1788 in the brain

About 5 μCi of [^{3}H]Ro 15-1788 (carrier-free) was injected into the tail vein of control or stress-loaded mice. At 30 min after injection, the mice were killed and brains were quickly removed. Each brain was homogenized with 1 mL of saline solution, and 0.2 mL of brain homogenate was sampled as a standard for the determination of extraction efficiency. One milligram of carrier Ro 15-1788 and 2 mL of dichloromethane were added into the rest of the brain homogenate, then radioactive materials were extracted. Extraction efficiency determined by comparison with a standard was more than 95%. Organic extractable materials were analyzed by thin layer chromatography (silicagel; methylene chloride:methanol, 9:1. and hexane:benzene:dioxane:ammonium hydroxide, 70:50:45:5).

Results

Biodistributions of [^{3}H]Ro 15-1788 in control mice

When carrier-free [^{3}H]Ro 15-1788 was administered alone, the tracer passed rapidly into the brain, and at 5 min after injection, the maximum peak of radioactivities in both blood and brain were observed as shown in Fig. 1A. There was a significant difference of radioactivity between each brain region, and the highest radioactivity was observed in the cerebral cortex which is the Bz receptor enriched area. The blood levels of the tracer were much lower than that observed in the brain, and rapidly declined as a single exponential curve with a half-life of about 10 min.

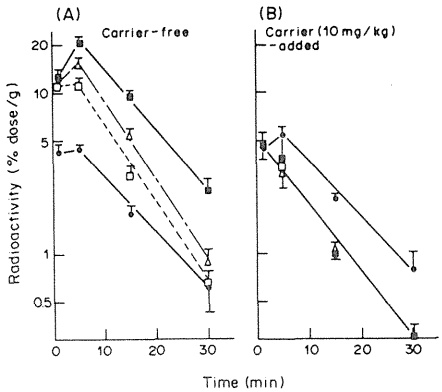

Fig. 1. Biodistributions of (A) carrier-free (0.011 nmol/mouse) or (B) carrier-added (10 mg/kg) [^{3}H]Ro 15-1788 in control mice after i.v. injection. Radioactivities in cerebral cortex (■——■), cerebellum (△—·—△), pons-medulla (□----□) and blood (●——●) were expressed as percentage dose administered per gram organ. Values are presented as average ±1 SD of three mice in each point.

Radioactivities in each brain region also rapidly decreased with almost the same half-life of blood activity, which indicated that *in vivo* distribution of this tracer rapidly reached the equilibrium state.

On the other hand, when the tracer was injected with a large amount of carrier Ro 15-1788, radioactivities in each brain region were lower than those in blood as shown in Fig. 1B. In addition, there was no significant difference of radioactivities between cerebral cortex, cerebellum and pons-medulla, in any experimental period, as shown in Fig. 1B.

Biodistribution of [^{3}H]Ro 15-1788 in stress-loaded mice

Both in the carrier-free and carrier-added state, the half-lives of blood levels were slightly higher in stress-loaded mice than those in the control group as shown in Figs 2A and B. Further significant changes in the biodistribution of carrier-free tracer were observed in stress-loaded mice, as shown in Figs 2A and 3A. Brain radioactivities increased over a period of 15 min after injection of tracer, while radioactivities in blood decreased. Moreover, the distribution pattern of radioactivity at 1 and 5 min after administration was greatly changed as compared with the control brains. Radioactivity in cerebral cortex was almost the same as that in cerebellum or pons-medulla at 5 min after injection. The reproducibility of the biodistribution of [^{3}H]Ro 15-1788 in stress-loaded mice was quite good as shown in Figs 2 and 3.

Effect of swimming conditions

The effect of swimming temperature on the biodistribution of carrier-free tracer is summarized in Table 1. A significant reduction of radioactivity in

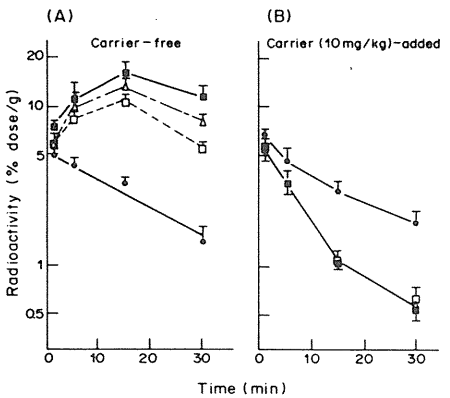

Fig. 2. Biodistributions of (A) carrier-free (0.011 nmol/mouse) or (B) carrier-added (10 mg/kg) [^{3}H]Ro 15-1788 in stress-loaded mice (forced to swim) after i.v. injection. The tracer was injected into mice within 3 min after having been forced to swim as described in the text. Radioactivities in cerebral cortex (■——■), cerebellum (△---△), pons-medulla (□---□) and blood (●——●) were expressed as percentage dose administered per gram organ. Values are presented as average ±1 SD of three mice in each point.

cerebral cortex was observed only when mice swam at 15°C. Moderate changes in biodistribution of [^{3}H]Ro 15-1788 were also observed in mice forced to swim at 25° and 37°C as compared with control mice. As shown in Fig. 4, drastic changes in radioactivity,

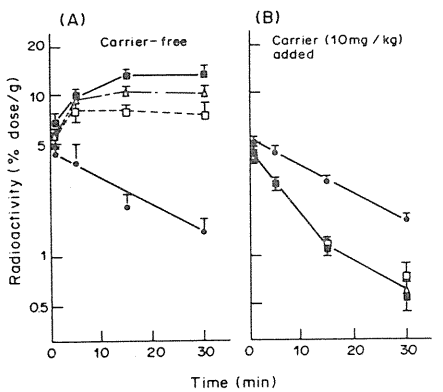

Fig. 3. Reproducibility of the biodistributions of [^{3}H]Ro 15-1788 in stress-loaded mice. Experimental conditions and presented values were as same as shown in Fig. 2.

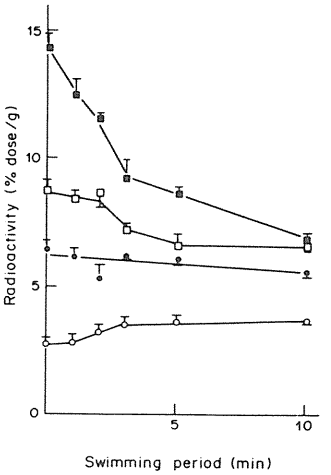

Fig. 4. Effect of swimming period on the biodistribution of [^{3}H]Ro 15-1788 at 5 min after i.v. injection of the tracer. Mice were forced to swim for various periods at 16°C as described in the text. Radioactivities in cerebral cortex (■——■), cerebellum (□——□), pons-medulla (●——●) and blood (○——○) were expressed as percentage dose administered per gram organ. Values are presented as average ±1 SD of three mice in each group.

Table 2. Biodistribution of [^{3}H]Ro 15-1788 at 5 min after injection with various dosage of carrier Ro 15-1788

Dose (μg/kg)		Radioactivity (% dose/g) Control	Stress-loaded*
0.034	Blood	3.74 ± 0.45	4.59 ± 0.32
	Cerebral cortex	15.6 ± 0.48	8.31 ± 0.86
	Cerebellum	13.5 ± 0.46	7.05 ± 0.47
	Pons-medulla	9.85 ± 0.59	6.71 ± 0.72
0.1	Blood	3.29 ± 0.31	4.06 ± 0.16
	Cerebral cortex	17.6 ± 1.0	7.49 ± 0.18
	Cerebellum	11.6 ± 0.8	6.89 ± 0.25
	Pons-medulla	8.65 ± 1.00	5.78 ± 0.35
3	Blood	3.00 ± 0.12	4.20 ± 0.16
	Cerebral cortex	12.5 ± 1.1	8.10 ± 0.50
	Cerebellum	7.63 ± 0.83	6.53 ± 0.20
	Pons-medulla	5.25 ± 0.48	5.31 ± 0.02
30	Blood	3.02 ± 0.16	4.40 ± 0.81
	Cerebral cortex	4.61 ± 0.63	5.18 ± 0.30
	Cerebellum	2.56 ± 0.32	3.53 ± 0.12
	Pons-medulla	2.26 ± 0.30	2.82 ± 0.45
300	Blood	3.25 ± 0.34	3.93 ± 0.39
	Cerebral cortex	1.73 ± 0.48	2.25 ± 0.09
	Cerebellum	1.38 ± 0.32	2.20 ± 0.23
	Pons-medulla	1.30 ± 0.54	1.87 ± 0.08

Three mice in each group; average ±1 SD.
* Mice were forced to swim for 5 min at 16°C.

Table 1. Effect of swimming temperature on the biodistribution of [^{3}H]Ro 15-1788

Temp. (°C)	% dose/g Blood	Cerebral cortex	Cerebellum	Pons-medulla
Control	2.94 ± 0.12	15.6 ± 0.78	11.2 ± 0.69	7.59 ± 0.20
15°C	3.30 ± 0.03	8.50 ± 1.46	7.64 ± 1.09	6.43 ± 0.57
25°C	3.42 ± 0.29	13.1 ± 0.4	9.44 ± 0.65	8.23 ± 1.42
37°C	2.99 ± 0.06	14.0 ± 0.8	9.83 ± 0.64	7.82 ± 1.08

Three mice in each group, average ± 1 SD.
Mice were forced to swim for 5 min at correspondent temperature.

Table 3. Radioactivities of [^{14}C]iodoantipyrine at 1 min after injection

	% Dose/g			
	Blood	Cortex	Cerebellum	Pons-medulla
Control	7.86 ± 0.78	5.91 ± 0.48	5.73 ± 0.14	5.62 ± 0.56
Forced-to-swim	9.53 ± 1.05	5.18 ± 0.32	6.34 ± 0.44	5.93 ± 0.33

Three mice in each group; average ± 1 SD.
Mice were forced to swim for 5 min at 16°C.

especially in the cerebral cortex, were observed according to the duration of swimming. Radioactivity in blood, cerebellum and pons-medulla was hardly changed compared with control, and 3 min of swimming was almost enough to produce a maximum change.

Effects of injected dosage of carrier Ro 15-1788

Radioactivities in blood, cerebral cortex, cerebellum and pons-medulla of control and stress-loaded mice (16°C for 5 min) under various loading dosages of carrier Ro 15-1788 are shown in Table 2. Radioactivities in each brain region decreased according to the increase of loading dosage both in control and stress-loaded mice, whereas radioactivities in blood were not significantly changed by loading carrier Ro 15-1788.

Relative regional blood flow determined by [^{14}C]iodoantipyrine

Radioactivities in blood, cerebral cortex, cerebellum and pons-medulla of stress-loaded mice at 1 min after injection of [^{14}C]iodoantipyrine hardly differed from that of control mice as shown in Table 3.

Stability of [^{3}H]Ro 15-1788 in the brain

Thin-layer chromatographic analysis of radioactive materials in the brain of control and stress-loaded mice were performed, and the results are shown in Fig. 5. Almost all radioactivities were due to unmetabolized [^{3}H]Ro 15-1788 itself both in control and stress-loaded mouse.

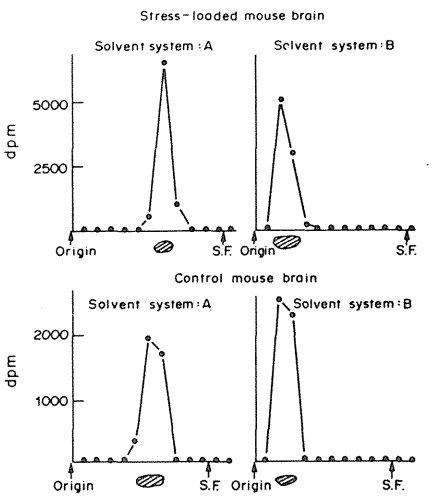

Fig. 5. Thin-layer chromatograms of radioactive materials in the brain removed at 30 min after injection of carrier-free (5 μCi, 0.055 nmol) [^{3}H]Ro 15-1788 into control or stress-loaded mice. ▨: Cold Ro-1788 detected by u.v. lump. Solvent system: A—methylene chloride–methanol; 9–1. B—hexane–benzene–dioxane–ammonium hydroxide; 70–50–45–5.

Discussion

First, we evaluated the *in vivo* stability of [^{3}H]Ro 15-1788 after i.v. injection, and found that it was quite stable in the brain for at least 30 min. However, there remained some possibility that water-soluble metabolites which cannot pass through the blood-brain barrier were present in peripheral tissues and in the blood. Since more than 95% of radioactivities observed in the brain were due to [^{3}H]Ro 15-1788 itself, we performed a simplified estimation of the *in vivo* specific binding of this tracer with Bz receptor from data obtained in these experiments, and the result is summarized in Table 4. The brain radioactivities observed after administration of the tracer with a large amount of carrier ligand were due to the nonspecific binding plus free ligand in the brain. The specific binding in each brain region could be estimated by the subtraction of radioactivity of carrier-added state from carrier-free state. In the control group, the specific binding of this tracer was largest in the cerebral cortex, next in the cerebellum and least in the pons-medulla. This *in vivo* distribution pattern of specific binding was very consistent

Table 4. Specific binding of [^{3}H]Ro 15-1788 (% dose/g)

Time	1 min	5 min	15 min	30 min
Control				
Cortex	8.18	16.9	8.07	2.19
Cerebellum	7.13	12.8	4.00	0.60
Pons-medulla	6.48	7.77	2.07	0.36
	(4.20)*	(4.56)	(1.78)	(0.64)
Stress-loaded-A				
Cortex	1.86	7.54	12.9	11.2
Cerebellum	0	6.39	11.8	7.46
Pons-medulla	0.13	4.92	9.49	4.84
	(4.91)	(4.15)	(3.31)	(1.45)
Stress-loaded-B				
Cortex	2.35	7.06	12.3	12.9
Cerebellum	1.23	6.58	9.41	9.28
Pons-medulla	1.13	5.25	7.13	6.69
	(4.41)	(3.96)	(2.08)	(1.47)

Each value of specific binding was calculated by subtraction of radioactivities in the carrier-added state from that in the carrier-free state as described in the text. Values are average of three mice in each group;
( )*: radioactivities in the blood.

with Bz receptor distribution in the brain reported previously.[12] In addition, because of low levels of nonspecific binding and free ligand in the brain, total radioactivity observed in carrier-free tracer seemed to be almost the same as the specific binding. Therefore, [^{11}C]Ro 15-1788, instead of ^{3}H-labeled ligand, may be a useful tool for the *in vivo* visualization of human brain Bz receptor distribution using positron emission CT.

The most important and interesting result of this study was that significantly different distribution of carrier-free tracer was observed in stress-loaded mice. Indeed, even in carrier-added state, slight change in half-lives of radioactivities in both blood and brain was observed. This slight change might be caused by alterations in some physiological functions such as renal clearance rate or metabolic degradation rate of the tracer. However, changes in biodistribution of carrier-free tracer were much more drastic compared with the carrier-added state. Brain radioactivities increased for a 15 min period following injection of carrier-free tracer, while brain radioactivities of carrier-added tracer decreased. These alterations seemed not to be due to such changes in physiological functions, but to changes in Bz receptor function in the brain, association or dissociation rate, or numbers of Bz receptor binding sites available. Changes in the specific binding of [^{3}H]Ro 15-1788 in stress-loaded mice as shown in Table 4, together with relatively unchanged blood levels of the tracer compared with control mice, strongly suggested that *in vivo* binding availability of Bz receptor, especially in the cerebral cortex, was rapidly reduced by acute stress, and reversibly recovered after the mice were removed from the water. In addition, relative regional blood flow determined by [^{14}C]iodoantipyrine did not differ between control and stress-loaded mice as shown in Table 3, which strongly supported the above speculation. The degree of these alterations in biodistribution was very dependent upon the stressful conditions as shown in Table 2 and Fig. 4.

In control mice, half-lives of radioactivities in the blood and each brain region were almost the same, which indicated that biodistribution of this tracer would reach an equilibrium state even at an early period after systematic administration. Under an equilibrium state, the specific binding of the ligand with receptor is expressed as the following equation;

$$X/F = K \cdot (B_{max} - X)$$

where X = specific binding, F = free ligand concentration, B_{max} = maximum number of binding site and K = affinity constant. When the X value is much smaller than B_{max} value, X/F value will reach the constant value (binding availability, $\alpha = K \cdot B_{max}$). Then, in the case of using a very high-specific radioactive ligand, this X/F value is almost the same as the binding availability (α). The free ligand concentration in the brain seemed to parallel that in the blood, because high lipophilic ligand can freely pass through the blood-brain barrier. We estimated *in vivo* specific binding of [^{3}H]Ro 15-1788 at various injected dosages of carrier by subtraction, and performed the Scatchard analysis as shown in Fig. 6. As the free ligand concentration in the brain could be assumed to be parallel to that in the blood, we used the ligand concentration in the blood estimated from radioactivities instead of free ligand concentration. Though several problems remained in this simplified analysis, it might be useful to clarify what kinds of change occured in brain Bz receptor function by acute stress. The results strongly suggested that these rapid alterations were mainly due to changes in binding kinetics, not in the numbers of binding sites available. One possible mechanism is the competitive inhibition of binding by endogeneous ligand or inhibitor.

We also investigated whether such alterations in *in vivo* binding kinetics of Bz agonists with Bz receptor were observed by inducing acute stress. However, as the *in vivo* specific binding of [^{3}H]flunitrazepam was very low (less than 30% of total radioactivity observed in the cerebral cortex at 5 min after injection of the tracer), we could not determine this. As previously reported,[12] the affinity constant of Bz agonists was significantly reduced by increasing the temperature, therefore a more specific radiolabeled agonist with high K value at 37°C should be developed for *in vivo* study of interaction between Bz agonist and Bz receptor.

Medina *et al.*[3] recently reported that using *in vitro* binding assay Bz receptor in the cerebral cortex and hippocampal formation of rat brains rapidly and reversibly decreased following forced swimming, and the rebound in numbers of Bz receptor binding sites at 1 h after stress-loading was observed.[3] In addition, Soubrie *et al.*[5] reported the decreased convulsant potency of picrotoxine and pentylentetrazol and enhanced [^{3}H]flunitrazepam binding following stressful manipulation in rat. An increase in cortical [^{3}H]diazepam binding *in vivo* following the witnessing of another rat being killed was also reported.[4] These observations strongly suggest that brain Bz receptor function is capable of alteration by physiological

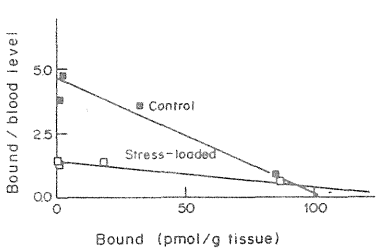

Fig. 6. Scatchard plots of *in vivo* binding of [^{3}H]Ro 15-1788 with cerebral cortex of control and stress-loaded mice. Mice were forced to swim for 5 min at 16°C. *In vivo* specific bindings were estimated by subtraction of correspondent radioactivities observed in carrier (300 μg/kg) added-state.

stimuli. Our results obtained in these experiments were very consistent with the above observations. However, Fur *et al.* found no significant difference of brain Bz receptor function (K_d or B_{max}) between controls and rats forced to swim.[13] These discrepancies seem to be caused by different experimental conditions, such as stressful conditions or tissue preparation method.

Even though the mechanism of these rapid and reversible changes in Bz receptor by acute stress is not clear, these changes seem to have an important role in physiological function. In some kinds of central nervous disorders such as schizopherenia, responsiveness to stress was reported to be abnormal.[14] Therefore, the positron emission tomographic study using [^{11}C]Ro 15-1788 may be valuable in finding some difference in central nervous system function to the stress in such psychiatric disorders, and we have just begun a clinical investigation into this.

Acknowledgements—The authors wish to thank Dr Y. Kashida and Dr Y. Tateno for fruitful discussions. Special thanks are also given to Roche Japan for the kind offer of Ro 15-1788.

References

1. Bliss E. L., Ailion J. and Zwanziger J. *J. Pharmac. Exp. Ther.* **164,** 122 (1968).
2. Kathryn H. D. and Wolfgang H. V. *J. Pharmac. Exp. Ther.* **223,** 348 (1982).
3. Medina J. H., Novas M. L. and Robertis E. D. *Eur. J. Pharmac.* **96,** 181 (1983).
4. Nutt D. J. and Minchin M. C. W. *J. Neurochem.* **41,** 1513 (1983).
5. Soubrie P., Thiebot M. H., Jobert A., Montastruc J. L., Hery F. and Hamon M. *Brain Res.* **189,** 505 (1980).
6. Comar D., Maziere M., Godot J. M., Berger G., Soussaline F., Menini Ch., Arfel G. and Naquet R. *Nature* **280,** 329 (1979).
7. Mintun M., Wooten G. F. and Raichle M. E. *Nuclear Medicine and Biology; Proc. 3rd World Congr. Nuclear Medicine and Biology II.* pp. 2208–2211. (Pergamon Press, Paris, 1982).
8. Wagner H. N., Burn H. D., Dannals R. F., Wong D. F., Längström B., Duelfer T., Frost J. J., Revert H. T. Links J. M., Rosenbloom L. S., Lukas S. E., Kramer A. V. and Kuhar M. J. *Science* **221,** 1264 (1983).
9. Maziere M., Premant C., Sastre J., Crouzel M., Comar D., Hantrage P., Kaijima M., Guilbert B. and Narquet R. *C.R. Acad. Sci. (Paris) Serie III* **296,** 871 (1983).
10. Maziere M., Hantraye P., Prenant C., Satre J. and Comar D. *Int. J. Appl. Radiat. Isot.* **35,** 973 (1984).
11. Ehrine E., Johnström P., Stone-Elander S., Willsson J. L. G., Paulis T. D., Farde L., Greitz T., Litton J. E., Persson A., Sedvall G. and Winden L. *J. Labelled Compd. Radiopharm.* **21,** 1161 (1984).
12. Möhler H. and Richards J. G. *Nature* **294,** 763 (1981).
13. Fur G. L., Guilloux F., Mitrani N., Mizoule J. and Uzan A. *J. Pharmac. Exp. Ther.* **211,** 305 (1979).
14. Rubin L. S. and Barry T. J. *Biol. Psychiat.* **5,** 181 (1972).

Int. J. Appl. Radiat. Isot. Vol. 36, No. 7, pp. 555–560, 1985
Printed in Great Britain

0020-708X/85 $3.00 + 0.00
Pergamon Press Ltd

Preparation of ^{13}N-β-phenethylamine*

TOSHIYOSHI TOMINAGA,[1] OSAMU INOUE,[2] TOSHIAKI IRIE[2]
KAZUTOSHI SUZUKI,[2] TOSHIO YAMASAKI[2] and MASAAKI HIROBE[1]

[1]Faculty of Pharmaceutical Sciences, University of Tokyo, 7-3-1 Hongo, Bunkyo-ku, Tokyo, 113, Japan and [2]Division of Clinical Research, National Institute of Radiological Sciences, 9-1 Anagawa-4-chome, Chiba-shi(Chiba), 260, Japan

(*Received* 12 *December* 1984; *in revised form* 16 *January* 1985)

Nitrogen-13-labelled β-phenethylamine([^{13}N]PEA) was synthesized by Hofmann rearrangement of [^{13}N]phenylpropionamide prepared from phenylpropionyl chloride and aqueous [^{13}N]ammonia solution. The reaction proceeded rapidly with a fairly good yield. [^{13}N]PEA was isolated using preparative thin-layer chromatography, and organ distribution in mice was studied preliminarily. After i.v. administration of [^{13}N]PEA, high accumulation and long-term retention of the radioactivity were observed in the brain and the heart.

Introduction

As previously reported, we have been developing a rapid preparation method of ^{13}N-labelled compounds using [^{13}N]ammonia aqueous solution as a precursor. We have already labelled a ^{13}N-amide ([^{13}N]nicotinamide) and nucleoside ([^{13}N]adenosine).[1] Since amines play very important roles in physiological functions as neurotransmitters and neuromodulators, synthesizing ^{13}N-labelled amines is of great significance for visualization of their biodisposition in live animals or human.

Nitrogen-13 labelling of amphetamine via imine from [^{13}N]ammonia has been reported. However, both the radiochemical yield and the specific activity were very low (3.5%, 8 Ci/mol, respectively).[2] We selected β-phenethylamine(PEA), which is an important neuromodulator, as a target compound and investigated its ^{13}N-labelling in the following route:

$$\mathrm{Ph(CH_2)_2COCl} \xrightarrow{^{13}NH_3} \mathrm{Ph(CH_2)_2CO^{13}NH_2} \xrightarrow{NaOBr} \mathrm{Ph(CH_2)_2\,^{13}NH_2}$$

We succeeded in the synthesis of [^{13}N]PEA in a fair yield even in a non-carrier-added state.

[^{13}N]PEA is supposed to be rapidly transferred to tissues after administration and oxidized into phenylacetic acid and $^{13}NH_3$, which is expected to be metabolically trapped. In order to confirm this, we also studied organ distribution of [^{13}N]PEA in mice.

In this paper we present the synthesis and the preliminary organ distribution study of [^{13}N]PEA.

Materials and Methods

1. *Materials*

Phenylpropionyl chloride, PEA and other chemicals were obtained from Wako Pure Chemical Industries Ltd (Tokyo, Japan). Phenylpropionamide (PAA) was synthesized from phenylpropionyl chloride and ammonia in our laboratory.

2. *Preparation of ^{13}N-ammonia*

The aqueous solution of [^{13}N]ammonia was prepared according to the method of Suzuki *et al.*;[3] briefly, proton-irradiated water was introduced into a reduction flask containing Devarda's alloy (100 mg) and sodium hydroxide (200 mg), and the radiolabelled ammonia was distilled in a stream of helium and collected in water.

3. *Labelling procedure*

The procedure is presented schematically in Fig. 1.

(*a*) *Synthesis of* [^{13}*N*]*phenylpropionamide* ([^{13}*N*]*PPA*). To 1 mL of $^{13}NH_3$-containing water, carrier ammonia (except for non-carrier-added synthesis), sodium hydroxide (1 mmol), and phenylpropionyl chloride (127 μmol) were added, and the reaction mixture was stirred vigorously for 30 s. The radiochemical yield was determined by thin-layer chromatography (TLC, silica gel, acetone).

(*b*) *Synthesis of* [^{13}*N*]*PEA*. To the reaction mixture of [^{13}N]PPA, sodium hypobromite (Table 2 shows the amount) was added and the mixture was heated on a boiling water bath for 5 min. After cooling, the mixture was extracted with 2 mL of water-saturated

* A preliminary report of this work was presented at the Fifth International Symposium on Radiopharmaceutical Chemistry, Tokyo, Japan, 9–13 July 1984. All correspondence should be addressed to National Institute of Radiological Sciences.

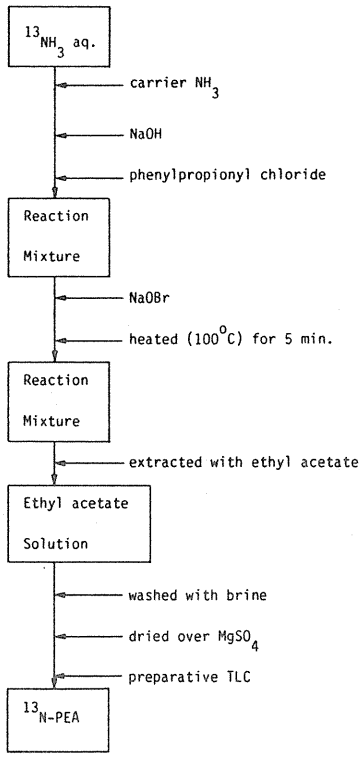

Fig. 1. Labelling procedure of [^{13}N]PEA.

ethyl acetate. The radiochemical yield was estimated from the extraction efficiency (fraction of the radioactivity extracted to the total activity) and the radiochemical purity of the extract determined by TLC [silica gel, chloroform:methanol (2:1)]. [^{13}N]PEA was purified from this extract by preparative TLC [silica gel, chloroform:methanol (2:1)].

4. *Identification of* [^{13}*N*]*PEA*

[^{13}N]PEA was identified with high performance liquid chromatography [HPLC, adsorbent, Finepak C-18 (JASCO), solvent, methanol:water (9:1)], and TLC using three solvent systems [silica gel, (A) chloroform–methanol (2:1), (B) acetone–water–14N-aqueous ammonia solution (2:1:0.1), (C) methanol–10%ammonium acetate (1:1)].

5. *Organ distribution of* [^{13}*N*]*PEA in mice*

The saline solution of [^{13}N]PEA was prepared in a carrier (50 μmol)-added state according to the method described above. [^{13}N]PEA (30 μCi, about 0.08 μmol) in 0.2 mL of saline was injected into tail veins of male ddy mice (13 weeks, about 40 g). After given time intervals, the animals were killed, the organs removed, weighed and counted in a well-scintillation counter ([NaI(Tl)].

Table 1. Labelling efficiency of [^{13}N]phenylpropionamide ([^{13}N]PPA)

Effect of NaOH*		Effect of carrier NH_3†	
NaOH (μmol)	Yield (%)	NH_3 (μmol)	Yield (%)
10	37	0	50
100	39	10	58
500	44	20	44
1000	56	50	54
2000	71	100	54

Labelling yield was determined by TLC as described in the text. Reaction conditions:
*Carrier NH_3 20 μmol, phenylpropionyl chloride 127 μmol, total volume 1 mL, room temperature, 1 min.
†NaOH 500 μmol, phenylpropionyl chloride 127 μmol, total volume 1 mL, room temperature 1 min.

Results

The effect of varying amounts of NaOH and carrier ammonia on the labelling yield of [^{13}N]PPA is shown in Table 1. [^{13}N]PPA was obtained in a very high yield (about 70%) even in a non-carrier-added state, and the labelling yield was mainly affected by the amount of NaOH.

[^{13}N]PEA was synthesized without isolating the intermediate amide in a short period (8–10 min). The labelling yield of [^{13}N]PEA was affected by the amount of carrier ammonia and sodium hypobromite as shown in Table 2. Under optimal conditions, it was obtained in a high yield (50%), but in a non-carrier-added state, the yield was lower (5%). The labelled [^{13}N]PEA was identified by HPLC (Fig. 3) and TLC (Fig. 2). The radiochemical purity of [^{13}N]PEA separated for organ distribution study was more than 90%.

The organ distribution of [^{13}N]PEA in mice is summarized in Table 3. [^{13}N]PEA rapidly transferred to the brain and the heart after intravenous injection, and the radioactivity in both organs remained for a long period.

Discussion

1. *Synthesis of* [^{13}*N*]*PEA*

The labelling yield of [^{13}N]PPA was much higher than that of [^{13}N]nicotinamide (about 25%, in Ref. 1). This may be attributed to differences in stability in water and reactivity of the acid chlorides. By using organic solution of [^{13}N]ammonia as a precursor, both amides are expected to be obtained in much higher yields.

Table 2. Labelling efficiency of [^{13}N]β-phenethylamine ([^{13}N]PEA)

Carrier NH_3 (μmol)	NaOBr (μmol)	Yield (%)
0	5	5
10	20	32
50	20	15
50	100	50
50	200	25
50	400	0

Labelling efficiency was determined by TLC as described in the text.
Reaction conditions: phenylpropionyl chloride 60 μmol, total volume 1 mL, 100 C, 5 min (Hofmann reaction).

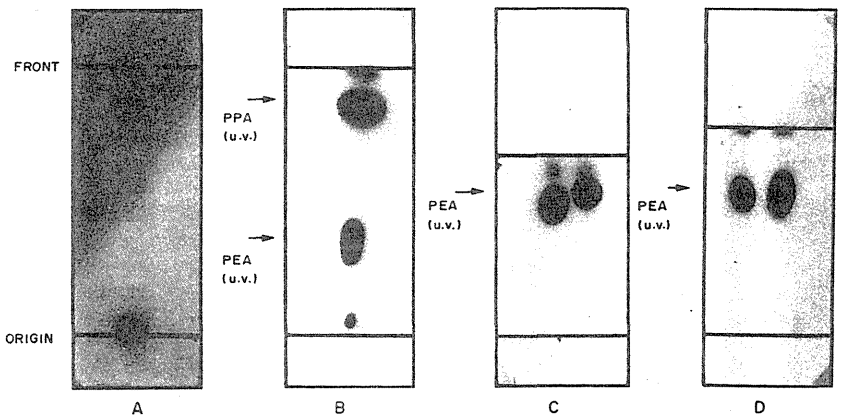

Fig. 2. TLC of $^{13}NH_3$, [^{13}N]PEA, and [^{13}N]PPA. A: $^{13}NH_3$, B: [^{13}N]PEA and [^{13}N]PPA, C, D: [^{13}N]PEA with (left) or without (right) carrier PEA. Plates: silica gel. Solvent system: chloroform:methanol (2:1) (A, B), 10% ammonium acetate:methanol (1:1) (C), acetone:water:14N-aqueous ammonia solution (2:1:0.1) (D).

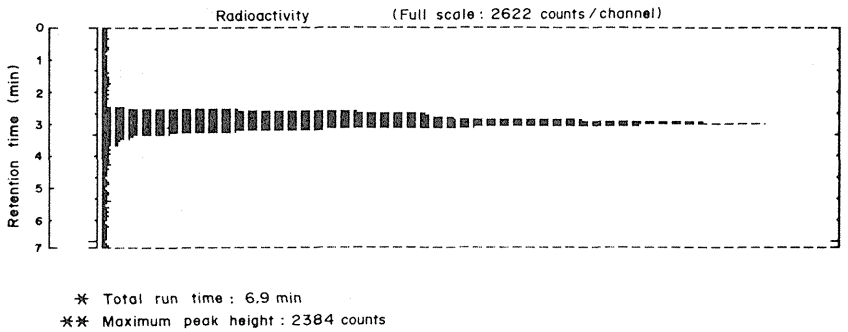

Fig. 3. HPLC of [^{13}N]PEA. *Conditions*; column: Finepak C-18 (JASCO), solvent: methanol:water (9:1), 2 mL/min. *Retention time*; [^{13}N]PEA (3.0 min), [^{13}N]PPA (2.6 min), $^{13}NH_3$ (>5.0 min).

Regarding the reaction time and yield, the Hofmann reaction was found to be more suitable as a labelling reaction than the reduction of imine.[2] Since the ratio of sodium hypobromite to amide generally affects the yield of amine and the amounts of by-products,[4] excess amounts of sodium hypobromite should not be added in order to avoid side reactions in the labelling. The lower yield in a non-carrier-added state may partly be attributed to the excess sodium hypobromite.

Under optimal conditions, about 400 mCi of [^{13}N]ammonia is obtainable with the cyclotron in our institute. Accordingly, sufficient amounts of [^{13}N]PEA can be prepared for practical use even in a non-carrier-added state using HPLC separation method.

This reaction is considered to be applicable for the labelling of other amines. We already synthesized [^{13}N]benzylamine in a similar way.

2. *Organ distribution of* [^{13}N]*PEA*

Phenethylamine (PEA), an endogenous amine that resembles amphetamine both structurally and pharmacologically, plays an important role as a neuromodulator in the central nervous system. Alterations in its biosynthesis and metabolism are presumed under profound stress[5] and in mental diseases.[6]

The synthesis and preliminary organ distribution of [^{11}C]PEA have been reported.[7] The radioactivity of intravenously injected [^{11}C]PEA was shown to be incorporated rapidly into the brain and then to decrease also rapidly from it.

On the other hand, after administration of [^{13}N]PEA, the radioactivity was retained at the brain and the heart as shown in Table 3. This long-term retention of radioactivity suggests that [^{13}N]PEA is deaminated by mitochondrial monoamine oxidase

Table 3. Organ distribution of [^{13}N]PEA in mice*: %dose/g organ

Organ	Time after i.v. injection (min)			
	1	10	20	30
Blood	2.24 ± 0.46	1.46 ± 0.04	1.47 ± 0.12	1.41 ± 0.13
Liver	2.89 ± 0.34	4.44 ± 0.30	4.74 ± 0.75	3.77 ± 0.47
Heart	7.90 ± 1.58	8.17 ± 0.47	6.73 ± 1.58	6.15 ± 0.80
Lung	9.07 ± 1.91	2.95 ± 0.14	2.94 ± 1.15	2.15 ± 0.56
Brain	3.66 ± 0.30	4.05 ± 0.40	3.48 ± 0.91	3.89 ± 0.49

*Male ddy mice (13 weeks, about 40 g), average ± 1 st SD.

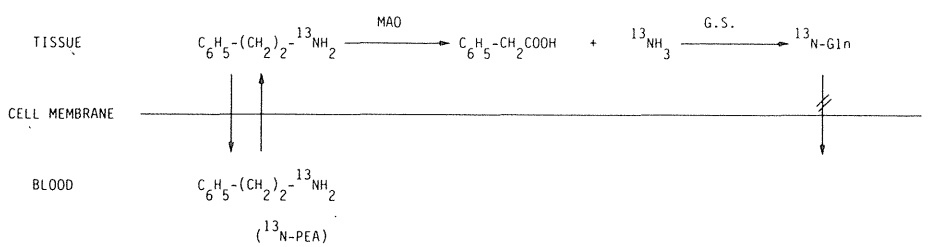

Fig. 4. Mechanism of metabolic trapping of [^{13}N]PEA. G.S.: glutamine synthetase, Gln: glutamine.

(MAO) and metabolically trapped in the form of [^{13}N]glutamine. The hypothetical scheme of biotransformation of [^{13}N]PEA is shown in Fig. 4.

Thus, the combination of [^{13}N]PEA and [^{11}C]PEA can be expected to contribute greatly to clarify the distribution and the metabolism of PEA in live animals including humans.

References

1. Irie T., Inoue O., Tominaga T., Suzuki K. and Yamasaki T. Abs. 5th. Int. Symp. on Radiopharmaceutical Chem. 263 (1984) *Int. J. Appl. Radiat. Isot.* In press.
2. Finn R. D., Christmann D. R. and Wolf A. P. *J. Labelled. Compd. Radiopharm.* **18,** 909 (1980).
3. Suzuki K. and Tamate K. *Int. J. Appl. Radiat. Isot.* **35,** 771 (1984).
4. Wallis E. S. and Lane J. F. *Organic Reaction* Vol. 3, p. 267 (John Wiley, New York, 1967).
5. Paulos M. E. and Tessel R. E. *Science* **215,** 1127 (1982).
6. Potkin S. G., Karoum F., Chuang L., Cannon-Spoor H. E., Phillips I. and Wyatt R. J. *Science* **206,** 470 (1979).
7. Jay M., Chaney J. E. and Digenis G. A. *Int. J. Appl. Radiat. Isot.* **32,** 345 (1981); Jay M. J. *Diss. Abstr. Int. B* **41,** 3794 (1981).

Int. J. Appl. Radiat. Isot. Vol. 36, No. 12, pp. 971–976, 1985
Printed in Great Britain.

0020-708X/85 $3.00 + 0.00

Computer-Controlled Large Scale Production of High Specific Activity [^{11}C]RO 15-1788 for PET Studies of Benzodiazepine Receptors

K. SUZUKI, O. INOUE, K. HASHIMOTO, T. YAMASAKI, M. KUCHIKI and K. TAMATE

National Institute of Radiological Sciences, 9-1, Anagawa-4-Chome, Chiba-Shi, 260, Japan

(*Received* 20 *May* 1985)

Ethyl 8-fluoro-5,6-dihydro-5-[^{11}C]methyl-6-oxo-4H-imidazo [1,5-a][1,4]benzodiazepine-3-carboxylate ([^{11}C]RO 15-1788) has been prepared automatically with high specific activity for *in vivo* visualization or quantitative analysis of brain benzodiazepine receptors. The yield, radiochemical yield, radiochemical purity and specific activity of the product ready for an i.v. injection were 276 ± 76 mCi, 50.8 ± 7.8%, 99.3 ± 0.3% and 2.9 ± 0.5 Ci/μmol, respectively, taking an average of the latest 3 runs. The time required was about 25 min. Each product was sufficient to carry out three successive clinical studies by positron emission tomography (PET). All the procedures other than evaporation and filtration at the final stage were carried out with specially designed equipment connected to a central control system for radioisotope production.

Introduction

The study of neuro-receptors with radiopharmaceuticals labeled with short-lived, positron-emitting radionuclides such as ^{11}C ($t_{1/2}$ = 20.4 min) and ^{18}F($t_{1/2}$ = 109.8 min) is a rapidly expanding area of investigation.[1–5] For this application it is important to obtain i.v. injectable radioligands with high specific activity since the binding capacity of the receptors with ligand is limited and the amount of carrier injected should be minimized to decrease pharmacological effects. For multiple clinical studies with the radioligand solution to be possible high activities must be prepared at the same time since in many cases the apparatus is contaminated after a production run and it takes a long time to start the next run, as is the case in $^{11}CH_3I$ preparation. Automatic production is important for the routine production of radiopharmaceuticals in order to lessen the radiation dose to the operators.

RO 15-1788 is known to be a benzodiazepine-receptor antagonist. The ^{11}C-labelled compound has already been synthesized by methylation of the nor compound with $^{11}CH_3I$[6,7] and its suitability for *in vivo* studies has been also evaluated.[6]

We have modified the previously reported procedure which involves methylation of the nor compound with $^{11}CH_3I$ and have developed computer-controlled equipment for large scale production, yielding an aqueous solution of [^{11}C]RO 15-1788 in high specific activity for i.v. injection.

Equipment

The equipment was designed to carry out the following processes automatically: leak check of the system; drying the production apparatus by heating reaction vessels and a CuO column under a pure nitrogen gas flow; loading nitrogen gas into the target box (14 kg/cm^2); successive conversion of the generated ^{11}C to $^{11}CO_2 \rightarrow {}^{11}CH_3OH \rightarrow {}^{11}CH_3I \rightarrow$ [^{11}C]RO 15-1788; purification of [^{11}C]RO 15-1788 by high performance liquid chromatography.

The apparatus for the production of [^{11}C]RO 15-1788 is shown in Fig. 1. It consists of a main part, the radioactivity flow line and an auxiliary part, a compressed air line, to actuate the system.

In the main part the components are connected by means of fine SUS-316 tubing (o.d. 1/16 in., i.d. 0.5 mm, from N_2 gas inlet to V4) and Teflon tubing (o.d. 3 mm, i.d. 2 mm, elsewhere to minimise dead volume). V1, V2, P1 and the target box are located closely since the pressure in this area is especially high (14 kg/cm^2). The reaction vessels are designed for minimum volume (≈10 mL). The solvent reservoir is for injecting the reaction mixture into the HPLC system and is useful for preventing problems from air bubbles. The photo sensor is to control the solvent volume in the reservoir in order to reduce diffusion of the sample in the solvent and to achieve good separation. The eluent from the column is monitored by a flow through radioactivity monitor (RS3) and u.v. The radioactive waste gas not absorbed on a

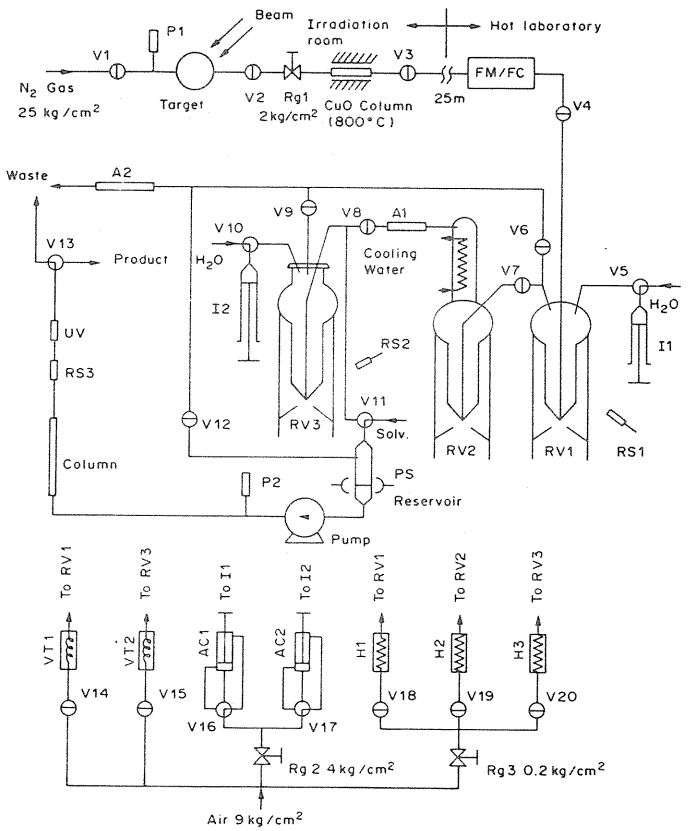

Fig. 1. Schematic diagram of the apparatus for the automatic production of [^{11}C]RO 15-1788 V1-V20; electric valves, RV1-RV3; reaction vessels connected to standardized attachments with cooling, heating and temperature measuring devices, P1 and P2; pressure transducers, Rg1-Rg3; pressure regulators, FM/FC; flow sensor/controller, I1 and I2; syringes for water injection, AC1 and AC2; air cylinder, H1-H3; heaters, VT1 and VT2; Vortex tubes for cooling, RS1-RS3; radioactivity sensors, PS; photosensor, u.v.; detector for u.v. absorption, A1; absorber (Askalite/P_2O_5), A2; absorber (Molecular Sieve 5A).

Molecular Sieve 5A is led to a storage tank (≈ 10 m^3) for decay.

In the auxiliary part, compressed air (9 kg/cm^2) is delivered to cooling devices (9 kg/cm^2, Vortex tube, Vortec Co., U.S.A.), heating devices (0.2 kg/cm^2, cylindrical heater) and air cylinders (4 kg/cm^2). Standardized fittings are used to attach the cooling, heating and measuring (thermocouple, etc.) devices to the reaction vessels, and temperatures between -15°C and 300°C are attained and controlled. Water injection into a reaction vessel is carried out with a syringe coupled to an air cylinder and a three-way electric valve. These cooling, heating and injection devices are all air-operated and suitable for compact assembling of components in a small box.

All the components are switched automatically by signals from radioactivity sensors, pressure transducers, flow sensors, thermocouples, photo sensors and a timer.

The equipment is controlled by the central system which is composed of a 16 bit computer (HP 9816), interfaced with its own CPU and many I/O ports (d.c. 24 V output; 305 channels, a.c. 100 V output; 175 channels, digital input (contact); 120 channels, analogue input 0–1 V; 128 channels, analogue output 0–10 V; 16 channels). It is able to control a maximum of five independent systems in parallel. A fundamental program is written in a HP Basic language and fixed. The control program for each system is given in a tabular form for the ease of development and modification, as shown in Table 1. Fairly complicated procedures can be controlled since up to six tables with 100 step program lines are available for individual equipment and many kinds of commands such as DO, AI and AO can be used. Step numbers can be changed according to the results obtained from AI, DI, TM, BR and US commands.

Figure 2 shows the target box which is constructed of aluminum. The inner shape (length 150 mm, inlet aperture 20 mm, outlet aperture 30 mm, volume

Table 1. An example of a table for a control program

Step	Command	Auxiliary Command	Branch	Parameter	Channels 1, 2, 3, ———, 8
1	AI	DS, LM, etc.	20	120	13, 24, ———————
(Analogue data input, scaling, jump to specified step if the condition is satisfied.)					
2	BS				5, 8, 13, ———————
(Set present analogue data of selected channels as background.)					
3	AO	——, DS		2500	5, 10, ———————
(Analogue data output and scaling for selected channels.)					
4	DI	——, DS	15	0 or 1	7, 3, 89, ———————
(Jump to specified step according to 'AND' or 'OR' conditions of digital input for the selected channels.)					
5	DO	——, DS		0 or 1	6, 35, 7, 15, ——
(Output DC 24 V or AC 100 V to the selected channels.)					
6	TM	——, SE	70	130	
(Set timer and jump to specified step when time is up)					
7	BR	——, CL	10	3	
(Jump to specified step for a given number of repetitions.)					
8	US		25	70	
(Subroutine command for more complicated control.)					
9	PA				
(Pause program execution of the present table for user's intervention. Other program execution is not affected.)					
10	NX			3	
(Jump to the first step of specified table.)					
——	——	——	——	——	——, ——, ———
——	——	——	——	——	——, ——, ———
——	——	——	——	——	——, ——, ———
100	——	——	——	——	——, ——, ———

75 mL) is conical to compensate for beam broadening by scattering in the aluminum foil and the target gas.[8] A metallic seal was used instead of a rubber "O" ring, because rubber would be decomposed by radiation during the irradiation. When the target box was first brought into use it was previously washed in acetone with an ultrasonic cleaner and dried in an oven at 250°C for 12 h.

Materials and Methods

Preparation of a THF solution of $LiAlH_4$

An apparatus distilling THF was constructed as shown in Fig. 3. An inert atmosphere was obtained by repeatedly filling the apparatus with nitrogen and evacuating it after the loading of THF and LAH($LiAlH_4$) into the flask. THF was distilled into a sealed vial containing a LAH pellet (Fluka Chemical Corp.) under a nitrogen atmosphere. One millilitre of the above THF solution saturated with LAH was diluted with 20 mL of pure THF which had been distilled into a vial not containing LAH and stored in a freezer.

Preparatory procedures and irradiation

Before irradiation the apparatus shown in Fig. 1 was dried by heating the CuO column (at 800°C), RV1, RV2 and RV3 (at 120°C) under a flow of pure

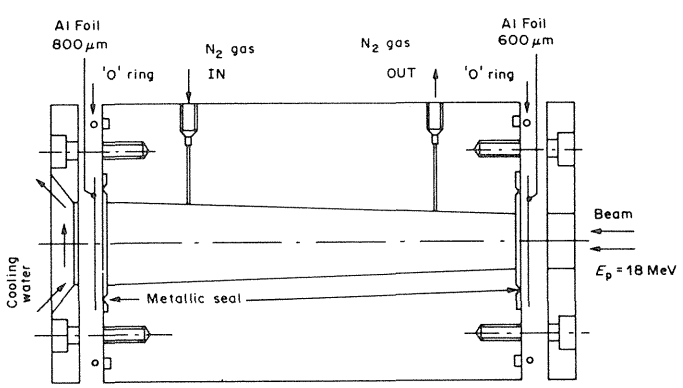

Fig. 2. Diagram of the target box. The inner surface is entirely of metal (Al) and the gas line connectors were designed for minimum volume.

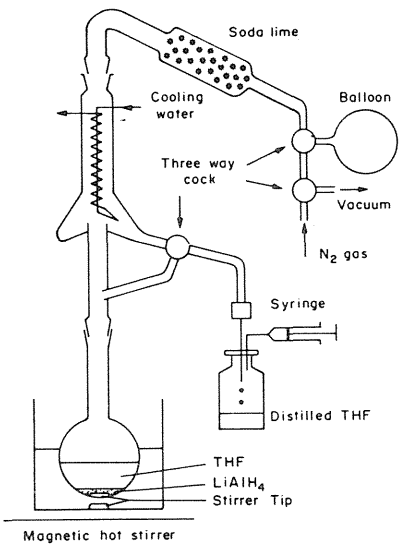

Fig. 3. Apparatus for THF distillation.

nitrogen (500 mL/min, purity >99.9998%, CO <0.5 ppm, CO_2 < 0.1 ppm) for 1–2 h. The target box (150 mm length, 14 kg/cm^2) was filled with pure nitrogen and irradiated by 18 MeV protons (14.2 MeV after 600 μmAl foil) from the NIRS AVF cyclotron at 16–20 μA for 32–48 min. The proton bean was focussed with a collimator (i.d. 10 mm, length 30 mm, Al).

During the irradiation, reagents were added into the individual reaction vessels (RV1: 1 mL THF solution of $LiAlH_4$, RV2: 1 mL of hydroiodic acid, RV3: 0.5 mL of DMF solution containing 1 mg RO 15-5528(nor-RO 15-1788) and *ca.* 0.9 mg NaH) and the HPLC line (column, pump, tube etc.) was washed by a sterilized buffer solution (6 mM-H_3PO_4 65:CH_3CN 35).

Synthesis of [^{11}C]RO 15-1788 for clinical use

^{11}C activity generated by the $^{14}N(p,\alpha)^{11}C$ reaction was converted to $^{11}CO_2$ by passage through the CuO column (at 800°C) and then introduced into the cooled reaction vessel RV1 (< −5°C) at a flow rate of 280 mL/min, where $^{11}CO_2$ was trapped by the following reaction

$$4^{11}CO_2 + 3LiAlH_4 \rightarrow 2LiAlO_2 + LiAl(O^{11}CH_3)_4.$$

When the flow rate decreased below 90 mL/min, THF in RV1 was evaporated under a nitrogen gas flow at 130°C for 70s. After cooling, 0.5 mL of water was added into RV1, followed by the reaction:

$$4LiAl(O^{11}CH_3)_4 + 4H_2O \rightarrow Al(OH)_3 + LiOH + 4^{11}CH_3OH$$

$^{11}CH_3OH$ was distilled into RV2(130°C) under a flow of nitrogen (70 mL/min), where $^{11}CH_3I$ was synthesized by reaction with HI under reflux, and then collected in RV3 at about −10°C after purification with Ascarite and phosphorus pentoxide. The methylation reaction was carried out in RV3 at 50°C for 1 min. The reaction mixture was transferred from RV3 into the reservoir and separated on a Megapak Sil C_{18-5} column (7.2 × 250 mm, JASCO, Tokyo, Japan) eluting with acetonitrile:6 mM H_3PO_4(35:65) at a flow rate of 5 mL/min. The fraction containing [^{11}C]RO 15-1788 was collected in a sterilized flask. The time-course of radioactivity and absorbance at 254 nm during the above procedure is shown in Fig. 4. This fraction was evaporated to dryness manually with a rotary evaporator, dissolved in 10 mL sterile isotonic saline solution and filtered through a 0.22 μm Milex filter.

The chemical and radiochemical purities of the filtrate were determined using a Finepak Sil C_{18-5} column (4.6 × 250 mm, JASCO, Tokyo, Japan) eluting with acetonitrile:6 mM-H_3PO_4 (60:40) at a flow rate of 4 mL/min. The amounts of RO 15-1788 and RO 15-5528 were determined by comparison with the corresponding standards. Pyrogen testing of the product was carried out with Pyrogent and Pyrospers reagents (Mallinckrodt Inc., St Louis, U.S.A.) after pH adjustment (6.0–7.5). Bactec Model R301 (Johnston Laboratory, Inc., U.S.A.) was used to test for the presence of bacteria in the product.

Results and Discussion

Table 2 shows the distribution of radioactivity in the system. The values listed in Table 2 should be reduced by several percent since they are calculated on the basis of the recovered ^{11}C radioactivity and small amounts of ^{11}C would be expected to remain in the target box and line. The radiochemical yield for the methylation reaction of RO 15-5528 with $^{11}CH_3I$ was estimated to be about 88% from comparison of the radioactivity in the product ([^{11}C]RO 15–1788) and in the waste(liq.), although some of the radioactivity in the waste would be attributed to [^{11}C]RO 15-1788 due to losses in the separation. About 15% of [^{11}C]RO 15-1788 remained in the membrane filter.

Table 3 summarizes the results obtained from the latest three runs which have been carried out after the perfection of the technique for the automatic production of [^{11}C]RO 15-1788. Radiochemical yield was

Table 2. ^{11}C activity distribution (%) in the system

	Run 1	Run 2	Run 3	Average
[^{11}C]RO 15-1788	(65.8)	(64.5)	(50.0)	(60.1 ± 8.8)
in vial	55.1	55.6	41.8	50.8 ± 7.8
filter	10.7	8.9	8.2	9.3 ± 1.3
RV1	5.1	3.6	7.3	5.3 ± 1.9
RV2	10.0	12.2	27.1	16.4 ± 9.3
RV3	0.7	1.8	0.4	1.0 ± 0.7
A1	2.8	4.2	7.3	4.8 ± 2.3
A2	3.7	6.7	2.7	4.4 ± 2.1
Waste(liq.)	12.0	6.9	5.3	8.1 ± 3.5

* *RV1, RV2, RV3, A1 and A2 are the same abbreviation with that in Fig. 1.

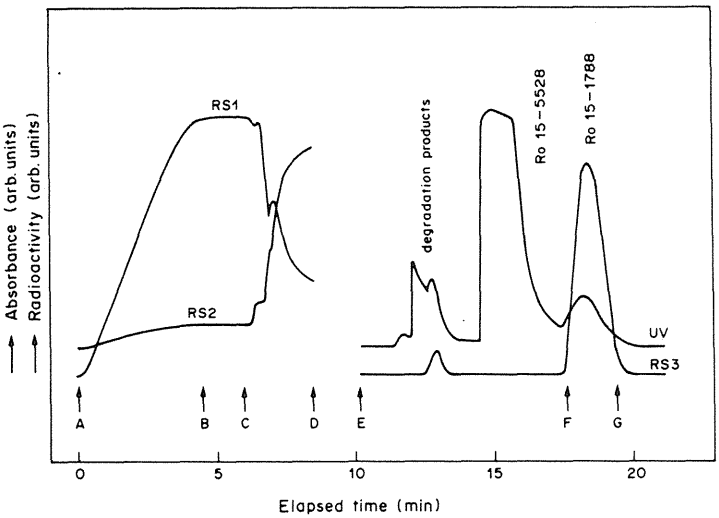

Fig. 4. A typical example of the automatic production of [^{11}C]RO 15-1788. RS1-RS3, u.v.; outputs from the corresponding sensors shown in Fig. 1. A; start of synthesis, collection of $^{11}CO_2$ into RV1, B; THF evaporation, C; cooling of RV1 and water injection, $^{11}CH_3I$ preparation and collection in the cooled RV3, D; reaction of $^{11}CH_3I$ with RO 15-5528 at 50°C for 1 min, transfer the mixture into the reservoir, E; start of purification, F and G; start and end of [^{11}C]RO 15-1788 separation.

assumed as a ratio of i.v. injectable [^{11}C]RO 15-1788 to the total radioactivity listed in Table 2. At NIRS, the specifications of [^{11}C]RO 15-1788 for injection are as follows: radiochemical purity >96%, specific activity >50 mCi/μmol, amount of RO 15-5528 <30 μg/10 mCi [^{11}C]RO 15-1788. An amount of 5–10 mCi of [^{11}C]RO 15-1788 are administered to a patient for a PET study and measurements are carried out for 30 min. Each product was sufficient to carry out three clinical studies since the yield (276 ± 76 mCi/batch) and the specific activity (2.9 ± 0.5 Ci/μmol) of [^{11}C]RO 15-1788 were very high, as demonstrated in Table 3.

Solutions of LAH in THF were stored in a freezer under an atmosphere of nitrogen. Each stored solution could be used for more than three weeks in the preparations of [^{11}C]RO 15-1788 with high specific activity at high yield. The use of the same solution is very helpful for routine production of the compound.

We consider that the high yield and the high specific activity of [^{11}C]RO 15-1788 were achieved by the following reasons. (A) Preventing contamination of the system with CO_2 by using pure nitrogen gas as a target material, decreasing the volume of the system by using a conical target (inner volume; 75 mL) and fine tubing (i.d. 0.5 mm), drying the radioactivity flow line by heating reaction vessels and the CuO column under a pure nitrogen gas flow, sealing the target box with metal instead of rubber, and careful preparation and handling of the THF solutions of LAH. (B) Use of DMF (m.p. = −61°C) as the solvent for trapping of $^{11}CH_3I$ at −10°C and the methylation reaction on RO 15-5528 (yield; >88% at 50°C for 1 min). (C) Automatic synthesis of [^{11}C]RO 15-1788 with the specially designed equipment connected to the central control system.

The amount of RO 15-1788 and RO 15-5528 present and also the radionuclidic and radiochemical purity and specific activity of [^{11}C]RO 15-1788, can be determined within 2 min using the conditions described above. This enables the quality control to be carried out before administration of the product to

Table 3. Results in the synthesis of [^{11}C]RO 15-1788 for clinical use

	Run 1	Run 2	Run 3	Average
Yield (mCi)	338	299	191	276 ± 76
Radiochemical yield (%)	55.1	55.6	41.8	50.8 ± 7.8
Radiochemical purity (%)	99.2	99.1	99.6	99.3 ± 0.3
Specific activity (Ci/μmol)	3.2	3.2	2.3	2.9 ± 0.5
Carrier RO 15-1788 (μmol)	0.107	0.094	0.082	0.094 ± 0.013
RO 15-5528 (μmol)	0.033	0.016	0.117	0.055 ± 0.054
Pyrogen and bacteria	free	free	free	free
Synthesis time (min)	23.4	26.6	25.3	25.1 ± 1.6

Irradiation; 14.2 MeV proton, 16–20 μA, 32–48 min.
Target gas; pure nitrogen (>99.9998%), 14 kg/cm^2, 15 cm length.
Yield and specific activity are the value for an i.v. injectable [^{11}C]RO 15-1788.

patients without any significant decrease in its quality. Attempts to detect pyrogens with Pyrogent reagent failed, even in a positive control solution (0.1 ng *E. Coli* endotoxin in 1 mL of 6 mM-phosphate buffer, detection limit of the endotoxin with Pyrogent; 0.01–0.05 ng/mL). From our observations this is caused by the presence of phosphate. Addition of Pyrosperse (metallo-modified polyanionic dispersants) to the test solution resolved this "false negative" phenomenon. [^{11}C]RO 15-1788 was used clinically without testing for pyrogens and bacteria when they were not detected in 3 successive preceeding runs, the tests being carried out after the decay of ^{11}C radioactivity.

With the equipment described above, $^{11}CH_3I$ can be produced at extremely high specific activity. Consequently the equipment may be modified for the synthesis of other ^{11}C-labelled ligands such as ^{11}C-labelled carfentanil[5] which must be produced at extremely high specific activity for receptor studies. The present system is suitable for modification and development since most of the components are standardized and the control program is in a tabular form.

Acknowledgements—The authors wish to thank Dr Y. Kasida and Dr Y. Tateno of NIRS and also Professor D. Ishii of Nagoya University for fruitful discussions. Special thanks are also given to the cyclotron crew of NIRS for their excellent support and to Roche Japan for kindly supplying RO 15-1788 and RO 15-5528.

References

1. Wagner H. N. Jr, Burns H. D., Dannals R. F., Wong D. F., Langstrom B., Duelfer T., Frost J. J., Ravert H. T., Links J. M., Rosenbloom S. B., Lukas S. E., Kramer A. V. and Kuhar M. J. *Science* **221,** 1264 (1983).
2. Wagner H. N. Jr, Dannals R. F., Frost J. J., Wong D. F., Ravert H. T., Wilson A. A., Links J. M., Burns H. D., Kuhar M. J. and Snyder S. H. *Radioisotopes* **34,** 103 (1985).
3. Comar D., Maziere M., Godot J. M., Berger G., Soussaline F., Menini CH., Arfel G. and Naquet R. *Nature* **280,** 329 (1979).
4. Garnett E. S., Firnau G. and Nahmias C. *Nature* **305,** 137 (1983).
5. Frost J. J., Wagner H. N. Jr, Dannals R. F., Ravert H. T., Links J. M., Wilson A. A., Burns H. D., Wong D. F., McPherson R. W., Rosenbaum A. E., Kuhar M. J. and Snyder S. H. *J. Comput. Assist. Tomogr.* **9,** 231 (1985).
6. Maziere M., Hantraye P., Prenant C., Sastre J. and Comar D. *Int. J. Appl. Radiat. Isot.* **35,** 973 (1984).
7. Ehrin E., Johnstrom P., Stone-Elander S., Nilsson J. L. G., de Paulis T., Farde L., Greitz T., Litton J.-E., Persson A., Sedrall G. and Widen L. *J. Labelled Compd. Radiopharm.* **21,** 1161 (1984).
8. Solin O., Heselius S-J., Lindblom P. and Manngard P. *J. Labelled Compd. Radiopharm.* **21,** 1275 (1984).

Nucl. Med. Biol. Vol. 13, No. 1, pp. 79–80, 1986
Int. J. Radiat. Appl. Instrum. Part B
Pergamon Journals Ltd 1986. Printed in Great Britain.
0883-2897/86 $3.00 + 0.00

Deuterium Isotope Effect of [$^{11}C_1$]N,N-Dimethylphenethyl-amine-α,α-d_2; Reduction in Metabolic Trapping Rate in Brain

KENJI HASHIMOTO,[1]* OSAMU INOUE,[2] KAZUTOSHI SUZUKI,[2] TOSHIRO YAMASAKI[2] and MASAHARU KOJIMA[1]

[1]Faculty of Pharmaceutical Sciences, University of Kyushu, 3–1–1 Maidashi, Fukuoka, 812, Japan and
[2]Division of Clinical Research, National Institute of Radiological Sciences, 9–1 Anagawa-4-chome, Chiba-shi, Chiba, 260, Japan

Introduction

Positron emission tomography is a non-invasive and potential method for the *in vivo* measurement of transport, metabolism and excretion rates of various substances. As previously reported, we have been developing a new radiotracer technique for the *in vivo* estimation of brain enzyme activity using the biotransformation of labeled substrate.[1] In this tracer method, the measurable range of changes in brain enzyme activity is mainly dependent upon two factors; enzymatic (V_{max}/K_m value) and physicochemical (K_{el}; the elimination rate from the brain) properties of substrate used as a tracer. N-Methyl phenethylamine derivatives rapidly entered into mouse brain, and deaminated by monoamine oxidase (MAO) to labeled metabolites which were trapped in the brain.[2] Among several tracers, [$^{11}C_1$]N,N-dimethylphenethylamine([$^{11}C_1$]DMPEA) was found to have suitable properties for the *in vivo* estimation of MAO-B activity in mouse brain.[2] The oxidative deamination rate of phenethylamine derivatives by MAO has been reported to be significantly reduced by substitution of the α-hydrogen with deuterium.[3] In this paper, we synthesized [$^{11}C_1$]N,N-dimethylphenethylamine-α,α-d_2-([$^{11}C_1$]DMPEA-α,α-d_2) and compared it with the biodistribution of [$^{11}C_1$]DMPEA in mice.

Materials and Methods

1. Materials

L-Deprenyl hydrochloride was kindly provided by Dr Knoll, Department of Pharmacology, Semmelweis University of Medicine, Budapest, Hungary. N-Methyl phenethylamine and lithium aluminum deuteride were purchased from Aldrich Chemical Corp., Milwaukee, WI.; phenylacetonitrile and other chemicals were purchased from WACO Pure Chemical Industries Ltd (Tokyo, Japan). Phenethylamine-α,α-d_2 was synthesized from phenylacetonitrile and lithium aluminum deutride. N-methyl phenethylamine-α,α-d_2 was synthesized according to the method of Johnstone *et al.*[4]

2. Preparation of [$^{11}C_1$]DMPEA and [$^{11}C_1$]DMPEA-α,α-d_2

[^{11}C]Methyl iodide was produced by the method of Suzuki *et al.*[5] [$^{11}C_1$]DMPEA and [$^{11}C_1$]DMPEA-α,α-d_2 were synthesized by the methylation of the corresponding N-methyl derivatives with [^{11}C]methyl iodide, and purified by HPLC-($CHCl_3$:MeOH:c.NH_3 = 1500:50:1). Radiochemical purity was determined by radio HPLC ($CHCl_3$:MeOH:c.NH_3 = 10:1:0.2).

3. Biodistribution of [$^{11}C_1$]DMPEA and [$^{11}C_1$]DMPEA-α,α-d_2

In this study 10–12 week old male C3H mice (35–40 g) were used. Two-tenths ml of [$^{11}C_1$]DMPEA (or [$^{11}C_1$]-DMPEA-α,α-d_2) solution (about 50 μCi) was intravenously injected into mice. Mice were killed by decapitation at 1, 5, 15, 30 and 60 min after injection of the tracer. Brains and blood were removed and weighed. Radioactivities in each organ were counted and expressed in percentage of injection dose.

4. Effect of inhibition of MAO on the production rate of radioactive metabolite in the brain

Male C3H mice (12 weeks old) were pretreated with various dosages (0, 0.01, 0.1, 10 mg/kg i.v.) of l-deprenyl, a specific MAO-B inhibitor. One hour after injection of l-deprenyl, about 50 μCi of [$^{11}C_1$]DMPEA-α,α-d_2 (0.2 mL) was injected intravenously. One hour after injection of the tracer, radioactivities in brain and blood were determined as described above.

Results and Discussion

Both [$^{11}C_1$]DMPEA and [$^{11}C_1$]DMPEA-α,α-d_2 were obtained with more than 99% of radiochemical purity and more than 100 mCi/μmol of specific activity. A radiochromatogram of [$^{11}C_1$]DMPEA-α,α-d_2 is shown in Fig. 1.

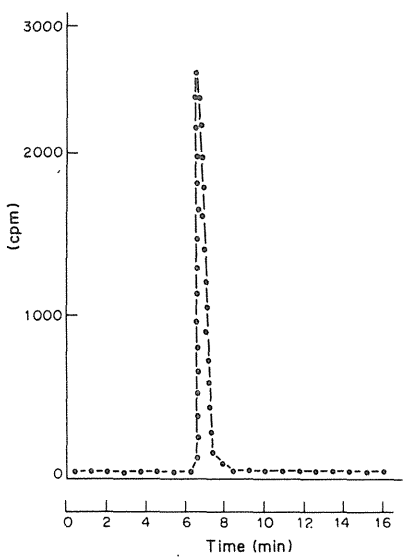

Fig. 1. HPLC of [$^{11}C_1$]DMPEA-α,α-d_2. Condition; column: Finepak SIL (JASCO). Solvent system: $CHCl_3$:MeOH:c.NH_3 = 10:1:0.2 2 mL/min. Retention time [$^{11}C_1$]DMPEA-α,α-d_2 (6.9 min).

* All correspondence should be addressed to National Institute of Radiological Sciences.

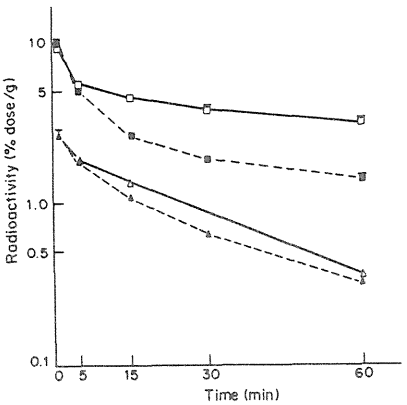

Fig. 2. Time courses of radioactivity in the blood and brain after injection of [$^{11}C_l$]DMPEA and [$^{11}C_l$]DMPEA-α,α-d_2 in mice. (△——△) radioactivity in blood of [$^{11}C_l$]DMPEA; (□——□) radioactivity in brain of [$^{11}C_l$]DMPEA; (▲-----▲) radioactivity in blood of [$^{11}C_l$]DMPEA-α,α-d_2; (■-----■) radioactivity in brain of [$^{11}C_l$]DMPEA-α,α-d_2.

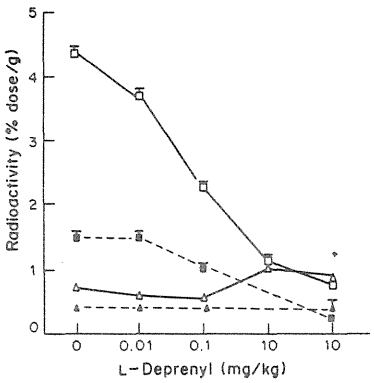

Fig. 3. Effects of pretreatment with various dosages of l-deprenyl on the radioactivity in blood and brain 1 h after injection of [$^{11}C_l$]DMPEA-α,α-d_2 and [^{3}H]DMPEA. (▲-----▲) radioactivity in blood of [$^{11}C_l$]DMPEA-α,α-d_2; (■-----■) radioactivity in brain of [$^{11}C_l$]DMPEA-α,α-d_2; (△——△) radioactivity in blood of [^{3}H]DMPEA; (□——□) radioactivity in brain of [^{3}H]DMPEA.

As shown in Fig. 2, the incorporation rate of [$^{11}C_l$]DMPEA-α,α-d_2 into mouse brain was almost the same as [$^{11}C_l$]DMPEA. In addition, there was no significant difference in the blood clearance curve between [$^{11}C_l$]-DMPEA and [$^{11}C_l$]DMPEA-α,α-d_2, which indicated that the distributed phase of DMPEA was not affected by substitution of α-hydrogen with deuterium. However, the slow component of radioactivity in the brain was remarkably reduced in [$^{11}C_l$]DMPEA-α,α-d_2 as shown in Fig. 2. These results indicated that the production rate of labeled metabolite ([$^{11}C_l$]dimethylamine) was reduced by substitution of α-hydrogen with deuterium. It can be seen that [$^{11}C_l$]DMPEA-α,α-d_2 was oxidized by MAO-B at a slower rate than [$^{11}C_l$]DMPEA. From this deuterium isotope effect it would be clear that the C—H bond was broken in the transition state and that cleavage of the C—H bond was involved in the MAO deamination reaction.

As shown in Fig. 3, the radioactivity which remained in the brain 1 h after injection of [$^{11}C_l$]DMPEA-α,α-d_2 was also significantly decreased by pretreatment with various dosages (0.01–10 mg/kg i.v.) of l-deprenyl in a dosage-dependent manner. The substitution of α-hydrogen with deuterium did not affect the selectivity of DMPEA for MAO-B in the mouse brain. As expected, the production rate of labeled metabolite in the mouse brain was remarkably reduced by substitution of α-hydrogen with deuterium.

A lot of deuterated compounds have been frequently used in the studies of biological systems.[6] Because the mass of deuterium (D) is higher than that of protium (H), the zero point vibrational energy of a C—D bond is lower than that of a C—H bond. It is found that the zero point vibrational energy effect is the only contributor to the isotope effect.[7]

Further, because there may be species difference of MAO-B activity, [$^{11}C_l$]DMPEA-α,α-d_2 would have high potency for the *in vivo* study of brain MAO-B in other species except the mouse.

In conclusion, the isotope effect is one of the useful tools for the drug design of metabolic trapping radiotracers.

Acknowledgements—The authors wish to thank Dr Y. Kashida for valuable advice and Mr K. Tamate for technical assistance.

References

1. Inoue O., Tominaga T., Yamasaki T. and Kinemuchi H. *J. Neurochem.* **44**, 210 (1985).
2. Inoue O., Tominaga T., Fukuda N., Suzuki K. and Yamasaki T. *Jap. J. Nucl. Med.* **21**, 671 (1984).
3. Yu P. H., Barclay S., Davis B. and Boulton A. A. *Biochem. Pharmacol.* **30**, 3089 (1981).
4. Johnston R. A. W., Payling D. W. and Thomas C. *J. Chem. Soc. C.* 2223 (1969).
5. Suzuki K., Inoue O., Hashimoto K., Yamasaki T., Kuchiki M. and Tamate K. *Int. J. Appl. Radiat. Isot.* In press.
6. Katz J. J. and Crespi H. L. *Isotope Effects in Chemical Reactions* pp. 286–363 (Van Nostrand, New York, 1970).
7. Thornton E. K. and Thornton E. R. *Ibid.* pp. 213–285.

RADIOISOTOPES, **34**, 537-542 (1985)

$^{55}Mn(p, 4n)^{52}Fe$ 反応による ^{52}Fe とミルキングによる ^{52m}Mn の生産

鈴木和年
放射線医学総合研究所サイクロトロン管理課
260 千葉市穴川 4-9-1

1985年5月29日　受理

73 MeV プロトンを用いて $^{55}Mn(p, 4n)^{52}Fe$, $^{55}Mn(p, n)^{55}Fe$ 反応の励起関数測定を行った。^{52}Fe の反応断面積の最大値は54 MeV で1.4 mb であった。Thick target yield は24.8 MBq/μA h (670 μCi/μA h) で出口エネルギーを39 MeV にしたときの ^{55}Fe 混入率は照射終了時(EOB) で0.45%と推定された。生産用には 60-44 MeV のプロトンを用い，核種純度99%以上，放射化学収率70-92%で $^{52}FeCl_3$ を得た。^{52m}Mn は陰イオン交換樹脂に吸着させた ^{52}Fe を 6 *N*-HCl で溶出することにより，繰り返し回収できた。核種純度は99.9%，収率は期待値の86%程度であった。^{52}Fe 中の ^{55}Fe 混入量は ^{52}Fe と ^{55}Fe の壊変時に放出される Mn の K_α-X 線の崩壊曲線を解析することにより，EOB から1-2日で決定できた。

Key Words: iron-52, milking, manganese-52*m*, excitation function

1. 緒　言

鉄の放射性医薬品としては，現在クエン酸第二鉄 (^{59}Fe) 注射液が承認されているが，^{59}Fe は半減期44.6日，β^-(100%)放出核種で，主な放出γ線も1 099 keV (55.5%)，1 292 keV (44.1%) で，通常のγ線カメラ用にはエネルギーが高すぎる。これに対し，^{52}Fe は半減期8.28時間で，崩壊特性 (β^+; 56.5%，γ 168.7 keV; 99.2%) も *in vivo* 診断用に適した核種であり[1-3]，しかも心筋診断に有効な ^{52m}Mn (半減期21.1分，β^++EC; 98.25%) の親核種としても利用できる[4,5]。

^{52}Fe は $^{52}Cr(^3He, 3n)^{52}Fe$[6-8]，$^{50}Cr(\alpha, 2n)^{52}Fe$[9,10]，$^{55}Mn(p, 4n)^{52}Fe$[4,11]，Ni(*p*, spall.) ^{52}Fe[4,12] および $^{54}Fe(\gamma, 2n)^{52}Fe$[13] など種々の核反応で生産される。これらの核反応はいずれも反応収率が低いが，そのうちでは，$(p, 4n)$ 反応と $(p, spall.)$ 反応が最も収率が高い。放医研のサイクロトロンのように60 MeV 程度のプロトンが効果的に利用できる場合は，$(p, 4n)$ 反応が収率の点で最も優れている。しかし，$^{55}Mn(p, 4n)^{52}Fe$ 反応と $^{55}Mn(p, n)^{55}Fe$ 反応はともに励起関数に関する報告がないため，^{52}Fe を高純度，高収率で得るためのプロトンのエネルギー領域は不明である。^{55}Fe はγ線を放出せず測定がきわめて困難であるが，半減期が2.7年と非常に長く，血液，脾臓，骨髄などに大きな被曝線量を与えるため[14]，その混入量を決定する必要がある。

一方，^{52m}Mn は分離精製した ^{52}Fe からミルキングにより何度も調製可能である[4,5,15]。

本報では $^{55}Mn(p, 4n)^{52}Fe$ 反応と $^{55}Mn(p, n)^{55}Fe$ 反応の励起関数測定，^{52}Fe と ^{52m}Mn の半自動生産，^{55}Fe の迅速定量法などについて述べる。

2. 研究方法

2・1 励起関数測定用試料の調製

マンガンの薄膜は市販されておらず，真空蒸着やめっきでも励起関数測定に使用可能な薄膜が得られないため，ホットプレス（柴山科学㈱，東京）を用いて200メッシュ，99.9%の高純度マンガン粉末を400-500°C，200-250 kg/cm² の圧力下で0.5-1時間放置し，半融した硬いマンガンペレット（直径12 mm，厚さ≈100 mg/cm²）を作製した。

サイクロトロンビームによる照射のように，ビームが試料の一部にしかあたらない場合，試料の厚さの均一度は測定結果に直接影響を与える。そこで，放医研ファン・デ・グラーフで発生させた中性子でマンガンペレットを均一に放射化し，$^{55}Mn(n, \gamma)^{56}Mn$ 反応により ^{56}Mn を生成させた。^{56}Mn の生成量を，内径3 mm，長さ50 mm の鉛製コリメータを通し，ペレットの種々の位置で，Ge(Li) 半導体検出器を用いて測定することにより，ペレットの厚さの均一度を測定した。

2・2 照射

ペレットは，前後に20 μm のアルミニウム窓を持つ厚さ1 mm，内径12.5 mm の黄銅製容器に封入した。これとエネルギー減衰用の100 μm 銅ばくを10-15個

交互に重ね，これを放医研サイクロトロンを用いて73 MeV と 60 MeV のプロトンで照射した。各ペレットでのプロトンエネルギーは，Hata ら[16]のRange/Stopping Power 表を用いて計算した。使用したコリメータは内径6mm，長さ30mmのアルミニウム製である。ビームがホイルやターゲットにあたったときに出る2次電子をふたたびターゲット側に押し戻し，正確な電流値を得るためにアルミニウム製のリペラ（内径20 mm，長さ30mm）を使用した。リペラを使用しない場合，ビームの種類やエネルギー，膜などにより多少異なるが，5－10%程度高い読みを与えた。

2・3 $^{52}FeCl_3$ とジェネレータ法による $^{52m}MnCl_2$ の製造

製造用には，2・1と同様ホットプレスを用いて直径12mm，厚さ2 g/cm²のマンガンペレットを調製した。照射は60 MeV のプロトン2－4 μA で行った。照射後，ターゲットをトロッコ，滑車，エアシリンダなどを用いて，遠隔的にホットセル内まで輸送し，電動ドライバ，マニピュレータを使って照射マンガンを取り出した。これを無機核種分離精製装置（協和精密㈱，東京）を使用して溶解・分離・精製を行った。溶解液中にはターゲット物質のマンガンが2価の状態で大量に存在し，その中に不純物として含まれていた鉄と，核反応で生成した ^{52}Fe などが0.1－数 mg 含まれている。しかし，6N-HCl 中では2価のマンガンは錯陰イオンを形成しないため，陰イオン交換カラムに吸着されず，分離に使用する陰イオン交換樹脂も少量で十分であった。これに対し，鉄は $FeCl_4^-$ を形成して強く陰イオン交換カラムに吸着される。一方，^{52}Fe は ^{52}Fe (β^+ 57%，EC 43%，半減期 8.28 時間) →^{52m}Mn により ^{52m}Mn に変わる。このときの ^{52m}Mn の生成量が最大となる時間 T_{max} は次式で表される。

$$T_{max}=\frac{\ln(\lambda_2/\lambda_1)}{\lambda_2-\lambda_1}=1.67\,h \qquad (1)$$

ここで λ_1, λ_2 はそれぞれ ^{52}Fe, ^{52m}Mn の崩壊定数である。したがって，^{52}Fe を陰イオン交換カラムに吸着させ，1－2時間放置した後，6N-HCl で ^{52m}Mn を溶出させることにより，半減期 21.1m の ^{52m}Mn を10時間以上にもわたって入手可能である。^{52}Fe は 0.1 N-HCl で簡単に溶出することができる。

2・4 ^{52}Fe 中の ^{55}Fe の定量

^{52}Fe の絶対量は，The Radiochemical Center 社 (Amersham, 英国) の9核種セット標準線源を用いて作製した，ある位置における Ge(Li) 半導体検出器の検出効率曲線から求めた168.7 keV の検出効率と，γ 線放出率，崩壊定数，同じ位置における ^{52}Fe の計数率などから計算された。このときの ^{52}Fe の定量誤差は5%程度と推定された。

^{52}Fe 中の ^{55}Fe の定量は，上のようにして調製した ^{52}Fe 溶液を1滴ずつ，ポリイミド製 KAPTON 膜(1.09 mg/cm², 東レ㈱) 上に滴下，蒸発乾固することにより点線源を作製し，Si(Li) 半導体検出器を用いて行った。

測定日時の制約がない場合，^{52}Fe, ^{52m}Mn, ^{52}Mn などが十分に減衰した後，^{55}Fe 由来の Mn の K_α-,K_β-X線 (^{55}Fe は γ 線を放出しない) を測定し，^{55}Fe の標準溶液 (LMRI, 仏) より作製した点線源と比較することにより ^{55}Fe の定量を行った。このさい，散乱の影響は無視できるものとして，試料の自己吸収補正を行った。

しかし，臨床用に ^{52}Fe を生産する場合，その純度は可能な限り早く決定しなければならない。同一エネルギーを放出する核種が n 個存在する場合，その壊変定数を $\lambda_1, \lambda_2, \cdots\cdots, \lambda_n$，種々の時刻における m 組の実測値を $(Y_1, t_1), (Y_2, t_2), \cdots\cdots, (Y_m, t_m)$，$t=0$ における各核種からの計数値を $A_1, A_2, \cdots\cdots, A_n$ とすると，任意の時刻 t における全計数値 Y は，

$$Y=A_1e^{-\lambda_1 t}+A_2e^{-\lambda_2 t}+\cdots+A_ne^{-\lambda_n t} \qquad (2)$$

と表される。最小二乗法を用いて求めた $A_1, A_2, \cdots\cdots, A_n$ と各核種のX線放出率 (EC 崩壊の場合，K殻螢光X線放出率，$K_{\alpha1}$, $K_{\alpha2}$, K_β 線の相対強度などから計算)，検出効率などから $t=0$ におけるそれぞれの核種の放射能量が求まる。これらの核種のうち1つが Ge(Li) 半導体検出器などで定量できれば，検出効率が不明であったり，自己吸収や散乱の割合が大きい場合にも，他の核種の定量が可能である。

3. 結　果

3・1 マンガンペレットの厚さの均一度測定

マンガンペレットの中性子照射により生成した ^{56}Mn の 846.8 keV（放出率 98.9%）γ 線の強度を，コリメータを通しペレットの種々の位置で測定した。測定は正味の計数値が 10 000になるまで継続した。ペレット上の互いに重なり合わない9点（直径3mm）の平均値は 0.450±0.0125（単位は任意で μCi 数に比例）であった。

したがって，ペレットの厚さのばらつきは，計数 10 000 の統計誤差，±1%を考慮に入れると 2×

(0.0125−0.0045)/0.450=0.036，すなわち4％程度と推定される。

3・2 励起関数

Fig. 1 にプロトンエネルギー 39－73 MeV の範囲内での $^{55}Mn(p,4n)^{52}Fe$，$^{55}Mn(p,n)^{55}Fe$ 反応に対する励起関数を示す。^{52}Fe の反応断面積 σ は54 MeV で最大値1.4 mb であった。これに対し ^{55}Fe に対する σ はプロトンエネルギー E_p の増加とともに単調減少傾向を示した。Fig. 2 には，ビームの出口エネルギーを39MeV としたときの入射エネルギーに対する ^{52}Fe と ^{55}Fe の収率をその比 $^{55}Fe/^{52}Fe$ とともに示した。図から分かるように，^{52}Fe の収量は E_p=73 MeV と 60 MeV に対してそれぞれ 24.8MBq/μA h(670 μCi/μA h)，14.1 MBq/μA h (380 μCi/μA h) であり，そのときの ^{55}Fe の混入量は ^{52}F に対しそれぞれ0.44，0.50％となることが予想される。入射エネルギーが増加するにつれ，鉄は純度，収量ともに向上することが期待される。入射エネルギーを一定にした場合には，出口エネルギーを上げることにより，^{52}Fe の収量をそれほど低下させることなく，純度向上が期待できる。

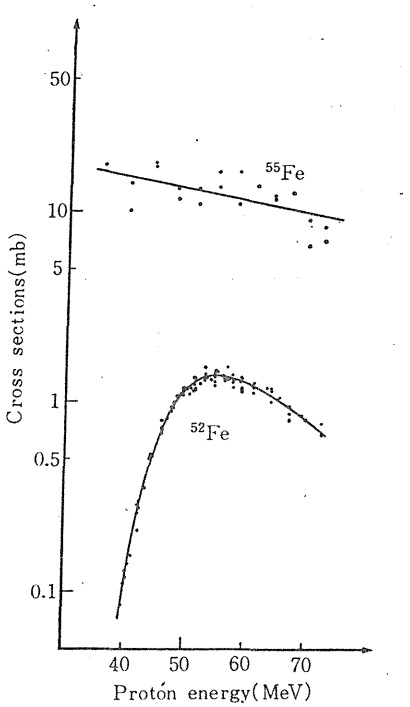

Fig. 1　Excitation functions of ^{52}Fe and ^{55}Fe by the $^{55}Mn(p,4n)^{52}Fe$ and $^{55}Mn(p,n)^{55}Fe$ reactions.

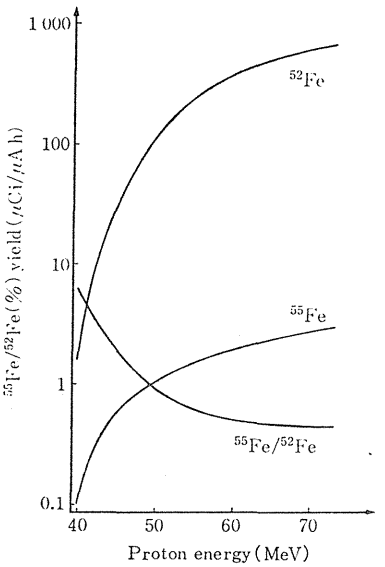

Fig. 2　Yields of ^{52}Fe, ^{55}Fe and its ratio (%). The curves are calculated on condition that the exit energy of the protons is 39 MeV.

3・3 $^{52}FeCl_3$ と $^{52m}MnCl_2$ の生産

Fig. 3に，ターゲット溶解液からのマンガン（^{52}Mn，他）の分離，ミルキングによる ^{52m}Mn の生成と ^{52}Fe 回収の1例を示す。この図はカラム出口に配置した Ge(Li) 半導体検出器で溶出液を連続的にモニタし，γ線スペクトル上の3個の関心エネルギー領域（ROI）のネットカウント変化を同時に記録したものである。この方法は高エネルギーγ線からのコンプトン散乱の影響を受けずに低エネルギーγ線の計数変化を測定できることに特長がある[17]。図から，①試料添加時や ^{52m}Mn 溶出時には，^{52}Fe はカラムからブレークスルーしない，②^{52}Mn は試料添加後の 6*N*-HCl 洗浄で除去される，③式(1)より予想されるように，送液停止時間が長くなるにつれ，^{52m}Mn 生成量も増大する，④0.1*N*-HCl を流すことにより ^{52}Fe が溶出し，その後は ^{52m}Mn も溶出しない，などの様子が分かった。1434 keV のγ線は ^{52m}Mn のみならず ^{52}Mn からも放出されるが，ここでは ^{52m}Mn からはほとんど(0.24％)放出されない ^{52}Mn の主放出γ線である936 keV (94.5％) も同時にモニタしており，ミルキング時における1434 keV のγ線ピークは ^{52m}Mn 由来のものであることが分かる。

^{52}Fe は44－60 MeV のエネルギー範囲のプロトンを使用して生産された。ターゲット中での ^{52}Fe の収量

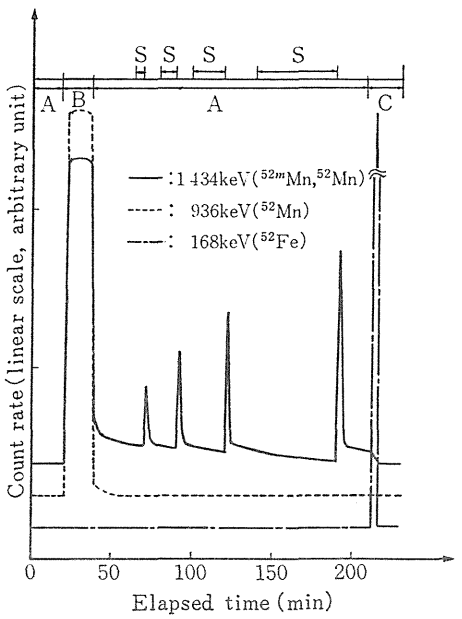

Column: Dowex 1-X8, 8 mmϕ×50 mm
Flow rate: 3.7 ml/min, S: Stop
Sample: Dissolved target solution (2.3 g Mn in 6*N*-HCl 50 ml)
Eluent: A, 6*N*-HCl; B, sample load; C, 0.1 *N*-HCl
Detector: Ge(Li) detector
Net counts increments for the regions of interest at 168, 936 and 1 434 keV were monitored simultaneously.

Fig. 3 Typical elution pattern of dissolved target solution from anion exchange column.

はFig. 2から期待される値の85－93%であった。^{52}Fe分離精製時の放射化学収率は70－92%の範囲で，その核種純度は照射終了時において99%以上であった。このとき検出された不純物は^{55}Fe(0.4－0.7%)，^{52}Mn(0.01－0.05%, ^{52}Feから生成)で，その他^{67}Ga, ^{54}Mn, ^{51}Cr, ^{48}V, ^{47}Scなどが微量検出された。

37 MBq (1 mCi) 以上の^{52m}Mnが103.6 MBq (2.8 mCi) の^{52}Fe (照射終了時) より数度にわたりミルキングすることができた。このときの収率は^{52}Feからの計算値に対し85－87%であり，核種純度は99.9%程度であった。このとき，^{47}Sc, ^{54}Mn, ^{67}Ga, ^{48}Vなどが微量検出された。

3・4 副生^{55}Feの定量

Fig. 4は，^{52}Fe点線源から放出されるMnのKα-X線をSi(Li)検出器で測定することにより得られた，^{52}Feと^{55}Feの計数率（照射終了時（EOB）換算値）と

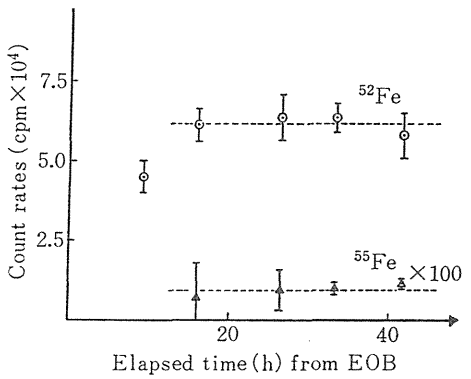

Fig. 4 Count rates of Mn-Kα X-ray from ^{52}Fe and ^{55}Fe at EOB. Calculated by decay curve analysis.

測定時点との関係を示したものである。各点は，照射終了後9時間から50時間の間に得られた50点の測定値を，時系列順に10点ずつ5グループに分け，それぞれのグループに対し2・4で述べた方法で^{52}Feと^{55}Feの計数率を求めたものである。簡単のため，^{52}Mn, ^{54}Mn由来のKβ-X線からの寄与は無視した。各点につけたばらつき表示は95%信頼限界範囲を示す。この結果と^{52}Fe, ^{55}FeのKα-X線放出率10.1, 23.4%より^{55}Fe/^{52}Fe=0.7%が得られた。

一方，同一試料を照射終了35日後に，^{55}Fe標準溶液より作製した点線源と比較し，かつ自己吸収補正することにより，^{55}Fe/^{52}Fe≈0.4%という結果が得られた。

4. 考　察

Fig. 2で得られた結果を，Table 1の文献値と比較した場合，①^{52}Cr(^{3}He, 3*n*)^{52}Feに比し，収率は高いが混入^{55}Feの割合が高い，②^{50}Cr(^{4}He, 2*n*)^{52}Feに比し収率，純度ともによい，③Ni(*p*, spall.)^{52}Feに対しては収率は同程度であるが純度はよい，④他の報告にある^{55}Mn(*p*, 4*n*)^{52}Feに比し収率が高い，などの特徴がある。以上の比較はすべて天然ターゲットを用いた場合のものである。(*p*, 4*n*) 反応の文献値が，本報告と同一の核反応を使用しているにも関わらず低収量であるのは以下の理由によるものと思われる。① SahaらはターゲットにMnO_2を使用しているため，実効収率が低い。ターゲット出口エネルギー不明のため，収量の比較が困難である。②Kuらは Mn 粉末を銅はくで挟み，70 μA の高電流値で照射している。このような条件下ではマンガン粉末は焼結することが予想され，厚さに局所的なばらつきを生じ，収率低下をもたらしているものと思われる。本報告では試料作製にホ

Table 1 ^{52}Fe production reactions

Particle	Reaction	Particle energy (MeV)	Yield (μCi/μA h)	$^{55}Fe/^{52}Fe$ (%)	Reference
^3He	$^{52}Cr(^3He,3n)$	45.5	50	0.001	6
	$^{52}Cr(^3He,3n)$	33	20	<0.07	7
	$^{52}Cr(^3He,3n)$	40	50		8
^4He	$^{50}Cr(^4He,2n)$	65	8	5-6	9
	$^{50}Cr(^4He,2n)$	30	3.3	14	10
p	$^{55}Mn(p,4n)$	65	160	<3	11
	$^{55}Mn(p,4n)$	70	200	0.7	4
	Ni(p, spallation)	200	120	2.0	4
	Ni(p, spallation)	588	700	3.3	12

(1 μCi=37 kBq)

ットプレスを使用し，高温・高圧でマンガンディスクを作製したため，照射中の試料の厚み変化がなく，高い収量が得られたものと思われる。

^{52}Fe 生産用の厚いターゲット中に生成した ^{52}Fe の量が，Fig. 3 の thick target yield から推定される値の85－93%しか得られなかった原因については，①励起関数から thick target yield を算出するさいの集積誤差，②^{52}Fe とともにターゲット中に生成する ^{52}Mn（^{52}Fe の約4倍の生成量）や ^{52m}Mn などからのコンプトン散乱による ^{52}Fe (168.7 keV) の測定誤差増大などが考えられる。

^{52}Fe 崩壊後の ^{52}Fe 溶液中には ^{52}Mn が0.01－0.05%検出されたが，これは ^{52}Fe が次の崩壊型式により生成した ^{52}Mn によるものと思われる。

$$^{52}Fe(8.28\,h) \xrightarrow[100\%]{\beta^+,EC} {}^{52m}Mn(21.1\,m) \xrightarrow[98.25\%]{\beta^+,EC} {}^{52}Cr$$
$$^{52m}Mn(21.1\,m) \xrightarrow[1.75\%]{IT} {}^{52}Mn(5.6\,d) \xrightarrow{\beta^+,EC\ 100\%} {}^{52}Cr$$

^{52}Mn の生成量は36時間後に最大となり，最初の ^{52}Fe 量の0.09%に達する。^{52m}Mn の場合は1.67時間後に最大となり，開始時の ^{52}Fe 量の86.9%となる。

Fig. 3に示すように ^{52}Fe, ^{52m}Mn 調製時，各核種からの放出γ線のネットカウントを各 ROI ごとにリアルタイムでモニタしたため，核種別の分取に効果的であるばかりでなく，核種純度の推定にも役立った。

^{55}Fe の崩壊曲線解析による定量では，照射終了後10時間程度では，^{55}Fe に対する ^{52}Fe の割合が2桁高く，^{55}Fe 定量誤差が非常に大きくなる。また，照射終了後時間が経ちすぎると ^{52}Fe の壊変補正計数が大きくなりすぎ，^{52}Fe の定量誤差が大きくなる。したがって ^{55}Fe の定量は照射終了後1－2日の間に行うのが適当と思われる。本実験では ^{52}Mn や ^{54}Mn からの K_β-X 線 (5.95 keV) の寄与を無視しているため，^{55}Fe 量は多少高めの値が得られているものと思われる。Mn の K_β-X 線 (6.49 keV) を解析すればこのような影響は避けられるが，その放出率が K_α-X 線の13.5%しかないため，測定誤差が大きくなる。このようにして得られた結果は，他の核種が壊変後，^{55}Fe 標準点線源と比較することにより得られた結果と多少異なる。しかしながら，大量の ^{52}Fe 中における ^{55}Fe 定量の困難さを考えればこの程度の誤差はしかたないものと思われる。崩壊曲線解析による ^{55}Fe の定量は，①照射終了後1－2日で結果が求まる，②自己吸収補正を行う必要がない，などの特長がある。

終わりに，本研究の推進を奨励していただいた樫田義彦博士，舘野之男博士，井戸達雄教授，山崎統四郎博士，平本俊幸博士，石井大道教授，技術的支援をいただいた玉手和彦氏，朽木満弘氏，中山隆氏，ファン・デ・グラーフ照射をしていただいた村越善次氏，高エネルギープロトン照射をしていただいたサイクロトロン管理課の方々に厚く感謝致します。

文　献

1) Anger, H.O. and Van Dyke, D.C.: *Science*, **144**, 1587 (1964)
2) Mary, E.A., O'Connell, Hows, J. and Lewis, S.M.: *Br. J. Radiol.*, **50**, 419 (1977)
3) Knopse, W.H., Rayudu, G.V.S., Cardello, M. et al.: *Cancer*, **37**, 1432 (1976)
4) Ku, H.T., Richards, P. Stang, G.L. et al.: *Radiology*, **132**, 475 (1979)

5) Atcher, W.R., Friedman, M.A., Huizenga, R.J. et al.: *J. Nucl. Med.*, **21**, 565 (1980)
6) Greene, M.W., Lebowitz, E., Richards, P. et al.: *Int. J. Appl. Radiat. Isot.*, **21**, 719 (1970)
7) Rayudu, G.V.S., Shrazi, S.P.H., Fordham, E.W. et al.: *ibid.*, **24**, 451 (1973)
8) Murakami, Y., Akiba, F. and Ezawa, O.: "Radiopharmaceuticals and Labelled Compounds", p. 257, IAEA, Vienna (1973)
9) Yano, Y. and Anger, H.O.: *Int. J. Appl. Radiat. Isot.*, **16**, 153 (1965)
10) Thakur, M.L., Nunn, A.D. and Waters, S.L.: *ibid.*, **22**, 481 (1971)
11) Saha, G.B. and Farrer, P.A.: *ibid.*, **22**, 495 (1971)
12) Sodd, V.J., Scholz, K.L. and Blue, J.W.: *Med. Phys.*, **1**, 25 (1974)
13) Lindner, L. and Johanna, C.K.: *Radiochimica Acta*, **26**, 97 (1979)
14) Lillicrap, S.C., Heather, S. and Clink, H.M.: "Radioactive Isotopen in Klinik und Forschung", Band 12. Int. Symp. Bad. Gastein., ed. Höfer (Egerman) (1976)
15) Herscheid, J.D.M., Vos, C.M. and Hoekstra, A.: *Int. J. Appl. Radiat. Isot.*, **34**, 883 (1983)
16) Hata, K., Baba, H. and Baba, S.: JAERI-M 5558 (1974)
17) Suzuki, K.: *Int J. Appl. Radiat. Isotopes*, **35**, 801 (1984)

Abstract

Production of ^{52}Fe by the ^{55}Mn($p, 4n$)^{52}Fe Reaction and Milking of ^{52m}Mn from ^{52}Fe

Kazutoshi SUZUKI
Section of Cyclotron, National Institute of Radiological Sciences
9-1, Anagawa 4-chome, Chiba-shi 260, Japan

The excitation functions were measured for the nuclear reactions of ^{55}Mn($p, 4n$)^{52}Fe *and* ^{55}Mn(p, n)^{55}Fe *by using thin manganese disks, specially prepared under a pressure of 200 - 250 kg/cm^2 at 400 - 500°C for 0.5 - 1 hour. The maximum cross section in the excitation function for the* ^{55}Mn($p, 4n$)^{52}Fe *reaction was found to be 1.4 mb at* E_p=*54 MeV. From the yield curve, 24.8 MBq/μA h (670 μCi/μA h) of* ^{52}Fe *was estimated to be produced with 0.45%* ^{55}Fe *contamination in the energy region between 73 and 39 MeV. Iron-52 was produced in the yield of 85 - 93% to the expected value from the yield curve in the energy region of 44 - 60 MeV. For the separation of* ^{52}Fe, *the radiochemical yield of* ^{52}FeCl$_3$ *was 70 - 92% and its radionuclidic purity was higher than 99%. Manganese-52m was obtained repeatedly by eluting the anion exchange column adsorbing* ^{52}Fe *with 6N-HCl in 99.9% radionuclidic purity and 86% yield to the expected value. The amount of* ^{55}Fe *in a large quantity of* ^{52}Fe *could be determined in 1 - 2 days from end of bambardment (EOB) by analyzing decay curve of* Mn-K$_\alpha$-*X ray from* ^{52}Fe *and* ^{55}Fe.

(Received May 29, 1985)

RADIOISOTOPES, **34**, 480-485 (1985)

Synthesis of *N*-Methyl and *N*-^{11}C-Methyl Spiperone by Phase Transfer Catalysis in Anhydrous Solvent

Hiroyoshi OMOKAWA, Akira TANAKA*, Mayumi IIO*,
Yoshiaki NISHIHARA**, Osamu INOUE***
and Toshio YAMAZAKI***

Faculty of Agriculture, Utsunomiya University
350, Mine-machi, Utsunomiya-shi, Tochigi Pref. 321
*Hiratsuka Research Laboratory, Sumitomo Heavy Industries, Ltd.
63-30, Yuhigaoka, Hiratsuka-shi, Kanagawa Pref. 254
**Nuclear Business Department Div., Sumitomo Heavy Industries, Ltd.
1, Kanda Mitoshiro-cho, Chiyoda-ku, Tokyo 101
***Division of Clinical Research, National Institute of Radiological Sciences
9-1, Anagawa 4-chome, Chiba-shi 260
Received March 23, 1985

Spiperone, a butyrophenone neuroleptic drug, has been used in binding studies of dopamine receptors.

Långström et al. developed N-^{11}C-methyl spiperone, and, in cooperate with Wagner et al., made it possible to visualize the distribution of dopamine receptors in the human brain in vivo. In this paper, we independently developed another synthetic method of N-^{11}C-methyl spiperone using the phase transfer catalyst in an anhydrous solvent.

Separation of the product is feasible only by passing the reactant solution through a Millipore filter and injecting it onto high pressure liquid chromatography (HPLC).

The time required for the synthesis and purification of N-^{11}C-methyl spiperone from ^{11}C-methyl iodide and spiperone was 20 min. Radiochemical yield exceeded 35% against ^{11}C-methyl iodide without correcting decay of the radioactivity.

Key Words: spiperone, carbon-11-*N*-methyl spiperone, dopamine receptor, phase transfer catalysis

1. Introduction

Positron emitting radionuclides such as carbon-11, nitrogen-13, oxygen-15 and fluorine-18 are being actively utilized in clinical researches and applications. Positron emitting radionuclides are easily produced by a compact cyclotron and compounds labelled with these radionuclides may make external detection feasible utilizing positron emission transaxial tomography (PETT).

Developments over the last decade of compounds labelled with these short half-life radionuclides (the half-time of ^{11}C is 20.4 min) on measuring metabolic rates in the brain and myocardium and of synthetic techniques open up new areas in nuclear medicine.

The application of PETT, especially in the psychiatric field, is noteworthy as a diagnostic agent for various diseases caused by aberration in brain receptors.

Spiperone, a butyrophenone neuroleptic drug (I, Fig. 1), has been used in binding studies of dopamine receptors.

Långström et al. synthesized *N*-^{11}C-methyl spiperone (II), by *N*-methylation of spiperone with ^{11}C-methyl iodide and in cooperate with Wagner et al., made it possible to visualize the distribution of dopamine receptors in the human brain[1),2)].

The syntheses of ^{11}C-methyl spiperone have recently been reported by Långström et al.[3)-5)] and Turton et al.[6)]

In this paper, we describe an another synthe-

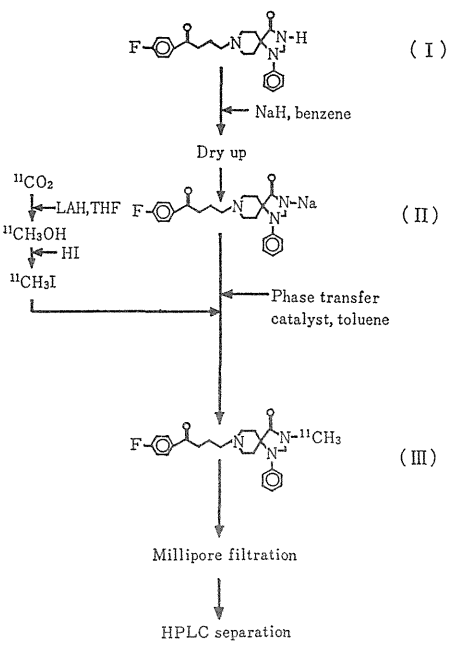

LAH: Lithium aluminium hydride
THF: Tetrahydrofuran

Fig. 1 Flow sheet of the synthesis of *N*-^{11}C-methyl spiperone.

tic method of *N*-^{11}C-methyl spiperone using phase transfer catalysis in anhydrous solvent.

2. Results and Discussion

N-methyl spiperone was already synthesized in 1964 by Janssen[7], but this method is not appliciable for the production of *N*-^{11}C-methyl spiperone.

Långström et al. reported a synthetic method of *N*-^{11}C-methyl spiperone from ^{11}C-methyl iodide and spiperone using tetra-*n*-butylammonium hydroxide solution as a catalyst in methylene chloride[3)-5)]. Turton et al. also developed a synthetic method of *N*-^{11}C-methyl spiperone using NaOH solution in acetone[6].

Spiperone, (8-(3-(*p*-fluorobenzoyl)propyl)-1-phenyl-1,3,8-triazaspiro(4,5)decan-4-one), (I) has 4 active groups for alkylation such as amide (CONH), tertialy amine and activated methylene ($COCH_2$). Therefore, sodium spiperone was chosen as a raw material to promote the methylation of amide.

In our method, *N*-^{11}C-methyl spiperone was synthesized by sodium spiperone (II) and ^{11}C-methyl iodide using a phase transfer catalyst such as tetra-*n*-butylammonium bromide or 18-crown-6 in anhydrous toluene with stirring at 50°C for 5 min. The product was separable by direct application of the reaction mixture onto preparative HPLC after Millipore filtration. Figure 1 shows the flow sheet of *N*-^{11}C-methyl spiperone synthesis and purification. Figure 2 shows a result of analytical HPLC after the Millipore filtration.

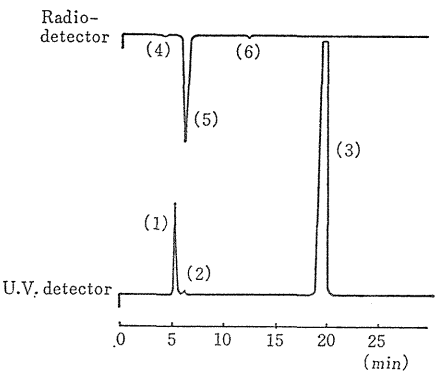

Column: YMC AM 312 (150×6 mm)
Eluant: 60% methanol, 0.01*M* triethylamine and 0.01*M* NaH_2PO_4, pH 6
Flow rate: 1 ml/min
(1): Spiperone (2) *N*-methyl spiperone
(3): Toluene (4): ^{11}C-methyl iodide
(5): *N*-^{11}C-methyl spiperone (6): Unknown

Fig. 2 Analytical HPLC of the reaction mixture.

The radio-detection confirmed that *N*-^{11}C-methyl spiperone was synthesized more than 98% against ^{11}C-methyl iodide.

Unreacted spiperone and non radioactive *N*-methyl spiperone produced by CO_2 were found by the U.V. detector.

The synthesis of *N*-^{11}C-methyl spiperone using anhydrous organic solvent is superior to the conventional methods, since the removal of water after the reaction is not required, and purification of the product is feasible only by passing the reaction mixture through a Millipore filter and injecting onto HPLC.

Sodium salt of spiperone used in this method was produced, for example, by reacting spiperone in an aromatic solvent with a strong base such as $NaNH_2$ or NaH under heating as mentioned in the US patent[7].

Table 1 Synthesis results

Catalyst	Yield of *N*-methyl spiperone(%)	Recovery of spiperone (%)
—	0	71
Tetra-*n*-butylammonium bromide	88	9
Tetra-*n*-butylphosphonium bromide	60	35
Tetra-*n*-butylammonium hydrogen sulfate	42	44
18-Crown-6	86	12
Tetra-*n*-butylammonium bromide*	0	20

* Solvent-H_2O phase system

The reaction mixture can be directly used for the methylation reaction. However, sodium salt of spiperone can be stored as a dry form after the removal of solvent.

Consequently, the necessary quantity of dry powder can be supplied as occasional demands, and such a compound may be suitable for hot synthesis.

Investigation was first performed using non radioactive materials to evaluate the effectiveness of catalysts.

Without a phase transfer catalyst, *N*-methyl compounds were scarcely obtained under the any condition so far tested.

Yields of *N*-methyl spiperone using various phase transfer catalysts are shown in Table 1.

Tetra-*n*-butylammonium bromide and 18-crown-6 showed excellent action of catalysis. The suitable solvents for the methylation process were aromatic hydrocarbons such as benzene and toluene dried with molecular sieves, and other solvents such as acetone, tetrahydrofuran (THF), *N*, *N*-dimethylformamide (DMF), and hexane showed lower yields (data not shown).

The phase transfer catalysts such as quaternary ammonium halides are generally used in the water-organic solvent phase system. Therefore, we tried the reaction of sodium spiperone and methyl iodide in the water-benzene system using tetra-*n*-butylammonium bromide. However in spite of the disappearance of spiperone, *N*-methyl compound could not be obtained.

This phenomenon might be caused by the formation of quaternary ammonium salts of spiperone which were transferred in the water phase. A few cases of solid–liquid phase reaction have already reported[8),9)]. It is interesting that a remarkable catalytic effect of the solid–liquid phase system appeared on the methylation of amide[10)].

In the present method, *N*-^{11}C-methyl spiperone was synthesized in 5 min from ^{11}C-methyl iodide and sodium spiperone with more than 98% radiochemical yield. As this method requires only a single vessel, automatic synthesis system will be easily constructed to avoid radiation exposure to the operator.

Labelled compounds should be synthesized in a high yield during a short time. The *N*-methylation reaction in anhydrous solvent using a phase transfer catalyst will be appreciable not only for the preparation of this compound but also for *N*-methylation of many useful compounds labelled with short half-life radionuclides.

3. Experimental

3·1 Instruments

Analytical HPLC was carried out by a reverse phase HPLC using YMC PACK AM 312 (ODS–5 μm, 150×6 mm). The eluant solution was prepared by adding triethylamine and sodium dihydrogen phosphate to 60% methanol to the final concentration of 0.01 *M* respectively and the mixture was adjusted pH 6 by phosphoric acid. Spiperone and *N*-methyl spiperone were eluted at 5.7 min and 6.8 min respectively with a flow rate of 1 ml/min. Monitoring of these compounds was performed with an U.V. detector at 250 nm (Hitachi model 635 M) and a NaI radio detector (Cambera model 802–3).

Preparative HPLC was carried out by YMC PACK A 324 (ODS–15 μm, 300×10 mm), and the eluant solution was prepared by the same method described above without adding sodium dihydrogen phosphate and the pH was adjusted to 7 to separate these compounds more clearly.

Spiperone and *N*-methyl spiperone were eluted at 10 min and 12.4 min respectively with a flow rate of 6 ml/min.

^{13}C-NMR (nuclear magnetic resonance) spectra of spiperone and *N*-methyl spiperone in $CDCl_3$ were measured at 25 MHz with a JEOL JNM–

FX100 spectrometer.

3·2 Synthesis of sodium spiperone

Sodium spiperone was obtained by the equimolor reaction of spiperone (200 mg) and NaH (23 mg in 60% oil) in anhydrous benzene (2 m*l*) in N_2. The mixture was stirred at room temperature for 15 min, and benzene was evaporated by a rotary evaporator. Sodium spiperone thus prepared was stored in a close-sealed vial reactor which could be kept in a cold and dark place for several months without change in quality.

3·3 Synthesis of *N*-methyl spiperone for structure determination

To sodium spiperone (500 mg) and 18-crown-6 (50 mg) in anhydrous benzene (5 m*l*), an equimolor amount of methyl iodide (80 μl) was added, and the mixture was stirred at 50°C for 20 min. After cooling, the insoluble material was filtered off with celite (1 g), and the filtrate was evaporated to dryness. Washing of the crude product with *n*-hexane afforded white crystals, which were chromatographed on a silica gel column (400×15 mm) with methylene chloride : methanol (92:8) to give 200 mg (40% yield) of pure *N*-methyl spiperone.

Figure 3 shows ^{13}C-NMR chemical shift (in $CDCl_3$) of spiperone and *N*-methyl spiperone. N-CH_3 carbon was observed at 27.5 ppm. The spectrum of *N*-methyl spiperone is identical with that of an authentic sample of *N*-methyl spiperone*.

3·4 Semimicro synthesis of *N*-methyl spiperone

To sodium spiperone (5 mg) and tetra-*n*-butylammonium bromide (5 mg) in anhydrous toluene (1 m*l*), an equimolor of methyl iodide (0.9 μl) was added, and the reaction mixture was stirred at 50°C for 5 min or sonicated 5 min in the water bath (50°C) with a sonicator (IUCHI VS-20, 32W).

After cooling, an insoluble material was filtered off, and the solution was analyzed by analytical HPLC.

N-methyl spiperone was obtained in the yield of 88% to 92%.

* Janssen Pharmaceutica, Beerse, Belgium

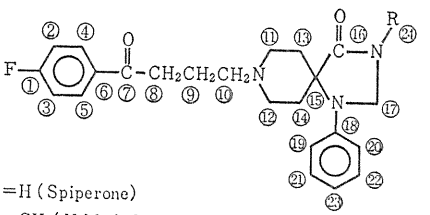

R=H (Spiperone)
R=CH_3(*N*-Methyl spiperone)

(ppm)

No.	Spiperone	Methyl spiperone
①	170.6	170.7
	160.5	160.5
②, ③	116.0	116.0
	115.1	115.1
④, ⑤	130.8	130.9
	130.5	130.5
⑥	133.7	133.7
	133.6	133.6
⑦	198.6	198.5
⑧	36.4	36.4
⑨	22.0	21.9
⑩	57.6	57.6
⑪, ⑫	49.7	49.6
⑬, ⑭	29.3	29.3
⑮	59.4	60.4
⑯	178.3	174.4
⑰	59.4	65.2
⑱	143.3	142.9
⑲, ⑳	115.9	115.4
㉑, ㉒	129.2	129.2
㉓	119.2	118.9
㉔	—	27.5

Fig. 3 ^{13}C-NMR chemical shift (tetra methyl silane basis) of spiperone and *N*-methyl spiperone in $CDCl_3$ measured at 25 MHz with a JEOL JNM-FX100 spectrometer.

3·5 Production of ^{11}C-methyl iodide

Carbon-11 was produced in the form of $^{11}CO_2$ *via* $^{14}N(p,\alpha)^{11}C$ reaction with proton on a target of nitrogen gas by a compact cyclotron (SUMITOMO CYPRIS Model 370).

^{11}C-methyl iodide was prepared by a ^{11}C-methyl iodide automatic synthesizer (SUMITOMO

CUPID Model C-11-B).

$^{11}CO_2$ was transferred by nitrogen current to a reaction vessel containing $LiAlH_4$ saturated in THF at −60°C.

After evaporation of the solvent, the $LiAlH_4$ complex obtained was directly converted into ^{11}C-methyl iodide by the addition of HI solution under reflux. ^{11}C-methyl iodide was carried over P_2O_5 and sodalime and finally collected at −60°C in anhydrous toluene.

3·6 Synthesis and purification of *N*-^{11}C-methyl spiperone

To sodium spiperone (2 mg) and tetra-*n*-butylammonium bromide (2 mg) or 18-crown-6 (2 mg), ^{11}C-methyl iodide in anhydrous toluene (250 μl) was added (1.5 GBq, corresponding to 40 mCi), and the mixture was stirred at 50°C for 3 to 5 min. After Millipore filtration (0.22 μm), the solution was injected onto preparative HPLC, and pure *N*-^{11}C-methyl spiperone was obtained.

Phase transfer catalyst used was eluted at 2.5 min.

Isolated *N*-^{11}C-methyl spiperone fraction was again analyzed with an analytical column. The radiochemical purity and the chemical purity were 100% and more than 95% respectively. A trace amount of spiperone was detected as an impurity. This synthesis produced about 0.56 GBq (15 mCi) of *N*-^{11}C-methyl spiperone after 20 min from the end of ^{11}C-methyl iodide synthesis.

Radiochemical yield exceeded 35% (not corrected for radioactive decay). The specific activity was 2.78 GBq/μmol (75 mCi/μmol) at the end of synthesis.

Acknowledgement

We are grateful to Prof. Dr. K. Yamashita, the Faculty of Agriculture, Tohoku University for his kind advice and identification of *N*-methyl spiperone. We also express our thanks to Eizai Co., Ltd. for their kind cooperation in offering spiperone and also to Dr. P. Ladurone of Janssen Pharmaceutica for providing us with an authentic sample of *N*-methyl spiperone.

References

1) Wagner, H.N. Jr., Burns, H.D., Dannals, R.F. et al.: Novel Symp. VII, Sweden, May 17–20 (1983)
2) Wagner, H.N. Jr., Burns, H.D., Dannals, R.F. et al.: *Science*, 221, 1264 (1983)
3) Ravert, H.T., Burns, H.D., Dannals, R.F. et al.: The Society of Nuclear Medicine 31st Annual Meeting, June 5–8, Los Angels (1984)
4) Dannals, R.F., Burns, H.D., Ravert, H.T. et al.: 5th Int. Symp. on Radiopharmaceutical Chem., July 9–13, Tokyo (1984)
5) Burns, H.D., Dannals, R.F., Långström, B. et al.: *J. Nucl. Med.*, 25, 1222 (1984)
6) Turton, D.R., Pike, V.W., Cartoon, M. et al.: 5th Int. Symp. on Radiopharmaceutical Chem., July 9–13, Tokyo (1984)
7) Janssen, P.A.: US Patent 3155670 (1964)
8) Zwierzak, A. and Sulewska, A.: *Synthesis*, 835 (1976)
9) Durst, H.D. and Liebeskind, L.: *J. Org. Chem.*, 39, 3271 (1974)
10) Omokawa, H. and Tanaka, A.: Japan Patent 59-044732 (1984)

要　旨

無水系における相間移動触媒による*N*-メチルおよび*N*-^{11}C-メチルスピペロンの合成

重川弘宜，田中　明*，飯尾真弓*，西原善明**，井上　修***，山崎統四郎***

宇都宮大学農学部　321 宇都宮市峰町 350

*住友重機械工業㈱平塚研究所　254 平塚市夕陽丘 63－30

**同，原子力開発本部　101 東京都千代田区神田美土代町 1 番地

***放射線医学総合研究所臨床研究部　260 千葉市穴川 4－9－1

ブチロフェノン系抗分裂症薬であるスピペロンは，ドーパミンレセプタの結合を研究するうえでよく用いられている。ロングストロームらは，新しく*N*-メチルスピペロンを合成し，ワーグナーらと共同で人間の脳のドーパミンレセプタ分布を生体で観察することを可能にした。われわれは独自にこの物質の合成を行い，無水系にて相間移動触媒を使用する方法を見出した。生成物の分離は反応液をミリポアフィルタに通し，高速液体クロマトグラフィに注入した。合成時間は$^{11}CH_3I$合成終了時より20分で，放射化学的収率は35%である。

《研究速報》

PK11195 の放射性医薬品としての可能性

井上　修*　山崎統四郎*　橋本　謙二**　小嶋　正治**

I. 序　論

高比放射能の標識リガンドを用いて，生体内での各種レセプターの分布やその活性を定量化し，新しい診断技術として開発する試みがなされ，すでに脳におけるドーパミンレセプター[1]，オピエートレセプター[2]，ベンゾジアゼピンレセプター[3]等に関しての報告がみられる．

ベンゾジアゼピンレセプターは，中枢性のレセプターと，心筋や腎などに主に存在するといわれる末梢性レセプターとに区別され，一般のマイナートランキライザーとしての薬理作用（抗不安，抗ケイレン，睡眠導入，筋弛緩）は中枢性のレセプターを介して発現することが判明している[4]．従来末梢性の Bz レセプターについては，その生理的役割が不明であったが，脳においてはグリアに主に存在すること[5]，またリンパ球，肺，心，腎，副腎等に高密度で存在することが報告されている[9,7]．最近，細胞の増殖との関連[8]や，心筋においては Ca チャンネルとの関連が指摘されており[9]，徐々にその生理機能が明らかになりつつある．末梢性の Bz レセプター測定用の機能リガンドとしては Ro5-4864 が従来用いられていたが，1983年に Fur らにより，特異的なアンタゴニストである PK11195 が開発された[10] (Fig. 1)．

リガンドレセプター結合の熱力学的解析の結果，アンタゴニストである PK11195 は，インキュベーション温度が 37°C になってもレセプターへの結合力はあまり低下しないことが判明しており[11]，インビボでのレセプター活性を定量化するには Ro5-4864 よりも優れていることが予想される．この PK 11195 についてはすでに Comar らにより，^{11}C の標識合成が報告されており[12]，また Fur らによりラット心筋も非常に高い取り込みがあることが報告されている[13]．著者らは，^{3}H-PK11195 のマウスにおける体内分布を検討し，心筋以外にも肺，副腎への取り込みが非常に高く，優れた放射性薬剤になる可能性が高いことが判明したのでここに報告する．

II. 方　法

^{3}H-PK11195 (87 Ci/mmol) は NEN より購入した．Ro5-4864 はロッシュ社 (Kamakura, Japan) より提供を受けた．その他の試薬は市販品を用いた．

^{3}H-PK11195 の生理食塩液 (1 μCi) 0.2 m*l* をマウス (C3H, ♂, 8～9 週齢) の尾静脈より投与し，1, 5, 10および20分後に屠殺して，血液，心，肺，腎，副腎，筋肉，脳を取り出し，それぞれの重量および放射能を測定した．

また，レセプターに対する特異的結合であるか否かについて検討するために，あらかじめ 20 mg/

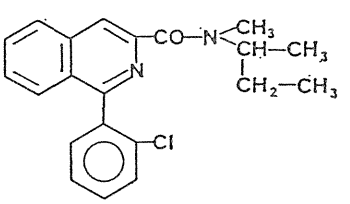

PK 11195

Fig. 1

* 放射線医学総合研究所臨床研究部
** 九州大学薬学部
受付：60年4月3日
最終稿受付：60年6月13日
別刷請求先：千葉市穴川 4-9-1 (〒260)
放射線医学総合研究所臨床研究部
井上　修

kg の Ro5-4864 (プロピレングリコール：エタノール 7:3, 0.1 ml) を腹腔内に投与し，5分後に ^{3}H-PK11195 を静注して投与5分後の放射能分布を求めた．またコントロール群として，プロピレングリコール，エタノール混液のみを腹腔内に前投与し，同様に ^{3}H-PK11195 の投与5分後の放射能分布を計測した．

Table 1 Biodistribution of ^{3}H-PK11195 in mice

(% Dose/g)

	1 min	5 min	10 min	20 min
Blood	6.46±3.85	2.11±0.19	2.22±1.58	0.99±0.10
Lung	137±31.8	27.2±5.16	20.1±0.57	15.3±2.70
Heart	22.7±4.25	13.5±3.12	10.2±2.04	7.54±0.57
Liver	2.43±0.44	4.72±0.36	6.62±0.36	6.52±0.68
Adrenal	37.3±7.04	56.8±21.5	66.3±3.49	71.5±28.8
Kidney	7.24±1.19	13.2±1.56	17.4±0.94	15.2±0.41
Muscle	1.85±0.18	2.58±0.21	2.02±0.21	1.54±0.02
Brain	3.78±1.45	2.12±0.45	1.69±0.55	0.97±0.28

Three mice in each group; average±1 s.d.

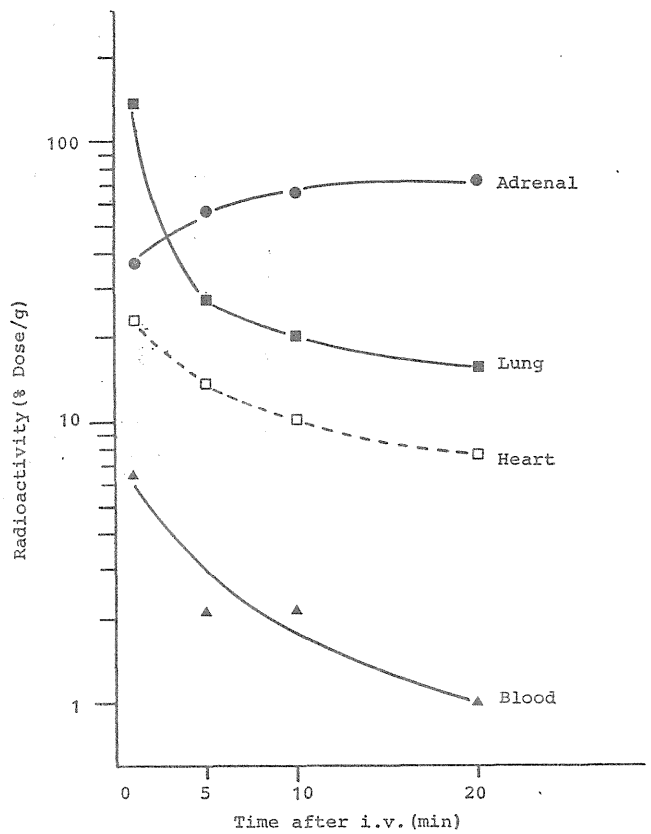

Fig. 2 Biodistribution of ^{3}H-PK11195 in mice.

Table 2 Effect of pretreatment with Ro5-4864 on biodistribution of ^{3}H-PK11195 at 5 min after injection into mice

	Control	Ro5-4864 (20 mg/kg)
Blood	3.15±0.38	2.05±0.08
Lung	49.2±4.79	6.51±0.85
Heart	18.0±7.44	4.11±1.91
Adrenal	94.7±14.9	84.5±5.07
Kidney	17.5±0.84	15.4±1.66
Brain	3.21±0.22	2.80±0.11

Three mice in each group; average±1 s.d.

III. 結　果

^{3}H-PK11195 のマウスにおける体内分布を Table 1 に示す．投与直後において，副腎＞肺＞心＞腎の順にきわめて高い割合で分布し，以後急速にその放射能は減少した．また脳にも比較的高い放射能の移行を認めた．Fig. 2 に，肺，心，副腎における放射能の経時変化を血中のそれと比較しているが，副腎を除いて各臓器とも血中とパラレルに変化しており，体内動態が比較的速く準平衡状態に到達することを示唆している．このことは将来レセプター活性を定量化する上できわめて有利な点であると思われる．

また，担体として非放射性の Ro5-4864 をあらかじめ処理した群では特に肺と心において著明な集積の低下を認めた (Table 2)．このことは，この各臓器における放射能の分布が主にレセプターとの特異的結合によるものであることを示しており，全放射能のうち肺では87%，心は77%以上が特異結合であった．

一方脳や副腎では Ro 5-4864 の前処理では放射能の集積度にそれほどの変化を認めないが，Ro 5-4864 と PK11195 との組織への移行速度の違いその他の条件を考慮したより厳密な方法を開発して，In Vivo での特異結合がどの程度あるかについて，検討を進める必要があろう．

IV. 考　察

Fur らはすでに ^{3}H-PK11195 をラットに投与し，心への放射能分布が高いこと，かつ，その放射能のうち少なくとも80%以上が，末梢性 Bz receptor に対する特異結合であることを示している．彼らはラットにおける心のプラトー到達時間は15分であることを報告しているが，われわれのマウスを用いた検討では静注直後が心放射能のピークであった．この差が種差によるものであるか否かについては今後の検討事項であろう．今回の実験結果で最も注目すべき点は，心，肺や副腎にこのトレーサーがきわめて高く分布し，しかも少なくとも心と肺においては，その大部分が末梢性 Bz receptor との特異結合によるものであるということにある．したがって，心機能の測定のみならず代謝臓器としての肺機能の検査にも今後の応用が期待されるトレーサーであるといえるであろう．一方，脳や副腎においては特異結合の割合が確定できなかったが，副腎における末梢性 Bz receptor は 50 pmol/mg protein 以上ときわめて高いことから特異結合の割合が高い可能性が十分あると考えられる．

現在，副腎スキャニング剤としては，^{131}I-アドステロールが用いられ，副腎皮質腫瘍等の診断に非常に有効であるといわれている．しかしながら，周囲組織におけるバックグラウンドが高いことからシンチグラム作成に投与後数日間の時間をおく必要がある．

また，製剤に含まれるアルコールによる副作用の発現も無視できない．一方 PK11195 は副腎への集積がきわめて高く，かつ，投与直後から撮影可能であるため，副腎機能の診断用トレーサーとしてきわめて高いポテンシャルを持っていると思われる．

また，脳においては末梢性 Bz receptor は主にグリア細胞に分布していることが報告されており，グリア細胞の活動をとらえることが可能となれば，その意義はきわめて高いと思われる．今後，末梢性 Bz receptor の生理機能について解明が進むことが予想されるし，またいくつかの病態モデル動物を用いた In Vivo での体内動態検討を通じて放射性薬剤としての有効性を確立していきたいと考えている．

謝辞 Ro5-4864を提供いただいたロッシュ社に深謝致します.

文 献

1) Wagner HN, Burn HD, Dannals RF, et al: Imaging dopamine receptors in the human brain by positron tomography. Science 221: 1264–1266, 1983
2) Dannals RF, Ravert HT, Frost JJ, et al: Radiosynthesis of an opiate receptor-binding radiotracer for positron emission tomography: ^{11}C-methyl-4-N-(1-oxopropyl)-N-phenylamino-4-piperidine carboxylate (^{11}C 4-carbomethoxycarfentanyl). Fifth Int Symp on Radiopharm Chem, Tokyo, pp. 186–188, 1984
3) Ehrin E, Johnstrom P, Stone-Elander S, et al: ^{11}C Labelling of ligands for PET studies of dopamine and benzodiazepine receptors. Fifth Int Symp on Radiopharm Chem, Tokyo, pp. 177–178, 1984
4) Squires R, Braestrup C: Benzodiazepine receptors in rat brain. Nature 266: 732–734, 1977
5) Benavides J, Quarteronet D, Imbault F, et al: Labelling peripheral type benzodiazepine binding sites in rat brain by using ^{3}H-PK11195, an isoquinoline carboxamide derivative: kinetic studies and autoradiographic localization. J Neurochem 41: 1744–1750, 1983
6) Le Fur G, Perrier N, Vaucher F, et al: Peripheral benzodiazepine binding sites: Effect of PK11195, 1-(2-chlorophenyl)-N-methyl-N-(1-methylpropyl)-3-isoquinoline-carboxamide. I. In vitro studies. Life Sci 32: 1830–1848, 1983
7) Benavides J, Malgouris C, Imbault F, et al: Peripheral type benzodiazepine binding sites it rat adrenal: binding studies with ^{3}H-PK11195 and autoradiographic localization. Arch Int Pharmacodyn 266: 38–49, 1983
8) Wang JKT, Morgan JI, Spector S: Benzodiazepine that bind at peripheral sites inhibits cell proliferation. Proc Natl Acad Sci USA 81: 753–756, 1984
9) Mestre M, Carriot T, Belin C, et al: Electrophysiological and pharmacological evidence that peripheral type benzodiazepine receptors are coupled to calcium channels in the heart. Life Sci 36: 391–402, 1985
10) Fur GL, Guilloux F, Rufat P, et al: Peripheral benzodiazepine binding sites: Effect of PK11195, 1-(2-chlorophenyl)-N-methyl-(1-methylpropyl)-3-isoquinoline-carboxamide. II. In vivo studies. Life Sci 32: 1849–1856, 1983
11) Fur GL, Vaucher N, Perrier ML, et al: Differentiation between two ligands for peripheral benzodiazepine binding sites, ^{3}H-Ro5-4864 and ^{3}HPK11195, by thermodynamic studies. Life Sci 33: 449–457, 1983
12) Camsonne R, Crouzel C, Comar D, et al: Synthesis of N-^{11}C-methyl, N-(methyl-1propyl), (chloro-2phenyl)-1 isoquinoline carboxamide-3 (PK11195): A new ligand for peripheral benzodiazepine receptors. J Labelled Compds Radiopharm 21: 985–991, 1984
13) Benavides J, Guilloux F, Rufat P, et al: In vivo labelling in several rat tissues of peripheral type benzodiazepine binding sites. Eur J Pharmacol 99: 1–7, 1984
14) Benavides J, Menager J, Burgevin MC, et al: Characterization of solubilized peripheral type benzodiazepine binding sites from rat adrenals by using ^{3}H-PK11195, an isoquinoline carboxamide derivatives. Biochem Parmacol 34: 167–170, 1985

Summary

Evaluation of ^{3}H-PK11195 as a Radioligand for the In Vivo Study of Peripheral Benzodiazepine Receptor

Osamu INOUE*, Toshio YAMASAKI*, Kenji HASHIMOTO**
and Masaharu KOJIMA**

**Division of Clinical Research, National Institute of Radiological Sciences*
***Faculty of Pharmaceutical Science, Kyushu University*

The potency of PK11195, which is a potent antagonist of peripheral type benzodiazepine receptor, as a radioligand for the in vivo study was evaluated by using ^{3}H-labelled compound. ^{3}H-PK11195 was highly distributed into mouse lung, heart and adrenal within 1 min after intravenous injection, and radioactivity in lung and heart rapidly decreased, while radioactivity in adrenal slightly increased. Saturation study using carrier Ro5-4864 indicated that more than 75% of total radioactivity in lung and heart was due to the specific binding with receptor, however the specific binding of this tracer in brain and adrenal was not clear in this study. This preliminary results strongly suggested that ^{11}C-PK11195 has a high potential as a radiopharmaceutical for the in vivo study of peripheral type benzodiazepine receptor function especially in lung, heart and adrenal.

Key words: Peripheral benzodiazepine receptor, PK11195, Lung, Heart, Adrenal.

《ノート》

^{11}C-Ro 15-1788 の前臨床段階における有効性と安全性の評価

Preclinical Evaluation of ^{11}C-Ro 15-1788 Solution for Injection as a Radiopharmaceutical

井上　修*　橋本　謙二*　山崎統四郎*　篠遠　仁*
舘野　之男*　鈴木　和年**　山口　寛***　樫田　義彦****

Osamu INOUE*, Kenji HASHIMOTO*, Toshiro YAMASAKI*
Hitoshi SHINOTO*, Yukio TATENO*, Kazutoshi SUZUKI**,
Hiroshi YAMAGUCHI*** and Yoshihiko KASHIDA****

*Division of Clinical Research, **Section of Cyclotron, ***Division of Physics,
****Senior Research Counselor, National Institute of Radiological Sciences

I. 序　論

Ro 15-1788 は Roche 社により開発された強力なベンゾジアゼピンのアンダゴニストであり，中枢神経系のベンゾジアゼピンレセプター（以下 Bz-R と略）に対しては，そのサブクラスを問わず非常に高い親和性を有することが示されている[1]．すでに Comar らにより ^{11}C による標識合成が示され，バブーンを用いた実験結果から脳内の放射能の大部分はレセプターに対する特異結合であることが示されている[2]．著者らはヒト脳における Bz-R の結合能を定量化し，生理学的応用や各種疾患の病態を把握することを目的として，^{11}C-Ro 15-1788 注射液の製法を確立し，前臨床段階における有効性と安全性との評価を行ったのでその結果を報告する．

* 放射線医学総合研究所臨床研究部
** 同　サイクロトロン管理課
*** 同　物理研究部
**** 同　特別研究員
受付：60年4月12日
最終稿受付：60年6月20日
別刷請求先：千葉市穴川 4–9–1　(〒260)
放射線医学総合研究所臨床研究部
井　上　　修

II. ^{11}C-Ro 15-1788 の製法

Comar らの原法[2]や Ehrin らの方法[3]を一部変更し，分離条件を変えることによって，水性注射剤として調製することができた．最終的に確立した製法を Fig. 1 および Table 1 に示す．

III. 小型動物における有効性の評価

1. 実験方法

上記の方法により調製した ^{11}C-Ro 15-1788 液 0.2 ml (約 100 μCi) をマウス (C_3H, ♂) に静注し，経時的に全脳および血液を取り出し重量および放射能を測定した．また ^{3}H-Ro 15-1788 生食液 (87 Ci/mmol, 1 μCi/0.2 ml) に，キャリアーとして非放射性の Ro 15-1788 を種々の濃度に添加し (3.4 ng/kg, 0.1 μg/kg, 3 μg/kg, 30 μg/kg, 300 μg/kg)，マウス静注 5 分後の，大脳皮質および血液の放射能分布を求めた．放射能測定は燃焼法により行った．

2. 結　果

^{11}C-Ro 15-1788 の体内挙動を Fig. 2 に示すが，静注後速やかに，脳へ移行し，以後単一指数関数

Key words: ^{11}C-Ro 15-1788, Benzodiazepine receptor.

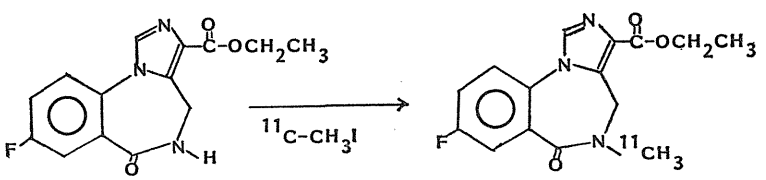

N-desmethyl derivative ^{11}C-Ro 15-1788

Fig. 1 Synthesis of ^{11}C-Ro 15-1788 solution for injection.

Table 1 製法

1. 高純度の N_2 ガスをターゲットに充填する (ターゲット圧 10–20 kg/cm²)
2. 反応経路をよく乾燥する.
3. 2–20 μA の Proton (10–16 MeV) を 10–40 分間照射する.
4. $^{11}CO_2$ 還元槽に LiA1H4-THF 溶液 (0.1–1.0 m*l*) を注入する.
5. Hl 槽に Hl (0.2–1 m*l*) を注入する.
6. 反応槽に N-desmethyl 体, NaH, の DMF 溶液 (0.2–0.5 m*l*) を注入する.
   {N-desmethyl 体 4 mg/m*l*, NaH-DMF (0.1 g/m*l*, 10 *l*)}
7. $^{11}CO_2$ を還元槽に導入し, 以後自動遠隔操作により, ^{11}C-Ro 15-1788 溶液を分離する. (アセトニトリル-0.1 M リン酸バッファー混合液, 逆相高速液体クロマトカラム C-18)
8. 溶媒を留去する (100°C 以下 -15 分以内)
9. 注射用生理食塩水液 (3–11 m*l*) にて溶解する.
10. 限外濾過膜, またはミリポアフィルタにて無菌バイアル中に濾過する.

的に放射能は減少した. この脳中放射能の減少は, 血中放射能の減少ときわめてパラレルに変化しており, このトレーサーは体内で比較的速く, 準平衡状態に到達することが推定される. また Fig. 3 に示すように, 非放射性のキャリアー Ro 15-1788 の投与量を増すに従って, 大脳皮質の放射能は著明に減少するが, 血中放射能はほとんど変化しない. この投与量による大脳皮質の放射能の減少は, Bz-R との結合に対する競合阻害によるものであり, Bz-R が最も高密度に分布している大脳皮質では, その放射能の 80% 以上は特異的結合によるものであることが判明した. 以上のように, このトレーサーは, 静注後, 速やかに脳へ移行し, Bz-R と特異的に結合することが明らかになった.

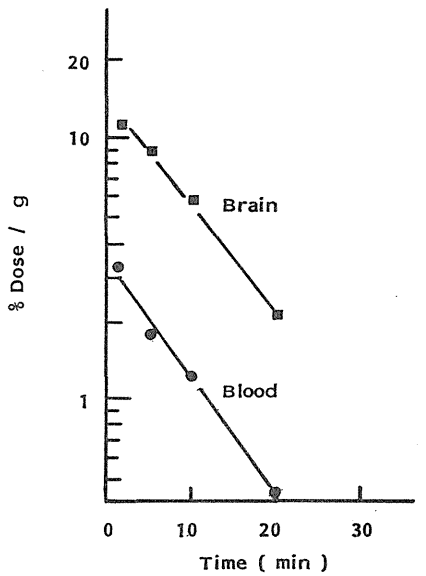

Fig. 2 Biodistributions of ^{11}C-Ro 15-1788 in mice (n=3).

IV. 品質試験結果

Table 2 に示すように, ^{11}C-Ro 15-1788 の規格および試験方法を定め, 3 Lot の製剤につき試験を行った結果, いずれの項目にも適合した. Table 3 に主な項目についての試験結果を示す.

V. 急性毒性試験

A. 主な含有成分

主成分である Ro 15-1788 のマウスまたはラットにおける LD50 値はそれぞれ 100–300 mg/kg i.v. (マウス), 100–1,000 mg/kg i.v. (ラット) である[4]. 10 mCi (100 mCi/μmol) を体重 60 kg のヒ

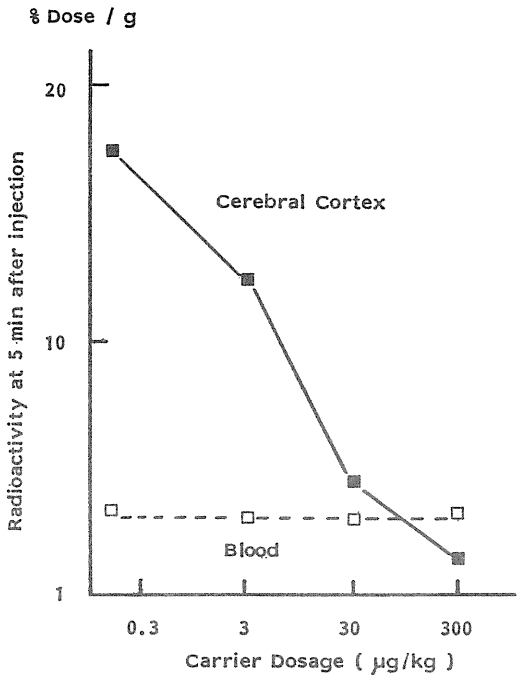

Fig. 3　Effect of carrier Ro 15-1788 on the biodistributions of ^{3}H-Ro 15-1788 in mice (n=3).

トに投与した場合少なくとも 30,000 倍以上の安全係数を有することになる．

分離精製の段階で微量混在してくる N-desmethyl 体については，マウスについては 5 mg/kg i.v. の投与量では，なんら異常を認めなかった．この 5 mg/kg を最大無作用量と仮定すると本注射剤の規格 (30 μg/10 mCi 以下) においては，10 mCi を体重 60 kg のヒトに投与した場合 10,000 倍以上の安全係数を有する．

B. 最終製剤の急性毒性

雄 C_3H マウス (7–8 週齢，体重約 30 g) を用い，各 Lot の最終製剤 0.2 m*l* を尾静脈より投与し，1 週間にわたって経過を観察した (n=10)．その結果 3 Lot ともに死亡例はなく，なんらの異常を認めなかった．この製剤を 10 mCi 投与した場合においても最低限 100 倍以上の安全係数を有することが判明した．

Table 2　^{11}C-Ro 15-1788 注射薬規格および試験方法

(1) 性　状	無色透明の液体
(2) 容　量	3–11 m*l*
(3) pH	pH 試験紙により pH を測定するとき 2.5–6.0 である
(4) 異　物	肉眼で観察するときこれを認めない
(5) 放射能	校正されたキュリーメーターで測定するとき 3 mCi 以上である
(6) 確認試験	①本品について，NaI (Tl) または Ge (Li) 検出器を用いてガンマ線スペクトルを描くとき，511 KeV においてピークを認める ②本品につき半減期を測定するとき，その値は 19–21 分である また，20分の測定間隔における残存率は 47–53% である
(7) 純度試験	①放射性核種異物：確認試験①により試験を行うとき，511 KeV 以外にピークを認めない ②放射性異物：ラジオ液体クロマトグラフ法 (C-18 逆相カラム CH_3CN-0.01 M H_3PO_4 1:1 または 3:2) にて検定するとき，^{11}C-Ro 15-1788 以外の不純物は 4% 以下である ③N-desmethyl 体含量：純度試験②により試験を行ったときの UV (254 nm) の吸光度と検量線より定量するとき 30 μg/10 mCi 以下である
(8) 比放射能	純度試験②により試験を行い，UV (254 nm) の吸光度と検量線より定量するとき，50 Ci/mmol 以上である
(9) 無菌性	放射性医薬品基準の無菌試験法，またはバクテック試験法により試験を行うとき無菌である
(10) 発熱性	放射性医薬品基準のエンドトキシン試験法により試験を行うとき，本品は発熱性物質を含まない

本規格のうち，(9)，(10) の項目については事後検定を行うことが可能である

Table 3 ^{11}C-Ro 15-1788 の規格試験成績

Lot No.	放射能 (mCi)	比放射能 (mCi/μmol)	放射化学的純度	放射核化学的純度	N-desmethyl 体 (μg/10 mCi)
Ro-001	68.2	417	>99%	>99%	3.0
Ro-002	32.0	196	>99%	>99%	2.2
Ro-003	40.2	673	>99%	>99%	1.0

VI. 被曝線量の推定

1. 方　法

^{3}H-Ro 15-1788, 0.2 m*l* (1 μCi, 0.01 nmol) をマウス (C_3H, ♂, 8–9 週齢) の尾静脈より投与し，経時的に血液，肝，心，肺，筋，脳を摘出し，その重量および放射能を測定して放射能分布を算出した．その結果に基づいて，各臓器における生物学的半減期を推定し，MIRD 法によりヒト (25歳，体重 60 kg) における被曝線量を推定した．なお，直接放射能分布を測定しなかった臓器については，その放射能濃度は血液中の放射能と同一であると仮定して計算した．

2. 結　果

Table 4 に ^{3}H-Ro 15-1788 のマウスにおける体内分布を示す．この結果に基づいて，各臓器における residence time A_h を求め，次式に従って臓器 r_k における被曝線量を推定した．

$$D(r_k)=\sum_h \tilde{A}_h \cdot S(r_k \leftarrow r_h)$$

$$\tau_h=\int_0^\infty A_h(t)/Ao \cdot dt \quad (hr)$$

ここで

$\tilde{A}_h = Ao\tau_h$: 臓器 r_h における the cumulated activity,

$S(r_k \leftarrow r_h)$: Absorbed dose per unit cumulated activity, (rad/Ci-hr) (MIRD pamphlet No. 11),

* 日本人の $S(r_k \leftarrow r_h)$ は MIRD の比吸収割合 (ICRP. Pub23) から日本人の体格を変数として「変換法」で計算した．

その結果を Table 5 に示す．

最大 5 mCi 投与したと仮定して，最も被曝線量が多い小腸においてもその値は約 300 mR と非常に少ないことがわかった．

Table 4 ^{3}H-Ro 15-1788 のマウス体内分布 (n=3)

%dose/g

	1 min	15 min	30 min	60 min
血液	4.65	1.10	1.49	0.233
肝臓	5.95	5.64	1.74	0.368
脾臓	2.40	0.657	0.439	0.194
小腸	6.80	36.95	13.81	6.72
腎臓	8.13	6.81	3.58	0.85
心臓	5.57	0.819	0.374	0.122
肺	5.99	1.07	0.485	0.165
睾丸	1.88	1.13	0.595	0.197
筋肉	3.74	1.35	0.462	0.107
膀胱	1.66	71.60	63.28	11.91
脳	9.71	5.47	1.93	0.229

Table 5 ^{11}C-Ro 15-1788 による主要臓器の推定被曝線量 (成人に 1 mCi を静脈内投与したとき)

	mRad
副　腎	6.2
膀　胱	51
小腸壁	78
大腸壁	6.3
肝	9.7
腎	12
肺	4.3
膵	3.8
脾	3.6
睾　丸	2.9
卵　巣	5.8
甲状腺	4.8
乳　腺	0.9
骨　(腕)	4.8
骨　(脚)	8.5
赤色骨ずい	3.1

VII. 結　論

^{11}C-Ro 15-1788 は，脳内の Bz-R と特異的に結

合し，かつ毒性，被曝線量からみても安全性の高い放射性薬剤であるといえる。

Ro 15-1788 および N-desmethyl 体を供与して下さった日本ロッシュ株式会社ならびに貴重な助言をいただいた中村圭二，岡田敏一両博士に深謝致します.

文　献

1) Hunkeler W, Mohler H, Pieri L, et al: Selective antagonists of benzodiazepines. Nature **290**: 514–516, 1981
2) Maziere M, Hantraye P, Prenant C, et al: Synthesis of Ethyl 8-Fluoro-5,6-dihydro-5-^{11}C methyl-6-oxo-4H-imidazo 1,5-a 1,4 benzodiazepine-3-carboxylate (Ro15-1788-^{11}C): A selective Radioligand for the In Vivo Study of Central Benzodiazepine Receptors by Positron Emission Tomography. Int J Appl Radiat Isot **35**: 973–976, 1984
3) Ehrin E, Johnstrom P, Stone-Elander S, et al: C-11 labelling of Ligands for PET Studies of Dopamine and Benzodiazepine Receptors. 5th Inter Symp on Radiopharm Chem July 9–13. Tokyo, 1984
4) Bonetti EP, Pireri L, Cumin R, et al: Benzodiazepine Antagonist Ro 15-1788: Neurological and Behavioral Effects. Psychopharmacology **78**: 8–18, 1982

A CENTRAL SYSTEM FOR THE SIMULTANEOUS CONTROL OF SEVERAL ITEMS OF EQUIPMENT FOR THE PREPARATION OF RADIOPHARMACEUTICALS

K. SUZUKI
National Institute of Radiological Sciences,
Chiba, Japan

Abstract

A CENTRAL SYSTEM FOR THE SIMULTANEOUS CONTROL OF SEVERAL ITEMS OF EQUIPMENT FOR THE PREPARATION OF RADIOPHARMACEUTICALS.

A new control system was developed for the preparation of short-lived radiopharmaceuticals. It has the following characteristics: (1) control and measurement of a large number of equipment components (digital output 480 channels, digital input 120 channels, analogue input 128 channels, analogue output 16 channels); (2) parallel control of maximally five items of equipment located in separate places; (3) easy programming procedure; and (4) easy construction of new equipment. To demonstrate the effectiveness of the system, two sets of equipment were constructed and connected to the system for the preparation of ^{11}C-labelled Flumazepil (Ro 15–1788) – a benzodiazepine receptor antagonist – and ^{13}N-labelled ammonia. The ^{11}C-labelled Ro 15–1788 (125 mCi) was obtained in 30 minutes, with a specific activity of 670 Ci/mmol and a radiochemical purity of $>$ 99%. During the synthesis of ^{11}C-labelled Ro 15–1788, the ^{13}N-labelled ammonia (180 mCi) was prepared in 5 minutes, with $>$ 99% radiochemical purity.

1. INTRODUCTION

Recently, some automated equipment has been developed for the production of cyclotron-produced radiopharmaceuticals [1–5]. This equipment is suitable for the routine production of selected compounds, such as ^{15}OO, $^{11}CO_2$, $^{13}NH_3$ and ^{18}F-FDG. It is often necessary to modify the equipment at hand or to develop new equipment in order to meet the requirements of nuclear medicine for new radiopharmaceuticals. For the user himself, it is nearly impossible to do this without special knowledge of computer programming, electronics, and so on. Furthermore, it takes a long time to develop new equipment, and it is expensive.

This paper presents a new control system which enables the user to develop or modify an automatic synthesis equipment for investigation or routine production of radiopharmaceuticals. The system can control several items of equipment in parallel, so as to use the cyclotron efficiently.

2. THE CENTRAL SYSTEM

A block diagram of the central system is shown in Fig.1. The system can deal with a large number of equipment components, such as electric valves, heaters, flow meters/controllers and radiation detectors, corresponding to the hardware of more than five standard items of equipment, for the production of various radiopharmaceuticals, e.g. $^{11}CH_3I$, $^{13}NH_3$, ^{18}F-FDG. Fast control and data transfer are possible (200 μs per analogue input) since the computer HP9816 (16 bits) is used as a system controller and is connected to an interface having its own CPU with ROM and RAM through the GPIB bus. The system is fixed and cabled; only the items of equipment are exchangeable. Several items of equipment can be connected simultaneously to one or more terminal boxes established in the working areas (hot cell, irradiation room, etc.), as shown in Fig.2. To prepare an automatic equipment, all that is necessary is to assemble the components of the equipment, such as sensors and electric valves, and to connect them by cables to the nearest terminal box.

The system program is designed to control maximally five items of equipment (corresponding to five jobs) in parallel. The central system is fixed and need not be changed, even if a part of an equipment item is modified or new equipment is installed, since all information required for control is given in tabular form for the corresponding job. Each job can contain at most six tables for control and one table for display. The display-only table is transferred internally to job six and is executed there when it is selected on the keyboard. Table I shows an example of a system program table, which can contain a 100-step program. The meaning of each command is described briefly. The commands are performed in the order of step number. The order can be changed when the commands AI (analogue input), DI (digital input), TM (timer), BR (jump without any condition) are carried out. Up to eight components can be controlled in one step by the commands AI (analogue input), BS (background subtraction), AO (analogue output), DI (digital input) and DO (digital output). One or two program tables are usually sufficient for the synthesis of a radiopharmaceutical. Other program tables are used for preparatory work, such as a leak check of a production system. The tables can be connected with each other by the NX command.

The flow of keyboard operation is shown in Fig.3. The system program can manage only one table for each job at a time, which is selected by the user from six tables for the corresponding job. Start/stop for each job and other commands are carried out by pressing the respective function keys. The meaning of each function key is displayed on a CRT and the proper meaning can be assigned to the function keys according to the stage of operation. Manual operation is also possible with the commands described in Table I. Each job has individual parameters, such as job number, table number, step number, start and end flags and timer-counter, to describe its present situation. The system program monitors

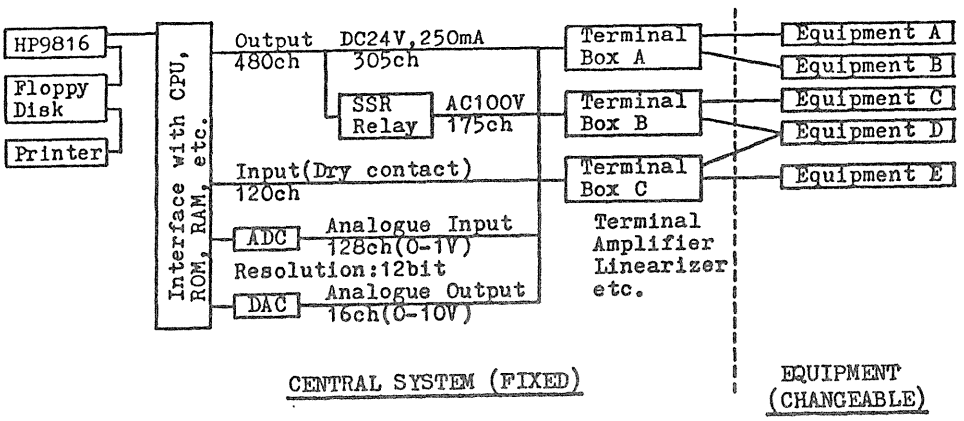

FIG.1. Block diagram of the central system, connected to several items of equipment.

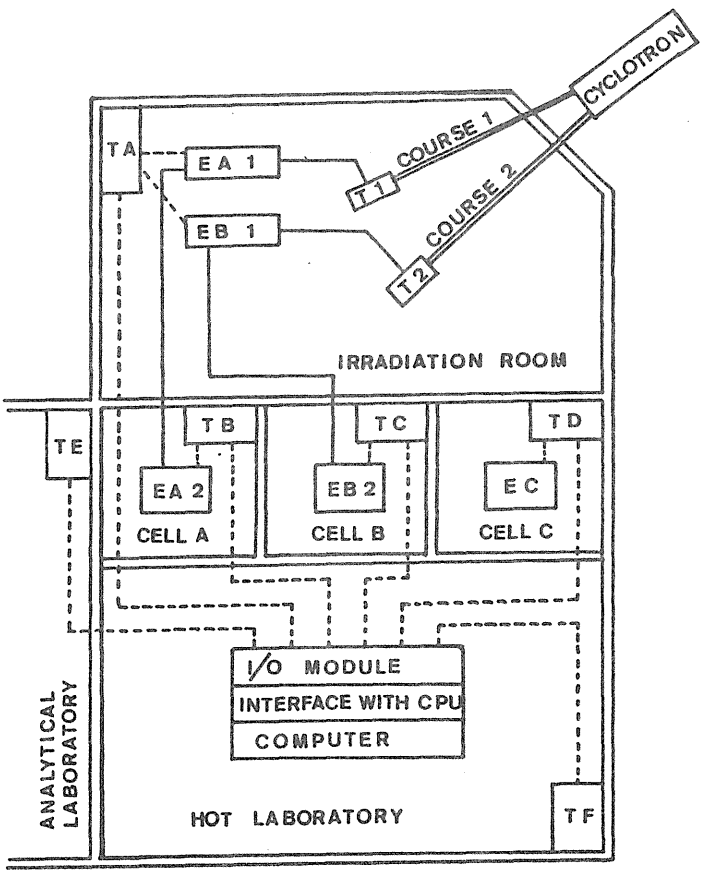

FIG.2. Central system connected to the equipment for the production of ^{11}C-labelled Flumazepil (Ro 15-1788) and ^{13}N-labelled ammonia.
T1, T2 – target boxes for ^{11}C and ^{13}N production; EA 1, EA 2 – equipment for ^{11}C-labelled Ro 15-1788; EB1, EB2 – equipment for $^{13}NH_3$ production; TA to TF – terminal boxes with amplifier, linearizer, etc.

TABLE I. CONTENTS OF A TABLE USED IN THE SYSTEM PROGRAM

Step	Command	Auxiliary command	Branch	Parameter	Channels 1, 2, 3, ..., 8
1	AI	DS, LM, etc.	20	120	13, 24, ...
	Analogue data input, scaling, jump to specified step if the condition is satisfied				
2	BS				5, 8, 13, ...
	Set present analogue data of selected channels as background				
3	AO	. . , DS		2500	5, 10, ...
	Analogue data output and scaling for selected channels				
4	DI	. . , DS	15	0 or 1	7, 3, 89, ...
	Jump to specified step according to 'AND' or 'OR' conditions of digital input for the selected channels				
5	DO	. . , DS		0 or 1	6, 35, 7, 15, ...
	Output DC 24 V or AC 100 V to the selected channels				
6	TM	. . , SE	70	130	
	Set timer and jump to specified step when time is up				
7	BR	. . , CL	10	3	
	Jump to specified step for a given number of repetitions				
8	US		25	70	
	Subroutine command for more complicated control				
9	PA				
	Interrupt program execution of the present table for user's intervention; other program execution is not affected				
10	NX			3	
	Jump to the first step of specified table				
--	--	--	--	--	--, --, --------
--	--	--	--	--	--, --, --------
--	--	--	--	--	--, --, --------
100	--	--	--	--	--, --, --------

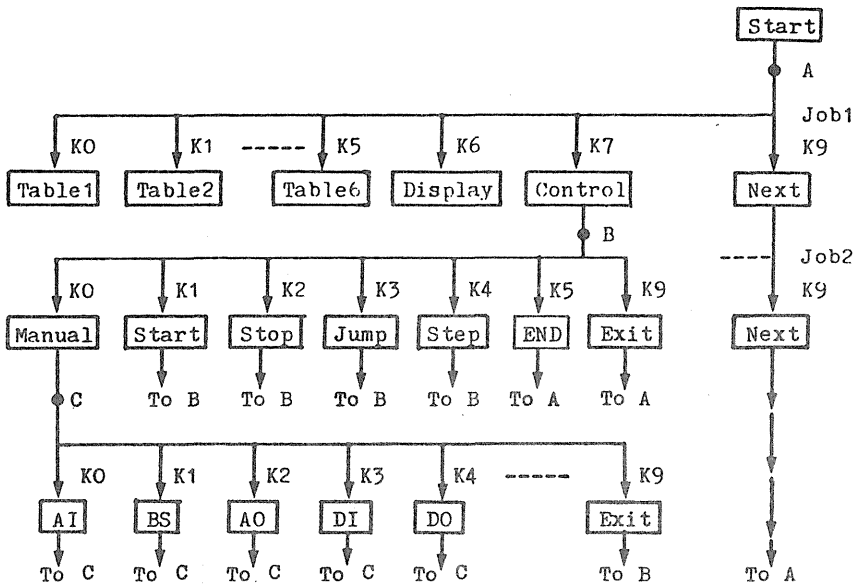

FIG.3. Flow of keyboard operation for the parallel control of several items of equipment. K0-K 9 – function keys; Table 1 to Table 6 – sequence of program tables described in Table I; manual – manual operation for AI, BS, AO, DI and DO commands; start/stop – start/stop of the program execution for the job; jump/step – go to next step in the sequence table before and after executing the present step.

and changes the parameters of each job, performing a one-step program for each job, successively in circles. When a function key is pressed, only the fact of intervention and the key number are memorized by the system and the command is carried out as soon as the system program comes to the corresponding job. The time required for the system program to make one cycle is about 0.3 s; because of this very short time interval, several items of equipment appear to be controlled at the same time.

3. APPLICATION OF THE SYSTEM

To demonstrate the effectiveness of the present system, two items of equipment were prepared by manually assembling electric valves, heaters, pressure sensors, etc. One is for the preparation of ^{11}C-labelled Flumazepil (Ro 15–1788) – a benzodiazepine receptor antagonist (Fig.4) – the other for $^{13}NH_3$ production (Fig.5). The labelling procedure is similar to that described by Ehrin et.al. [6].

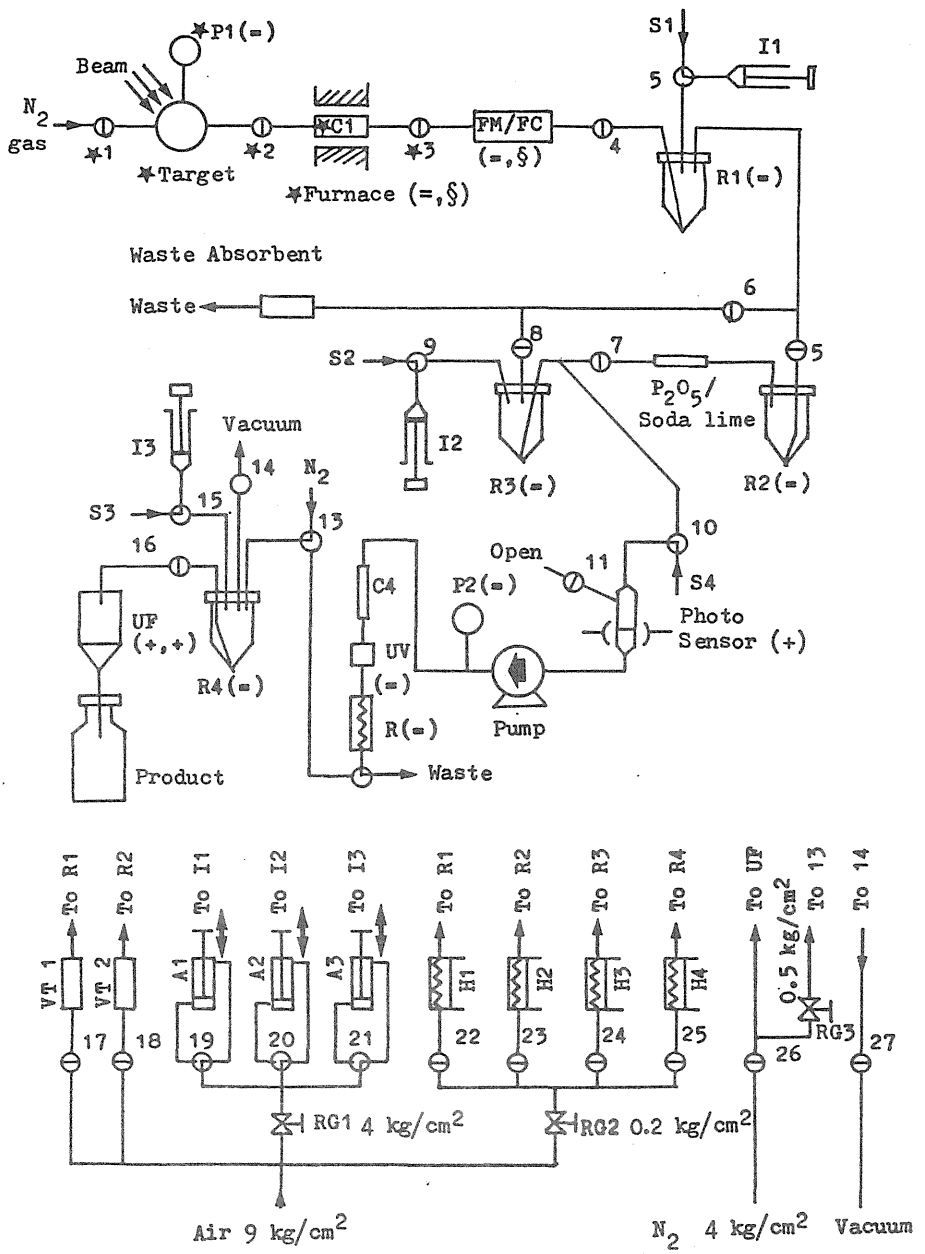

FIG.4. Diagram for the production and purification of Ro 15-1788 with $^{11}CH_3I$.
1 to 27 – electric valves; P1, P2 – pressure sensors; FM/FC – flow meter and flow controller; R1 to R4 – reaction vessels; I1 to I3 – injectors; S1 to S4 – solutions; C1 – CuO column (800°C); C2 – HPLC ^{18}C reverse-phase column; R – radioactivity sensor; VT1, VT2 – cooling tubes (-10°C); A1 to A3 – air cylinders; H1 to H4 – heaters; RG1 to RG3 – pressure regulators; UF – ultrafiltration equipment [8]*; = is AI; § is AO; + is DI; ★ is components assembled in EA1 (Fig.2); other components are in EA2.*

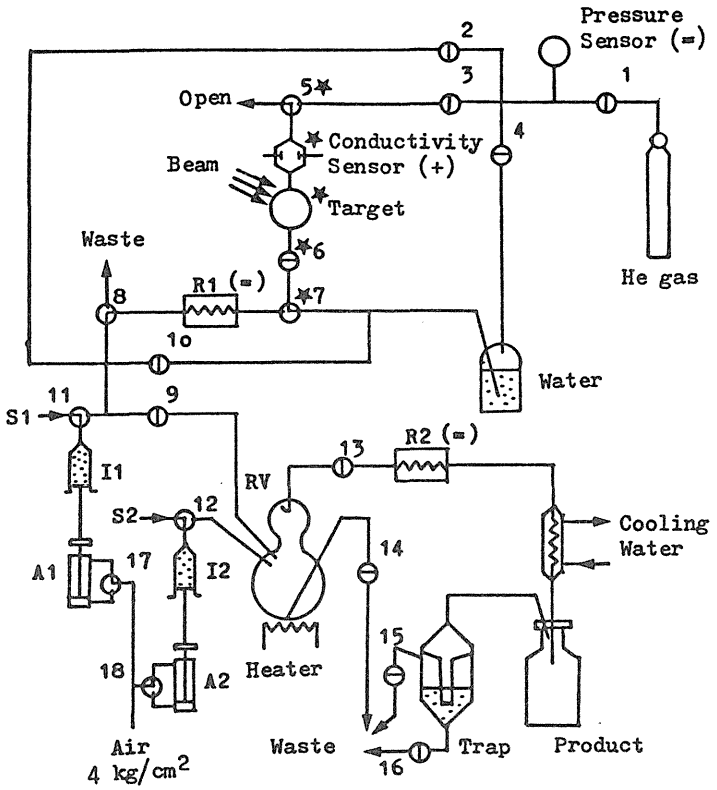

FIG.5. Diagram for $^{13}NH_3$ production.
1 to 18 – electric valves; R1 and R2 – radioactivity sensors; I1 and I2 – injectors; A1 and A2 – air cylinders; S1 – 10N NaOH; S2 – 10% $TiCl_3$; RV – reaction vessel; ★ – components assembled in EB1 (Fig.2); other components are in EB2; + is DI; = is AI.

Pure nitrogen gas (purity > 99.9998%) was introduced into the target box (inner diameter: 20 mm at inlet, 30 mm at outlet; length 150 mm) at a pressure of 14 kg/cm^2 and the target was bombarded by 14 MeV protons from the NIRS isochronous cyclotron. The irradiated gas was led into the reduction vessel (containing 1 mL of tetrahydrofuran (THF) with $LiAlH_4$) after passing through the CuO column (800°C) at a flow rate of 200 mL/min. One millilitre of water was injected into the vessel after evaporation of THF. The generated ^{11}C-labelled methanol was evaporated into the second vessel, containing conc. HI, and converted to $^{11}CH_3I$, which was trapped in the third vessel, containing 500 μL of dimethylformamide (DMF) with 2.5 mg of NaH and 2.5 μmol Ro 15-5528 at −2°C. The mixture was allowed to react for one minute at 50°C and was then transferred into the reservoir for HPLC. The reaction vessel and the tube line were washed with 1 mL H_2O. The product was purified by ^{18}C reverse-phase

column chromatography (Nihon Bunko KK, Tokyo), using acetonitrile: 0.01M H_3PO_4 (40:60) as the mobile phase, at a flow rate of 3 mL/min. Up to this point, everything proceeded automatically. Evaporation of the solvent, addition of 5 mL sterile isotonic saline and filtration were carried out manually because of the slow speed of evaporation. The synthesis time was about 30 min. The ^{11}C-labelled Ro15-1788 (125 mCi) was obtained with a specific activity of 670 Ci/mmol and > 99% radiochemical purity.[1] Pyrogens were not detected in the product.

The $^{13}NH_3$ was synthesized by the $TiCl_3$ method [7]; the diagram for $^{13}NH_3$ production is shown in Fig.5. Distilled water was introduced into the target box by helium gas pressure. The water level was determined with a conductivity sensor. After filling, the water level was somewhat lowered by applying a pressure from the opposite direction, in order to avoid electric noise during irradiation. Only a concentrated fraction of ^{13}N activity of the irradiated water was collected in the reduction vessel and then 5 mL of 10N NaOH and 5 mL of 10% $TiCl_3$ solution were injected into the vessel. The $^{13}NH_3$ generated was evaporated into a sterilized vial. The synthesis time was about 5 min. The radiochemical yield was about 80% and the radiochemical purity was > 99%.

By using this central system, the equipment for the production of ^{11}C-labelled Ro 15-1788 and $^{13}NH_3$ could be controlled as if two specially designed separate controllers had been used. The programming procedure required to make the equipment work was to fill in the program tables, as demonstrated in Table I, and to fill in an I/O condition table determining the scaling parameters of time span and offset for analogue input and output. The tables for the two different items of equipment are not interdependent. The heating and cooling devices, the glassware and the solvent injectors, etc., used in the development of the equipment, are standardized.

With this central system and the standardized components, it is easier and quicker for the user to modify equipment for the preparation of short-lived radiopharmaceuticals and to develop new equipment; also, the costs involved are lower.

ACKNOWLEDGEMENTS

The author wishes to thank Dr. O. Inoue, Dr. T. Yamasaki, Dr. Y. Kasida of NIRS and Prof. D. Ishii of Nagoya University for fruitful discussions. Mr. M. Kuchiki and Mr. K. Tamate are thanked for their technical support. Special thanks are also given to the cyclotron crew of NIRS.

[1] Ci = 37 GBq.

REFERENCES

[1] SUZUKI, K., TAMATE, K., Int. J. Appl. Radiat. Isot. 358 (1984) 771.
[2] IIDA, S., et al., "Remote-controlled synthesis system for production of C-11 hydrogen cyanide", Radiopharmaceutical Chemistry (Proc. 5th Int. Symp. Tokyo, 1984), Business Centre for Academic Societies, Tokyo (1984) 312.
[3] PALMER, A.J., et al., "Preparation of carbon-11 labelled erythromycin – a lactobionate for the study of the antibiotic in vivo", Radiopharmaceutical Chemistry (Proc. 4th Int. Symp. Jülich, 1982), Kernforschungsanlage Jülich GmbH (1982) 5.
[4] BLESSING, G., et al., "A computer-controlled automatic apparatus for radiochemical separation of ^{75}Br and synthesis of ^{75}Br-labelled radiopharmaceuticals", ibid., p. 63.
[5] IWATA, R., et al., "Fully automated synthesis system of ^{18}F-2-deoxy-2-fluoro-D-glucose", ibid., p. 80.
[6] EHRIN, E., et al., "C-11-labelling of ligands for PET studies of dopamine and benzodiazepine receptors", Radiopharmaceutical Chemistry (Proc. 5th Int. Symp. Tokyo, 1984), Business Centre for Academic Societies, Tokyo (1984) 177.
[7] KRIZEK, H., et al., J. Nucl. Med. 14 (1973) 629.
[8] SUZUKI, K., et al., Nucl. Med. Commun. 5 (1984) 19.

RADIOISOTOPES, 35, 127-129 (1986)

ノート

$^{18}F^-$ を利用する標識合成装置の開発

在間直樹，入江俊章*，福士　清*，山崎統四郎*，西原善明**
東京ニュークリア・サービス㈱　110 東京都台東区東上野 3-15-14
*放射線医学総合研究所　260 千葉市穴川 4-9-1
**住友重機械工業㈱　100 東京都千代田区神田美土代町 1

1985年12月5日　受理

Key Words: fluorine-18-labelled compounds, oxygen-18-enriched water, fluorinating reagent

1. はじめに

^{18}F はサイクロトロンによって製造される短寿命ポジトロン放出核種の中でも比較的長い半減期（109.8分）をもち，その化学的特性，エネルギー特性からポジトロンエミッショントモグラフィと組合わせた核医学診断研究に利用される放射薬剤の重要な標識核種である。最近，^{18}F-フッ化物によるステロイド[1]，炭水化物[2]，脂肪酸[3]，ブチロフェノン系弛緩薬[4]，核酸塩基[5]の標識合成がなされ，^{18}F-アニオンはきわめて重要な標識前駆体となってきた。

^{18}F-アニオンの製造法としては ^{18}O 濃縮水をターゲット物質とした $^{18}O(p,n)^{18}F$ 反応による方法がその汎用性と収量の点で優れている。しかし，ターゲット物質が高価であるため，ターゲットを小型化して1回使用量を低減化する，ターゲット物質の再利用を図る，等の対策が必要である。われわれは後者の方式により，照射後のターゲット水から ^{18}O 濃縮水を分離回収すると同時に，得られた無水の ^{18}F をアルカリ金属フッ化物やテトラアルキルアンモニウムフッ化物として固定化し，引続き任意の標識合成反応が可能な装置を試作開発したので，その概要を報告する。

2. 装置の構成および性能

Fig. 1に装置の系統図を，Fig. 2に装置の外観写真を示す。また，装置の操作手順例をTable 1に示す。

反応器（内容積 20 ml）は総テフロン製で回収したターゲット水の蒸留と，^{18}F-アニオンから ^{18}F-フッ化物の調製，さらに ^{18}F-フッ化物を前駆体とする ^{18}F-標識化合物の合成を行うことができる。蒸留された ^{18}O 濃縮水はガラス製冷却器に冷気を吹きつけて回収される。^{18}F は加えたアルカリ金属塩やアルキルアンモニウム塩として反応器中にほぼ完全に捕集され，その後の標識合成反応に用いられたり，必要に応じて有機溶媒中に可溶化して回収される。

Table 1 Handling procedure of the system for ^{18}F labelled compound production (example)

Step	Action	Elapse time(min)
1	Target water recovery	3
2	Evaporation	20
3	Cooling	5
4	Injection of solvent with crown ether	1
5	Heating and stirring	15
6	Solvent recovery	1
7	Enriched water recovery	1

反応器には常温から200 °C 程度まで迅速に加熱－冷却を行うことのできるヒータと冷却機能が備わり，反応器内外に配置した温度センサを用いて温度調節ができるようになっている。また，反応器内の水を効率的に蒸留するための減圧ポンプと反応器内の ^{18}F-フッ化物を効率的に有機溶媒中に可溶化させるための撹拌装置を有する。さらに，KOH, CsOH などのアルカリ金属の水酸化物や，必要に応じて KF などのキャリアを反応器に注入する経路も付設されている。ターゲット水の回収から ^{18}F 標識試薬の調製－標識合成反応，^{18}O 濃縮水回収まで操作はすべて別置のコントローラにより遠隔で行うことができる。

本装置を利用して，照射した ^{18}O 濃縮水（1.5%濃縮）にKOHあるいは KF（10 μmol）を加え蒸留，^{18}F を無水の $K^{18}F$ として捕集し，これをクラウンエーテル（18-Crown-6）100 μmol を含むジメチルホルムアミド（DMF）溶液として回収する実験を行った。その結果の一覧を Table 2 に示す。^{18}F-フッ素化試薬であ

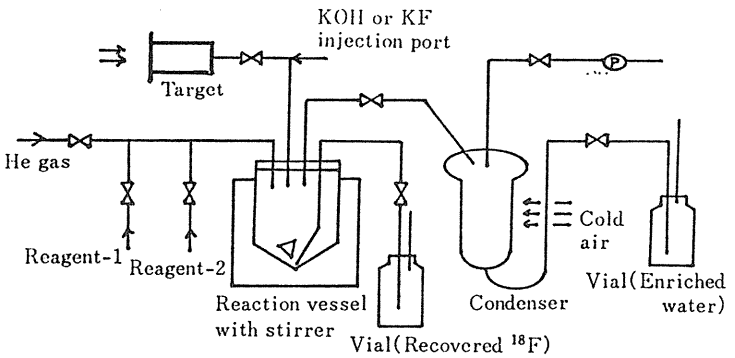

⋈ : Solenoid valve

Ⓟ : Pump

Fig. 1 Scheme of the synthetic system for the production of ^{18}F-labelled compounds.

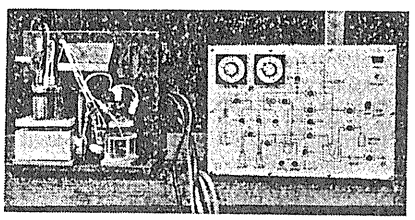

(a) Left: Synthesis system (b) Right: Operation controller

Fig. 2 Photographic view of the synthetic system for the production of ^{18}F labelled compounds.

Table 2 Recovery yield data of as ^{18}F-fluoride ($K^{18}F$) in organic solvent and ^{18}O water

Run	^{18}F Recovery Activity (mCi)	(Bq)	Yield (%)	^{18}O Water recovery Yield (%)
1	4.0	1.5×10^{8}	45	95
2	7.9	2.9×10^{8}	70	85
3	3.9	1.4×10^{8}	35	92
4	73.0*	2.7×10^{9}	42	90
5	4.3	1.6×10^{8}	53	88
Av.			49	90

Note: Nuclear reaction: $^{18}O(p,n)^{18}F$
Particle: p 18 MeV
Irradiation: 10 μA, 110 min
Target volume: 7 ml
Target: 1.5% of ^{18}O enriched water
(*: 20% of ^{18}O enriched water)

る $K^{18}F$ は，若干のばらつきはあるものの平均49%と効率良く調製-回収され，つぎのステップの反応に供された。また，^{18}O 濃縮水も体積比で平均90%と効率良く回収され，^{18}F 放射能の混入も1%以下であった。

^{18}F-KF with carrier KF 10 μmol/crown ether 100 μmol in DMF 6 ml
↓ ←Trimethylpurin-6-ylammonium chloride 34 μmol
Heating 30 min, 100 °C
↓
Filtration (Silica Sep Pak)
↓
Elution with ethanol–ethyl acetate
↓
Evaporation with 3 ml of toluene below 60 °C
↓
^{18}F-6-Fluoropurine
↓ ←DMSO 200 μl, K_2CO_3 30 mg, benzyl chloride 50 μl
Stirring at 50 °C, 60 min
↓
Separation silica gel column with benzene-ethyl acetate (3:2)
↓
^{18}F-6-Fluoro-9-benzylpurine

Fig. 3 The scheme of handling procedure for ^{18}F-6-fluoropurine and ^{18}F-6-fluoro-9-benzylpurine preparation.

さらに，20% ^{18}O 濃縮水を照射し，本装置を利用することによって得られた $K^{18}F$/クラウンエーテル 2.7 GBq(73 mCi)を用いて，Fig. 3 の方法により ^{18}F-6-フルオロプリン 510 MBq(13.8 mCi)および ^{18}F-6-フルオロ-9-ベンジルプリン 55 MBq(1.5 mCi)を合成し，^{18}F-フッ素化試薬である $K^{18}F$ の有効性を確認した。なお，このときの放射化学的収率はそれぞれ24%，5

%，合成時間は$K^{18}F$調製時点よりおのおの40分，150分であった。

なお，本装置を用いて回収された^{18}O濃縮水への溶媒（本実験ではクラウンエーテルの溶媒として用いたDMF）の混入の有無をガスクロマトグラフィ（カラム：SE 30，2 mm×2 m）を用いて調べたところ，一部の試料の中に経路内に残存していたと思われるDMFが検出された。したがって，^{18}O濃縮水の再利用にあたっては，再蒸留を行うこととした。

3. 問題点と今後の課題

実験の繰返しにより，以下の問題点が明らかになった。

反応器に回収したターゲット水を蒸留したのち，反応器内に付着した$K^{18}F$などの形で固定化された塩をクラウンエーテルを含む溶媒を加えて加熱-撹拌させるが，このときの溶解性が均一でなく利用しうる^{18}F-フッ素化試薬の回収率に若干のばらつきが生じている。また，反応器部にはターゲット水を回収-蒸留する水溶液系ラインと，本来水を嫌う有機溶媒系ラインが共存しており，使用後のラインの洗浄が不十分だと前述のように回収水中への有機溶媒の混入も起こりうる。これらの問題点の解決のために反応器の形状や撹拌機構の改良，経路の洗浄・交換等保守管理方法の改善も図っていく必要がある。

さらに，本装置は^{18}F-アニオンを利用したcarrier free（あるいはno carrier added）の^{18}F-標識化合物合成をめざしているが，本装置の反応器および経路はすべてテフロン製なため，これらからのF原子の溶出も無視しえず，合成後化合物の比放射能低下という問題の可能性もあり，今後の課題として残されている。

本装置の後段に，分離・精製を目的とした装置を組み合わせ，またマイクロプロセッサを有するコントローラで制御することにより，今後は種々の^{18}F-標識化合物の自動合成が可能となるであろう。

本装置の実験を行うにあたり，サイクロトロンの運転と種々の有益な御助言をしていただいた放医研技術部サイクロトロン管理課の皆様に感謝致します。

文　献

1) Irie, T., Fukushi, K. and Ido, T.: *Int. J. Appl. Radiat. Isot.*, 33, 1449－1452 (1982)
2) Tewson, T.J.: *J. Nucl. Med.*, 24, 718－721 (1984)
3) Coenen, H.H., Schuller, M. and Stocklin, G.: Proc. 5th Int. Symp. Radiopharm. Chem., 214－215 (1984)
4) Arnett, C.D., Shiue, C.Y., Wolf, A.P. et al.: *J. Nucl. Med.*, 25, P 63 (1984)
5) Kilbourn, M.R., Welch, M.J., Dence, C.S. et al.: *Int. J. Appl. Radiat. Isot.*, 35, 591－598 (1984)

Abstract

Development of the Synthetic System for the Production of ^{18}F-Labelled Compounds. Naoki ZAIMA, Toshiaki IRIE*, Kiyoshi FUKUSHI*, Toshiro YAMASAKI* and Yoshiaki NISHIHARA**: Tokyo Nuclear Services Co., 15-14, Higashi Ueno 3-chome, Taito-ku, Tokyo 110, *National Institute of Radiological Science 9-1, Anagawa 4-chome, Chiba-shi 260, **Sumitomo Heavy Industries Co., 1, Kandamitoshiro-cho, Chiyoda-ku, Tokyo 101.

A synthetic system for the preparation of ^{18}F-fluorinating reagent from ^{18}F anion was developed. This system is also equipped with a device to recover the expensive ^{18}O-enriched target water. By using this system, we have effectively prepared ^{18}F-KF/crown ether as a fluorinating reagent, and at the same time recovered ^{18}O-enriched water in good yield. Furthermore, the synthesis of ^{18}F-fluoropurine and ^{18}F-6-fluoro-9-benzylpurine was performed by this system.

(Received December 5, 1985)

UTILIZATION OF NON-NEGATIVITY CONSTRAINTS IN RECONSTRUCTION OF EMISSION TOMOGRAMS

E. TANAKA, N. NOHARA, T. TOMITANI and M. YAMAMOTO
National Institute of Radiological Sciences, Anagawa, Chiba-shi, Japan

1. INTRODUCTION

Emission computed tomography (ECT) has gained recognition in the past decade as a valuable tool in nuclear medicine imaging. The ECT falls into one of two categories: positron ECT and single-photon ECT(SPECT)[1]. The ECT has the advantage of higher object contrast than planar imaging, but at the same time has often suffered from a lack of sufficient count densities to achieve statistically smooth images. The poor counting statistics is due to limited isotope dosage to patients, limited counting time and limited count rate capability of the imaging devices. Fast dynamic studies require reduction of total number of counts to be accumulated per image, and high resolution imaging further reduces count density per resolution cell. The magnitude of statistical noise of an image depends on various factors such as the radionuclide distribution, the total number of counts, the number of resolution cells in the object area, etc., but it also depends on the reconstruction algorithm, because the statistical noise is amplified in the stage of image reconstruction.

A common problem in the reconstruction of ECT images is the correction for attenuation of photons in patients. For positron ECT, the attenuation is independent of position along a projection line and the correction is performed for projections using transmission scan data. Then, convolution-backprojection algorithms are widely used for image reconstruction. In SPECT, the correction is more difficult, because the attenuation of photons depends on the depth in the body. For non-uniform attenuation objects, an adequate correction is performed by means of iterative reconstruction techniques. In most of the clinical applications, however, algorithms based on the convolution principle with approximate attenuation correction are used assuming a uniform attenuation in the body contour[2-4].

It has been pointed out that the incorporation of a priori information on radionuclide distribution in the reconstruction process may be effective to reduce the statistical noise artefacts[5]. The most useful a priori information is the non-negativity constraints, that is any reconstructed radionuclide image should not have negative densities. The convolution method with poor counting statistics may produce many negative pixels so that it is expected that a modification using the non-negativity constraints will be useful to improve signal-to-noise ratio in the low density area of an image.

The non-negativity constraints are used in some iterative reconstruction algorithms. In EM (estimation maximization) algorithms based on maximum likelihood concept, the constraints are automatically included[5-8], but its performance on statistical noise has not been fully investigated. The method also has a drawback of computational slowness.

The major objectives of this paper are to find a practical recon-

struction method involving the non-negativity constraints, and to evaluate its effectiveness in terms of improvement of image quality. The methods discussed are a modification from a convolution method, the EM algorithm and a hybrid method of convolution and EM-algorithm. Throughout this work, we assume that the detector system has an ideal spatial resolution and effects of scattering and attenuation of photons in patients are neglected.

2. MODIFICATION FROM CONVOLUTION-BACKPROJECTION IMAGES

2.1. Negative smoothing and image dividing technique

In an image reconstructed by a convolution method, statistical fluctuation of a pixel density has a negative correlation with those of the surrounding pixels[9]. If a pixel has a negative density it may be compensated with positive densities of the surrounding pixels. The compensation can be performed by convolving a two-dimensional filter to the negative pixel. The treatments for all negative pixels will result in local compensations between positive and negative fluctuations without excessive loss of spatial resolution. In the simulation study shown later, the filter function shown in Fig. 1 was used and the filtering was performed 8-times repeatedly. We call this procedure "negative smoothing".

1/12	1/6	1/12
1/6	0	1/6
1/12	1/6	1/12

FIGURE 1. Filter used for negative smoothing.

The simple negative smoothing is effective in the image area where the true density is zero or very low, but not in high density areas. If the image is divided into a number of sub-images and all the sub-images are summed after being treated by the negative smoothing individually, the non-negativity constraints may become more effective, because the number of negative pixels increases with decreasing the total number of events involved. This method is named "image dividing technique".

A series of sub-images may be obtained as time lapse images in a dynamic study mode. This is applicable when we obtain an average image in a certain period of time from a series of dynamic images. Another simple method is the division by angular views. For example, the total number of views is even and is sufficiently large, two sub-images can be reconstructed from even number views and odd number views, respectively.

When only a set of projection data is available and the number of views is not sufficiently large to perform the angular division mentioned above, the set of projections can be divided into two sub-sets by a binomial distribution law. The law states that a count number, n, is divided into n_1 and n_2 ($n_2=n-n_1$) with a probability:

$$P(n_1, n) = \frac{n!}{n_1!\, n_2!} \left(\frac{1}{2}\right)^n. \qquad (1)$$

In practice, a read-out table producing n_1 from a given value of n and a random number generated by a computer is prepared once and is stored in a memory. For a large n-value, eq.(1) is approximated by a Gaussian probability distribution function, and n_1 and n_2 are obtained by

$$n_1 = n/2 + q\sqrt{n/2}, \qquad n_2 = n - n_1, \tag{2}$$

where q is a variable following a Gaussian probability distribution with a standard deviation of unity and zero mean. A read-out table producing q-value from a random generator is also stored.

By repeating the "binomial dividing method", an original set of projection data can be divided into 2,4,8$\cdots$ sub-sets, from each of which an image is reconstructed.

2.2. Simulation experiments

Simulations were performed with two mathematical phantoms shown in Fig. 2. The phantoms are 20 cm in diameter. Sixty projections are generated from the phantom with a bin width of 0.42 cm, and images are reconstructed in a 60 x 60 matrix. The pixel size is 0.42 cm. Shepp-Logan filter is used as the convolution kernel with linear interpolation.

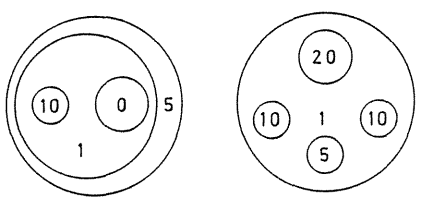

Phantom #1 Phantom #2

FIGURE 2. Mathematical phantoms used for simulation experiments. The diameters of the phantoms are 20 cm. Values in the figures are the relative activities.

Figures 3 and 4 show the results of the simulation. In both the figures, (a) is the image reconstructed by convolution method without noise, (b) is the convolution image with noise, (c) is the image obtained by cutting negative pixels from (b). Image (d) is obtained by the negative smoothing from image (b). Images (e) and (f) are obtained by image dividing technique from 8 sub-images using the binomial dividing method. Image (e) is the simple sum of the 8 sub-images treated by the negative smoothing each, and (f) is obtained by additional negative smoothing from (e).

It is seen that the simple negative smoothing is effective to reduce the noise at low density areas but positive streak-like artefacts still remain. On the other hand, the artefacts decrease by the image dividing technique. A major drawback of the image dividing method is, however, that it needs a longer computation time for convolution reconstruction in proportion to the number of sub-images.

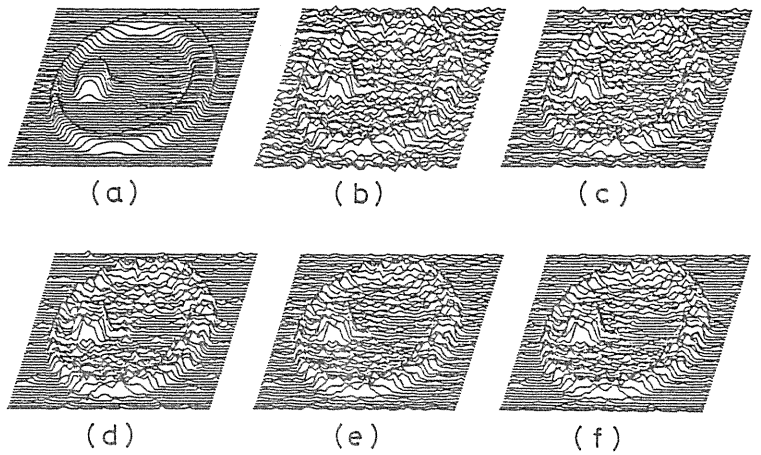

FIGURE 3. Images obtained by modifying convolution image of Phantom #1.
(a) Convolution image without noise.
(b) Convolution image with statistical noise. The total number of events is 100,000.
(c) Image obtained by cutting negative pixels from (b).
(d) Image obtained by negative smoothing from (b).
(e) Image obtained by summing 8 sub-images treated by negative smoothing. The sub-images are obtained by binomial dividing technique.
(f) Image obtained by additional negative smoothing from (e).

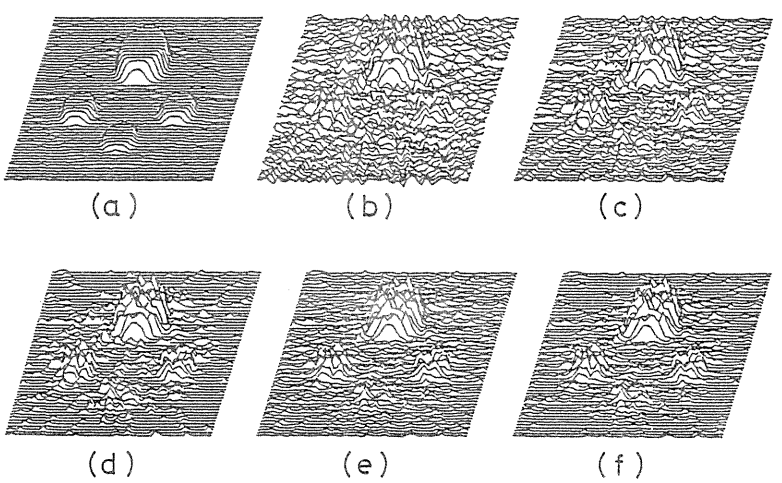

FIGURE 4. Images obtained by modifying convolution image of Phantom #2. (a)-(f) are the same as those in Fig. 3 except that the total number of events is 30,000.

3. EM ALGORITHM AND ITS MODIFICATION

3.1. EM algorithm (Mode A)

The EM algorithm proposed by Shepp and Vardi and others[6-8] is an iterative reconstruction technique for finding a maximum likelihood estimate. Letting s(b) be the image density in a pixel b (see Fig. 5), the iteration process is expressed by

$$s^{new}(b) = s^{old}(b)\ C(b), \tag{3}$$

where C(b) is a correction factor to be multiplied to an old image. The correction factor C(b) is obtained by

$$C(b) = \sum_{d} \frac{n(d)}{m(d)}\ p(b,d), \tag{4}$$

$$m(d) = \sum_{b'} s^{old}(b')\ p(b',d), \tag{5}$$

where d is a "detector tube" or a "projection bin", n(d) is the number of detected events in bin d, and m(d) is the "forward projection" on bin d calculated by eq.(5) from an old image. The function p(b,d) is the probability that emission in a pixel b is detected in bin d.

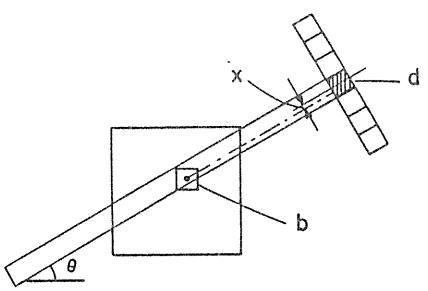

FIGURE 5. Illustration of pixel, b, and detector tube, d. x is the central distance between the pixel and the detector tube. θ is the view angle.

The choice of p(b,d) is important to discuss the performance of the EM algorithm. We assume that emission density is uniform in a square pixel, and that p(b,d) is proportional to the overlapping area between the pixel b and the detector tube d. The probability p(b,d) can be expressed as a function of the view angle θ and the central distance x between the pixel and the detector tube on the projection (see Fig. 5). Then we have

$$p(b,d) = p(\theta,x). \tag{6}$$

We can calculate p(θ,x) for all view angles and various values of x, and store it as a two-dimensional table in a computer. The size of the table is not large because p(θ,x) has non-zero value only for a limited range of x.

In practice, for each view angle, forward projection of an image is obtained with a sufficiently fine pitch (1/15 of the bin width) assuming that the emission of a pixel is concentrated at the center of the pixel, and the obtained projection is convolved with p(θ,x).

A simpler $p(\theta,x)$ function, which is independent of view angle θ, was tested, but it produced small artefacts in images due to the interference between pixels and projection bins. Then, the following studies are performed with the more sophisticated $p(\theta,x)$ function described above.

General features of the EM algorithm are as follows. (a) Non-negativity constraints are automatically involved as long as the initial image is positive. (b) Speed of recovery of a source distribution is inversely proportional to the spatial frequency of the distribution, that is, a lower frequency component is reconstructed by a fewer iteration cycles than a higher frequency component. (c) The DC component is recovered by the first iteration, and the total number of events is preserved in the following iterations. (d) Spatial resolution generally increases with added iteration cycles, but it depends on many other factors such as the source distribution, the number of pixels in the reconstruction area, the average density of the point of interest, etc.

3.2. Speeding up of EM algorithm and simulation experiments

A drawback of the EM algorithm is slow speed of execution. Most of the computation time is spent in the calculation of forward projections and a matrix of correction factors $C(b)$ for all the pixels. A simple method of speeding up is "angle skipping". For example, if iterations are performed using only odd number views and even number views in turn, the computation time per iteration is roughly halved.

Another effective method is the amplification of $C(b)$ by replacing it with $C(b)^k$ in eq.(3) where $k > 1$. With this amplification, however, the total number of events is not preserved and the image tends to oscillate at a low spatial frequency for a large k-value. To prevent the oscillation of the D.C. component, eq.(3) is modified as follows:

$$s^{new}(b) = s^{old}(b)\ [C(b)]^k [N_T \,/\, \sum_{b'} s^{old}(b')]^{k-1}, \qquad (7)$$

where N_T is the total number of events of the observed projections. With this modification, the iteration was quite stable for a k-value less than about 3.5. The total number of events is preserved in the estimate at each iteration. The speed of convergence is almost proportional to the k-value. Thus, combining the angle skipping and the $C(b)$ amplification, the computation time is effectively reduced. Following studies were performed by odd-even angle skipping with the $C(b)$ amplification with $k=3$.

Computer simulations have been made to investigate the performance of the EM algorithms for mathematical phantoms. We assume that 60 projections are measured with an equal angular interval in an angular range π, and we assume 60 detector tubes equally spaced and closely packed in a projection. The "measured" data, $n(d)$, are generated by calculating emission density in each detector tube. Blurring due to spatial resolution of actual photon detectors or collimators is not taken into account. Attenuation and scattering of photons in the phantoms are again neglected. Images are reconstructed in a 60 x 60 matrix. The pixel size and the bin (detector tube) width are 0.42 cm.

First, we have studied the convergence rate. Figure 6 shows the rms error of images as a function of iteration cycle for Phantom #1 shown in Fig. 2 without noise. The iteration was started from a uniform image. The curve A is obtained with the original EM algorithm, and curve A-S is obtained by applying 1:6:1 smoothing in the measured projections before

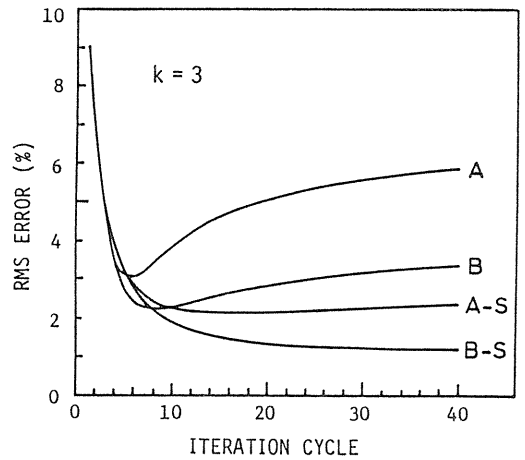

FIGURE 6. Root mean square error of noise free images obtained by EM algorithms as a function of iteration cycle. The iterations are speeded up with k=3. The phantom is Phantom #1 shown in Fig. 2.
Curve A : Mode A (Original EM algorithm)
Curve A-S : Mode A with projections smoothed by 1:6:1 filter
Curve B : Mode B (Modified EM algorithm)
Curve B-S : Mode B with projections smoothed by 7-point averaging after 5-point expanding

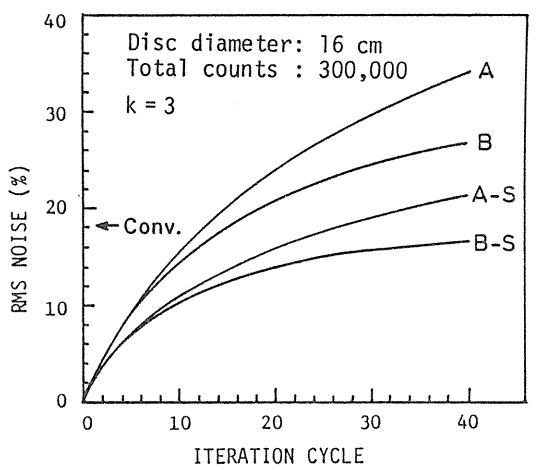

FIGURE 7. Root mean square noise of images obtained by EM algorithms as a function of iteration cycle. The phantom is a uniform disc of 16 cm in diameter. Total number of events is 300,000. The rms noise is calculated in a circular area of 12 cm in diameter. Curves A, A-S, B, and B-S are the same as those in Fig. 6.

iterations. The rms error shown in the figure is the difference from the convolution image. The value is the average of all pixels in the object region, and is normalized by the maximum value of the emission density.

Figure 7 shows the rms noise of a uniform disc phantom of 16 cm in diameter. The rms value is an average value in the area of 12 cm in diameter. The number of total events is 3×10^5. The curve A is the original EM algorithm and A-S is obtained with the smoothed projections. The rms noise of the convolution image is 18.1 % (shown by an arrow in the figure). Figure 8 shows the images after 40 iterations.

These results indicate that the original algorithm enhances the edge of the phantom excessively with the increase of iteration cycles unless suitable smoothing is applied to the projections. With noisy projections, the root mean square noise of the reconstructed image increases beyond the noise level of the convolution image. The main reason for this is considered as follows. An iteration cycle involves two steps of interpolations of data points represented by p(b,d) in eq.(4) and p(b',d) in eq.(5), respectively. Nevertheless, the iterative correction works in such a way that the "smoothed" forward-projections agree with "un-smoothed" measured-projections, and accordingly the image converges to the one having excessive high-frequency component.

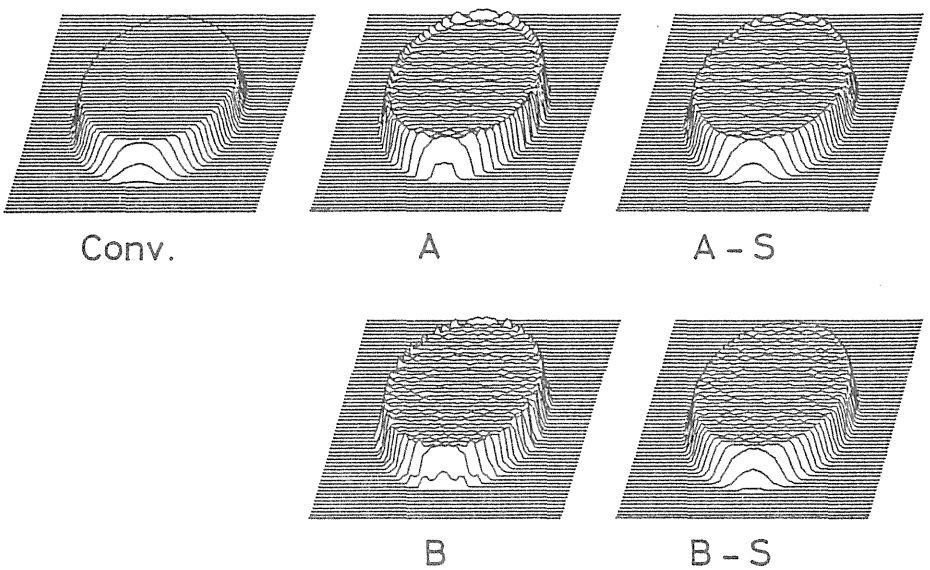

FIGURE 8. Images of a uniform disc phantom without statistical noise. The phantom diameter is 16 cm and pixel size is 0.42 cm. Number of iterations is 40 (k=3).

Conv.: Convolution-backprojection method with Shepp-Logan filter (linear interpolation)
A : Mode A (Original EM algorithm)
A-S : Mode A with projections smoothed by 1:6:1 filter
B : Mode B (Modified EM algorithm)
B-S : Mode B with projections smoothed by 7-point averaging after 5-point expanding

3.3. Modified EM algorithm (Mode B)

To overcome the drawback of the original EM algorithm, a modified algorithm has been developed. As shown in Fig. 9, we consider an imaginary detector tube array, in which one of the detector tubes directly faces to the center of the pixel b. Letting d_i be an imaginary detector tube, eqs.(4) and (5) are replaced by

$$C(b) = \sum_{d_i} \frac{n(d_i)}{m(d_i)} p(b,d_i), \tag{8}$$

$$m(d_i) = \sum_{b'} s^{old}(b') \, p(b',d_i), \tag{9}$$

where $n(d_i)$ is the number of counts in bin d_i estimated from measured counts $n(d)$ by linear interpolation.

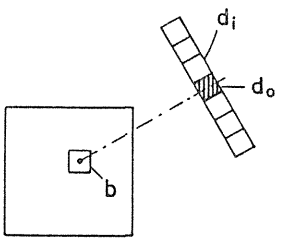

FIGURE 9. Illustration of imaginary detector tube array, d_i, for a pixel, b, in the modified EM algorithm. A detector tube, d_o, faces directly to the pixel.

For a projection at a view angle, $p(b,d_i)$ has the largest value for the directly facing bin, d_o, and the $p(b,d_i)$ for the other bins is negligibly small compared to $p(b,d_o)$ as long as the pixel size is equal to or smaller than the bin width. Then, we can assume that $p(b,d_o)$ is constant for all view angles and is equal to 1/N where N is the number of views. Under this condition, eq.(8) is further simplified and we have

$$C(b) = (1/N) \sum_{d_o} n(d_o)/m(d_o), \tag{10}$$

$$m(d_o) = \sum_{b'} s^{old}(b') \, p(b',d_o). \tag{11}$$

With this modification, the smoothing effect in an iteration cycle is small and the correction factor C(b) is obtained from the ratios of "smoothed" measured-projections to "un-smoothed" forward-projections. We call this algorithm "Mode B" and the original one "Mode A" in the following discussions. The computation time is nearly equal for both the modes.

The results of simulation experiments using Mode B are shown in Figs. 6 and 7 as curves B. Note that the rms noise in Mode B tends to saturate more rapidly to a smaller value than Mode A. Even with Mode B, however, the rms noise increases beyond the noise level of the convolution image as

the number of iterations increases. Edge sharpening effect is still seen in the reconstructed image (see Fig. 8). The reason for this is considered as follows. The pixels have a finite size, in which emission density is assumed to be uniform, and hence neighboring two projection bins should have a certain correlation in their values, while the statistical fluctuations occur independently. This results in the excessive enhancement of high frequency noise.

To reduce this effect, an additional smoothing of projection data is required. The observed projections are expanded in a finer pitch (1/5 of the bin width) by linear interpolation, and 7-point running average is applied to them. The rms error and the rms noise are shown in Figs. 6 and 7 as curves B-S, and the 40-th iteration is in Fig. 8. It is seen that Mode B with the smoothed projections gives comparable noise and resolution as the convolution method.

4. HYBRID METHOD OF CONVOLUTION AND EM ALGORITHM

The EM algorithm needs a large number of iterations to recover the spatial resolution even with a suitable speed-up method if the iterations are started from a uniform image. The required number of iterations will be greatly reduced by starting the iteration from a convolution image. The initial image must be positive, then the convolution image is treated by a non-linear operation to remove negative or zero density. In this "hybrid method", the spatial resolution is fully recovered by the convolution reconstruction and the density distortion caused by the non-linear operation will be corrected by a small number of iterations.

The non-linear operation used here is expressed by

$$\left.\begin{aligned} s_o &= s_i && (\, s_i \geq s_t \,) \\ &= s_t \exp[(s_i/s_t) - 1\,] && (\, s_i < s_t \,), \end{aligned}\right\} \qquad (12)$$

where s_i and s_o are the pixel values before and after the operation, respectively, and s_t is a threshold value. We call this operation "Diode cut" from the similarity to the diode characteristics. Note that the distortion produced by the diode cut occurs mainly in low spatial frequencies for which the iterative correction is very fast.

Examples of images of Phantom #1 reconstructed by the hybrid method are shown in Fig. 10. In the figures, (a) is the phantom, (b) is the convolution image, (c) is the initial image of iteration (processed by the diode cut) and (d)-(f) are the images after 2, 4, 6, 8 iterations. In the EM algorithm, Mode B is used with smoothed projections described before (7-point averaging for expanded projections). The threshold value s_t in the diode cut is a half the maximum density. Figure 11 shows another example. The lower-row images were obtained by applying 9-point weighted smoothing to the upper-row. Note that 4 or 6 iterations yield reasonable images, and that the signal-to-noise ratio in the low density area is greatly improved compared to the convolution method.

5. NOISE REDUCTION BY MEANS OF NON-NEGATIVITY CONSTRAINTS

It is of interest to compare noise magnitude between images reconstructed with the EM algorithm and the convolution method with an identical spatial resolution. The reconstruction resolution of the EM algorithm can not be uniquely defined, but in the present test, Mode B with 40 iterations from smoothed projections seems to yield almost the same resolution as the convolution method (see Fig. 8). As shown in Fig. 7, no appreciable

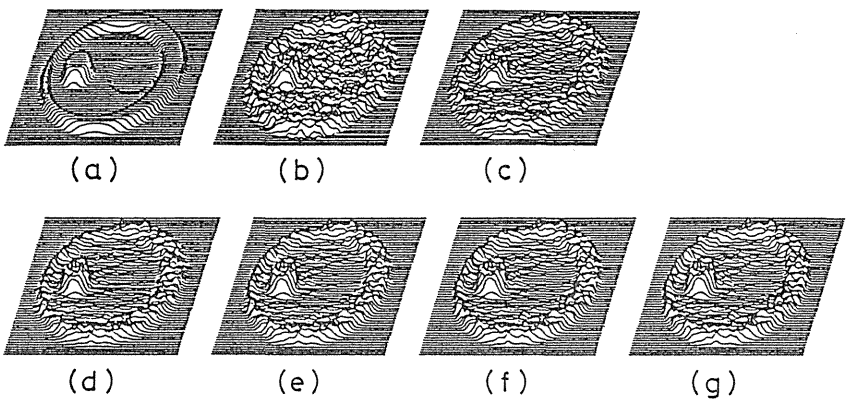

FIGURE 10. Images of Phantom #1 obtained with hybrid method. The total number of events is 100,000.
(a) Convolution image without noise
(b) Convolution image with noise
(c) Initial image of iteration obtained by diode cut from (b)
(d-g) Images after 2, 4, 6, 8 iterations, respectively

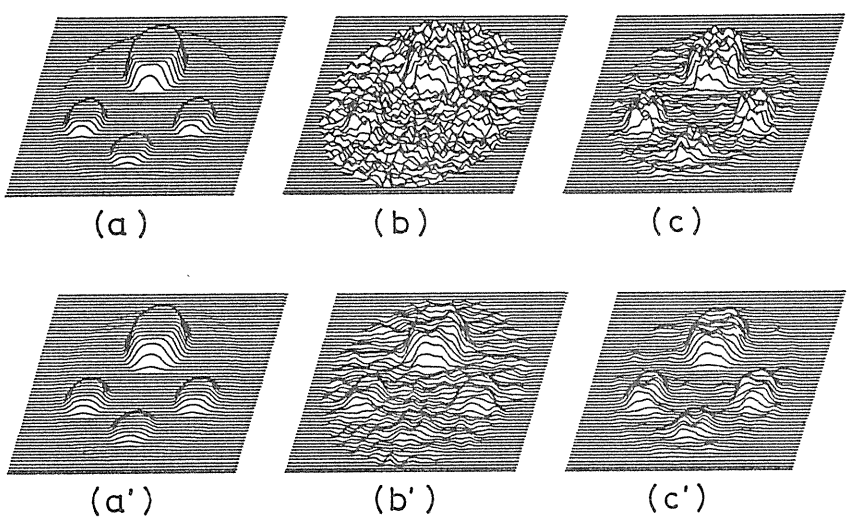

FIGURE 11. Images of Phantom #2 obtained with hybrid method. The total number of events is 30,000.
(a) Convolution image without noise
(b) Convolution image with noise
(c) Image after 6 iterations with noise
(a')-(c') are obtained by 9-point weighted smoothing from (a)-(c).

difference is observed in the rms noise between the two methods where the non-negativity constraints are not effective. The texture of noise is also similar in the two images. In low density areas in Figs. 10 and 11, however, the EM algorithm produces much less noise than the convolution method, which is apparently due to the non-negativity.

To estimate the effect of non-negativity on the noise, we shall consider a simple model. When the constraints are not involved as in the convolution images, the density, s, of a pixel tends to fluctuate around a mean value, s_m, according to a Gaussian probability distribution:

$$P(s) = \frac{1}{\sqrt{2\pi}\,\sigma} \exp\left[-\frac{1}{2}\left(\frac{s - s_m}{\sigma}\right)^2\right], \tag{13}$$

where σ is the standard deviation.

When non-negativity constraints are incorporated, the negative pixels are forced to be zero or a small positive value, and the positive values of pixels are compressed toward zero value in such a way that the mean value is kept constant. Assuming that the compression occurs linearly, the new distribution will be expressed by:

$$\left.\begin{aligned} P'(s) &= \frac{1}{\sqrt{2\pi}\,\gamma\sigma} \exp\left[-\frac{1}{2}\left(\frac{s - \gamma s_m}{\gamma\sigma}\right)^2\right] && (s > \varepsilon) \\ &= \int_{-\infty}^{\varepsilon} P(s)\, ds && (s = \varepsilon) \\ &= 0, && (s < \varepsilon) \end{aligned}\right\} \tag{14}$$

where ε is a sufficiently small density and γ is the factor of compression defined by

$$\int_{-\infty}^{+\infty} s\, P'(s) ds = s_m. \tag{15}$$

The factor of reduction for rms noise is then expressed by

$$F_{rms} = \left[\frac{\int_0^{+\infty} (s - s_m)^2 P'(s)\, ds}{\int_{-\infty}^{+\infty} (s - s_m)^2\, P(s)\, ds}\right]^{1/2} \tag{16}$$

The value of F_{rms} is plotted in Fig. 12 as a function of s_m/σ.

To check the validity of eq. (16), simulation experiments were performed with two mathematical phantoms. The one is a uniform disc phantom of 20 cm in diameter, and the other is a 20 cm diameter disc with an annular hot area of 2 cm width at the periphery. The rms noise is calculated in the central area of 12 cm in diameter. The two experimental points are plotted in Fig. 12, which indicates reasonable agreements with the theoretical model. The distributions of pixel values are shown in Fig. 13.

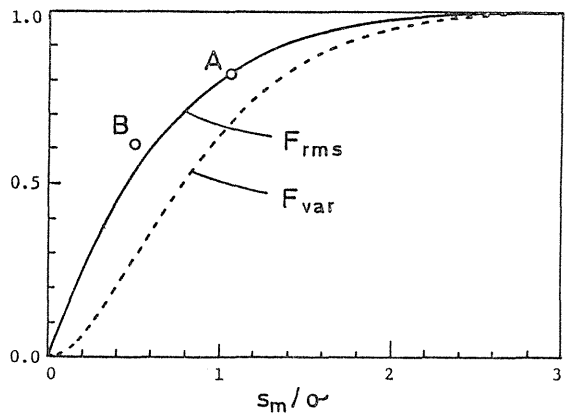

FIGURE 12. Factor of reduction for rms noise, F_{rms}, and for variance, F_{var}, by the use of non-negativity constraints. Points A and B represent the results of simulation experiments.

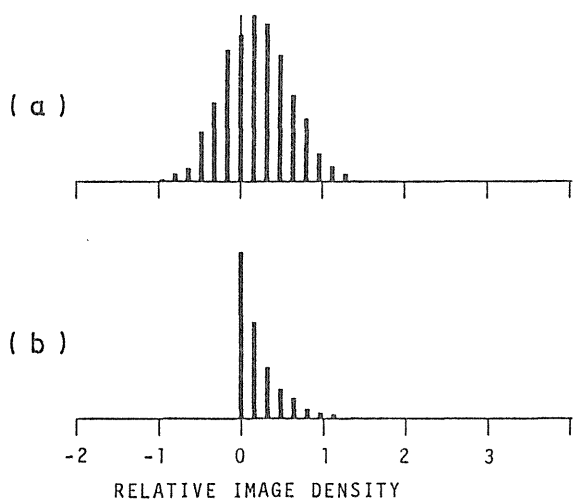

FIGURE 13. Distributions of pixel densities in the simulation experiment shown as point B in Fig. 12.
(a) Convolution image
(b) EM algorithm (Mode B with projection smoothing)

6. SUMMARY AND CONCLUSIONS

We have tested various methods of image reconstruction involving the use of non-negativity constraints. The negative smoothing of convolution images is the most simple and rapid method, but it is difficult to suppress positive streak artefacts. The image dividing method with the negative smoothing is effective to improve the above drawback. The method may be useful when an average image is obtained from a series of dynamic images.

The EM algorithm essentially satisfies the non-negativity constraints, but the convergence is very slow. To improve the computation speed, two methods have been developed; the one is angle skipping and the other is the amplification of correction factors. The original algorithm has an effect of edge sharpening, and it causes excessive increase in the noise magnitude in high density areas. To improve the convergence characteristics, a modified algorithm, Mode B, has been developed. With this mode, however, the rms noise still increases beyond the noise level of the convolution images as increasing iteration cycle. This fact implies that the maximum likelihood estimates achieved by the EM algorithms are not the most likely as practical emission images. A suitable smoothing must be applied to the measured projections to suppress the excessive noise amplification and to make the reconstruction resolution comparable to the convolution method.

In the present studies, the most promising method is the hybrid method which is composed of a convolutional reconstruction, a non-linear operation for removing negative pixels (diode cut) and several cycles of iterations of the modified EM algorithm. By using the speed up techniques in the iterations, the computation time is about 3-4 times longer than the simple convolution reconstruction.

The relative magnitude of rms noise has been evaluated between the convolution method and the EM algorithm with a similar reconstruction resolution. The rms noise in low density areas is apparently reduced with the EM algorithm by virtue of the non-negativity constraints, although no essential difference has been observed in high density areas.

It is concluded that the use of non-negativity constraints dramatically increases the signal-to-noise ratio in low density area of images and it improves the quality of high contrast images obtained with poor counting statistics. This is particularly important in the future developments of ECT technique because the count density per pixel decreases appreciably as one attempts to develop higher resolution imaging devices or to perform faster dynamic studies.

This work was supported in part by grants from the Ministry of Education and the Ministry of Health and Welfare, Japan.

REFERENCES

1. Budinger TF, Derenzo SE, Gullberg GT, Greenberg WL and Huesman RH : Emission computer assisted tomography with single-photon and positron annihilation photon emitters. J Comput Assist Tomogr 1:131-145, 1977
2. Sorenson JA : Quantitative measurement of radioactivity in vivo by whole-body counting. In : Instrumentation in Nuclear Medicine, Vol.2. Ed. by GJ Hine and JA Sorenson, New York, Academic Press, 1974, pp 311-348
3. Chang LT : A method for attenuation correction in radionuclide computed tomography. IEEE Trans Nucl Sci NS-25:638-643, 1978

4. Tanaka E, Toyama H and Murayama H : Convolutional image reconstruction for quantitative single photon emission computed tomography. Phys Med Biol 29:1489-1500, 1984
5. Snyder DL : Utilization of side information in emission tomography. IEEE Trans Nucl Sci NS-31:533-537, 1984
6. Rockmore AJ and Macovski A : A maximum likelihood approach to emission image reconstruction from projections. IEEE Trans Nucl Sci NS-23:1428-1432, 1976
7. Shepp LA and Vardi Y : Maximum likelihood reconstruction for emission tomography. IEEE Trans Med Imag MI-1:113-122, 1982
8. Lange K and Carson R : EM reconstruction algorithms for emission and transmission tomography. J Comput Assist Tomogr 8:306-316, 1984
9. Tanaka E and Murayama H : Properties of statistical noise in positron emission tomography. In : Proceedings of International Workshop on Physics and Engineering in Medical Imaging (Pacific Grove, 1982), IEEE Comput Soc 82CH1751-7, 1982, pp 158-164

July 1985 3 : 45

＜研究速報＞

A Proposed Method for Distinguishing between BaF_2 Detectors Coupled to a Photo Sensor for High Resolution Time-of-flight Positron Emission Tomographs

Mikio YAMAMOTO*

＜**Abstract**＞ A method is proposed to identify which of a group of photo emitters coupled to a photo sensor is actually emitting. It is suggested that the method presented may be applied to BaF_2 scintillation detectors for high resolution time-of-flight positron emission tomographs (TOF-PETs). Small BaF_2 scintillators are coupled to an available size of photomultiplier(PMT) and optical filters are inserted between them. The filters differ from each other and each filter corresponds to an emitter, resulting in transmission of different and identifiable ratios of emitted photons to the PMT. The ratio of the numbers of received photons of the longer wave lengths to shorter wave lengths can be used to distinguish the photo-emitting emitter, even if the total number of photo emissions change.

INTRODUCTION

It is necessary in certain fields to identify which of a group of photo emitters coupled to a photo sensor is actually emitting. An idea for the above purpose is presented in this paper.

For example, in positron emission tomographs (PETs), the highest possible spatial resolution that can practically be achieved is at a half of the detector width in discrete detector systems. Thus, there is a growing trend forward the use of narrower detector widths (for example, 4 mm width of $Bi_4Ge_3O_{12}$ scintillation crystal [1]).

However, there is no photomultiplier tube (PMT) of acceptable quality small enough to couple to the crystal one to one. Thus, crystals are coupled to PMTs, and output signals from the PMTs are used to identify the scintillating crystal (coding method [2, 3]). Another method used is to couple the crystals to a special position-sensitive PMT [1, 4].

In time-of-flight positron emission tomographs (TOF-PETs) [5, 6], information concerning the time-of-flight difference between a pair of annihilation photons is important, and the order of accuracy needed is 10^{-10} seconds. Therefore, the three TOF-PETs in operation use one-to-one type detectors (a CsF or BaF_2 scintillator coupled to a PMT) so as to collect as many scintillation photons as possible and to make the timing information more accurate. However, the one-to-one type can not be used for high resolution TOF-PETs.

It is suggested in this paper that the method presented may be applied to BaF_2 scintillation

* Division of Physics, National Institute of Radiological Sciences [9-1 Anagawa-4, Chiba 260 Japan]

Key words: barium fluoride, positron emission tomography, emission tomography, time-of-flight, scintillation counter

detectors for high resolution TOF-PETs.

PRINCIPLE

Photo emitters are coupled to a photo sensor. Linearity of input and output of the photo sensor is assumed here. The photo-emitting emitter can not be distinguished from the others without modification of the configuration, because the qualities of all the photo emitters are the same.

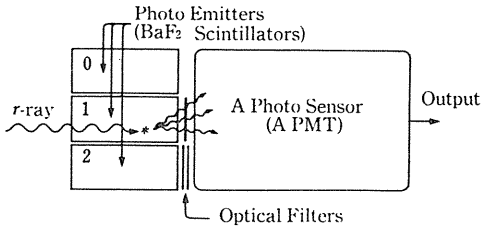

Fig. 1 Configuration of a high resolution detector unit.

Therefore, optical filters are placed between the photo emitters and the photo sensor, as shown in **Fig. 1**. The filters differ from each other and each filter corresponds to an emitter, resulting in transmission of different and identifiable ratios of emitted photons to the photo sensor.

The photo-emitting emitter can easily be identified by simple analysis of the output of the photo sensor if the numbers of emitted photons are constant, except sor minor fluctuations.

However, in most cases, the number of emitted photons has a dynamic range and the number is not constant. In these cases, the following conditions are necessary for photo emitters: at least two different components of photons having different wave lengths (**Fig. 2**), and different decay times (**Fig. 3**). The ratio of numbers of photons of the componentse is constant except for statistical fluctuations.

The optical filters used for the above cases should absorb or transmit special wave length ranges. The filter functions should differ from each other and correspond to the emitters as illustrated in Fig. 2. The filters shown in Fig. 2 absorb the longer wave length component.

Thus, the photo sensor receives different numbers of the longer wave length photons from each photo emitter, though the numbers of the shorter wave length photons are not affected significantly by the filters (Fig. 3). The ratio of the numbers of received photons of the longer wave lengths to shorter wave lengths can be used to distinguish the photo-emitting emitter, even if the total number of photo emissions change.

BaF_2 DETECTOR

BaF_2 scintillation counters are the best detectors available for the TOF-PETs at present [7-10].

Two components of scintillation photons are emitted from BaF_2 when positron annihilation photons (511 keV) interact with the BaF_2. The longer wave length component has a peak at 310 nm and the shorter component at 220 nm [8] as illustrated in Fig. 2. The decay time constant are 620 ns for the longer wave length component and 0.6 ns for the shorter component [8]. The reported total number of photoelectron yield due to 511 keV photon's incidence ranges from 700 to 1000, and from 70 to 200 for the shorter component [7-10]. BaF_2 fulfills the conditions necessary for photo emitters, as mentioned in the previous section.

BaF_2 scintillators are coupled to a PMT equipped with an ultraviolet window and optical

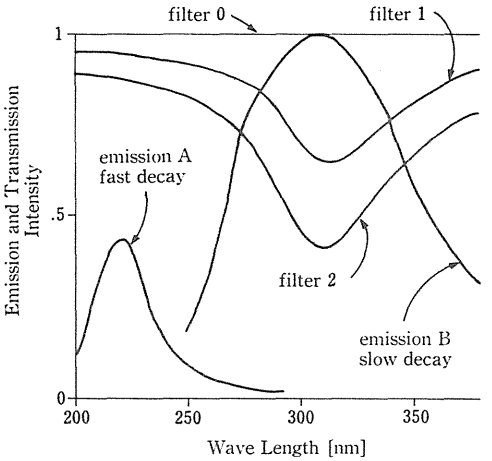

Fig. 2 Illustration of scintillation photo spectrum of BaF_2 impacted by 511 keV photons (reference [7]), and illustration of preferable optical filter functions (transmission rate) for BaF_2.

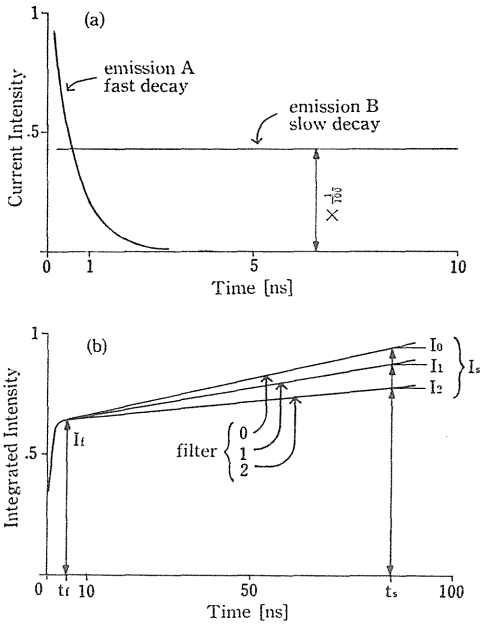

Fig. 3 (a) Illustration of current intensity of the PMT output due to the photo emissions of the fast and slow decay components.
(b) Illustration of the integrated value of the total PMT output and the holding.

filters are inserted between them, as shown in Fig. 1.

It is very easy to find filter materials (for example, silicon oil) to absorb photons of the shorter wave length. Photons of the fast decay component are absorbed by the filter in this case. Thus, it is difficult to get good timing information in gamma-ray detection.

It is not easy to find filter materials to absorb only the long wave length range. A possibility is a multi-layer thin film of dielectric substances (SiO_2 and Al_2O_3), which is presently under development.

An easy explanation of signal processing of the output of the PMT is as follows: the output current is integrated as shown in **Fig. 3 (b)**. The integrated value I_f is held at t_f, where t_f is longer than the decay time constant of the shorter wave length component. The integrated value I_s at t_s is held again. The expected value is I_0, I_1 or I_2 which corresponds to the scintillator. The selection of t_s becomes a trade-off between the level of precision of I_s and the count rate capability. The ratio I_s/I_f can be used to identify the scintillating scintillator.

Techniques of a pulse shape discrimination will be used to distinguish the scintillator in practice, instead of the above mentioned signal processing.

CONCLUSION

The presented idea may make possible identification of the photo-emitting emitter in a group of photo emitters coupled to a photo sensor.

It is suggested that the idea may be applicable to BaF_2 detectors for high resolution time-of-flight positron emission tomographs with available photomultipliers. Statistical considerations and experiments are being prepared.

REFERENCES

[1] Tomitani T, Nohara N, Murayama H et al: Development of a high resolution positron CT for animal studies. IEEE Nucl Sci **NS-32**: , 1985

[2] Murayama H, Nohara N, Tanaka E et al: A quad BGO detector and its timing and positioning discriminator for positron computed tomography. Nucl Instr Meth **192**: 501-511, 1982

[3] Yamamoto M, Kawaguchi F: Quad-detector arrangement and sampling characteristics in rotary positron tomography: POSITOLOGICA II. IEEE Trans Med Imaging **MI-1**: 136-142, 1982

[4] Murayama H, Tanaka E, Nohara N et al: Twin BGO detectors for high resolution positron emission tomography. Nucl Instr Meth **221**: 633-640, 1984

[5] Ter-Pogossian MM, Ficke DC, Yamamoto M et al: Design characteristics and preliminary testing of Super PETT I, a positron emission tomograph utilizing photon time-of-flight information (TOF PET). Time-of-flight tomography. IEEE Comp Soc **448**: 37-41, 1982

[6] Yamamoto M, Hoffman GR, Ficke DC et al: Imaging algorithm and image quality in time-of-flight assisted positron computed tomography: Super PETT I. Same as [5]: 125-129, 1982

[7] Laval M, Moszynski M, Allemand R et al: Barium fluoride inorganic scintillator for subnanosecond timing. Nucl Instr Meth **206**: 169-176, 1983

[8] Moszynski M, Allemand R, Cormoreche E et al: Further study of scintillation counters with BaF_2 Crystals for time-of-flight positron tomography in medicine. Nucl Instr Meth **226**: 534-541, 1984

[9] Wong WH, Mullani NA, Wardworth G et al: Characteristics of small barium fluoride (BaF_2) scintillator for high intrinsic resolution time-of-flight positron emission tomography. IEEE Nucl Sci **NS-31**:381-386, 1984

[10] Hutchins GD, Votaw JR, Funk KM et al: A one-dimensional multigated time-of-flight acquisition system. IEEE Trans Nucl Sci **NS-32**: 835-838, 1985

* * *

18.28

ADVANTAGES OF THE UTILIZATION OF TIME-OF-FLIGHT INFORMATION IN POSITRON EMISSION TOMOGRAPHY

Mikio Yamamoto

Division of Physics, National Institute of Radiological Sciences
9-1, Anagawa-4, Chiba-shi 260 Japan

INTRODUCTION

Time-of-flight positron emission tomograph (TOF-PET) utilizes additional information not utilized by conventional PET (1-6). It gives the annihilation position between a pair of detectors. In this paper, advantages of the utilization of TOF are discussed, and simple equations to assess a couple of them are given. The equations explain the experimental tendency of the gain of the variance reduction ratio of images achieved by the utilization of TOF to increase as activity in the object increases. The model is based on the random coincidence reduction effect using TOF. It is shown that the gain asymptotically approaches a saturation value as the activity increases. The effective coincidence time window of TOF-PETs can be defined simply as 1.5 times FWHM of the TOF time resolution.

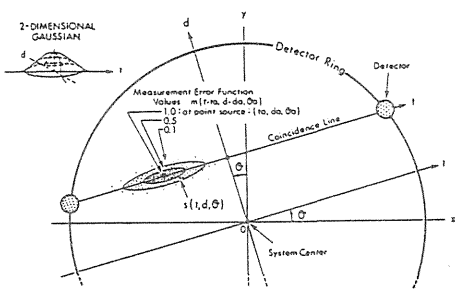

Fig.1 Coordinates and measurement error in TOF-PET.
t: TOF axis, d: distance from center,
θ: projection angle.

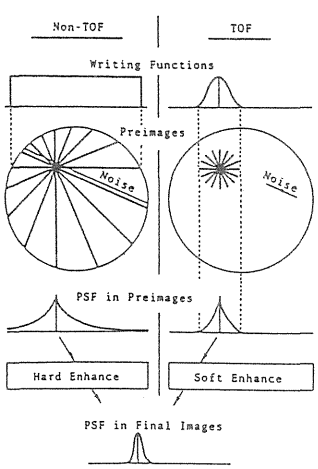

Fig.2 Principal differences between image reconstruction with and without TOF utilization.

IMAGING PROCESS

Coordinates and the principle of optimal imaging (2) for TOF-PET are shown in Fig.1-2.

Coincidence event information is converted to an address on a three dimensional (3D) projection, the so called 3D sinogram (t,d,θ), and a count is added on the address. The sinogram is corrected for the attenuation by an object, random coincidences and other factors. The corrected sinogram is convolved by a measurement error function along the t-axis to optimize the signal-to-noise ratio images. This convolution is performed with the one dimensional optimal function (2). The corrected 3D sinogram is 3D backprojected on a 2D pre-image array. The preimage is filtered with a point symmetric function to get a final-image with a desired point spread function. The optimal filter is shown in reference (2).

NOISE REDUCTION

Localization Effect of TOF in Reconstruction

Effects of statistical noise reduction with TOF in imaging is indicated by TOF gain (Eq.1). It is a ratio of variances, V_{CON} to V_{TOF}, where V_{CON} (CON = conventional) is the variance of reconstruction without utilizing TOF and V_{TOF} is the variance of reconstruction utilizing TOF.

On optimally processed images of a cylindrical uniform phantom whose diameter is W_o, the gain explained by Fig.1 can be represented simply by the following equation based on references (7,8).

$$\text{TOF gain} \equiv \frac{V_{con}}{V_{TOF}} \approx \frac{W_o C_o}{1.5\, W_t C_o} = \frac{W_o}{1.5\, W_t} \qquad (1)$$

where C_o is a measured count density at the central part of the phantom (fig.3) and W_t is FWHM of TOF resolution.

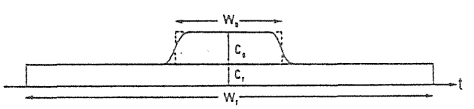

Fig.3 Count density along TOF axis.

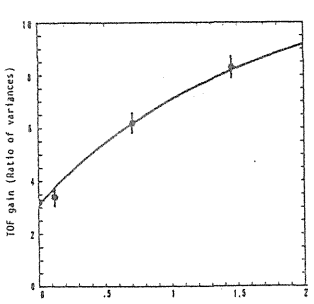

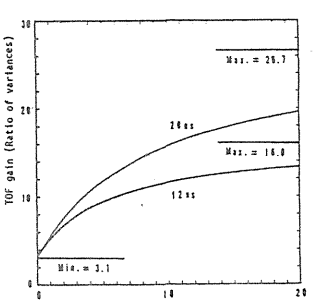

Fig.4 (Left) Fitting to experimental data on Super PETT I.
Fig.5 (Right) Theoretical tendency of the random to true ratio dependence. However, on real systems it is difficult to operate at more than a value of three of the random to true ratio without any distortion of images.

The unit of all W's should be the same, i.e., length or time, where 1 ns corresponds to 15 cm.

Random Coincidence Reduction Effect

Random coincidences are accidental coincidence counts of photons from different atoms. The count density C_r is flat in the coincidence window W_w except for statistical noise as in Fig.3. Even if the average value of random counts are subtracted, the effect of statistical noise due to random counts remains. Thus the random reduction with TOF is important, especially for high activity studies.

The effect is estimated using an analogy of the C_o and C_r and the width, W_o and W_w. The effect of difference in shape at the edge is negligible to the center of the images. Thus Eq.1 is easily extended to include C_r as follows.

$$\text{TOF gain} = \frac{W_o C_o + W_r C_r}{1.5\, W_t (C_o + C_r)} \qquad (2)$$

$$= \frac{R + T}{1.5\, W_t (T/W_o + R/W_w)} = \frac{1 + R/T}{1.5\, W_t (\frac{1}{W_o} + \frac{R/T}{W_w})} \qquad (3)$$

where true coincidence counts T and random counts R without TOF are represented as follows.

$$T = \int C_o(t)\,dt = C_o W_o$$
$$R = \int C_r(t)\,dt = C_r W_w \qquad (4)$$

In the extreme case of R = 0, Eq.3 goes to Eq.1, and in the case of R = ∞ Eq.3 goes to Eq.5.

$$(\text{TOF gain})_{R=\infty} = \frac{R/T}{1.5\, W_t (R/T/W_w)} = \frac{W_w}{1.5\, W_t} \qquad (5)$$

This means that the value of TOF gain asymptotically approaches the value given by Eq.5, and the effective coincidence window for TOF-PET is 1.5 times of FWHM of the TOF resolution. This value is 1.5 times larger than the definition in (9), and fits closely to experiments as follows.

In Fig.5, experimental data on Super PETT I (3) closely fits the carve of Eq.3. The TOF resolution W_t is 500 ps (7.5 cm) and the coincidence window W_w is 12 ns. The uniform cylindrical phantom (35 cm in diameter x 11.5 cm high) is measured at three activity points. The error bars show the estimated standard deviations. A point at zero activity is the result of a computer simulation.

In fig.6, the random to true ratio dependence of the TOF gain given by Eq.3 shows the theoretical tendency. A uniform 35 cm diameter phantom, W_t as 500 ps, W_w as 12 ns and 20 ns (typical for conventional PETs) are assumed.

Random Rejection from Transmission Data

Transmission scans are performed using an external source to correct photon attenuation by a body. The shape (such as a ring) of the source is known, thus the part around the source can be distinguished from the other (noise only) by TOF and the latter can be thrown away (2). This method significantly improves image quality, especially for bodies.

Scattered Coincidence Reduction Effect

Scattered coincidences can not distinguished from true coincidences when the coincidence line passes through the object unless TOF is utilized. Some of them are addressed out of the object with TOF and they can be rejected (2,6).

OTHER ADVANTAGES

On-line Monitor Imaging

A coincidence event with TOF gives an address on a 2D image array. Thus, on-line tomographic imaging is possible without using the image reconstruction process. However the present status of TOF resolution is broad (3 to 10 cm of FWHM) and the image resolution is very poor. Thus this is only for an on-line monitor.

Three-Dimensional Imaging

On a multi detector-ring PET, all inter ring coincidences can be used with TOF (5). Localization effect along the coincidence line can be applicable to true 3D imaging.

Simultaneous Measurement of Emission and Transmission Data

Emission data and transmission data can be measured simultaneously. The two kind of data can be distinguished by TOF.

Reduced Number of Angular Samplings

On the TOF-PET, the writing function is shorter than the conventional PET (Fig.2). Thus, a reduced amount of angular sampling is sufficient to reconstruct an image without star-like artifacts. The ratio of the numbers of sampling needed for TOF-PET and the conventional method is W_t/W_o. This figure is consistent with the images of a simulational study (10). This advantage is applicable to a fast imaging process (8).

Software Correction of Timing Offset

Each coincidence pair has a timing offset due to the cable length difference and the electronics component difference. However, it is very difficult to adjust them individually by hand, because number of coincidence lines is nearly 10^4 in multi-ring PETs. This adjustment is easily realized using software with TOF (2).

DISCUSSIONS AND CONCLUSION

Utilization of TOF in PET has several advantages, as discussed in this paper. The disadvantage is the complexity of both the system and data processing. At present, detectors good for TOF (BaF_2 and CsF) have about 70 % of coincidence efficiency of BGO. Thus TOF gain is 0.7 times the given value when compared to BGO PET.

TOF-PET is especially good when high activity dosage is given, such as in dynamic studies.

The auther gratefully acknowledges useful suggestions on TOF-PET by Drs. E.Tanaka, N.Nohara and T.Tomitani of NIRS, and Dr. M.M. Ter-Pogossian and D.C. Ficke of Washington University, St.Louis.

REFERENCES

(1) Ter-Pogossian MM, Ficke DC, Yamamoto M, Hood JT: Design characteristics and preliminary testing of Super PETT I, a positron emission tomograph utilizing photon time-of-flight information (TOF PET). Time-of-flight tomography, IEEE Comp Soc No.448:37-41, 1982
(2) Yamamoto M, Hoffman GR, Ficke DC, Ter-Pogossian MM: Imaging algorithm and image quality in time-of-flight assisted positron computed tomography: Super PETT I. Same as (1):125-129, 1982
(3) Yamamoto M, Ficke DC, Ter-Pogossian MM: Experimental assessment of the gain acheived by the utilization of time-of-flight information in a positron emission tomograph (Super PETT I). IEEE Trans Med Imag MI-1: 187-192, 1982
(4) Yamamoto M, Ficke DC, Ter-Pogossian MM: Effect of the software coincidence timing window method in time-of-flight assisted positron computer tomography: Super PETT I. IEEE Trans Nucl Sci NS-30:711-714, 1983
(5) Mullani NA, Wong WH, Hartz RK, Yerian K, Philippe EA, Gould KL: Design of TOFPET: a high resolution time-of-flight positron camera (TOF PET). Same as (1):31-36, 1983
(6) Garicd R, Allemand R, Cormoreche E, Laval M, Moszynski M: The "LETT" positron tomograph architecture and time-of-flight improvements. Same as (1):25-29, 1983
(7) Tomitani T: Image reconstruction and noise evaluation in photon time-of-flight assisted positron emission tomography. IEEE Trans Nucl Sci NS-28:4582-4589, 1981
(8) Tanaka E: Line-writing data acquisition and signal-to-noise ratio in time-of-flight positron emission tomography. Same as (1): No.488:101-108, 1983
(9) Holmes TJ, Snyder DL, Ficke DC: The effect of accidental coincidences in time-of-flight positron emission tomography. IEEE Trans MI-3:68-77, 1984
(10) Tomitani T: Simulation study of reconstruction with practical writing functions and noise evaluation in time-of-flight assisted positron computed tomography. Same as (1):117-124, 1983

Presented at IEEE 1985 Nuclear Science Symposium, San Francisco, Oct. 23-25, 1985. IEEE Trans. Nucl. Sci. NS-33(1), 1986.

A DECONVOLUTION FUNCTION FOR SINGLE PHOTON EMISSION COMPUTED TOMOGRAPHY WITH CONSTANT ATTENUATION

Takehiro Tomitani

Division of Physics
National Institute of Radiological Sciences
9-1, Anagawa 4-Chome, Chiba-shi, 260. Japan

Abstract

A shift-invariant spatial deconvolution function for single-photon-emission computerized tomography with constant attenuation is presented. Image reconstruction algorithm is similar to conventional convolution-backprojection algorithm except that exponential weight is applied in backprojection process. The deconvolution function was obtained as a solution of a generalized Schlömilch's integral equation. A method to solve the integral equation is described briefly. The present deconvolution function is incorporated with frequency roll-off and image resolution can be preset. At the extreme of ideal image reconstruction, the deconvolution function is identical to that deduced by Kim et al.[9] and its Fourier transform was proved to be identical to the filter deduced by Tretiak and Delaney[6] and Gullburg and Budinger[5]. Variance of the reconstructed image was analyzed and some numerical results were given. The algorithm was tested with computer simulation.

Introduction

The difficulty in the quantitative imaging with single photon emission computed tomography arises from the fact that the measured projection data are line integrals of the product of two unknown functions in two-dimensional space, that is, radioactivity concentration and the photon escape probability out of the body. The fact that gamma ray attenuation coefficient of the body is not constant makes the problem more complex. However, most of the existing reconstruction algorithms assume that gamma ray attenuation coefficient is uniform inside the body and that the shape of the body is known and convex.

The attenuation compensation was first carried out by iterative convolution method[1-3]. Tretiak and Delaney[4] investigated an analytical way and showed that, if the measured projections are modified to the fictitious projections measured on the lines which pass through the center, the modified projections are independent of the shape of the attenuation medium. For this reason, this modified projection will be referred to as "center projection" in this paper. They also showed that the image can be reconstructed by backprojection with exponential weights after deconvolution of the center projections. The deconvolution function is shift-invariant and is given as a solution of an integral equation, which they solved in a numerical way.

Gullberg and Budinger[5] and Tretiak and Metz[6] concurrently solved this problem in frequency domain. The former group tested various filters by computer simulations and the latter group investigated mathematical properties from the view point of the theory of distribution. Bellini et al.[7,8] compensated for attenuation on the two-dimensional Fourier transform of projection data. Kim et al.[9] deduced an inversion formula by use of the solution of Abel's integral equation.

The author[10] solved the integral equation analytically by means of series expansion with respect to linear attenuation coefficient.

Formulation of the problem

The formulation of the problem of the image reconstruction of single photon emission computed tomography will be outlined after Tretiak and Delaney.[4] Detailed descriptions should be referred to in the original paper.

The algorithm assumes that gamma ray attenuation coefficient of the absorbing medium is constant and its shape is known and convex. Let $i(\underline{r})$ denote two-dimensional radioisotope distribution. Referring to Fig.1, the measured projection, $p_m(t,\theta)$, through uniform attenuation medium of μ, at a direction $\underline{\theta}=(\cos\theta,\sin\theta)$, with the lateral distance, t, measured from the center is

$$p_m(t,\theta) = \frac{1}{2\pi}\int_{\Omega} d\underline{r}\cdot i(\underline{r})\cdot\delta(t-\langle\underline{r}\cdot\underline{\theta}\rangle)\cdot \exp\{-\mu\left(d(t,\theta)-\langle\underline{r}\cdot\underline{\theta}'\rangle\right)\} \qquad (1)$$

where $\delta(\cdot)$ indicates Dirac's delta function, while $\underline{r}$ and $\underline{\theta}'$ are defined as $\underline{r}=(x,y)$ and $(-\sin\theta,\cos\theta)$, respectively. $\langle\ \cdot\ \rangle$ denotes dot product and $d(t,\theta)$ denotes length of the attenuation medium along the direction $\underline{\theta}'$, measured from the line crossing the center. Since $d(t,\theta)$ is known for any t and θ, then multipling both sides of eq.(1) by a factor $\exp\{\mu d(t,\theta)\}$, we get the center projection $p(t,\theta)$.

$$p(t,\theta) = \frac{1}{2\pi}\int_{\Omega} d\underline{r}\cdot i(\underline{r})\cdot\delta(t-\langle\underline{r}\cdot\underline{\theta}\rangle)\cdot\exp\{\mu\langle\underline{r}\cdot\underline{\theta}'\rangle\} \qquad (2)$$

Let $f(t;\mu)$ denote a one-dimensional deconvolution function, then the filtered projection is $p(t,\theta)*f(t;\mu)$. By backprojecting it onto the image plane with the exponential weight, we get the reconstructed image, $\hat{i}(\underline{r})$,

$$\hat{i}(\underline{r}) = \int_0^{2\pi} d\theta\cdot\{p(t,\theta)*f(t;\mu)\}\cdot\exp\{-\mu\langle\underline{r}\cdot\underline{\theta}'\rangle\}. \qquad (3)$$

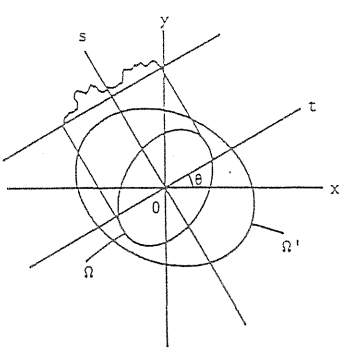

Fig. 1. Definitions of coordinates (x,y) and (t,s). Ω indicates the domain in which radioactivity distributes and Ω' indicates absorbing medium.

This work was supported in part by a Grant-in-Aid for the Cancer Research from the Ministry of Health and Welfare, the Japanese Government.

The point spread function, h(r) is

$$h(r) = \frac{1}{2\pi}\int_0^{2\pi} d\theta\cdot f(\langle \underline{r}\cdot\underline{\theta}\rangle;\mu)\cdot\exp\{-\mu\langle \underline{r}\cdot\underline{\theta}'\rangle\}$$
$$= \frac{1}{2\pi}\int_0^{2\pi} d\theta\cdot f(r\cdot\sin\theta;\mu)\cdot\exp\{-\mu r\cdot\cos\theta)\}. \qquad (4)$$

In order to avoid excessive noise enhancement through reconstruction process, image reconstruction with finite spatial resolution will be considered. When h(r) is specified and, as such, the spatial resolution is specified, the problem is to solve an integral equation (4) with respect to the unknown function f(t;μ).

It is assumed here that a one-dimensional deconvolution function f(t;μ) is even so as to obtain shift-invariant filtering. Then eq.(4) is modified to

$$h(r) = \frac{2}{\pi}\int_0^{\pi/2} f(r\cdot\sin\theta;\mu)\cdot\cosh(\mu r\cdot\cos\theta)d\theta. \qquad (5)$$

When μ=0, the problem is a simple reconstruction without attenuation and eq.(5) is

$$h(r) = \frac{2}{\pi}\int_0^{\pi/2} f(r\cdot\sin\theta)d\theta. \qquad (6)$$

This equation is known as Schlömilch's integral equation and the solution is

$$f(r) = h(0) + r\int_0^{\pi/2} \dot{h}(r\cdot\sin\theta)d\theta, \qquad (7)$$

where $\dot{h}(\cdot)$ indicates the first derivative of $h(\cdot)$.

Derivation of analytical expression of one-dimensional deconvolution function

Generalized Schlömilch's integral equation

A generalized Schlömilch's integral equation is to solve the following equation with respect to f(x;μ), when h(·) and g(·) are given.

$$h(r) = \frac{2}{\pi}\int_0^{\pi/2} f(r\cdot\sin\theta;\mu)\cdot g(\mu r\cdot\cos\theta)d\theta. \qquad (8)$$

Here we asume that both f(x;μ) and g(μx) can be expanded into power series of μ and the expansions are uniformly convergent with respect to μ, i.e.,

$$f(x;\mu) = \sum_{n=0}^{\infty} f_n(x)\mu^n, \quad g(\mu x) = \sum_{m=0}^{\infty} g_m\cdot(\mu x)^m. \qquad (9)$$

With these expansions, eq.(8) can be rewritten as

$$h(r) = \frac{2}{\pi}\int_0^{\pi/2}\{\sum_{n=0}^{\infty} f_n(r\cdot\sin\theta)\mu^n\}\{\sum_{m=0}^{\infty} g_m(r\mu\cdot\cos\theta)^m\}d\theta. \quad (8')$$

By equating the same power of μ on both sides of eq. (8'), we get the following set of equations.

$$h(r) = g_0\frac{2}{\pi}\int_0^{\pi/2} f_0(r\cdot\sin\theta)d\theta, \qquad (10)$$

$$0 = \frac{2}{\pi}\int_0^{\pi/2}\{\sum_{k=0}^{n} g_{n-k}\, r^{n-k}\, f_k(r\cdot\sin\theta)\cdot\cos^{n-k}\theta\}d\theta. \qquad (11)$$

Eq.(10) is a Schlömilch's integral equation with respect to $f_0(r)$, whose solution is given in eq.(7). Eq.(11) can be modified to

$$-\frac{1}{g_0}\sum_{k=0}^{n-1} g_{n-k}\, r^{n-k}\,\frac{2}{\pi}\int_0^{\pi/2} f_k(r\cdot\sin\theta)\cdot\cos^{n-k}\theta\cdot d\theta$$
$$= \frac{2}{\pi}\int_0^{\pi/2} f_n(r\cdot\sin\theta)\, d\theta. \qquad (11')$$

If f_k's are known up to k=n-1, then the left hand side of eq.(11') consists of integrals of known functions, so that eq.(11') is also a Schlömilch's integral equation with respect to unknown function f_n and can be solved in the same way. By mathematical induction, all f_n's are solved and, hence, f(x;μ) is obtained with eq. (9). Thus generalized Schlömilch's integral equation was formally solved.

Derivation of a one-dimensional deconvolution function

Here, a special case of the generalized Schlömilch's integral equation in which g(x) is equal to cosh(x) will be considered. Expansion coefficients are $g_{2n}=1/(2n)!$ for n=0,1,···,∞. Specifically, when n=0, $g_0=1$ and eq.(10) is identical to eq.(6). Since we are looking for an even deconvolution function, all odd terms of f_n's can be excluded. Then eq.(11) is

$$0 = \sum_{k=0}^{n}\frac{r^{2n-2k}}{(2n-2k)!}\frac{2}{\pi}\int_0^{\pi/2} f_{2k}(r\cdot\sin\theta)\cdot\cos^{2n-2k}\theta\, d\theta. \qquad (12)$$

To simplify the expression, let us introduce the following operator.

$$R_n[\Psi](r) = \frac{1}{2\pi}\int_0^{2\pi}\Psi(r\cdot\sin\theta)\cdot\cos^n\theta\, d\theta. \qquad (13)$$

In the case that Ψ(·) is even, it can be written as;

$$R_n[\Psi](r) = \frac{2}{\pi}\int_0^{\pi/2}\Psi(r\cdot\sin\theta)\cdot\cos^n\theta\, d\theta. \qquad (13')$$

When n=0,

$$R_0[\psi](r) = \frac{1}{2\pi}\int_0^{2\pi}\Psi(r\cdot\sin\theta)\, d\theta,$$

which can be interpreted as "rotational mean", since the right hand side means that the function Ψ(·) is rotated around the origin and summed up over 0 to 2π and the resultant sum is divided by 2π. When n≠0, the operator can be interpreted as rotational mean with the weight $\cos^n\theta$.

With this operator notation, equations (10) and (12) can be rewritten as

$$h(r) = R_0[f_0](r), \qquad (10')$$

$$0 = \sum_{k=0}^{n}\frac{r^{2n-2k}}{(2n-2k)!} R_{2n-2k}[f_{2k}](r). \qquad (12')$$

The operator in eq.(13) has the following property.

$$R_{2k}[f_{2m}](r) = -\frac{r^2}{2m(2k+1)} R_{2k+2}[f_{2m-2}](r). \qquad (14)$$

When n=0, the inversion is given by eq.(7) and may be defined as

$$R_0^{-1}[h](r) = h(0) + r\int_0^{\pi/2}\dot{h}(r\cdot\sin\theta)\, d\theta, \qquad (15)$$

which has the property (appendix 1)

$$R_0^{-1}[r^n R_n[\psi]](r) = \frac{\pi}{2}(n-1)r\, R_0[r^{n-1}R_{n-2}[\psi]](r). \quad (16)$$

From eq.(12), $f_{2n}(r)$ can be written as

$$f_{2n}(r) = -R_0^{-1}[\sum_{k=0}^{n-1}\frac{r^{2n-2k}}{(2n-2k)!} R_{2n-2k}[f_{2k}]](r). \qquad (17)$$

By applying eq.(14) and eq.(16) to eq.(17) successively, the function $f_{2n}(r)$ can be represented by $f_0(r)$ as

$$f_{2n}(r) = R_0^{-1}[\frac{(-)^n r^{2n}}{(2n)!} R_{2n}[f_0]](r)$$
$$= \frac{\pi}{2}\frac{(-)^n(2n-1)}{(2n)!}\, r\, R_0[r^{2n-1} R_{2n-2}[f_0]](r). \qquad (18)$$

Finally, by inserting it into eq.(9), f(x;μ) can be obtained. (appendix 1)

Derivation of the deconvolution function for Gaussian point spread function

When the point spread function, h(r), is a Gaussian function, $h(r)= 1/(2\pi\sigma^2)\exp\{-r^2/(2\sigma^2)\}$, where σ is the standard deviation, then the solution of the integral equation (10) is calculated to be

$$f_0(r) = \frac{1}{2\pi\sigma^2}[1 - \frac{r}{\sigma^2}\int_0^r \exp\{-\frac{r^2-v^2}{2\sigma^2}\}dv]$$

$$= \frac{1}{2\pi\sigma^2 r}\left[1 - \frac{r^2}{\sigma^2}\sum_{k=0}^{\infty}\frac{(-)^k}{(2k+1)!!}\left(\frac{r}{\sigma}\right)^{2k}\right]$$

$$= \frac{1}{2\pi\sigma^2}\frac{\partial}{\partial r}\, r\int_0^{\pi/2}\exp\{-\frac{r^2\cos^2\theta}{2\sigma^2}\}\cdot\cos\theta\, d\theta \qquad (19)$$

This function is a deconvolution function without attenuation which was deduced by Tanaka et al[11,12]By substituting $f_0(r)$ into eq.(18), we get eq.(20).(appendix 2)

$$f_{2n}(r) = \frac{1}{2\pi\sigma^2}\frac{\partial}{\partial r}\frac{r^{2n+1}}{(2n)!}\int_0^{\pi/2}\exp\{-\frac{r^2\cos^2\theta}{2\sigma^2}\}\sin^{2n}\theta\cos\theta d\theta \qquad (20)$$

By inserting it into eq.(9), the deconvolution function, $f(r;\mu)$, turned out to be eq.(21).(appendix 2)

$$f(r;\mu) = \frac{1}{2\pi\sigma^2}\frac{\partial}{\partial r}\, r\int_0^{\pi/2}\exp\{-\frac{r^2\cos^2\theta}{2\sigma^2}\}\cos(\mu r\cdot\sin\theta)\cos\theta d\theta \qquad (21)$$

Note that this deconvolution function coincides with eq.(19), when $\mu=0$ i.e. no attenuation, as is expected. The deconvolution function $f(r;\mu)$ is shown in Fig.2.

Fourier transform of the deconvolution function

Direct calculation of one-dimensional Fourier transform leads to the following expression

$$F(X) = \int_{-\infty}^{\infty} f(x)\cdot e^{2\pi xXi}dx = \pi|X|\varepsilon(|X|-\nu)\exp\{-2\pi^2\sigma^2(X^2-\nu^2)\} \qquad (22)$$

where $\mu=2\pi\nu$ and

$$\varepsilon(x) = \begin{cases} 0 & \text{for } x<0 \\ 1 & \text{for } x\geq 0. \end{cases} \qquad (23)$$

This result coincides with the filter deduced by Metz and Tretiak[6] in the limit $\sigma\to 0$.

Steep jump of the filter at $|X|=\nu$ can be understood by the analogy of the mechanical oscillation with dumping. The system cannot propagate waves whose frequency is below the critical dumping frequency.

The factor $\pi|X|$ on the right hand side of eq.(22) is related to the perfect reconstruction with $\mu=0$. The factor $\exp\{-2\pi^2\sigma^2(X^2-\nu^2)\}$ is due to frequency roll-off. The factor $\varepsilon(|X|-\nu)$ is specific to the reconstruction with attenuation.

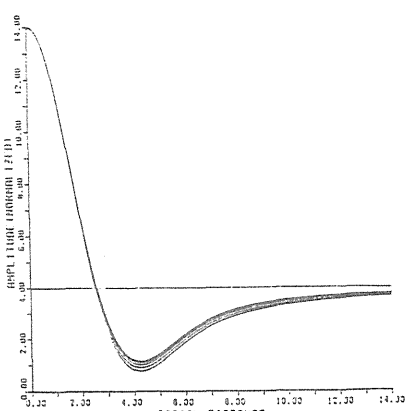

Fig. 2. Deconvolution functions for linear attenuation coefficients of 0, 0.05, 0.10, 0.15, 0.20 and 0.25 cm^{-1} (from top to bottom).

Variance of the reconstructed images

Using the parameters t,s,d and θ shown in fig. 1, reconstructed image intensity $\hat{i}(x,y)$ is calculated as

$$\hat{i}(x,y) = \int_0^{2\pi} p_m(t,\theta)\cdot\exp\{\mu d(t,\theta)\} * f(t;\mu)\cdot e^{-\mu s}d\theta. \qquad (24)$$

and its variance is calculated to be;

$$\text{var}\ \hat{i}(x,y) = \int_0^{2\pi} p_m(t,\theta)\cdot\exp\{2\mu d(t,\theta)\} * f^2(t;\mu)\cdot e^{-2\mu s}d\theta. \qquad (25)$$

Let us consider a uniform disk source of radius, ρ cm, which emits α photons/cm^2. If detection efficiency of the system is ε, then the measured projection(/radian) is calculated as;

$$p_m(t,\theta) = \frac{\alpha\varepsilon}{2\pi\mu}\,(1 - e^{-2\mu d}), \qquad (26)$$

where $d=\sqrt{\rho^2-t^2}$. Let i_0 denote αε, then $i_0/2\pi$ indicates event rate on the projection line without attenuation. In this case, the reconstructed image intensity $\hat{i}(x,y)$ is calculated as

$$\hat{i}(x,y) = \frac{i_0}{2\pi\mu}\int_0^{2\pi} 2\sinh(\mu d) * f(t;\mu)\cdot e^{-\mu s}d\theta, \qquad (27)$$

and its variance is

$$\text{var}\ \hat{i}(x,y) = \frac{i_0}{2\pi\mu}\int_0^{2\pi}(e^{2\mu d}-1) * f^2(t;\mu)\cdot e^{-2\mu s}\, d\theta. \qquad (28)$$

Image variance at the center of a disk is

$$\text{var}\ \hat{i}(0,0) = 0.0353\,\frac{e^{2\mu\rho}-1}{\mu\sigma^3}\cdot i_0. \qquad (29)$$

This expresion holds for $\rho\gg\sigma$. When there is no attenuation, that is, $\mu=0$.

$$\lim_{\mu\to 0}\ \text{var}\ \hat{i}(0,0) = \frac{0.0353(2\rho)}{\sigma^3}\, i_0. \qquad (29')$$

which coincides with the expression in reference (13). The image variance is plotted as a function of disk radius with attenuation coefficient as a parameter in fig. 3. The image variance as a function of position is plotted in fig. 4 for fwhm resolution of 1.0cm, ρ=10 cm and $\mu=0.15cm^{-1}$. The variance increases as the point moves away from the center of the disk due to exponential weight applied in the backprojection process as was pointed out in the discussion in ref.(4).

Total observed counts, N, was calculated as;

$$N = \int_0^{2\pi}d\theta\int_{-\rho}^{\rho} p_m(t,\theta)dt = \frac{2i_0}{\mu}\int_0^{2\pi}\{1-\exp(-2\mu\sqrt{\rho^2-t^2})\}dt$$

$$= i_0\pi\rho^2\cdot\phi(\mu\rho), \qquad (30)$$

where $\phi(x)=\{I_1(x)-L_1(x)\}/x$, in which $I_1(\cdot)$ and $L_1(\cdot)$ are the first order modified Bessel function of the first kind and the first order Struve function, respectively. With eq.(30), i_0 can be calculated from given total counts. By inserting i_0 value into eq.(29), the image variance at the center can be calculated.

Computer simulation

The proposed deconvolution function was tested with computer simulation. Projection bin size was set at 2mm. The number of views are 256 equally sampled over 360 degrees. All reconstructed images consist of 128x128 picture elelments with 2 mm bin width. Detector response was assumed ideal. In the case of noise-free test, center projections were calculated directly. In fig. 5, the point responses are shown for image resolutions of 0.5, 1.0, 1.5 and 2 cm full width at half maximum. Full widths at half maximum measured from the reconstructed images are plotted in fig. 6 virsus preassigned widths and are in good agreement with the latter. Point images are shown in fig. 7 for μ of 0.10, 0.15, 0.20 and 0.25

cm^{-1}, in which image resolution was assumed as 0.5cm fwhm. Artifacts outside the peak area increase as μ increases due to larger exponential weight, but are not serious even in the largest value of μ.

Uniformity of the reconstructed image was tested with a noise-free flood phantom of radius of 9cm. The results are shown in fig. 8 for μ=0.10, 0.15, 0.20 and 0.25 cm^{-1} in which resolution was assumed as 0.5cm (fwhm). This test ensures that image restoration of D.C. and low frequency components are satisfactory.

The reconstructed images of pie phantom with noise are shown in fig. 9 as a function of total counts, in which μ is assumed as 0.15cm^{-1} and image resolution is assumed as 0.5cm fwhm. Hot spot diameters are 2.5, 3, 3.5, 4, 5 and 6.2 mm. The separation between hot spots is four times the diamter.

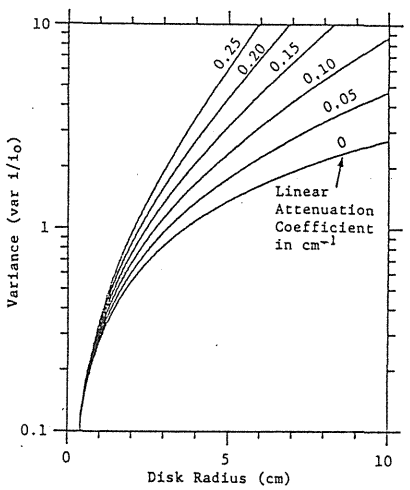

Fig. 3 Variance at the center of a disk as a function of disk radius. The image resolution is assumed as 1.5cm fwhm.

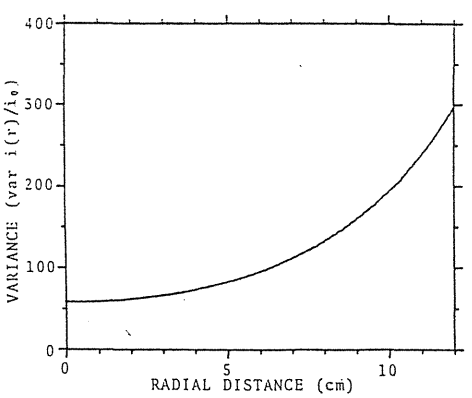

Fig. 4. Variance of a disk source as a function of distance from the center, where linear attenuation coefficient is assumed as 0.15cm^{-1} and image resolution is assumed as 1 cm fwhm.

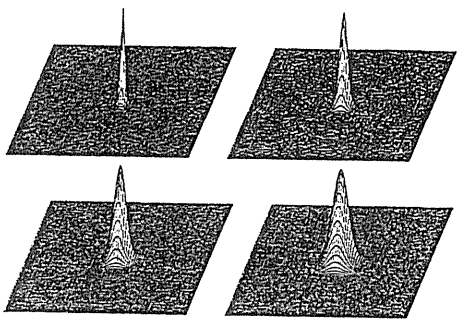

Fig. 5. Bird's eye views of a point source with fwhm of 0.5cm(upper left), 1.0cm(upper right), 1.5cm(lower left) and 2.0cm(lower right), respectively. Linear attenuation coefficient of 0.15cm^{-1} was assumed.

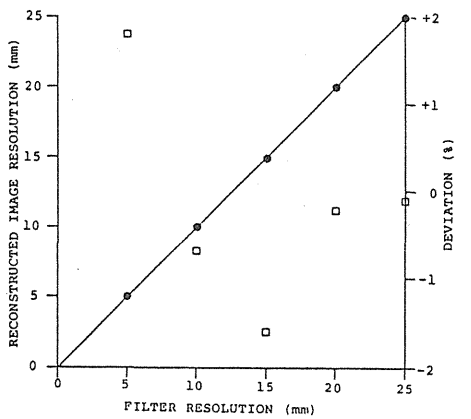

Fig. 6. Comparison of the preassigned image resolution and that measured from the reconstructed image.

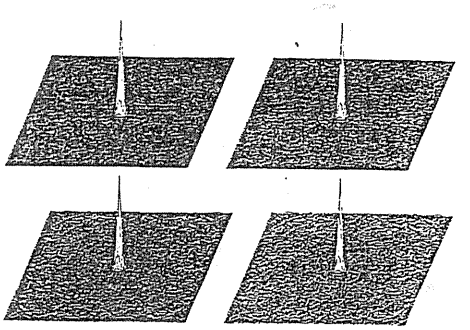

Fig. 7. Bird's eye views of a point source with fwhm of 0.5cm for linear attenuation coefficient of 0.10 (upper left), 0.15(upper right), 0.20(lower left) and 0.25(lower right) (cm^{-1}), respectively.

Discussions and Conclusions

A solution of generalized Schlömilch's integral equation is given. By applying it to the attenuated Radon transform, a deconvolution function was obtained. The function is equivalent to those presented in ref. 5, 6 and 9 except frequency roll-off factor. This kind of algorithms has a tendency that noise is enhanced toward the periphery of the image due to exponential weight in the backprojection process. A merit lies in shift-invariance. Meanwhile, Tanaka[14] derived a space-dependent deconvolution function with space-dependent back-projection weight numerically and showed that noise decreases toward the periphery. This suggests that there may be another solution to the problem, if the restriction of shift-invariance on the filter is abandoned. Since single photon ECT data is redundant with respect to the angle, so plurality of solution might exist. The solution presented by Bellini et al.[7,8] has somewhat different aspects, so that interrelationship as well as noise characteristics of their algorithm has to be investigated.

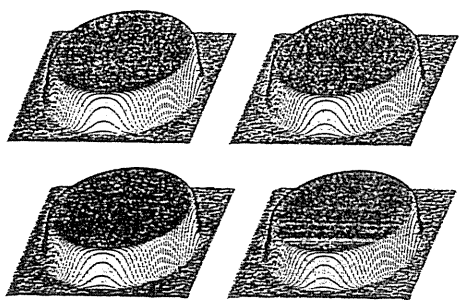

Fig. 8. Bird's eye views of a disk phantom with linnear attenuation coefficient of 0.10(upper left), 0.15(upper right), 0.20(lower left) and 0.25(lower right) (cm^{-1}), respectively. Image resolution was assumed as 0.5cm fwhm.

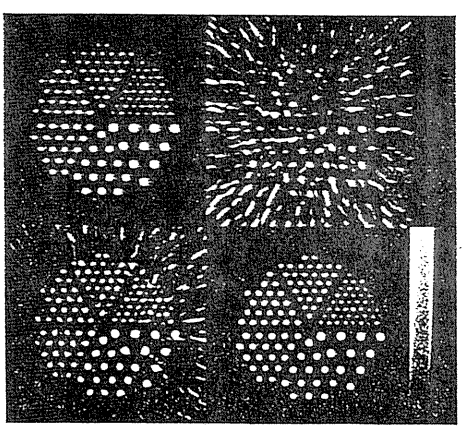

Fig 9. Reconstructed images of a pie phantom as a function of total counts, N. μ=0.15cm^{-1} was assumed. Upper left: without noise, upper right: $N=10^4$, lower left: $N=10^5$, lower right: $N=10^6$.

Acknowledgements

The author acknowledges E. Tanaka, N. Nohara, M. Yamamoto and H. Murayama for their valuable discussions and interests to this problem. He is grateful to M. Chiba and M. Moriyama for their assistance during the preparation of this manuscript.

Appendix 1

Proofs for equations (14), (16) and (17) will be given below.

Theorem 1. Let f(r) be a function, whose n-th order rotational mean exists, then for $n\geq 2$,

$$R_0^{-1}[r^n R_n[f]](r) = \frac{\pi}{2}(n-1)rR_0[r^{n-1}R_{n-2}[f]](r). \quad \text{(A-1)}$$

Proof: By inserting $h(r)=r^nR_n[f](r)$ into eq.(7) and by performing the integration by part,

$$\begin{aligned} &R_0^{-1}[r^nR_n[f]](r) \\ &= r^nR_n[f](r)\big|_{r=0} + r\int_0^{\pi/2}\{x^nR_n[f](x)\}'\big|_{x=rsin\theta}d\theta \\ &= r\int_0^{\pi/2}[nx^nR_n[f](x) + x^n\{R_n[f](x)\}']_{x=rsin\theta}d\theta \\ &= \frac{\pi}{2}(n-1)rR_0[r^{n-1}R_{n-2}[f]](r). \qquad \text{q.e.d.} \end{aligned} \quad \text{(A-2)}$$

Theorem 2. For $f_{2n}(r)$ defined by a set of eq.(11') and for $n\geq 1$,

$$f_{2n}(r) = -\frac{1}{2n}r\int_0^r f_{2n-2}(t)\,dt. \quad \text{(A-3)}$$

Proof will be given after the following lemmas.

Lemma 2-1. Under the same condition as thorem 2,

$$R_{2k}[r\int_0^r f_{2n-2}(t)dt](r) = \frac{r^2}{(2k+1)}R_{2k+2}[f_{2n-2}](r). \quad \text{(A-4)}$$

This lemma can be deduced by the integration by part.

Lemma 2-2. (Descending relationship) If theorem 2 holds, then

$$R_{2k}[f_{2n}](r) = -\frac{r^2}{2n(2k+1)}R_{2k+2}[f_{2n-2}](r). \quad \text{(A-5)}$$

Proof: By inserting eq.(A-3) into the left hand side of eq.(A-5), the right hand side of eq.(A-5) results.

Lemma 2-3. Assume that theorem 2 and hence lemma 2-1 hold for $n\geq 1$, $n\geq k$ and $k\geq 0$, then,

$$\frac{r^{2n-2k}R_{2n-2k}[f_{2k}](r)}{(2n-2k)!} = \frac{(-)^k r^{2n}R_{2n}[f_0](r)}{(2n-2k)!!(2k)!!(2n-1)!!}. \quad \text{(A-6)}$$

This lemma can be proved by application of lemma 2-2 successively.

Proof of theorem 2. Since f_{2n}'s are the solution of the integral equation (12'), it is sufficient to show that the right hand side of the theorem satisfies integral equation (12').

For n=1, the integral equation (12') reduces to

$$R_0[f_2](r) + \frac{1}{2!}r^2R_2[f_0](r) = 0. \quad \text{(A-7)}$$

By replacing $f_{2n}(r)$ to the right hand side of eq.(A-4) and by applying lemma 2-1 to the first term of eq.(A-7), the left hand side of eq.(A-7) is equal to 0.

Assume that eq.(A-3) holds up to n-1, then eq.(A-6)

holds up to n-1. By replacing $f_{2n}(r)$ to the right hand side of eq.(A-3), the first term of eq.(12')

$$= -\frac{1}{2n} R_0[r\int_0^r f_{2n-2}(t)dt](r) = -\frac{r^2}{2n} R_2[f_{2n-2}](r)$$

$$= \frac{(-)^n r^{2n}}{(2n)!} R_{2n}[f_0](r). \qquad (A-8)$$

By inserting this for k=n and lemma 2-3 for k<n-1 into eq.(12'), then the right hand side of eq.(12')

$$= \frac{(-)^n r^{2n}}{(2n)!} R_{2n}[f_0](r)$$

$$+ \sum_{k=0}^{n-1} \frac{(-)^k r^{2n}}{(2n-2k)!!(2k)!!(2n-1)!!} R_{2n}[f_0](r)$$

$$= \frac{r^{2n}}{(2n)!} R_{2n}[f_0](r) \sum_{k=0}^{n} {}_nC_k (-)^k = 0. \qquad (A-9)$$

By mathematical induction, theorem 2 holds for any n≥1.

Appendix 2

Deduction of equations (20) and (21) will be given. By replacing $f_0(r)$ in eq.(18) to the second expression of eq.(19),

$$f_{2n}(r) = \frac{\pi}{2} \frac{(-)^n(2n-1)}{(2n)!} rR_0[r^{2n-1}R_{2n-2}[$$

$$\frac{1}{2\pi\sigma^2} \sum_{k=0}^{\infty} \frac{(-)^k}{(2k-1)!!} \left(\frac{r}{\sigma}\right)^{2k}]](r)$$

$$= \frac{1}{2\pi\sigma^2} \frac{2}{\pi} \frac{(-)^n(2n-1)}{(2n)!} r^{2n} \sum_{k=0}^{\infty} \frac{(-)^k}{(2k-1)!!} \left(\frac{r}{\sigma}\right)^{2k}.$$

$$\int_0^{\pi/2} \sin^{2n+2k-1}\phi \, d\phi \int_0^{\pi/2} \sin^{2k}\theta \cdot \cos^{2n-2}\theta \, d\theta$$

$$= \frac{1}{2\pi\sigma^2} \frac{(-)^n r^{2n}}{(2n)!!} \sum_{k=0}^{\infty} \frac{(-)^k}{(2n+2k-1)!!} \left(\frac{r}{\sigma}\right)^{2k}$$

$$= \frac{1}{2\pi\sigma^2} \frac{1}{(2n+1)!} \frac{\partial}{\partial r} r \, F\left(1, n+\frac{3}{2}; -\frac{r^2}{2\sigma^2}\right)$$

$$= \frac{1}{2\pi\sigma^2} \frac{\partial}{\partial r} \frac{r^{2n+1}}{(2n)!!} \int_0^{\pi/2} \exp\left\{-\frac{r^2\cos^2\theta}{2\sigma^2}\right\} \sin^{2n}\theta \cos\theta d\theta.$$

(A-10)

in which $F(\alpha,\beta;z)$ denotes confluent hypergeometric function. Thus eq.(20) was deduced. The deduction of eq.(21) is rather straight forward.

$$f(r;\mu) = \sum_{n=0}^{\infty} f_{2n}(r) (\mu)^{2n}$$

$$= \frac{1}{2\pi\sigma^2} \frac{\partial}{\partial r} r \int_0^{\pi/2} \exp\left\{-\frac{r^2}{2\sigma^2}\cos^2\theta\right\} \cdot$$

$$\sum_{n=0}^{\infty} \frac{(-)^n}{(2n)!} (\mu r \sin\theta)^{2n} \cos\theta \, d\theta .$$

$$= \frac{1}{2\pi\sigma^2} \frac{\partial}{\partial r} r \int_0^{\pi/2} \exp\left\{-\frac{r^2}{2\sigma^2}\cos^2\theta\right\} \cos(\mu r \sin\theta)\cos\theta \, d\theta$$

q.e.d. (A-11)

References

1. D. B. Kay and J. W. Keyes Jr., "First order corrections for absorption and resolution compensation in radionuclide Fourier tomography," J. Nucl. Med. 16: 540, 1975.

2. T.E. Walters, W. Simon, D.A. Chesler, J.A. Correia and S.J. Riederer, "Radionuclide axial tomography with correction for internal absorption," in "Information Processing in Scintigraphy," C. Raymond and A. Todd-Pokropek, Eds., proc. 4th Int. conf.,Orsay, France, pp. 333-342, 1975.

3. L. T. Chang, "A method for attenuation correction in radionuclide computed tomography," IEEE Trans. Nucl. Sci., NS-25(2):638, 1978.

4. O. J. Tretiak and P. Delaney, "The exponential convolution algorithm for emission computed axial tomography," in "Information Processing in Medical Imaging," proc. 5th Int. conf., Nashville, 1977, A. B. Brill and R. R. Price, Eds., ORNL/BCTIC-2:26, 1978.

5. G. T. Gullberg and T. F. Budinger, "The use of filtering methods to compensate for constat attenuation in single-photon emission computed tomography," IEEE Trans. Biomed. Eng., BME-28(2):142, 1981.

6. O. Tretiak and C. Metz, "The exponential Radon Transform," SIAM J. Appl. Math., 39(2):341, 1980.

7. S. Bellini, M. Piacentini, C. Cafforio and F. Rocca, "Compensation of tissue absorption in emission tomography," IEEE Trans. Acoustics, Speech and Signal Processing ASSP-27(3):213, 1979.

8. S. Bellini and M. Piacentini, "Design of a computerized emission tomographic system," Signal Processing 1:125, 1979.

9. K. I. Kim, R. P. Tewarson, Y. Bizais and R. W. Rowe, "Inversion for the attenuated Radon Transform with constant Attenuation," IEEE Trans. Nucl. Sci. NS-31 (1):538, 1984.

10. T. Tomitani, "A deconvolution function for single-photon emission computerized tomography with constant attenuation,"(in japanese) NIPPON ACTA RADIOLOGICA 43(4):643, 1983.

11. E. Tanaka and T. A. Iinuma, "Correction functions for optimizing the reconstructed image in transverse section scan," Phys. Med. Biol. 20:789, 1975.

12. E. Tanaka and T. A. Iinuma, "Correction functions and statistical noises in transverse section picture reconstruction," Compt. Biol. Med. 6:295, 1976.

13. T. Tomitani, "Image reconstruction and noise evaluation in photon time-of-flight assisted positron emission tomography," IEEE Trans. Nucl. Sci. NS-28 (6):4582, 1981.

14. E. Tanaka, "Quantitative image reconstruction with weighted backprojection for single photon emission computed tomography, " J. Comput. Assist. Tomogr. 7:692, 1983.

11

BODY EDGE DETECTION FOR ATTENUATION COMPENSATION BY CALCULATION IN EMISSION CT

Takehiro TOMITANI

Div. of Physics, National Inst. of Radiological Sciences

Introduction

In emission computed tomography(ECT), measured projection data are modulated by attenuation inside the body. In SPECT, attenuation compensation by calculation is a standard practice. In PECT, separate attenuation measurement with an external source is widely adopted, since it measures exact body attenuation factor. Additional noise is introduced due to finite statistics of transmission measurement and attenuation compensation by calculation may be preferred in some instances. Attenuation compensation by calculation postulates that attenuation coefficient is uniform inside the body. Attenuation factors are calculated from a body edge contour whose accuracy critically affects final result. This article presents a new edge detection algorithm which, based on differential geometry, enables direct calculation of object edge contour from the edge informations obtained on a sinogram.

Contour Detection Algorithm

Relationship between Edge on Sinogram and That of an Object Assume that the edge contour of an object is convex, then an edge point on the sinogram determines a tangent of an object edge. In Fig. 1a, a point P on the edge of a projection with lateral distance t from the origine with an angle θ relative to y-axis, determines a tangential line l which contacts with an object at a point Q. A tangential line can be represented as

$$y - t\sin\theta = -\cot\theta\,(x - t\cos\theta). \tag{1}$$

Also a tangential line with a view angle $\theta+\Delta\theta$ and with a lateral distance $(t+\Delta t)$ is

$$y - (t + \Delta t)\sin(\theta + \Delta\theta) = -\cot(\theta + \Delta\theta)\{x - \cos(\theta + \Delta\theta)\}. \tag{2}$$

A cross point of the lines in eq.(1) and eq. (2) approaches, on the extreme of $\Delta\theta\to 0$, to a point of contact, which is calculated to be;

$$\begin{aligned} x &= t\cos\theta - \dot{t}\sin\theta , \\ y &= t\sin\theta + \dot{t}\cos\theta . \end{aligned} \tag{3}$$

Eq.(3) indicates that a point of contact can be calculated from a series of edge points $t(\theta)$ on the sinogram and its θ-derivative. Note that equations (3) hold for a concave object. If there were a means to find out an edge of a concave object on the sinogram, equations (3) would allow calculation of an edge contour of a concave object.

Smoothing of an Edge Contour and Calculation of Intercept The edge contour on the sinogram is periodic and bounded, so that its Fourier transform exists. The edge contour can be smoothed away by retaining lower order Fourier coefficients. This procedure is similar to the phase analysis in cardiac studies. $\dot{t}(\theta)$. can be calculated in a similar way. To calculate an intercept of a projection line with a body contour, first, rotate body contour, $(x(\theta),y(\theta))$ by $-\theta$, then calculate intercept of $x=t$ with the rotated body contour.

Compensation of Skull Effect in Brain Imaging In the case of brain studies, linear attenuation coefficient of a skull is substantially higher than that of soft tissue. What matters is not its shape but rather its length intercepted by a projection

line. The latter can be approximated by the difference of two ellipses. Note that a projection of an ellipse is also an ellipse regardless of the directions of the major and minor axes, so that major and minor radii along with its center can be calculated easily from the minimum and maximum of x-corrdinate of the contour data.

Results

Edge Detection on Sinogram and Number of Fourier Coefficients Thresholding method was adopted due to its simplicity. The threshold is determined as ((mean sinogram intensity over angle along a center of sinogram) - (mean sinogram intensity outside the object over angle))x0.2, where a factor 0.2 is determined by experience. Using lenth of a contour as a measure of its "smoothness", necessary number of Fourier coefficients was turned out to be 5~6.

Algorithm Test on a Sample Data An example of contour detection is shown in Fig. 2 superimposed on the reconstructed image. The image is a head section of a rabit injected with ^{11}C-labeled Ro 15-1788, a recepter ligand imaged with a high resolution PET for animal studies the characteristics of which is presented in the preceding presentation. Image shape is rather singular, yet the present algorithm reproduces its edge contour clearly. Total counts of projection data is only 24k, which indicates that the algorithm is fairly robust against noise. The algorithm was also tested on head tomograms measured with POGITOLOGICA I and worked as well.

Conclusions

The proposed algorithm enables calculation of a body contour directly from the edge found on a sinogram and is persistent against noise. In the case of brain studies, the effect of heterogenity due to skull can be mostly compensated for by approximating it by two ellipses. The proposed algorithm is applicable equally to SPECT data with slight modification. In the latter case, projection data are measured over 2π radians instead of π radians in the former case, so that two edge informations are available in the latter case.

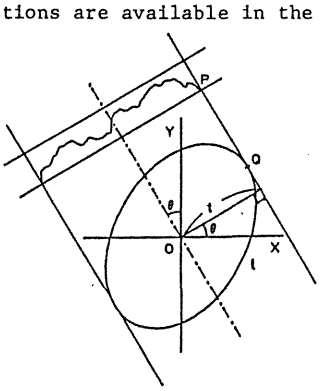

Fig. 1a

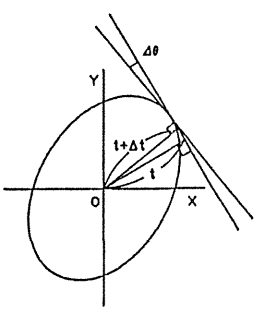

Fig. 1b

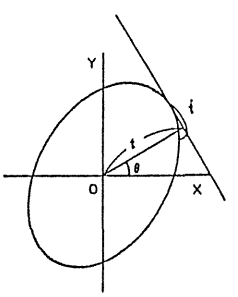

Fig. 1c

Fig. 1. a)Relationship between an object edge, a tangent and an edge on a projection, b)tangents with an angle θ and θ+Δθ and c)relationship between $t(\theta)$, $\dot{t}(\theta)$ and a point of contact.

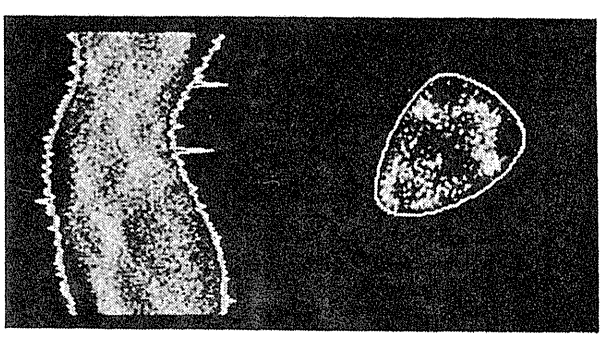

Fig. 2. A detected projection edge superimposed on a sinogram (left) and a synthesized contour superimposed on a reconstructed image(right).

＜研　究＞

ポジトロンCTの空間分解能の限界

野原　功全*　富谷　武浩*　山本　幹男*
村山　秀雄*　田中　栄一*

要旨　ポジトロンCTの高解像力化が進むにつれて，ポジトロンの消滅事象にともなう物理的特性が空間分解能の限界を与える因子として問題となる．物理的因子としてポジトロンの生体中における飛程と消滅放射線の角度揺動が考えられ，これらの因子について3種類のポジトロン放出核種の線線源応答を求め，最終画像における空間分解能の限界を円形リング型ポジトロンCTの検出器リング直径の関数として求めた．

はじめに

ポジトロンCTの高解像力化は臨床的な要求が強く，ポジトロンCTの開発が始まった当初からBGO結晶の小型化や，小型光電子増倍管の開発など高解像力化の研究が進められてきた．高解像力化をはかる上での問題としては，使用する検出器結晶を小型化することによる感度の低下が間接的に高解像力化に限界を与えているが，これとは別に，空間分解能の限界を与える直接的な因子として，ポジトロンの消滅事象における物理的特性に基づくものがある．すなわち，ポジトロンの生体組織中での飛程と消滅放射線の180°からの揺動である．これらの因子は検出器の固有空間分解能がたとえ無限小となっても，最終画像に対して有限な空間分解能を与えることになる．

本研究は，これらの物理的因子が空間分解能にどのような限界をもたらすかをポジトロンのエネルギーが異なる3種のポジトロン放出核種に対して評価したものである．

* 放射線医学総合研究所物理研究部〔〒260 千葉市穴川4-9-1〕
受付：昭和60年9月30日
最終稿受付：昭和60年10月11日

Key words: positron emission tomography, positron range, angular deviation, spatial resolution

Table 1 Maximum energy of positron and its maximum range in water

Isotope	β^+ end point (MeV)	Maximum range (mm)
^{18}F	0.635	2.42
^{64}Cu	0.656	2.55
^{11}C	0.959	4.18
^{13}N	1.197	5.40
^{15}O	1.723	8.19
^{68}Ga	1.898	9.32
^{82}Rb	3.148	16.3

ポジトロン飛程と角度揺動

ポジトロンCTに使用される主なポジトロン放出核種は^{11}C, ^{13}N, ^{15}O, ^{18}F, ^{68}Ga, ^{82}Rbなどである．これらの核種のポジトロンの最大エネルギーは0.635から3.15 MeVの範囲にあり〔1〕，また，それらの水中における最大飛程は2.4 mmから16.3 mmの範囲である（**Table 1**）．ただし，これらの最大飛程がそのままポジトロンCTの空間分解能に現れるわけではない．

Derenzo〔2〕は，点線源から放出されるポジトロンの消滅点の空間的な分布を狭いスリットに投影したとき，その投影像は線源からの距離rの関数として急峻に減少する成分と緩やかに減少する成分の二つの指数関数の和$q(r)$で表せることを実験的に示した．すなわち，

Table 2 Parameters giving the point spread function in projection [2]

Isotope	^{11}C	^{68}Ga	^{82}Rb
β^+ end point (MeV)	0.959	1.898	3.148
A	0.916	0.811	0.898
r_1 (mm)	0.078	0.162	0.301
r_2 (mm)	0.457	1.15	2.99

$$q(r)=A\ \exp(-r/r_1)+(1-A)\times \exp(-r/r_2) \quad \cdots\cdots\cdots\cdots(1)$$

ここに，r は線源位置からポジトロン消滅点までの投影上での距離であり，A は急峻に減少する成分の全成分に対する相対強度，r_1 と r_2 はそれぞれの成分の平均距離を与えるパラメータである．これらのパラメータの値は，ポジトロンのエネルギーがほぼ 1 MeV ずつ異なる三つの核種 ^{11}C, ^{68}Ga, ^{82}Rb については **Table 2** に示したごとくである．また，消滅放射線の角度揺動に関しては，Colombino ら[3] の詳細な実験データから求めた実験式がある．

ここで，空間分解能の限界をポジトロン CT 装置のスライス厚に無関係に評価するために，ポジトロンの飛程および消滅放射線の角度揺動に基づく投影を線状のポジトロン線源に対して求めることにする．線線源に対する投影として，飛程による線広がり関数を $P_r(r)$，角度揺動による線広がり関数を $P_a(r)$，そして，同時計数検出器対の線応答を $P_d(r)$ とすれば，円形リング型ポジトロン CT の中心軸上にある線線源に対する投影 $P(r)$ は，これらの各投影の重畳積分によって与えられる．すなわち，

$$P(r)=P_r(r)*P_a(r)*P_d(r) \quad \cdots\cdots\cdots(2)$$

ここに，＊印は重畳積分を意味する．$P_r(r)$ は（1）式から数値積分によって求められ，また，$P_a(r)$ も同様に上述の実験式から数値積分によって求められる．角度揺動による広がりはポジトロンの消滅点から検出器までの距離に比例するので，円形リング型検出器の場合，リングの中心軸上に置かれた線線源に対しては，広がりの大きさ Δt は検出器リング直径 D に比例する．また，円形リング検出器の中での線源の位置による広がりの大きさの変化は，**Fig. 1** に

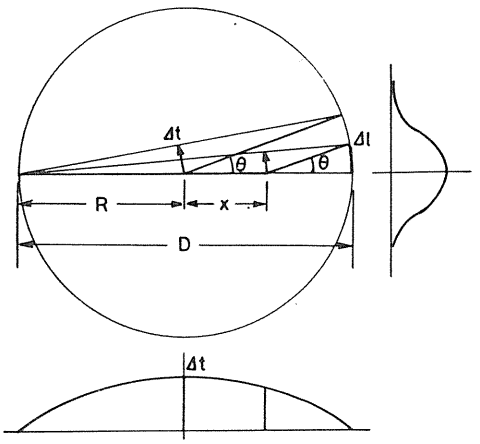

$$\Delta t=\Delta l\cdot\frac{R+x}{D}=\frac{R^2-x^2}{D}\cdot\theta \qquad \Delta l=(R-x)\cdot\theta$$

Fig. 1 Resolution loss owing to angular deviation.

示すように，検出器リングの半径を R，検出器リングの中心から線源までの距離を x，消滅放射線の 180° からのずれ角を θ とすると，

$$\Delta t=\frac{R^2-x^2}{2R}\cdot\theta \quad \cdots\cdots\cdots\cdots(3)$$

と表せる．すなわち，角度揺動による広がりは線源がリングの中心にあるときが最も大きく，リングの周辺に行くにしたがって小さくなる．したがって，以下の計算では広がりの最も大きいリング中心軸上の線線源に対して評価を行った．また，空間分解能の限界を求めるために，同時計数検出器対の線線源応答 $P_d(r)$ としては無限小の解像幅，すなわちデルタ関数を想定した．

結　果

Fig. 2 は（1）式から数値積分によって求めた 3 種のポジトロン放出核種 ^{11}C, ^{68}Ga および ^{82}Rb の線線源に対する投影像 $P_r(r)$ である．また，**Fig. 3** は直径 80 cm の検出器リングの中心軸上の線線源に対する投影で，点線で示した曲線は角度揺動のみの投影 $P_a(r)$ であり，実線

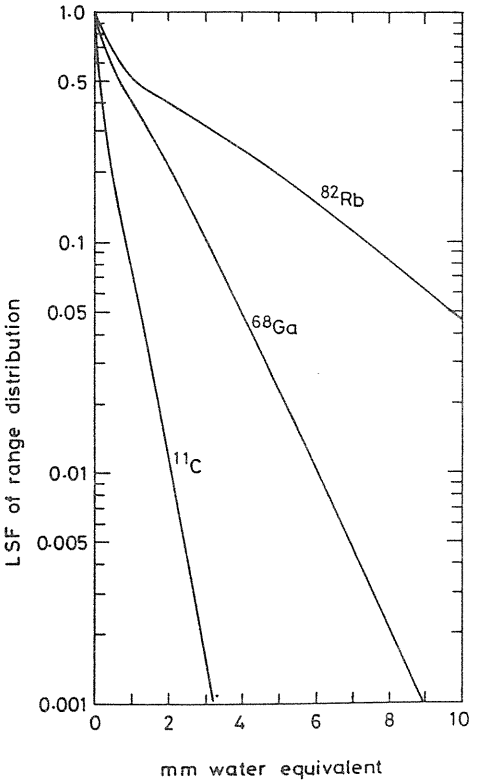

Fig. 2 Line spread functions in projection due to postron range distribution.

で示した3本の曲線は，角度揺動による広がりにそれぞれの核種のポジトロンの飛程による広がりを重畳積分することによって得た広がり関数である．これらの投影をもとにそれぞれを再構成して得た画像上での線広がり関数は **Fig. 4** に示したようになる．ここでも同じく点線で示した曲線は角度揺動のみのものであり，実線で示した3本の曲線は角度揺動とポジトロンの飛程の両因子を考慮した線広がり関数である．

Fig. 3 および 4 で求めたと同様の線広がり関数を検出器リングの半径の関数として求めたものが **Fig. 5** および **Fig. 6** である．Fig. 5 は投影上での線広がり関数，Fig. 6 は画像上での線広がり関数である．すなわち，ポジトロンの飛程と消滅放射線の角度揺動のみによる投影を使って求めた線線源応答を示している．両図において，実線は線広がり関数の半値幅，点線は（1/10）値幅である．

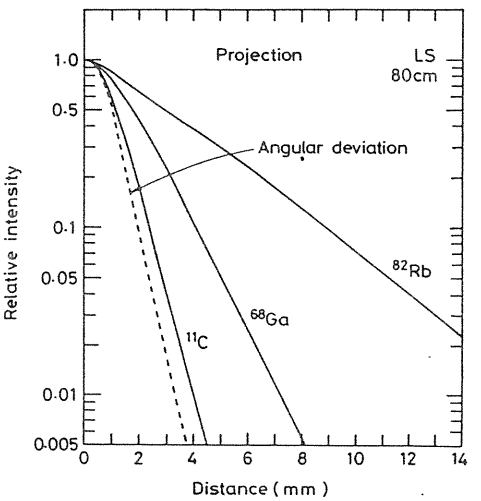

Fig. 3 Line spread functions in projection due to angular deviation of annihilation photons convolved with line spread functions due to positron ranges (solid curve) and without (dashed curve), assuming a line source on the central aixs of a 80 cm diameter detector ring.

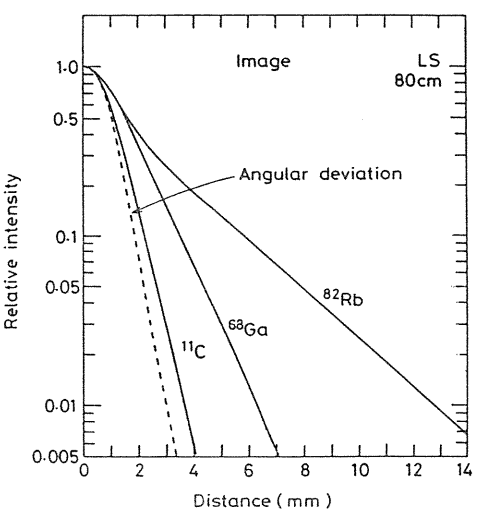

Fig. 4 Line spread functions in image reconstructed from projections given in Fig. 3.

考　察

消滅放射線の角度揺動による線広がり関数はガウス分布に近い形であるが，ポジトロン飛程による線広がりは，線源近傍で鋭い突起状の分

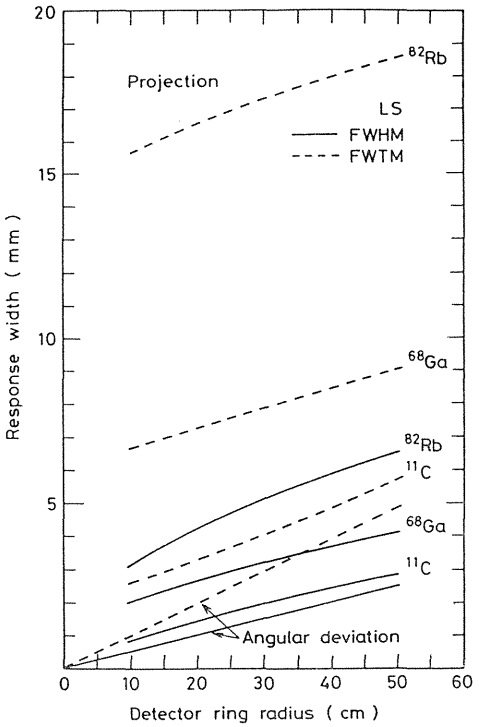

Fig. 5 Full widths at half maximum and at tenth maximum of the line source response in projection as a function of detector ring radius.

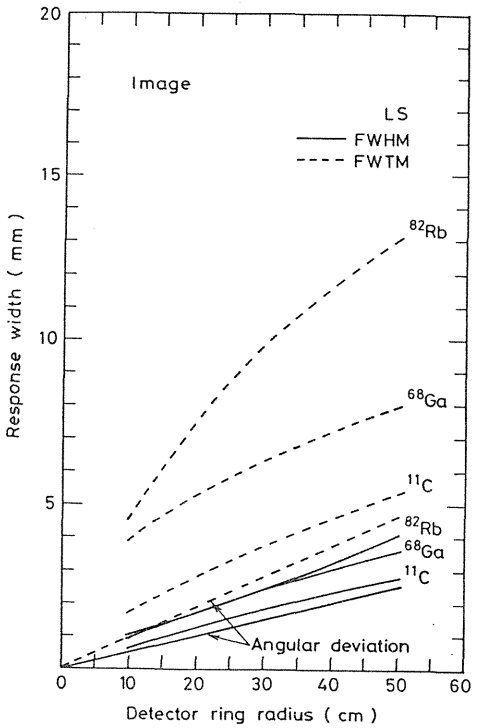

Fig. 6 Full widths at half maximum and at tenth maximum of the line source response in image as a function of detector ring radius.

布を示し，線源から離れたところで緩やかな傾斜の裾をもっている．それゆえ，これらの二つの線広がりの重畳は Fig. 4 に示したように，線源の近傍においては角度揺動のために鋭い突起部分はまるめられ，線源から離れたところではポジトロン飛程の緩やかな傾斜の裾が残るような線広がりとなる．この裾の部分は画像にバックグラウンドを与えるような効果を持つため，画像のコントラストを低下させる．田中ら〔4〕は，このポジトロン飛程を補正する再構成フィルタを提案している．

ところで，（2）式を使って検出器の固有空間分解能が有限の値をもつ場合についても同様の評価を行うことができる〔5〕．たとえば，同時計数検出器対の線線源応答がガウス関数で与えられるとし，Fig. 3 および 4 と同じ条件の 80 cm 直径の検出器リングで，検出器分解能が半値幅で 2 mm，(1/10) 値幅で 3.65 mm の場

Table 3 Spatial resolution achieved by detector ring having detector pair resolution of 2 mm FWHM and 3.65 mm FWTM. Ring diameter is 80 cm

		FWHM (mm)	FWTM (mm)
Detector resolution		2.00	3.65
Angular deviation		2.07	3.76
Ang-dev + Range	^{11}C	2.34	4.57
	^{68}Ga	3.11	7.21
	^{82}Rb	3.27	11.66
Ang-dev + Range + Detector	^{11}C	3.16	5.97
	^{68}Ga	4.05	8.43
	^{82}Rb	4.66	13.73

合の最終的な解像力は **Table 3** に示したような値となる.

結　論

ポジトロン CT の空間分解能の限界値を，ポジトロンの水中における飛程および消滅放射線の角度揺動から評価した．角度揺動のみによる空間分解能は，半径が 10 cm から 50 cm の円形リング検出器では，半値幅で 0.5 mm から 2.5 mm の値をとることを示した．また，これにポジトロンの飛程および検出器の固有空間分解能を考慮することによりポジトロン CT の到達可能な解像力を線線源の場合について示した．

参考文献

〔1〕 Cho ZH, Chan JK, Ericksson L et al: Positron ranges obtained from biomedically important positron emmitting radionuclides. J Nucl Med **16**: 1174-1176, 1975

〔2〕 Derenzo SE: Precesion measurement of annihilation point spread function distributions for medically important positron emitters. Proc. 5th Intern. Conf. Positron Annihilation. Lake Yamanaka, Japan, April 8-11, 1979

〔3〕Colombino P, Fiscella B and Trossi L: Study of positronium in water and ice from 22 to −144°C by annihilation quanta measurements. Nuovo Cimento **38**: 707-723, 1965

〔4〕 田中栄一，野原功全：高解像力ポジトロン CT における陽電子飛程におけるぼけの修正. 核医学 **21**: 1166, 1984

〔5〕 Nohara N, Tanaka E, Tomitani T et al: Analytical study of performance of high resolution positron emission computed tomographs for animal study. IEEE Trans Nucl Sci **NS-32**: 818-821, 1985

<Summary>

Resolution Limit in Positron Emission Computed Tomography

Norimasa NOHARA, Takehiro TOMITANI, Mikio YAMAMOTO,
Hideo MURAYAMA & Eiichi TANAKA

Division of Physics, National Institute of Radiological Sciences
9-1, Anagawa-4-chome, Chiba-shi 260, Japan

There are two fundamental factors limiting the spatial resolution in developing high resolution positron emission tomographs. One is the finite range of positrons before annihilation and the other the deviation from 180 degrees of annihilation photons. The purpose of this paper is to evaluate the effect of the factors on the spatial resolution in reconstructed images. Since line spread functions allow to make the evaluation free from slice thickness, the line spread functions in projection for positron range and angular deviation were calculated from experimental data in leteratures. The physical limitations of the spatial resolution in reconstructed images were estimated for line sources of ^{11}C, ^{68}Ga and ^{82}Rb positioned on the central axis of circular ring detectors, as a function of ring radius ranging from 10 to 50 cm.

* * *

IN VIVO MEASUREMENT OF BRAIN BENZODIAZEPINE RECEPTOR AND ITS APPLICATION

Toshiro Yamasaki
Osamu Inoue
Kenji Hashimoto
Hitoshi Shinotoh
Yukio Tateno
Takashi Ito
Kazutoshi Suzuki*
Yoshihiko Kashida**

Division of Clinical Research
* Section of Cyclotron
** Senior Research Counselor
National Institute of Radiological Sciences
Chiba, Japan

I. INTRODUCTION

Positron CT is rapidly growing in clinical importance, as new tracers including specific ligands for neuroreceptors are developed (1-4). Although practical results are still preliminary, these new tracers will enable us not only to diagnose biochemical derangements occurring in the diseased human brain, but also to make direct measurements of psychological states of mind.

Stress plays an important role as a trigger or as an effector in some kinds of disease. In animal experiments, significant changes in the neurotransmission system in the stressed brain have been reported (5,6). In addition, several reports indicate that central benzodiazepine-receptor binding with its ligand was changeable in response to physiological stimulation in animal studies (7-9). However, there is no direct method for measuring such alterations caused by stress in a living brain.

In this study, the biodistribution of a central type benzodiazepine antagonist, (H-3)-Ro15-1788 (10) (FIGURE 1) in control and stress-loaded mice was measured, and a method to detect changes of benzodiazepine-receptor function in human brain in several conditions using (C-11)-Ro15-1788 (11) (FIGURE 1) is presented.

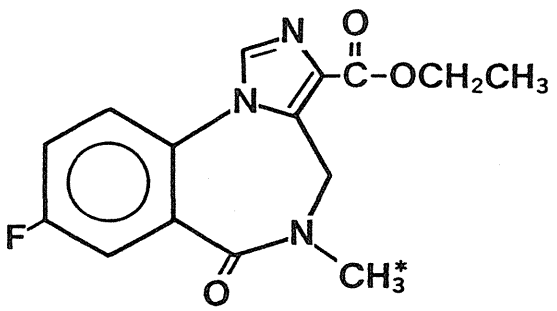

M.W. 303.3

FIGURE 1. Ro15-1788.

II. ANIMAL EXPERIMENTS

Before the human study was undertaken, the biodistribution of (H-3)-Ro15-1788 in control and stress-loaded mice was compared; the details of this study will be reported in another paper (12). The stress was produced by forcing the mice to swim in a water basin at 16 °C for 5 min. Within 3 min after the forced swimming was terminated the tracer was injected.

In control mice, carrier-free (H-3)-Ro15-1788 was selectively and highly distributed in the brain. There were significant differences in radioactivity among various brain regions; the highest level was observed in the cerebral cortex, which is the benzodiazepine receptor rich area (13,14). The brain kinetics of (H-3)-Ro15-1788 in control experiments showed a high uptake by the brain, immediately after the intravenous injection; the maximum was reached after about 5 min, then a relatively rapid decrease occurred (FIGURE 2, left).

In stress-loaded mice, significant changes of the time-activity curves using carrier-free tracer were observed (FIGURE 3, left). Brain radioactivity increased over a period of 15 min after the tracer was injected, whereas radioactivity in the blood decreased. Moreover, a

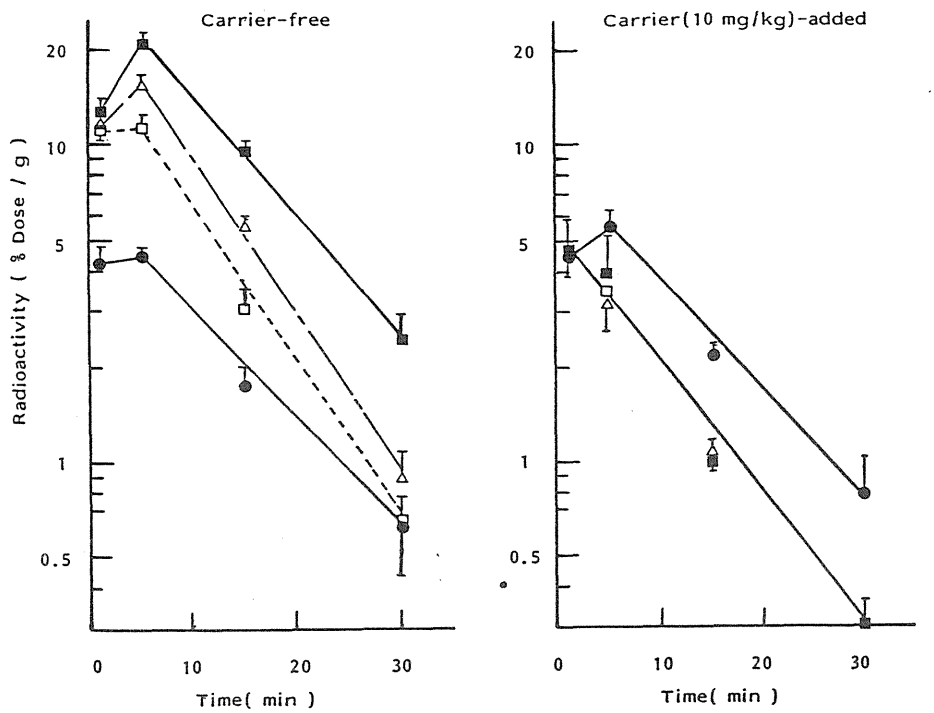

FIGURE 2. Biodistributions of carrier-free (0.011 nmol/mouse); (left), or carrier-added (10 mg/kg); (right) (H-3)-Ro15-1788 in control mice after intravenous injection. Radioactivity in cerebral cortex (■---■), cerebellum (Δ---Δ), pons-medulla (□---□) and blood (●---●) was expressed as percentage dose administered per gram of organ. Values are presented as avarage ± 1 s.d. of three mice at each point.

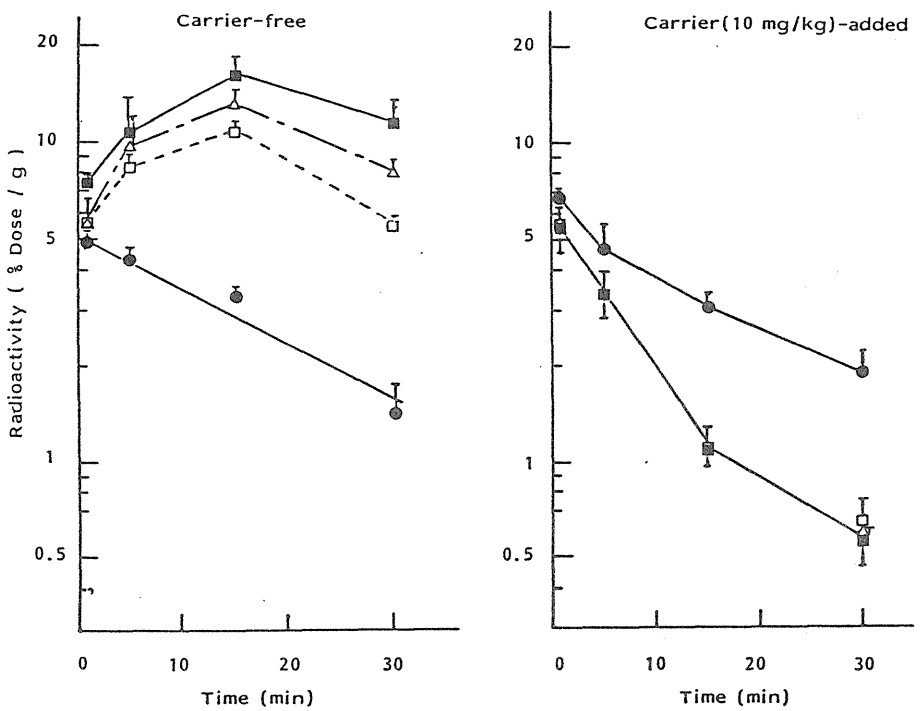

FIGURE 3. Biodistributions of carrier-free (0.011 nmol/mouse); (left), or carrier-added (10 mg/kg); (right) (H-3)-Ro15-1788 in stress-loaded mice (forced swimming) after intravenous injection. The tracer was injected within 3 min after forced swimming as described in the text. Radioactivity in cerebral cortex (■---■), cerebellum (Δ---Δ), pons-medulla (□---□) and blood (●---●) was expressed as percentage dose administered per gram of organ. Values are presented as avarage ± 1 s.d. of three mice at each point.

smaller amount of the tracer accumulated in the brain at 1, and 5 min after administration than accumulated in the control mice.

In control and stress-loaded experiments using carrier-added tracer, tracer accumulation in the brain was very low and no significant changes were observed(FIGURE 2, 3-right).

III. HUMAN STUDIES

For the human study, Ro15-1788 labelled with a high specific activity (0.3-1 Ci/ μmol) with (C-11) by a mehthylation process was used. Approximately 5 mCi of (C-11)-Ro15-1788 was injected intravenously into each normal volunteer. Sequential measurement of the brain radioactivity was performed at 5 slice levels, for 20, 30 or 40 min after the tracer was injected, using a positron CT system "Positologica-II" originally developed by our Institute (15). While external measurements were being made, venous blood samples were collected in all cases. In one case, a saturation study was carried out using 30 mg of non-radioactive Ro15-1788 as a carrier. In this series 9 human studies were performed on 7 normal volunteers.

In a typical case a high and homogenous distribution of (C-11) labelled ligands in the cerebral cortex was observed soon after the tracer was administered. (C-11) was also highly concentrated in the cerebellar cortex and moderately distributed in the basal ganglia and thalamus. A low concentration of activity was observed in the brain stem and white matter (FIGURE 4).

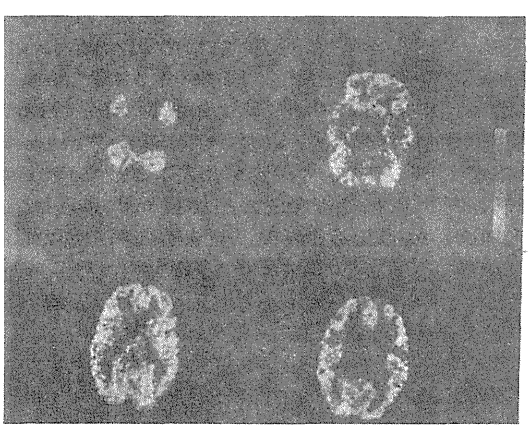

FIGURE 4. Normal human brain images using (C-11)-Ro15-1788. The interval of each slice is 18 mm.

FIGURE 5 shows sequential images of the cerebellar level in a normal volunteer in a resting state. These images were taken during the 30 min period immediately after the injection. Kinetic curves of these two areas, cerebellar and frontal base, are shown in FIGURE 6. The peak time of the two curves is different: the peak of the curve in the frontal area is later and higher.

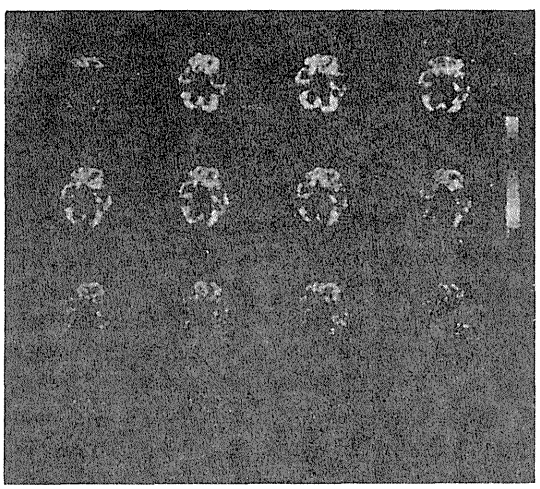

FIGURE 5. Sequential images of cerebellar and frontal base level in a normal volunteer using (C-11)-Ro15-1788. 2 min. per frame.

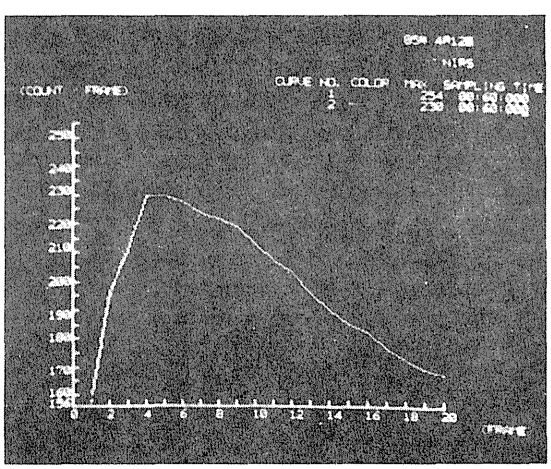

FIGURE 6. Kinetic curves of (C-11)-Ro15-1788 in frontal base (1) and cerebellar cortex (2). 0 - 20 min.

FIGURE 7 also shows the brain kinetics of (C-11)-Ro15-1788. These time activity curves were recorded in another normal volunteer in a resting state. The maximum accumulation of tracers in the brain occurred within 10 min. After that, the activity decreased gradually until the end of the study. FUGURE 8 shows the kinetic curves in another case. In this experiment, the volunteer was very nervous, because it was the first trial using (C-11)-Ro15-1788. Furthermore he had received painful manipulations accidentally before the study. In this case activity of the cerebral cortex continued to increase for more than 10 min after the tracer was injected. This pattern of the cerebral cortex time activity curve is the same as that observed in the animal with stress loading.

Besides these usual tracer studies, a saturation experiment was performed in one volunteer. Thirty min before the tracer was injected, 30 mg of non-radioactive Ro15-1788 was administered orally, afterwards, the study with (C-11)-Ro15-1788 was carried out. In this study almost no specific brain uptake was seen; so the activity in the brain seemed to reflect mainly blood perfusion and non-specific binding of the tracer (FIGURE 9). FIGURE 10 shows sequential brain CT images of this individual from 0 to 20 min after the tracer was injected.

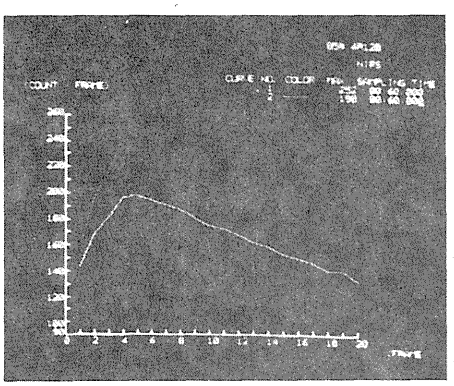

FIGURE 7. (C-11)-Ro15-1788 time activity curves in human brain (0 - 20 min, in resting state, 1 : frontal cortex, 2 : striatal region).

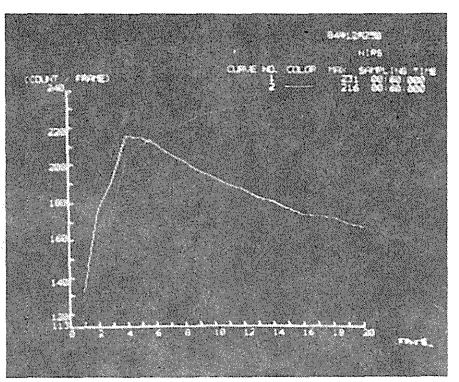

FIGURE 8. (C-11)-Ro15-1788 time activity curves in human brain (0 - 20 min., in stressful state, 1 : frontal cortex, 2 : striatal region).

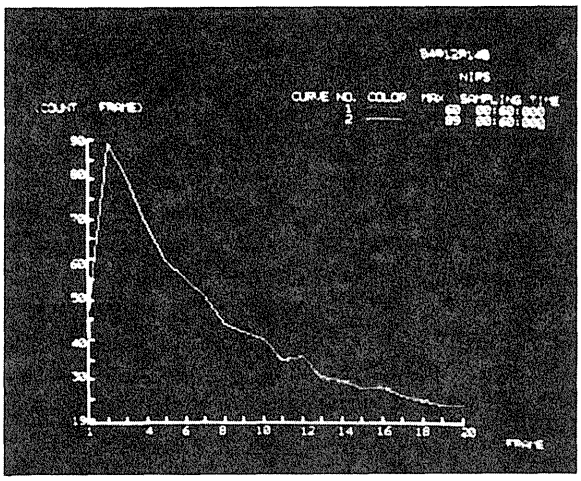

FIGURE 9. (C-11)-Ro15-1788 time activity curves in human brain, after saturation using carrier doses of Ro15-1788. (0 - 20 min., 1: temporal cortex, 2 : cerebellar cortex).

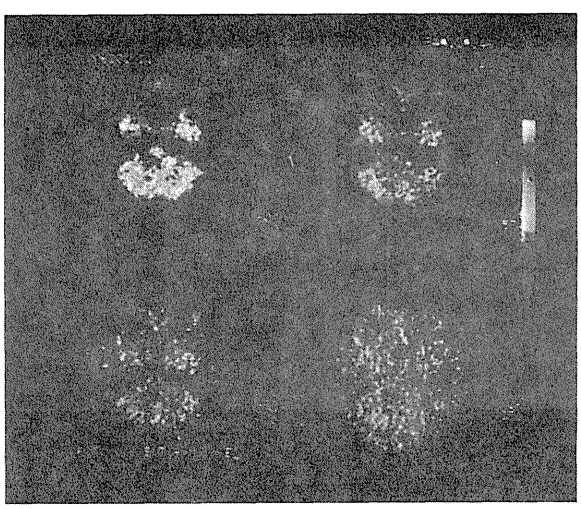

FIGURE 10. (C-11)-Ro15-1788 sequential images of cerebellar level in a normal case, after saturation using carrier doses of Ro15-1788. 5 min. per frame.

IV. DISCUSSION AND CONCLUSIONS

Before the study, the in vivo stability of (H-3)-Ro15-1788 after intravenous injection was evaluated using animals; it was found to be stable in the brain for at least 30 min.

The brain radioactivity observed after the tracer was injected after a large amount of carrier ligands was administered is due to the nonspecific binding plus free ligands in the brain. The specific binding of ligands in each brain region could be estimated by subtracting the radioactivity in the carrier-added state from that in the carrier-free state. However, the total radioactivity observed using the carrier-free tracer seemed to be almost the same as that of the specific binding, because of the low levels of nonspecific binding and free ligand in the brain.

The distribution and concentration of the tracer was highest in the cerebral cortex; the concentration in brain stem and white matter was low. This in vivo distribution pattern of the tracer is consistent with benzodiazepine receptor distribution in the brain reported previously (10).

The most important and interesting finding in this study is the significant different time course of cerebral activity observed between the stressful and resting states after the injection of the carrier-free tracer; this difference was observed in the human and animal studies. These alterations seem not to be due to changes in a physiological condition, such as blood flow, but to changes in benzodiazepine receptor function in the brain, association or dissociation rate, or the numbers of benzodiazepine binding site available, because no such difference was found using carrier-added tracers.

From these results, it will be concluded that the positron CT study using (C-11)-Ro15-1788 with high specific activity will become a new technic to detect changes of psychological conditions in the human brain and to diagnose certain kinds of neuropsychiatric disease.

ACKNOWLEDGEMENT

We thank Dr. K. Nakamura, Japan Roche Research Center for providing us desmethyl derivative of Ro15-1788 and Mr. K. Tamate, Mr. Kuchiki for their technical assistance.

REFERENCES

1. Wagner, H. N. and Burns, Jr. H. D. et al., Science 221:1264 (1983).
2. Ehrin, E. and Johnström, P. et al., C-11-Labelling of Ligands for PET Studies of Dopamine and Benzodiazepine Receptors, in 5th Int. Symp. on Radiopharm. Chem., July 9-13, Tokyo (1984).
3. Dannals, R. F. and Ravert, H. T. et al., Radiosynthesis of Opiate Receptor-Binding Radiotracer for Positron Emission Tomography: (^{11}C Methyl)-Methyl-4-N-(1-Oxopropyl)-N-Phenylamino-4-Piperidine Carboxylate (^{11}C 4-Carbomethoxyfentanyl), in 5th Int. Symp. on Radiopharm. Chem., July 9-13, Tokyo (1984).
4. Hantraye, P. and Kajima, M. et al., Neuroscience Letters, 48:115 (1984).
5. Bliss, E. L. and Ailion, J. et al., J. Pharmacol. Exp. Ther., 164:122 (1968).
6. Kathryn, H. D. and Wolfgang, H. V., J. Pharmacol. Exp. Ther., 223:348 (1982).
7. Medina, J. H. and Novas, M. L. et al., Eur. J. Pharmacol, 96:181 (1983).
8. Nutt, D. J. and Minchin, M. C. W., J. Neurochem., 41:1513 (1983).
9. Soubrie, P. and Thiebot, M. H. et al., Brain Res., 189:505 (1980).
10. Mohler, H. and Richards, J. G., Nature, 294:763 (1981).
11. Maziere, M. and Prenant, C. et al., C. R. Acad. Sc. Paris, 296:871 (1983).
12. Inoue, O. and Akimoto, Y. et al., Alterations in Biodistribution of ^{3}H-Ro15-1788 in Mice by Acute Stress: Possible Change in In Vivo Binding Availability of Brain Benzodiazepine Receptor, Submitted in J. Nucl. Med. & Biol.
13. Richards, J. G. and Möhler, H., Neuropharmacology, 23:233 (1984).
14. Braestrup, C. and Albrechtsen, R. et al., Nature 269:702 (1977).
15. Tamaki, K. and Tanaka, E. et al., IEEE Trans. Nucl. Sci., NS-30, 734 (1983).

《原　著》

心ポジトロンCTにおけるFast Dynamic Studyの有用性

吉田　勝哉*　氷見　寿治*　増田　善昭*　稲垣　義明*
福田　信男**　山崎統四郎**　舘野　之男**

要旨　局所血流をみるトレーサーである$^{13}NH_3$を健常例に急速静注し，ポジトロンCTにより6秒ずつ連続20回のデータ収集(fast dynamic study)を行った．最初0–6秒の画像では，^{13}Nは主に右房，右室腔に存在し，さらに肺を経て12–18秒では左房，左室腔へ移行する．その後心腔から^{13}Nが洗い出されて左室心筋横断像が得られた．また心筋の時間放射能曲線を，画像上で心腔から心筋への放射能濃度の混じり合いを補正することにより得ることができた．心腔の時間放射能曲線は，心筋からの放射能濃度の影響のない左房腔に関心領域を設定して得た．これによりポジトロンCTによるfast dynamic studyが，トレーサーの心腔および心筋での経時的変化をとらえる有用な方法であることが示された．

I. はじめに

ポジトロンCTの出現により，心筋の局所血流や代謝の非侵襲的評価が可能になるものと期待されている[1]．われわれは局所血流測定のためのトレーサーである^{13}N-アンモニア($^{13}NH_3$)を使用して心ポジトロンCTを行っている[2]．ポジトロンCTでは，動的解析(dynamic study)を行ってトレーサーの組織での経時的変化をとらえることが，そのトレーサーの組織内動態を知る上で重要である[3]．特に心臓を対象とする際は，この方法の利点として横断像の左心腔と心筋に関心領域を設定することで，血中と心筋の時間放射能曲線を同時に得ることができる．一方心拍動や呼吸による動きの影響などのため，心腔と心筋の放射能濃度が画像上混じり合うといったこの臓器に特有の問題もある[4]．また$^{13}NH_3$のように心筋への取り込み率が高く[5]，静注後1分以内に心筋に取り込まれてしまうトレーサーでは，その取り込み過程をとらえるために，dynamic studyにおける1回のデータ収集時間を秒単位まで短くすることが必要である．

そこで今回われわれは，臨床例で$^{13}NH_3$の心筋への取り込み過程を研究するため，6秒ずつ連続20回のデータ収集すなわちfast dynamic studyを行った．さらに心腔，心筋で定量的な時間放射能曲線を得るための試みを検討したので報告する．

II. 対象と方法

(1) ポジトロンCT装置

使用したポジトロンCT装置(ポジトロジカ-II)は，直径85 cmの円周上に160個のBGO検出器を配列した検出器リング3層から成り，18 mm間隔で5スライスの撮影を同時に行うことができる．空間分解能は半値幅として，視野中心および周辺部でそれぞれ9.2 mm, 12 mmである．感度はリング内およびリング間スライスで28, 38 kcps/μCi/mlである．本装置の詳細は別に報告されている[6,7]．

(2) 放射性医薬品

$^{13}NH_3$水溶液は，放医研サイクロトロンと$^{13}NH_3$自動合成装置を使って生成した[8]．

* 千葉大学医学部第三内科
** 放射線医学総合研究所臨床研究部
受付：60年1月23日
最終稿受付：60年2月25日
別刷請求先：千葉市亥鼻1–8–1　(〒280)
千葉大学医学部第三内科
吉　田　勝　哉

(3) 対象および撮影法

われわれは $^{13}NH_3$ による fast dynamic study を健常および各種心疾患例，計20症例に行った．今回は本法の基礎的検討を行うために，この中から健常4例を選び対象とした．平均年齢は51歳である．被検者は検査台上に仰臥位とし，$^{13}NH_3$ 水溶液 6.0～9.4 mCi を上腕正中静脈から約2秒以内で静注し，さらに生理食塩水約 10 m*l* でフラッシュして急速注入とした．静注と同時に6秒ずつ連続20回のデータ収集を行い，その後さらに同一部位で30秒のデータ収集を追加した．なお収集カウント数は，左室中央部レベルの1断面につき，最初の6秒で 8.6～16.3 万カウント，次の6秒で 16.6～22.0 万カウント，114～120秒で 6.0～9.4 万カウントであった．このようにして収集したデータは，検出器の感度不均一補正，患者測定部位の γ 線減弱補正，偶発同時計数の差し引きなどの前処理を行ったのち，重畳積分法を用いて画像再構成した．

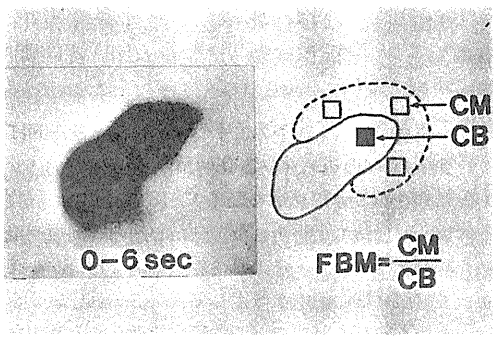

Fig. 1 Fractional spillover from blood to myocardium (FBM) was determined by assigning regions of interest to the right ventricular blood pool (CB) and the area surrounding CB (CM).

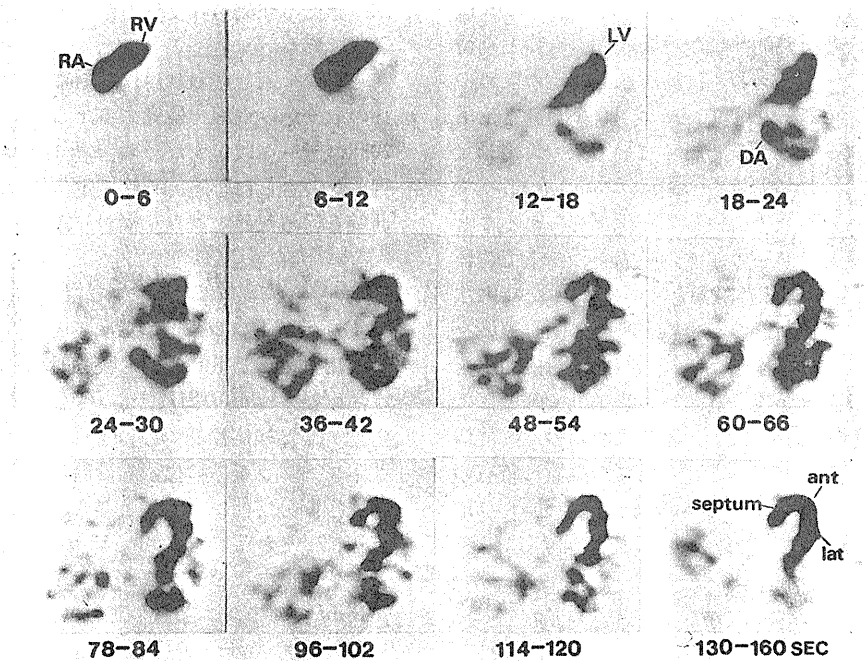

Fig. 2 Serial 6-second PCT images obtained at the midventricular level after bolus venous injection of N-13 ammonia in a normal case. RA=right atrium; RV and LV=right and left ventricles; DA=descending aorta; ant=anterior; lat=lateral wall of the left ventricle; septum=interventricular septum.

(4) 時間放射能曲線

左心腔については，左室上部レベルの断面で，左室心筋からの放射能濃度の混じり合いのない左房腔に関心領域 (ROI) を設定した．

左室心筋については，左室中央部レベルの断面で，左室前壁および側壁の中心部に合計4個のROIをとり，これを平均して左室心筋の放射能濃度とした．なお心室中隔については，右室腔放射能濃度に影響されるため除外した．さらに左室腔放射能濃度の左室心筋への混じり合い (Fractional spillover from blood to myocardium: FBM) を推定し，これから左室心筋の真の放射能濃度の算出を試みた．まず静注後130～160秒に収集したデータで，最大カウントの50%を閾値として左室心筋の辺縁を決める．これをトレーサーが主として左室腔に存在する12～18秒の画像に重ね，その内膜面に一致する左室腔辺縁の閾値を求める．次いで右房，右室腔にトレーサーがほぼ限局する0～6秒の画像に，これと同一の閾値で右房，右室腔の辺縁を求め，その周囲に左室心筋と同じ大きさの心筋を仮想する (Fig. 1)．そして右室腔，仮想心筋の中心部にROIを設定し，右室腔放射能濃度 (CB)，仮想心筋放射能濃度 (CM) を求め，これよりFBMは，CM/CBとして算出する．そして経時的に得られる左房内放射能濃度 (X)，左室心筋放射能濃度 (Y) から，真の左室心筋放射能濃度 (Z) は，$Z=Y-FBM\cdot X$ として得た．

なお時間放射能曲線の作成にあたっては減衰の補正を行い，放射能濃度は1絵素あたりのカウントをarbitrary unitsとして表示した．

III. 結　果

(1) 連続横断像

全例で良質な画像が得られ，$^{13}NH_3$ が静注後右心系，肺，左心系を経て心筋に取り込まれる状態を，連続横断像としてとらえることができた．左室中央部レベルの断面では (Fig. 2)，0～6秒で右房，右室腔にトレーサーがあり，肺を経て12～

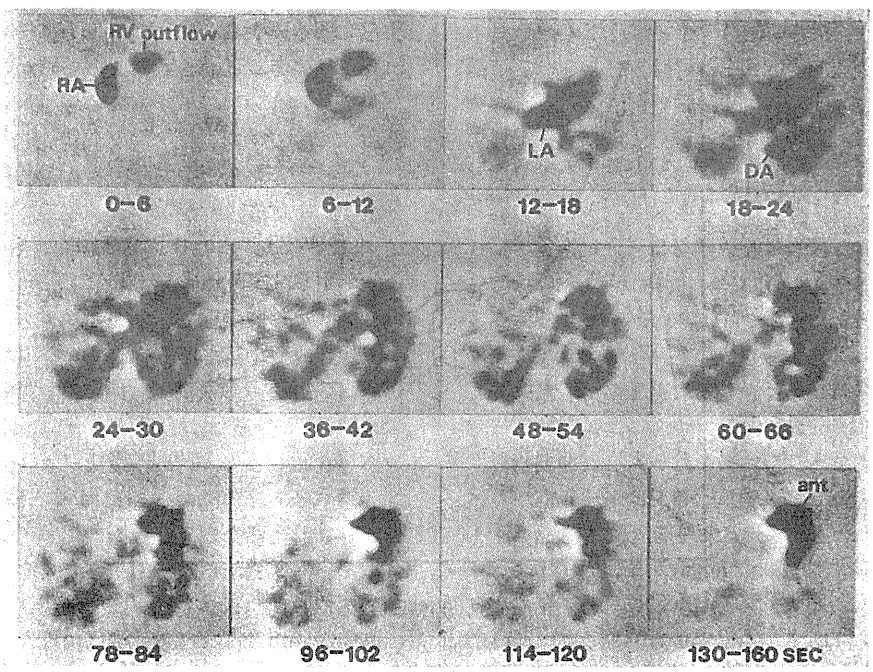

Fig. 3 Serial 6-second PCT images obtained at the highventricular level in the same case. LA=left atrium.

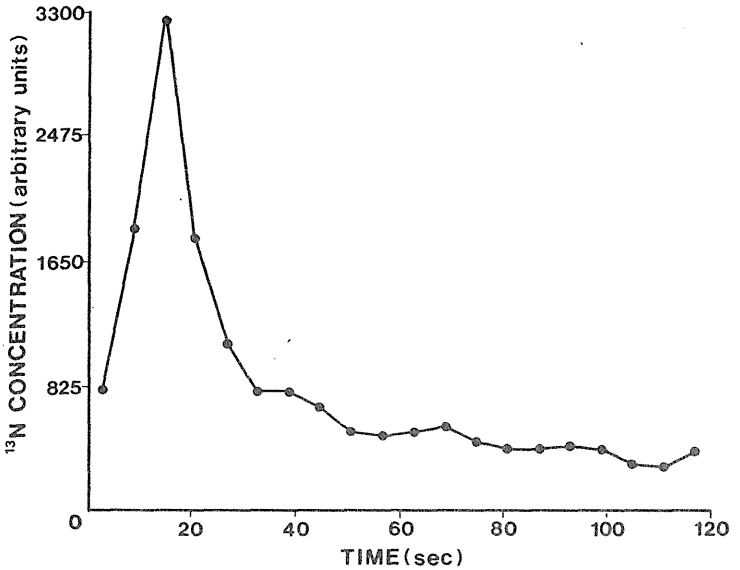

Fig. 4 Blood pool time-activity curves were obtained from these serial PCT images by assigning a region of interest over the left atrium.

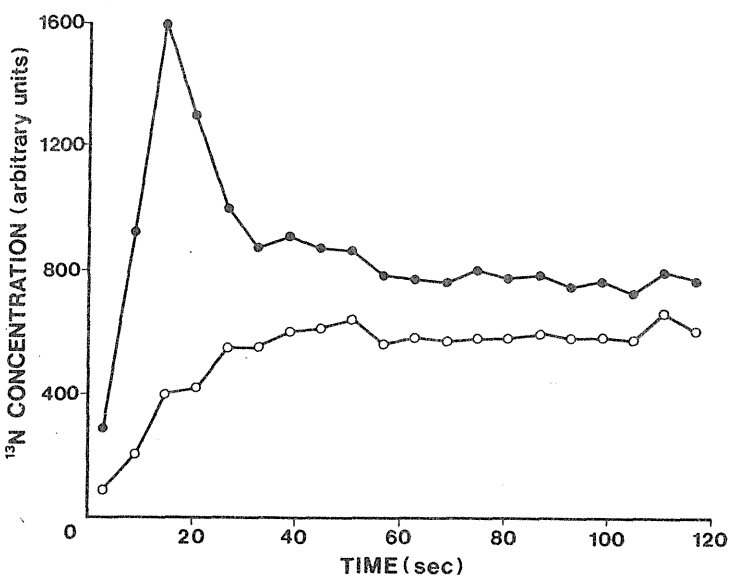

Fig. 5 Myocardial time-activity curves before (solid circles) and after (open circles) correction for cross-contamination from blood to myocardium.

18秒で主として左室腔にトレーサーが集積する．さらに30秒あたりまでは，心腔，心筋，肺の濃度がほぼ同一となって各臓器のコントラストがつかなくなる．その後徐々に肺，心腔からトレーサーが洗い出されて，60秒あたりから左室心筋が描出される．これより18 mm頭側の左室上部レベルの断面では(Fig. 3)，0～6秒で右房，右室流出路にトレーサーがあり，肺を経て12～18秒で左房腔にトレーサーが集積する．その後左室上部心筋が描出される．

(2) 時間放射能曲線

左心腔については，左室上部レベルの断面で左房腔にROIをとることで，左室心筋からの放射能濃度の混じり合いのない，動脈血の放射能濃度の経時的変化をとらえることができた(Fig. 4)．

左室心筋については，左室腔からの放射能濃度の混じり合いの程度(FBM)を前述した方法により算出し，これより真の左室心筋放射能濃度を求めた(Fig. 5)．この際FBMは38～42%であった．補正後の時間放射能曲線についてみると左室心筋へは$^{13}NH_3$は約60秒までにすみやかに取り込まれ，その後ほぼ一定の濃度となることが示された．

IV. 考　察

今回の検討により，6秒ずつ連続20回という，1回のデータ収集時間のきわめて短いdynamic studyでも連続横断像が得られることが示された．Ter-Pogossianらは，ポジトロンCTによるdynamic studyで，1回のデータ収集時間が1分以内のものをfast dynamic studyと呼ぶことを提唱している[3]．今回のわれわれの検討は，現在までに報告されているポジトロンCTによるdynamic studyでは，1回のデータ収集時間がもっとも短いもので，$^{13}NH_3$のように心筋への取り込み率が高く，静注後1分以内に心筋に取り込まれてしまうトレーサーでも，その取り込み過程を連続横断像としてとらえ得ることが示された．これにより心腔，心筋の時間放射能曲線から，そのトレーサーの心筋内動態を解析することも可能である[9]．この際心臓は，左心腔に関心領域を設定することで，動脈血の放射能濃度も非侵襲的に知り得るという利点がある．しかしこのためには定量的な時間放射能曲線を得ることが必要で，まだいくつかの克服すべき技術的課題がある．

第1に，心拍動や呼吸による動きの影響，および左室壁厚が正常で約10 mmに対し，現在一般的に使われている全身用ポジトロンCT装置の半値幅も約10 mm前後であることなどのために，心腔と心筋の放射能濃度が画像上で混じり合う問題がある．Henzeらは犬の実験でその補正を試みているが[4]，彼らの方法では心筋の壁厚，心腔の径の正確な測定が不可欠であり，臨床応用には問題がある．また心拍動の影響を除くため心電図同期も行っているが，今回のように1回のデータ収集時間が秒単位の場合，これも困難である．そこで今回われわれは，心腔については使用装置が多断層装置である利点を生かし，左室上部レベルの断面で左房腔にROIを設定した．これにより，心筋の影響を受けない動脈血の放射能濃度を知ることが可能となった．また心筋については，最初の6秒の画像でトレーサーがほぼ右房，右室腔に限局していることを利用して，左室腔放射能濃度の左室心筋への影響を画像上で推定して，左室心筋放射能濃度の補正を行った．

第2に，心腔内に高濃度のトレーサーが存在する場合でもその定量性が求められるので，ポジトロンCT装置の高計数率特性が問題となる．今回われわれは6.0～9.2 mCiの$^{13}NH_3$を静注したが，この範囲では静注後6～18秒あたりで計数率が1断面あたり20～30 kcpsとなり，アイソトープ濃度と計数率との直線性にズレが生じ，10～20%計数効率が低下する．今後定量的な心腔，心筋の時間放射能曲線を得るためには，これを補正するかあるいはトレーサー静注量をさらに少なくするか，いずれかの対策が必要である．以上の2点はポジトロンCTによるdynamic studyを心臓に応用する際に解決すべき技術的課題であり，今後定量化に向けてさらに検討を進めたい．

以上の検討より得た補正された心筋の時間放射能曲線から，健常心筋では$^{13}NH_3$は静注後1分

以内にすみやかに取り込まれ，その後ほぼ一定の濃度となることが示された．Mullaniらは^{82}Rbを使った犬の実験で，静注後の心筋への取り込み過程を時間放射能曲線としてとらえることで，トレーサーの取り込み率を測定し，これにより正確な心筋血流評価が可能であると報告している[10]．$^{13}NH_3$についても，動脈血と心筋の定量的な時間放射能曲線を得ることができれば，これを解析することにより局所血流を測定することが可能になると思われる．

V. 結　語

臨床例に$^{13}NH_3$を静注し，ポジトロンCT装置により6秒ずつ20回のデータ収集(fast dynamic study)を行うことで，心筋への取り込み過程を連続横断像としてとらえ，左心腔，左室心筋の時間放射能曲線を得ることが可能となった．

文　献

1) 吉田勝哉，増田善昭，山崎統四郎，他：ポジトロンCTの心血管系への応用．呼吸と循環 32: 241–248, 1984
2) 宍戸文男，舘野之男，吉田勝哉，他：$^{13}NH_3$による心筋ポジトロンCTイメージングの心筋梗塞診断への応用——Positologica-IIによる経時的イメージと多断層イメージ——．核医学 21: 799–804, 1984
3) Ter-Pogossian MM: Special characteristics and potential for dynamic function studies with PET. Semin Nucl Med 11: 13–23, 1981
4) Henze E, Huang S-C, Ratib O, et al: Measurement of regional tissue and blood-pool radiotracer concentration from serial tomographic images of the heart. J Nucl Med 24: 987–996, 1983
5) Schelbert HR, Phelps ME, Huang S-C, et al: N-13 ammonia as an indicater of myocardial blood flow. Circulation 63: 1259–1272, 1981
6) Tanaka E, Nohara N, Tomitani T, et al: Analytical study of the performance of a multilayer positron computed tomography scanner. J Comput Assist Tomogr 6: 350–364, 1982
7) Takami K, Ueda K, Okajima K, et al: Performance study of whole-body, multislice positron computed tomograph—Positologica-II—. IEEE Trans Nucl Sci NS-30: 734–738, 1983
8) 井戸達雄，岩田　錬：全自動短寿命ラジオアイソトープ標識化合物合成装置の試作——$^{13}NH_3$全自動合成装置——．Radioisotopes 30: 1–6, 1981
9) Budinger TF: Dynamic transmission computed tomography, emission tomography, and nuclear magnetic resonance methods of measuring physiologic parameters. Mayo Clin Proc 57: suppl: 67–77, 1982
10) Mullani NA, Goldstein RA, Gould KL, et al: Myocardial perfusion with rubidium-82. I. Measurements of extraction fraction and flow with external detectors. J Nucl Med 24: 898–906, 1983

Summary

Usefulness of Fast Dynamic Study in Cardiac Positron CT

Katsuya YOSHIDA*, Toshiharu HIMI*, Yoshiaki MASUDA*, Yoshiaki INAGAKI*, Nobuo FUKUDA**, Toshiro YAMASAKI** and Yukio TATENO**

*Third Department of Internal Medicine, Chiba University School of Medicine
**Division of Clinical Research, National Institute of Radiological Sciences

The purpose of this study is to evaluate the usefulness of the Positron CT (PCT) approach to the investigation of dynamic physiologic processes of the heart. Serial 6-second PCT scans for 2 minutes (fast dynamic study) were performed in 4 normal cases after bolus venous injection of $^{13}NH_3$.

On the first image (0–6 sec), ^{13}N activity was primarily in the right atrium and ventricle. On the third image (12–18 sec), it was primarily in the left atrium and ventricle. After clearance from blood, the left ventricular myocardium was well visualized. Myocardial time-activity curves were derived from these serial PCT images after correction for cross-contamination from blood to myocardium. Blood pool time-activity curves were determined by assigning a region of interest over the left atrium that had no effect of spillover of radioactvity from myocardium.

Our preliminary work indicated the potential usefulness of fast dynamic PCT for the observation of physiologic processes of the heart.

Key words: $^{13}NH_3$, Fast dynamic study, Cardiac positron CT.

《原　著》

^{11}C-Ro 15-1788 ポジトロン CT による in vivo ベンゾジアゼピン・レセプターの研究

篠遠　仁*　山崎統四郎*　井上　修*　伊藤　高司*
橋本　謙二*　舘野　之男*　池平　博夫*　鈴木　和年**
樫田　義彦***

要旨　正常ボランティア 15 名を対象として ^{11}C-Ro 15-1788の臨床治験を行い，有効性および安全性を評価した．^{11}C-Ro15-1788 の脳内移行性は良好であり，大脳皮質にてもっとも高い取り込みが見られた．トレーサー投与初期にはトレーサーの分布は大脳皮質，基底核，視床，小脳で高く正常脳血流の分布と相似していたが，時間経過とともに大脳皮質でのトレーサーの集積が目立つようになり，小脳，基底核，視床での集積は中等度で，脳幹部では低いなど in vitro の検索によるベンゾジアゼピン・レセプターの分布 (B_{max}) と相似するものとなった．飽和実験ではコントロール実験と比較しトレーサー投与後 20 分の時点の大脳皮質の放射能は 20～30％にまで減少した．一時間にて投与されたトレーサーの約半分が尿中に排泄された．

I. はじめに

ベンゾジアゼピン系薬剤は，抗不安薬，睡眠薬，抗けいれん薬として広く臨床に用いられている．ベンゾジアゼピン系薬剤には，脳内に特異的作用部位“レセプター”が存在し[1~3]，レセプターに対する内在性リガンドの存在も推定されている[2,4]．動物実験ではけいれん[5,6]，ストレス負荷[7,8]，薬物投与におけるベンゾジアゼピン・レセプターの変化[9,10]が報告され，人の剖検脳における検索でもハンチントン舞踏病[11~13]，アルツハイマー病[14]などにおいてベンゾジアゼピン・レセプターの異常が指摘されている．

ポジトロン標識薬剤およびポジトロン CT を用いての人の in vivo におけるベンゾジアゼピン・レセプターの測定を行うことができれば，人間の脳機能の解明，神経精神疾患の病態，原因究明，レセプター占有と薬理効果との関係などの薬理学的研究に多くの情報をもたらすものと期待される．

Ro 15-1788 は，ベンゾジアゼピンのアンタゴニスト[15,16]であり，1983年 Mazière らによって ^{11}C-Ro 15-1788 の合成の報告がされている[17]．ポジトロン CT を用いたヒヒにおける実験により，^{11}C-Ro 15-1788 は in vivo においても特異的結合の割合の高い優れたトレーサーであることが示されている[18,19]．また最近人における動態の報告もなされた[20]．

われわれは，先に ^{11}C-Ro 15-1788 の前臨床段階の評価を行い報告した[21]．今回，正常ボランティア 15 名を対象とし，11 C-Ro 15-1788 の臨床治験を行い脳内および全身のトレーサーの動態を測定し，有効性および安全性の評価を行ったので報告する．

II. 対象および方法

対象は 21 歳より 70 歳までの健康成人男性 15 名である (20 歳代 9 名，30 歳代 1 名，40 歳代 1 名，50 歳代 2 名，60 歳代 1 名，70 歳代 1 名)．被験者には検査前に十分な検査内容，目的の説明が行わ

* 放射線医学総合研究所臨床研究部
** 同　サイクロトン管理課
*** 同　特別研究員
受付：60 年 6 月 20 日
最終稿受付：60 年 8 月 14 日
別刷請求先：千葉市穴川 4 丁目 9-1 (〒260)
放射線医学総合研究所臨床研究部
篠遠　仁

れ承諾が得られた．被験者には薬物を常用している者はなく，検査前2週間以内に特別な薬は服用していない．各被験者の体重は理想体重の−12〜+11%の範囲にあった．

^{11}C-Ro 15-1788は，Ro 15-1788のN-desmethyl体のメチル化により合成し規格試験を行ったのち臨床に供された[22]．比放射能は規格試験時に280〜3,180 mCi/μ molであった．

脳内動態の測定はポジトロジカII[23]により行った．被験者はスキャナー台に安静閉眼状態にて仰臥し，5スライスのうち最も下位のスライスが眼窩外耳孔線上10 mmとなるよう位置ぎめをおこなった．透過スキャンを行ったのち，あらかじめ確保された肘静脈より2.1〜9.5 mCi (投与時比放射能64〜1,740 mCi/μ mol, 0.9〜16.2 g)の^{11}C-Ro 15-1788を投与した．トレーサー投与直後より1分間のダイナミックスキャンを20〜40回繰り返した．これらのデーターより検出器の感度補正，体内吸収補正，偶発同時計数の補正の後18 mmごと5スライスの画像再構成を行った．再構成画像は日立社製データー処理装置HARPに転送し，減衰補正を行った後，脳内各領域にライトペンにて関心領域を設け時間放射能曲線を作成した．また1分間のダイナミックスキャンの画像を複数重ね合わせることにより任意の測定時間の画像を作成した．

トレーサーの投与後1分より，経時的に4〜15回静脈採血を行い，血液中総放射能およびジクロロメタンまたはクロロフォルムにより抽出された分画の放射能をウエル型カウンターで測定した．

^{68}Ge-^{68}Ga標準溶液を用いた実験によりキャリ

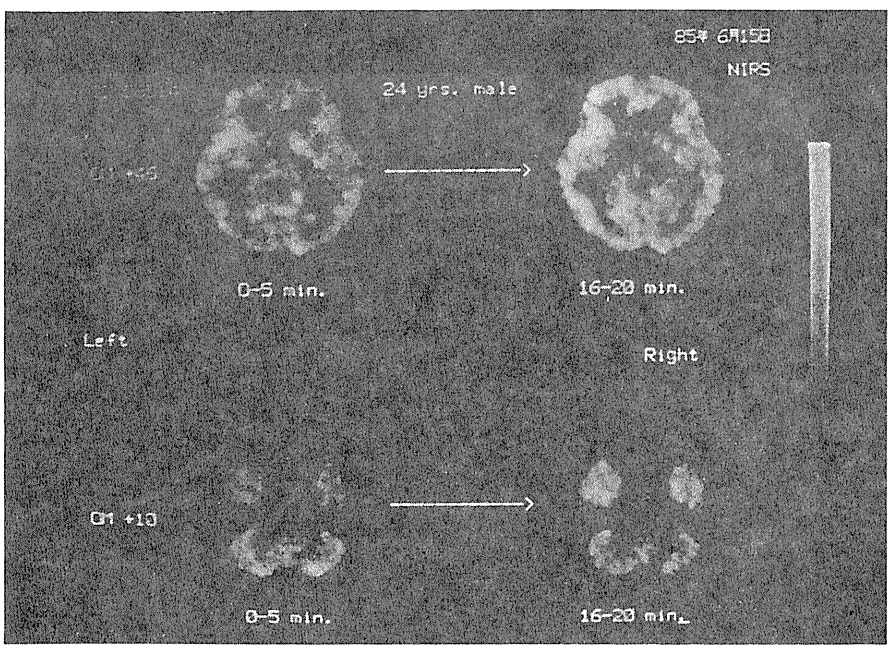

Fig. 1 PET scan of a 24-year-old male volunteer following intravenous injection of carbon-11-labeled Ro 15-1788. Initially (0–5 min.), the cerebral cortex, the basal ganglia and the thalamus were clearly visible. The radioactivity increased in the cerebral cortex at the later time of the study (16–20 min.), whereas the accumulation of ^{11}C in the basal ganglia and the thalamus began to decrease. The radioactivity in the cerebellar cortex was initially (0–5 min.) higher than that in the temporal cortex. This pattern was reversed later (16–20 min.). These images were cross-scaled.

ブレーション係数を求め，脳内放射能濃度および血液中放射能濃度を投与したトレーサーの放射能との比により現した (% DOSE/m*l*).

2名の被験者におき，トレーサー投与後の全身分布をガンマカメラ (GE 社製 Maxi Camera 400 AC/T) にて撮影した．コリメーターは高エネルギー用のもの (MG 2503 BB) を用いた．

4名の被験者では，検査終了後に排尿させ尿中放射能を測定した．

3名のボランティアにトレーサー投与30分前に非標識の Ro 15-1788 をそれぞれ 0.3 mg/kg, 0.5 mg/kg, 1.1 mg/kg 経口にて服用させ脳内動態をコントロール実験と比較した．

III. 結　果

トレーサー投与初期には ^{11}C の分布は大脳皮質，基底核，視床および小脳にて高かった．その後の脳内各領域のトレーサーの動態は異なり，しだいに大脳皮質における ^{11}C の集積が目立つようになった．大脳皮質の中では後頭葉内側部にてやや高いほかはおおよそ一様の分布が見られた (Fig. 1). 大脳皮質の時間放射能曲線のピークはトレーサー投与後 5～11 分 (n=13)にあり，さらに 5～11 分平衡を保った後，徐々に低下した．前頭皮質ではピークで $9.3\pm2\times10^{-3}$% DOSE/m*l* の取り込みが見られた．基底核，視床，小脳の放射能はピークが2～7分にあり，基底核，視床では1～6分平衡を保った後，小脳では 3～9 分平衡を保った後，大脳皮質と比較してすみやかに低下した (Fig. 2). 脳幹のピークは1～3分にありピーク値でも $3.3\pm1.1\times10^{-3}$% DOSE/m*l* と低かった．白質のピークは2～7分にあり，ピークで $5.2\pm1.6\times10^{-3}$% DOSE/m*l* の取り込みが見られた (Table 1).

血液中総放射能は6分程度まですみやかに低下し，その後徐々に低下または一過性に軽度上昇するものもあった (10～20分の平均傾斜 1.1±1.5% min^{-1}, n=11). 血液中総放射能と有機溶媒中に抽出された分画の放射能との差は 3～8 分にて徐々に開大した．有機溶媒中に抽出された分画の放射能の 10～20 分における平均傾斜は 3.2±1.2%

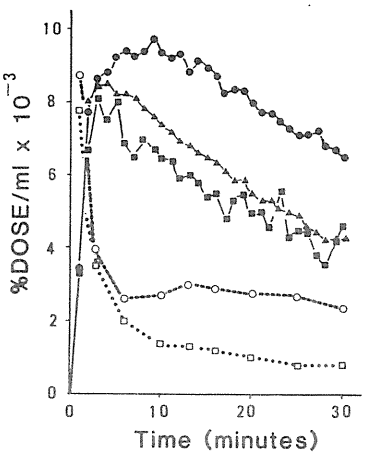

Fig. 2 Time activity curves in some regions of the brain and the blood. The data shown are from a 24-year-old male and are a qualitative representation of the entire group. ROI (region of interest) of the frontal cortex and the basal ganglia were placed in the left hemisphere at the OM +46 mm level, as no asymmetric accumulation of ^{11}C was observed. ROI of the cerebellar cortex was placed at the OM +10 mm level.
(●—●) Frontal cortex, (■—■) Basal ganglia, (▲—▲) Cerebellar cortex, (○----○) Total blood and (□·····□) Organic solvent extracted fraction.

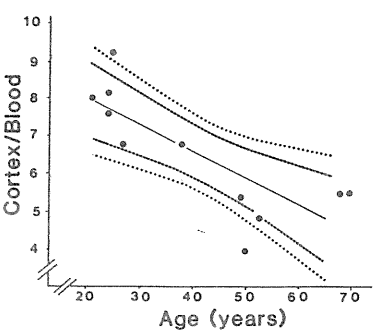

Fig. 3 Age related-decline in Frontal cortex/Blood ratio of ^{11}C radioactivity at 20 minutes post-injection. The data was fitted to a straight line (Y=9.38−0.07X). The lines (-------) (·····) show 99 and 95 percent confidence limits to the regression line respectively.

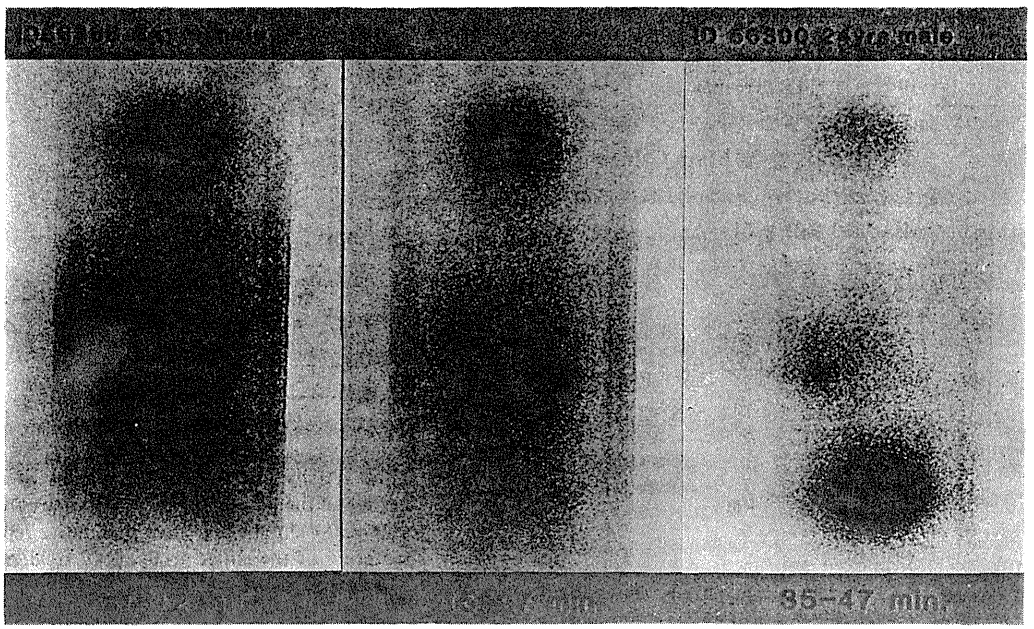

Fig. 4 Whole body scan of two 24-year-old male volunteers after the intravenous injection of carbon-11-labeled Ro 15-1788. At 0–12 minutes postinjection, high accumulation of ^{11}C was in the head, the lower thoracic and the upper abdominal region. At 15–27 minutes, high accumulation of ^{11}C was observed in the brain and the liver. Small amount of ^{11}C was observed in the gallbladder and in the urinary bladder. At 35–47 minutes, the highest accumulation of ^{11}C was in the urinary bladder and small amount of ^{11}C was accumulated in the gallbladder. The relative distirbution of ^{11}C in the brain and the liver was considerably low at this time. The decay correction of ^{11}C was not performed in these images.

min^{-3} (n=11) であった．トレーサー投与後20分で血液中総放射能は $3.2\pm1.0\times10^{-3}$% DOSE/m*l* であり，有機溶媒中に抽出された分画の放射能は $1.3\pm0.2\times10^{-3}$% DOSE/m*l* であった．20分の時点における前頭皮質と有機溶媒抽出分画の放射能比は 6.5±1.6 (n=11) であった．なお被験者を20歳代 (n=5) と50歳以上 (n=4) との二群に分けると前頭皮質と有機溶媒抽出分画の放射能の比は 7.9±0.9 であり，後者では 5.1±0.6 であった (Fig. 3).

4名の被験者におけるトレーサーの尿中排泄量は，トレーサー投与後の30分の時点では10% (n=2)，40分の時点で36% (n=1)，1時間の時点では47% (n=1) であった．

全身スキャンでは0～12分には脳および下胸部より上腹部にかけて高いトレーサーの集積が見られ，15～27分には脳および肝に高いトレーサーの集積が見られ，一部は胆嚢および膀胱に排泄が開始されていた．35～47分には脳および肝のトレーサーは減少しており多くは膀胱に集積し，一部は胆嚢に集積していた (Fig. 4).

飽和実験において，0.5 mg/kg, 1.1 mg/kg の非標識の Ro 15-1788 を服用した2名の被験者では，脳内各領域とも同様に放射能のピークはトレーサー投与後2分にあり，すみやかに低下した．20分の時点における脳内各領域の放射能分布はおおよそ一様となっていた (Table 1, Fig. 5)．20分の時点における前頭皮質の放射能はコントロール実験と比較し，0.3 mg/kg, 0.5 mg/kg, 1.1 mg/kg を服用した3名の被験者におきそれぞれ48%, 22%, 31% にまで減少した．20分の時点における大脳

Table 1 Brain uptake of ^{11}C and its peak in control experiments and saturation experiments

Structure		2 min. (%DOSE×10^{-3})	Peak point (minutes)	Peak height (%DOSE×10^{-3})	20 min. (%DOSE×10^{-3})
Frontal cortex	(control)	7.3±1.9	8.3±2.0	9.3±2.3	8.1±2.0
	(saturation)	6.1±2.3	2	6.1±2.3	1.9±0.8
Temporal cortex	(control)	7.7±2.0	9.2±2.1	9.7±2.5	8.7±2.2
	(saturation)	6.4±2.0	2	6.4±2,0	2.2±0.8
Occipital cortex	(control)	8.6±2.2	8.3±1.7	10.8±2.7	9.2±2.5
	(saturation)	7.0±2.1	2	7.0±2.1	2.2±0.8
Basal ganglia	(control)	7.5±1.8	4.4±1.3	8.4±1.9	5.6±1.2
	(saturation)	5.8±2.1	2	5.8±2.1	1.5±0.7
Thalamus	(control)	6.8±1.9	4.2±1.3	7.6±2.1	5.1±1.9
	(saturation)	6.1±2.0	2	6.1±2.0	1.9±0.8
Cerebellum	(control)	7.1±1.7	4.1±1.0	7.6±2.1	5.5±1.9
	(saturation)	5.9±1.1	2	5.9±1.1	1.9±0.8
Brain stem	(control)	3.4±1.2	2.1±0.5	3.3±1.1	2.1±0.8
	(saturation)	2.9±0.1	2	2.9±0.1	1.8±0.9
White matter	(control)	4.6±1.2	4.5±1.5	5.2±1.6	3.6±1.0
	(saturation)	4.2±1.2	2	4.2±1.2	1.9±0.5

(mean±S.D., control experiment; n=13, saturation experiment; n=2)

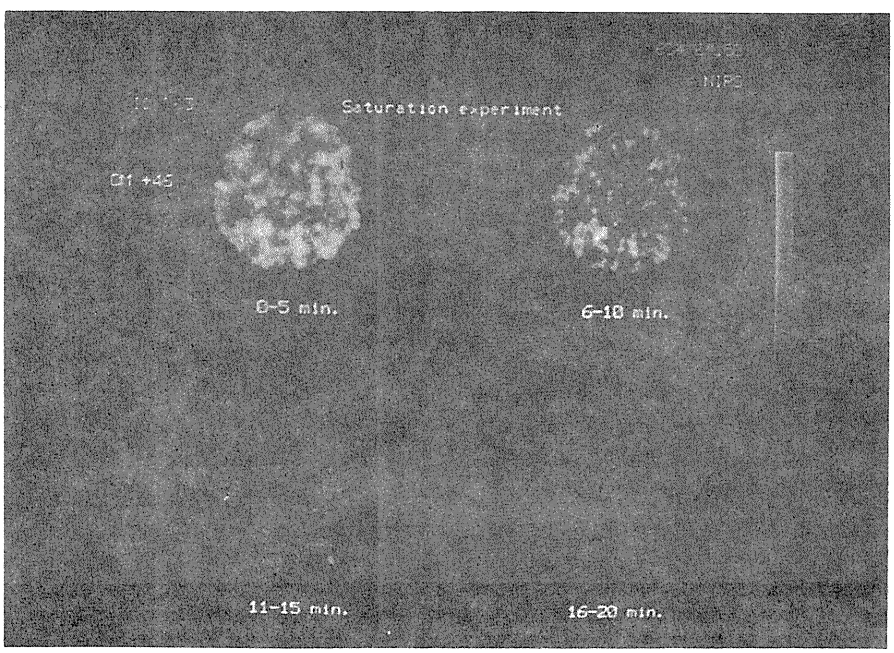

Fig. 5 Serial images in the saturation experiment. This subject, a 53-year-old male, took 1.1 mg/kg of cold Ro 15-1788 30 minutes prior to injection orally. These images show rapid decrease of ^{11}C through out the brain.

皮質と血液（有機溶媒抽出分画）との放射能の比は1.1 mg/kgを服用した被験者において1.5と低かった．

検査後1名の被験者でごく軽度のふらつき感を訴えたものがあったが，他には本検査による異常を訴えた者はなく，7名の被験者において行った検査前後の一般血液検査でも異常を認めた者はいなかった．

IV. 考　察

^{11}C-Ro 15-1788静注後，脳内放射能はすみやかに上昇し高い取り込みが見られ，本トレーサーの脳内移行性は良好であると考えられた．

トレーサー投与後5分程までは，大脳皮質，基底核，視床，小脳にトレーサーの集積が高く，正常人における脳血流の分布[24,25]と相似する分布であった．10分以後では，基底核，視床，小脳のトレーサーの集積は減少し大脳皮質との差が明瞭となり，脳幹ではトレーサーの集積がきわめて低いなど，in vitroの検索による人脳のベンゾジアゼピン・レセプターの分布（maximum number of binding sites）[3,11,26]と相似するものとなった．なお，白質のほうが脳幹に比べトレーサーの分布が高いのは部分容積効果により灰白質が混入するためと考えられた．

Ro 15-1788は正常人に単独で投与された場合には作用をもたず[27,28]，被験者に負担をかけずに飽和実験を行うことができた．十分なキャリアーを加えた飽和実験時の脳内放射能は〖血液中＋フリー＋非特異的結合〗のトレーサーの放射能を反映したものと考えられる．またコントロール実験との差は特異的結合を反映したものと考えられる．このことより，コントロール実験においてトレーサー投与初期には〖血液中＋フリー＋非特異的結合〗のトレーサーの放射能の占める割合が高いが時間経過とともに特異的結合したトレーサーの放射能の占める割合が高くなり，脳内各領域のベンゾジアゼピン・レセプターの分布に相関したイメージが現れるものと思われる．なおトレーサー投与後20分の時点における大脳皮質での特異的結合の占める割合は70～80％と考えられる．さらに大量のキャリアーを加えた場合には脳内放射能の減少がさらにすみやかになる可能性もあるが，本実験の結果はトレーサー投与後10分の時点で0.05 mg/kgの非標識Ro 15-1788を静注してdisplacementを行ったSamsonらの結果[20]と一致している．^{11}C-Ro 15-1788は比較的短い検査時間において特異的結合の割合が高い分布を得ることができ，レセプターの異常，変化をとらえるのに優れたトレーサーであるといえよう．

また本トレーサーは約5 mCiの投与により十分な情報を得ることができ被曝線量は少なくてすむものと考えられた（Table 2）．

トレーサー投与後3～8分にて血液中総放射能濃度と有機溶媒にて抽出される分画との差が開いてくるが，これは^{11}C-Ro 15-1788が代謝され水溶性の代謝産物が生じてくるためと考えられる．ヒヒを用いた実験にて約80分までは脱メチル化は起こらないことが報告されており[19]，代謝は主に

Table 2 Estimated exposure dose by injection of ^{11}C-Ro 15-1788 in human (MIRD method)[21]

Organ	mRad/mCi
Adrenal gland	6.2
Bladder	51
Small intestine	78
Large intestine	6.3
Kidney	12
Liver	9.7
Lung	4.3
Pancreas	3.8
Spleen	3.6
Testis	2.9
Ovary	8.9
Thymus	3.2
Thyroid	4.8
Uterus	5.8
Breast	0.9
Skull	5.8
Ribs	1.6
Spine	5.8
Pelvis	3.6
Arm bone	4.8
Leg bone	8.5
Red marrow	3.1

エステル基が加水分解される形で行われるのであろう．有機溶媒中に抽出された分画の放射能はほとんど未変化の ^{11}C-Ro 15-1788であると考えられた．血液中総放射能が一過性に軽度上昇することがあるのは末梢臓器（肝など）より代謝産物が血液中に放出されるためと推定される．投与されたトレーサーの一部は胆汁中に排泄され大部分は水溶性代謝産物として腎よりすみやかに排泄されるものと考えられる．トレーサーの尿中への排泄はすみやかであるので検査後直ちに排尿させることにより被曝線量をさらに軽減させることができる．

大脳皮質と血液（有機溶媒抽出分画）との放射能の比が若年群と中高年群とで異なる．これは両者にてレセプターの結合状態が異なる可能性のほか，血液中でトレーサーと蛋白との結合状態が異なる可能性，脳内の非特異的結合の状態が異なる可能性，脳血流の変化の影響なども考慮しなければならないであろう．老化の脳内レセプターに対する影響は今後追求すべき課題である．

以上 ^{11}C-Ro 15-1788 ポジトロン CT 検査は非侵襲的かつ安全な検査であり，in vivo ベンゾジアゼピン・レセプター測定に大きなポテンシャルをもつ方法と考えられた．

V. まとめ

1) 正常ボランティア 15 名を対象として ^{11}C-Ro 15-1788 の臨床治験を行い，本トレーサーの有効性および安全性を検討した．

2) ^{11}C-Ro 15-1788 の脳内移行性は良好であり大脳皮質にてもっとも高い取り込みが見られた．

3) トレーサー投与後20分の時点における脳内分布は in vitro の検索によるベンゾジアゼピン・レセプターの分布と相似するものであった．

4) 飽和実験ではコントロール実験と比較しトレーサー投与後 20 分の時点における大脳皮質の放射能は 20～30％にまで低下した．

5) 1時間にて投与されたトレーサーの約半分が尿中に排泄された．

6) 本検査による特別な副作用は認められなかった．

謝辞：Ro15-1788 および N-desmethyl 体を供与してくださった日本ロッシュ株式会社ならびに貴重な助言をいただいた中村圭二，岡田敏一両博士に深謝いたします．

文　献

1) Möhler H, Okada T: Benzodiazepine receptor: Demonstration in the central nervous system. Science 198: 849–851, 1977
2) Squires RF, Braestrup C: Benzodiazepine receptors in rat brain. Nature 266: 732–734, 1977
3) Braestrup C, Albrechtsen R, Squires RF: High densities of benzodiazepine receptors in human cortical areas. Nature 269: 702–704, 1977
4) 岡田敏一：ベンゾジアゼピン・レセプター．神経精神薬理 2: 5–16, 1980
5) Paul SM, Skolnick P: Rapid changes in brain benzodiazepine receptors after experimental seizures. Science 202: 892–894, 1978
6) Robertson HA: Audiogenic seizures: Increased benzodiazepine receptor binding in a susceptible strain of mice. Eur J Pharmacol 66: 249–252, 1980
7) Medina JH, Novas ML, Wolfman CNV, et al: Benzodiazepine receptors in rat cerebral cortex and hippocampus undergo rapid and reversible changes after acute stress. Neurosci 9: 331–335, 1983
8) Soubrie P, Thiebot MH, Jobert A, et al: Decreased convulsant potency of picrotoxin and pentetrazol and enhanced (^{3}H) Flunitrazepam cortical binding following stressful manipulations in rats. Brain Res 189: 505–517, 1980
9) Medina JH, Novas ML, Robertis ED: Chronic Ro 15-1788 treatment increases the number of benzodiazepine receptors in rat cerebral cortex and hippocampus. Eur J Pharmacol 90: 125–128, 1983
10) Rosenberg SHC, Chiu TH: Decreased ^{3}H-Diazepam binding in a specific response to chronic benzodiazepine treatment. Life Sci 24: 803–804, 1979
11) Möhler H, Okada T: The benzodiazepine receptor in normal and pathological human brain. Brit J Psychiat 133: 261–268, 1978
12) Reisine TD, Wastek GJ, Speth RC, et al: Alterations in the benzodiazepine receptor of Huntington's diseased human brain. Brain Res 165: 183–187, 1979
13) Walker FU, Young AB, Penney JB: Benzodiazepine and GABA receptors in early Huntington's disease. Neurology (Cleaveland) 34: 1237–1240, 1984
14) Owen F, Poulter M, Waddington JL, et al: (^{3}H)Ro 05-4864 and (^{3}H)Flunitrazepam binding in kainate-lesioned rat striatum and in temporal cortex of brains from patients with senile dementia of the

Alzheimer type. Brain Res 278: 373–375, 1983
15) Hunkeler W, Möhler H, Pieri L, et al: Selective antagonists of benzodiazepines. Nature 290: 514–516, 1981
16) Bonetti EP, Pieri L, Cumin R, et al: Benzodiazapine antagonist Ro 15-1788: Neurological and behavioral effects. 78: 8–18, 1982
17) Mazière M, Hantraye P, Prenant C, et al: Synthesis of Ethyl 8-Fluoro-5,6-dihydro-5-(^{11}C)methyl-6-oxo-4H-imidazo(1,5-a)(1,4)benzodiazepine-3-carboxylate (Ro 15-1788-^{11}C) A specific radioligand for the in vivo study of central benzodiazepine receptors by positron emission tomography. Int J Appl Radiat Isot 35: 973–976, 1984
18) Mazière M, Prenant C, Sastre J, et al: ^{11}C-Ro 15-1788 et ^{11}C-Flunitrazepam, deux coordinats pour l'étude par tomographie par positons des sites de liaison des benzodizépines. C R Acad Sc Paris Série III 296: 871–876, 1983
19) Hantraye P, Kaijima M, Prenant C, et al: Central type benzodiazepine binding sites: A positron emission tomography study in the baboon's brain. Neurosci Lett 48: 115–120, 1984
20) Samson Y, Hantraye P, Baron JC, et al: Kinetics and displacement of (^{11}C)Ro 15-1788, a benzodiazepine antagonist, studied in human brain in vivo by positron tomography. Eur J Pharmacol 110: 247–251, 1985
21) 井上 修, 橋本謙二, 山崎統四郎, 他：^{11}C-Ro 15-1788の前臨床段階における有効性と安全性の評価. 核医学 22 (11): 1711–1715, 1985
22) Suzuki K, Inoue O, Hashimoto K, et al: Computer-controled large scale production of high specific activity ^{11}C-Ro 15-1788 for PET studies of benzodiazepine receptors. Int J Appl Radiat Isot (in press)
23) Takami K, Ueda K, Okajima K, et al: Performance of whole-body, multislice positron computed tomograph—Positologica II—. IEEE Trans Nucl Sci 30: 734–738, 1983
24) Yamamoto YL, Meyer E, Menon D, et al: Regional cerebral blood flow measurement and dynamic positron emission tomography. Heiss WD, Phelps ME. eds. Positron emission tomography. Springer Verlag, Berlin Heiderberg New York, pp. 78–84, 1983
25) Grandiè PL, Baron JC, Soussaline F, et al: Coupling between blood flow and oxygen utilization in the normal human brain. Arch Neurol 40: 230–236, 1983
26) Luabeya MK, Malateaux JM, Laduron PM: Regional and cortical laminar distributions of serotonin S_2, benzodiazepine, muscarinic, and dopamine D_2 receptors in human brain. J Neurochem 43: 1068–1071, 1984
27) Darragh, A, Lambe RJ, Scully M, et al: Investigation in man of the efficacy of a benzodiazepine antagonist, Ro 15-1788. Lancet 2: 8–10, 1981
28) Darragh A, Lambe R, Kenny M, et al: Tolerance of healthy volunteers to intravenous administration of the benzodiazepine antagonist Ro 15-1788. Eur J Clin Pharmacol 24: 569–570, 1983

Summary

A Study of Benzodiazepine Receptor in Human Brain Using ^{11}C-Ro 15-1788 and Positron Emission Tomography

Hitoshi SHINOTOH*, Toshirou YAMASAKI*, Osamu INOUE*, Takashi ITOH*, Kenji HASHIMOTO*, Yukio TATENO*, Hiroo IKEHIRA*, Kazutoshi SUZUKI** and Yoshihiko KASHIDA***

**Division of Clinical Research, **Section of Cyclotron, ***Senior Research Counselor, National Institute of Radiological Sciences*
Address correspondence: Dr. Hitoshi Shinotoh
Division of Clinical Research, National Institute of Radiological Science
9-1, Anagawa 4-chome, Chiba-shi 260, Japan

A study of benzodiazepine receptor was performed in 15 healthy normal volunteers using carbon-11 labeled Ro 15-1788 and positron emission tomography. The brain kinetics of ^{11}C-Ro 15-1788 showed a high uptake of the tracer by the brain, the maximum of which was within 20 minutes. The early distribution of the tracer after injection showed a regional distribution similar to that of any perfusion tracer with high activity in the cerebral cortex, the basal ganglia, the thalamus and the cerebellum. The peak of the radioactivity was reached earlier in the basal ganglia, the thalamus and the cerebellum than in the cerebral cortex. The accumulation of ^{11}C was highest in the cerebral cortex, moderate in the thalamus, the basal ganglia and the cerebellum and low in the brain stem at 20 minutes post-injection. The distribution of the tracer at 20 minutes post-injection was approximately parallel to the known distribution of benzodiazepine receptors (B_{max}) in human in vitro.

Cold Ro 15-1788 was administered with the dose of 0.3 mg/kg, 0.5 mg/kg and 1.1 mg/kg in three volunteers 30 minutes prior to injection. The radioactivity in the cerebral cortex were reduced to 48%, 22%, and 31% of those in the control experiments respectively.

About half of the injected tracer was excreted in the urine at 1 hour after injection.

^{11}C-Ro 15-1788 is a potent radioligand to study benzodiazepine receptors in vivo in human.

Key words: Positron emission tomography, Benzodiazepine, Receptor, Ro 15-1788.

昭和６０年度第１回短寿命及び陽電子ＲＩの診断利用に関する研究委員会議事概要

日　時：昭和60年７月29日(月)10：00~14：00
場　所：霞山会館
委員出席者：舘野之男(委員長)、田中栄一、山崎統四郎、飯沼　武、樫田義彦、黒澤淳、小嶋正治、鈴木徳治、高橋道人、寺尾允男、鳥塚莞爾、野崎　正、葉杖正昭、村山　智、山田　隆
オブザーバー：井上　修、鈴木和年、福田信男、山根昭子、玉手和彦、富永俊義、橋本謙二、篠遠　仁、内田　淳、伊藤高司
委員欠席者：有水　昇、飯尾正宏、広部雅昭、井戸達雄
配布資料：
① 11C－DMPEA注射剤の前臨床段階における有効性と安全性の評価
② サイクロトロン製造放射薬剤品質管理基準改正について

議事概要
1. 井上より新規薬剤11C－DMPEA注射剤の前臨床段階における有効性と安全性の評価および臨床利用計画について報告がなされた。
11C－DMPEA注射剤のpH、DMPEAの末梢における代謝などについての質問がなされ、井上より説明が行われた後、11C－DMPEAの臨床治験開始の承認がなされた。
2. 一般の新規放射薬剤の前臨床段階の安全性の評価の方法について、放医研または日本アイソトープ協会において審議することとなった。
3. サイクロトロン製造放射薬剤品質管理基準改正については、次回に審議をもちこすこととなった。

昭和６０年度第１回粒子線治療研究委員会／粒子線治療臨床部会合同会議議事概要

日　時：昭和60年８月２日(金)10：00~14：00
場　所：霞山会館(東京都千代田区)
出席者：委員長　恒元　博
委　員　柄川　順、春日　猛、松田忠義、飯田孔陽、鎌田力三郎、北川俊夫、尾内能夫、稲田哲雄、津屋旭、入江五朗、坂本澄彦、飯沼武
部会員　伊藤晴夫、尾形佳郎、笠松達弘、花岡英弥、荒居龍雄、石川達雄、森田新六
説明者　川島勝弘、大原　弘、丸山隆司、青木芳朗、河内清光、山田　隆、中野隆史、五味弘道、小池幸子、石井　猛、鈴木治夫(事務局)
配布資料：
1. 特別研究経過報告
2. 速中性子線治療の研究計画
3. 陽子線治療の研究計画
4. 医用重粒子加速器計画
5. 粒子線治療物理研究部会及び生物研究部会報告

6. 他の研究組織との研究交流
7. 重粒子線治療の目標
8. ＬＢＬにおける治療計画

議事概要：

委員長より昭和６０年度における研究実行計画の概要説明があり、陽子線垂直ビーム治療のための整備と、医用重粒子加速器の概念設計研究が今年度の重点課題である旨紹介された。

1. 臨床トライアルに関する討議

ａ．速中性子線治療

昭和５０年１１月から昭和６０年４月までに１２５８例（初回治療９７６例）が速中性子線治療を受けた。今回は多型性神経膠腫の治療成績が報告され、照射線量、及び標的容積の設定など今後の治療方針について討議が行なわれた。

速中性子線治療の評価を充実するため、治療技術の改善は今後とも必要である。

ｂ．陽子線治療

昭和５４年１０月から昭和６０年７月までに３０例が陽子線治療を受けた。筑波大学における臨床トライアルの経過を含めて討議が行なわれ悪性黒色腫に対する陽子線の効果は病理組織型によってかなり影響されること、脳腫瘍治療の場合には照射野の設定と線量配分についても十分経験を積み重ねる必要がある旨報告された。

2. 物理生物部会報告に関する討議

陽子線垂直ビーム用コリメーターの設計に関して、特にmulti－leafコリメーターの型状とボーラスの使用方法について討議が行なわれた。医用重粒子線加速器の概念設計研究に関しては概念調査の成果に基づいて研究をすすめることになった。

3. 重イオン治療に関する討議

委員長より重イオン治療の目的と治療技術、並びに治療に必要な設備と組織作りに関する基本方針の提示があり、引き続き遠藤（臨床）よりＬＢＬにおいて用いられている重イオン治療計画法が紹介された。討議の中では、ａ）治療の再現性を確保するために必要な技術開発、ｂ）腫瘍の総合画像診断法の充実の必要性がそれぞれ強調された。

4. 他研究組織との交流

文部省がん特別研究（Ｉ）、厚生省対がん戦略研究事業、及び筑波大学粒子線医科学センターにおけるこれまでの研究内容がそれぞれ紹介され、各組織との情報交換を密にして粒子線治療研究を推進することになった。

特別研究「重粒子線等の医学利用に関する調査研究」
昭和60年度　班員名簿

（班　長）	恒元　博	病院部長
（副班長）	舘野之男	臨床研究部長
（顧　問）	松沢秀夫	特別研究員
	樫田義彦	〃
	市川龍資	医用サイクロトロン委員会委員長
	吉川元之	技術部放射線安全課長
	山田　隆	技術部サイクロトロン管理課長

1. 医用重粒子加速器に関する調査研究

丸山隆司	物理研究部第3研究室長
松沢秀夫	特別研究員
田中栄一	物理研究部長
野原功全	物理研究部第1研究室長
川島勝弘	〃　第2研究室長
星野一雄	〃　第2研究室
平岡　武	〃　〃
野田　豊	〃　第3研究室
中島敏行	〃　第4研究室長
喜多尾憲助	〃　第4研究室
河内清光	〃　〃
金井達明	〃　〃
河村正一	化学研究部長
江藤久美	生物研究部第2研究室長
大原　弘	生理病理研究部生理第2研究室
飯沼　武	臨床研究部第4研究室長
石川達雄	〃　第2研究室長
中村　譲	〃　第2研究室
遠藤真広	〃　〃
恒元　博	病院部長
荒居龍雄	病院部医務課長
森田新六	病院部医務課医長
技術部サイクロトロン管理課	

技術部技術課
技術部放射線安全課

2. 重粒子線治療システムに関する研究

(1) 重粒子線治療に関する臨床的研究

石川達雄	臨床研究部第4研究室長
安藤興一	〃 第4研究室
古川重夫	〃 〃
小池幸子	〃 〃
恒元博	病院部長
荒居龍雄	病院部医務課長
森田新六	〃 医務課
青木芳朗	〃 〃
中野隆史	〃 〃
五味弘道	〃 〃

(2) 重粒子線治療に関する技術的研究

川島勝弘	物理研究部第2研究室長
星野一雄	〃 第2研究室
平岡武	〃 〃
丸山隆司	〃 第3研究室長
野田豊	〃 第3研究室
中島敏行	〃 第4研究室長
河内清光	〃 第4研究室
金井達明	〃 〃
石川達雄	臨床研究部第4研究室長
古川重夫	〃 第4研究室
中村譲	〃 第2研究室
森田新六	病院部医務課
岡崎実	〃 〃
坂下邦雄	〃 〃
熊谷和正	〃 〃

(3) 重粒子線治療に関する生物学的研究

大原弘	生理病理研究部生理第2研究室
安藤興一	臨床研究部第4研究室

小島栄一	障害基礎研究部第1研究室
金井達明	物理研究部第4研究室
山口寛	〃　第3研究室
大野忠夫	薬学研究部第2研究室

(4) 重粒子線治療計画に関する研究

飯沼武	臨床研究部第2研究室長
中村譲	〃　第2研究室
松本徹	〃　〃
遠藤真広	〃　〃
池平博夫	〃　第3研究室
古川重夫	〃　第4研究室
石川達雄	〃　第4研究室長
舘野之男	臨床研究部長

3. 重粒子線治療のための医学診断に関する調査研究

(1) 診断用核医学薬剤の開発に関する研究

山崎統四郎	臨床研究部第1研究室長
福士清	〃　第1研究室
入江俊章	〃　〃
井上修	〃　〃
鈴木和年	技術部サイクロトロン管理課

(2) 核医学の測定技術の開発に関する研究

田中栄一	物理研究部第1研究室長
野原功全	〃　第1研究室
富谷武浩	〃　〃
山本幹男	〃　〃
村山秀雄	〃　〃
山崎統四郎	臨床研究部第1研究室長
飯沼武	〃　第2研究室長
舘野之男	臨床研究部長

(3) 画像診断の臨床応用に関する研究

舘野之男	臨床研究部長
山崎統四郎	臨床研究部第1研究室長

井　上　　修	臨床研究部	第1研究室
福　田　信　男	〃	第3研究室
池　平　博　夫	〃	〃
篠　遠　　仁	〃	〃
飯　沼　　武	〃	第2研究室長
松　本　　徹	〃	第2研究室

特別研究「重粒子線等の医学利用に
関する調査研究」論文集　第２集

編集委員　恒元　博
　　舘野之男
編集協力　田中　昭
　　進士賀一

千葉市穴川４－９－１
放射線医学総合研究所
Tel. 0472－51－2111